UNIVERSIDADE D
COIMBRA

Joana Filipa Pires d'Oliveira Quaresma

OPTICAL FIBER METROLOGY FOR DETONATION CHARACTERIZATION OF ENERGETIC MATERIALS

Tese no âmbito do doutoramento em Engenharia Mecânica, ramo Aerodinâmica, Riscos Naturais e Tecnológicos orientada pelos Professores Doutores José Leandro Simões de Andrade Campos e Ricardo António Lopes Mendes e apresentada ao Departamento de Engenharia Mecanica da Faculdade de Ciências e Tecnologia da Universidade de Coimbra.

Maio de 2021

Faculty of Sciences and Technology of the University of Coimbra

OPTICAL FIBER METROLOGY FOR DETONATION CHARACTERIZATION OF ENERGETIC MATERIALS

Joana Filipa Pires d'Oliveira Quaresma

Doctoral Thesis in Mechanical Engineering, in the field of Aerodynamics, Natural and Technological Risks, supervised by Professor Doctor José Leandro Simões de Andrade Campos and Professor Doctor Ricardo António Lopes Mendes, submitted to the Department of Mechanical Engineering of the Faculty of Sciences and Technology of the University of Coimbra.

May 2021

1 2 9 0

UNIVERSIDADE D COIMBRA

A mesma esquizofrénica humanidade que é capaz de enviar instrumentos a um planeta para estudar a composição das suas rochas, assiste indiferente à morte de milhões de pessoas pela fome. Chega-se mais facilmente a Marte neste tempo do que ao nosso próprio semelhante.

José Saramago, em Discurso pronunciado no Banquete Nobel, 1998

ACKNOWLEDGEMENTS

"When we fight we not always win, but if we don't fight, we will always lose". This was the sentence chosen for my master thesis, but it is even more adequate for this Ph.D. thesis. Here is the end of a huge battle that, for many times, seemed to be lost during its path. It was not easy, it was not pleasant, many troubles appeared during these years, as a battle should be. But now it is finished and all the bad parts of the battle were compensated. I am very grateful to all that were with me in this fight, even to the ones that behaved more like enemies than to belonging to my army. To those, thank you for making me stronger.

Thank you, Professor José Campos, Thomas Keicher, Lukas Deimling, and Stefan Löbbecke for giving me the opportunity of doing this Ph.D. at Fraunhofer ICT.

To Professor Ricardo Mendes, my deepest and heartful thank you. You were the savior of this thesis, without you this battle would be already lost for some years. Thank you for transmitting such valuable knowledge, for the patience in explaining everything, for supporting me on the hardest working times, for the long hours in Zoom, for this huge accomplishment. Thank you very much! To LEDAP, thank you for supporting my Ph.D.

Thank you to João Pimenta, for all the support from Portugal that he always gave me, professionally and personally. To my friends in ICT that made the lunchtimes so pleasant, made me feel less alone, helped me when needed, and I know that some of you will stay with me for life. Thank you Ligia Radulescu, Giancarlo Piscopo, Angelos Poyzoidis, Slobodan ("Slobo") Panic, Gunnar Kronis, Sven Hafner, and Matthias Kühn. Thank you very much, Thorsten Klahn and Stephanie Kühn, for having me at your home and for becoming such good friends. Thank you to all group 8 of Energetic Materials and to all that directly and indirectly contributed to my thesis at ICT.

My special thank you to my parents that always supported me and taught me the value of the study. Especially to my mother, Maria da Conceição Pires, she was always there and she is a reference for me. To my uncle and aunt Edgar and Teresa Sepúlveda that were always there to support me and, mostly, my mother. It helped me a lot in winning this battle. Thank you! And to Teresa Costa, my mother by heart that I always can count.

Thank you very much to my life partner, Christoph Krahl, for always loving me, supporting me, and always being there. You passed really hard times and I am so thankful that you were always there, showing your love for me. You were really important during this journey.

Thank you to my best friends Inês Drumond and Mariana Correia, for always being there for me. You don't know how important our text/voice messages and talks were important to me to stand this Ph.D. and all the problems involved in being an emigrant. Thank you to my dear friends, Joana Grade and Sara Teixeira, for always showing me your friendship and love when we were together.

To all my Portuguese friends in Karlsruhe, my thank you very much for making me feel at home, for your support in the hard times, and for your presence in the good ones. Especially to Suzy Dunker, Mário Moreira, and Paulo Silveira.

To the family and friends of Christoph, my thank you for accepting me as one of your own.

Abstract

Detonation metrology is essential for the development of energetic materials, to characterize existing explosives, and to characterize materials behavior under high pressures. This work aimed to develop metrology based on optical fibers probes to be applied on the characterization of the detonation and/or shock process, as well as based on a light converting system that is not expensive and which signals are easy to read.

To achieve these objectives, multimode PMMA optical fibers (250 μm diameter) working as bare or protected probes, with stainless steel tubes, were tested. Two working methods, in terms of radiation generation, were applied and discussed. In the optical passive method (OPM), the optical fiber probes capture the radiation generated by the detonation/shock process, originating a positive electrical signal. The optical active method (OAM) consists of transmitting laser radiation (660 nm) through the optical fiber probes that lose their transmission properties when shocked by a detonation or shock wave, which originate negative electrical signals.

The different probes and methods were extensively studied to determine their limitations and were used to determine detonation velocity and pressure of Seismoplast, a PETN-based explosive with a density of 1.56 g/cm^3. These limitations make that different probes have to be used on the OAM, according to the parameter that is desired to measure and to the shape of the charge.

To find the P_{CJ}, the movements $x(t)$ of the shock waves generated by the detonation of Seismoplast in three inert materials were characterized. With the explosive/inert material interface shock velocities were possible to find the pressures and particle velocities and, through the impedance matching technique (IMT) it was determined the CJ pressure of Seismoplast.

For rectangular cross-section charges using the OPM with the two different probes, the detonation velocities of Seismoplast obtained ranged from 7237 to 7336 m/s, with standard deviations between 1.1 and 6.0 %. For the active optical method, the experimental results for detonation velocity varied between 7258 and 7367 m/s and were obtained with a standard deviation range of 0.6 to 1.7 %.

The OAM with bare optical probes was used to measure the induced shock wave velocities generated by Seismoplast on different thicknesses of PMMA (1–9 mm), aluminum, and copper (1–7 mm). Based on the shock wave velocities at the interfaces between the explosive and the inert barriers, the CJ pressure of Seismoplast was determined as 21.2 GPa. Based on the CJ point (P_{CJ}, $u_{P,\,CJ}$) and using an empirical method proposed by Cooper, it was possible to estimate the Hugoniot of detonation products of Seismoplast.

The OAM, with bare and protected optical probes, was used to determine the detonation velocity of two other compositions, HWC (based on RDX) with a density of 1.68 g/cm^3, and TKX-50, an energetic ionic salt with a density of 1.70 g/cm^3. This method with bare optical probes was also used to estimate the detonation pressure of TKX-50.

Keywords Detonation and shock physics, PETN-based explosive, Optical fiber metrology; Detonation velocity, CJ pressure.

Resumo

A metrologia da detonação é essencial para o desenvolvimento de materiais energéticos, para a caracterização dos explosivos existentes, e para caracterizar o comportamento dos materiais sobre altas pressões. Este trabalho teve como objectivo desenvolver uma metrologia de detonação baseada em fibras ópticas que é independente da radiação gerada pelo processo de detonação/choque, e que incorpora um conjunto de componentes para o sistema de conversão optoeléctrico relativamente simples.

As sondas utilizadas nesta metrologia são baseadas em fibras ópticas multimode de PMMA (250 μm de diâmetro). Estas sondas consistiram em fibras ópticas desprotegidas, ou protegidas com tubos de aço inox. Foram aplicados e discutidos dois métodos de funcionamento desta metrologia, em termos da radiação gerada. No método óptico passivo (MOP), as sondas de fibra óptica capturam a radiação gerada pelo processo de detonação/choque, dando origem a um sinal eléctrico positivo. O método óptico activo (MOA) consiste na transmissão de radiação laser (660 nm) através das sondas de fibra óptica, as quais perdem a capacidade de transmissão quando são chocadas por uma onda de detonação ou de choque, originando sinais eléctricos negativos.

Os métodos foram testados na determinação da velocidade (D) e pressão (P_{CJ}) de detonação do Seismoplast, um explosivo baseado em PETN com densidade de 1.56 g/cm^3. Os diferentes métodos e sondas foram estudados intensivamente para determinar as suas limitações, as quais fazem com que tenham de ser usadas sondas diferentes no MOA, de acordo com o parâmetro que é desejado medir.

Para determinar a P_{CJ} foi necessário caracterizar o movimento $x(t)$ da onda de choque gerada pela detonação do Seismoplast em três materiais inertes diferentes (PMMA, alumínio e cobre). Com as velocidades de choque nas interfaces explosivo/material inerte foi possível calcular as respectivas pressões e velocidades do ponto material e, através da técnica de adaptação de impedâncias, obteve-se a pressão de CJ do Seismoplast.

Quando se utilizou o MOP em cargas de secção rectangular com os dois tipos diferentes de sondas, as velocidades de detonação medidas variaram entre 7237 e 7336 m/s,

com desvios padrões entre 1.1 e 6%; para o MOA, os resultados experimentais da velocidade de detonação variaram entre 7258 e 7367 m/s, com desvios padrões a variar entre 0.6 e 1.7%.

O MOA com sondas de fibras ópticas desprotegidas foi utilizado para determinar a velocidade da onda de choque induzida pelo Seismoplast em função das espessuras de PMMA, alumínio e cobre. Com base nas velocidades da onda de choque calculadas nas interfaces explosivo/barreira inerte, o resultado para a pressão de CJ do Seismoplast foi de 21.2 GPa.

A partir da determinação do ponto de CJ (P_{CJ}, $u_{P,\,CJ}$) e do método empírico proposto por Cooper, foi possível estimar a curva de Hugoniot para os produtos de detonação do Seismoplast.

O MOA, com sondas de fibras ópticas desprotegidas e protegidas, foi utilizado para determinar a velocidade de detonação de outras duas composições, HWC (baseado em RDX) com densidade 1.68 g/cm^3, e TKX-50, um sal iónico energético com densidade 1.70 g/cm^3. Este método também foi ultilizado, com sondas ópticas desprotegidas, para estimar a pressão de detonação do TKX-50.

Palavras-chave: Física do choque e da detonação, Explosivo baseado em PETN, Metrologia com fibra óptica, Velocidade de detonação, Pressão de CJ.

Contents

LIST OF FIGURES

LIST OF TABLES

LIST OF SYMBOLS AND ACRONYMS/ ABBREVIATIONS

List of Symbols

B – magnetic induction field

c – speed of light

C_b – sound velocity of a material

c_P – specific heat at constant pressure

c_V – specific heat at constant volume

D – detonation velocity

e – internal energy of the products of the reaction

E_0 – constant voltage

$E(t)$ - electromotive force

f – frequency

$f_b(t)$ – frequency of the beat signal

f_d – Doppler-shifted frequency

f_S – crystal frequency

f_0 - initial laser frequency

F – external forces

h – enthalpy

I_s – constant current flowing through a probe

K - piezoresistive coefficient

l – length

$L(t)$– probe's length according to time

m – image magnification

n – number of moles or refraction index

N – clock number

p – pressure

p_0 – initial pressure or ambient pressure

$P(t)$ – pressure according to time

$\mathcal{P}$ – period of a full beat cycle

q – heat

R – resistance

r_{p} – probe's electric resistance per length unit

$r(t)$ – resistance according to time

s – entropy

S – standard error of the regression line; dimensionless constant

T – temperature

TDM – theoretical maximum density

T_0 – initial temperature

u – local flow velocity

u_P – particle velocity

V – specific volume

$v(t)$ – velocity

v – velocity according to time

$V(t)$ – voltage probe output according to time

w – work

u_{fs} – free-surface velocity

u_{P} – Particle velocity

U_{S} – Shock wave velocity

Z – impedance relation

Δt – time interval

Δx – distance

ε_{r} – relative permittivity of the material

φ(t) – instantaneous phase

γ – specific heat ratio

λ_{c} – cutoff wavelength

λ_{g} – interference wavelength

λ_L – wavelength of the laser

λ_0 – free-space wavelength

ρ – density of the products of reaction

$\mathcal{R}$ – constant of the perfect gases

Acronyms/Abbreviations

ABOP – active bare optical probe

ADC - analog-to-digital converter

APOP – active protected optical probe

ASE – amplified spontaneous emission

BOP – bare optical probe

CCD – charged-coupled device

CFBG – chirped fiber Bragg grating

CJ – Chapman-Jouguet

DW – detonation wave

DRZ – detonation reaction zone

EEx – emulsion explosives

EM – energetic material

EMF - electromotive force

EoS – equation of state

EPV - electromagnetic particle velocity

fps – frames per second

FT – fall time

FPGA – field programable gate array

FPI – Fabry-Perot interferometer

GOF – glass optical fibers

HP – Hugoniot curve of the detonation products

HWC – RDX/Wax/Graphite

ICCD – intensified charged-coupled device

IMT – impedance matching technique

LCD – liquid-crystal display

LCS – laser control system

MCP – micro-channel plate

MFOP – multi-fiber optical probe

MI – microwave interferometry

N – clock number

OAM – optical active method

OECS – optoelectric converter system

OF – optical fiber

OPM – optical passive method

PBOP – passive bare optical probe

PBX – plastic bonded explosive

PDV – photonic Doppler velocimetry

PETN – pentaerythritol tetranitrate

PMMA – polymethylmethacrylate

POP – protected optical probe

PPOP – passive protected optical probe

R – Rayleigh

R^{-1} – inverse of the Rayleigh

REC – rectangular section explosive charge

RSS – reflecting specimen surface

RT – rise time

SiO_2 – silica

SMA – subminiature version A

SW – shock wave

TATB – triaminotrinitrobenzene

TKX-50 – dihydroxylammonium 5,5′-bistetrazole-1,1′-diolate

VISAR – velocity interferometer system for any reflector

WDM – wavelength division multiplexing

ZND – Zeldovich - von Neumann – Döring

FRAMEWORK AND OBJECTIVES

Detonation metrology is essential for the development of energetic materials, to characterize existing explosives, and to characterize materials behavior under high pressures.

Energetic materials (EMs) have important applications in the military and civil areas of our society, like weaponized explosives, aircraft flares, tunnels construction, explosion welding, metal forming, shock compaction of materials, and synthesis of nanoparticles. When new EMs are developed, there is the need for small-scale testing, due to the tens, or a few, hundred grams that the synthesis processes can produce before being up-scaled. The follow-up of the development of homemade explosives and improvised explosives devices demands detonation metrologies that can characterize the detonation of some kilograms of these compositions. Due to these, detonation metrology should be adaptable to small and big-scale testing.

Many detonation metrologies have complex and/or expensive set-ups, which demand some hours of preparation before the test, like the electromagnetic particle velocity (EPV) gauges, VISAR, and streak cameras. Some detonation metrologies need complex software and/or mathematical treatment to evaluate the generated data, such as microwave interferometry, and PDV. Other detonation techniques have difficult calibration processes, like rotating-mirror cameras and manganin gauges. Some detonation methods demand the execution of several tests for the characterization of only one parameter, like the use of electro contact type of probes, or the shock-induced polarization.

This work had as objectives:

- the development of detonation metrology that can be used during the development of energetic materials, that can characterize existing explosives and the material's behavior under high pressures.
- The developed detonation metrology should be applicable to small (some tens of gram) and bigger-scale (several hundred grams) testing.
- The new technique has to be easy to assemble, have a simple set-up, and be based on relatively cheap and commercially available components.

- It should be capable of withstanding rough handling and, simultaneously, disturb less as possible the detonation/shock process.
- The used set-up should be able to measure more than one parameter per experiment. In this case, the CJ pressure and the detonation velocity should be measured simultaneously.
- The measurement technique does not need calibration processes.
- The generated data should be easy to read and easy to extract the needed parameters, preferentially without any kind of software, to be accessible to all kinds of users.

Considering the previous points, the main objectives of this thesis are the following:

- To develop a technique based on optical fibers that can record the radiation generated by the detonation/shock process, as well as that, can be independent of it since many inert materials do not emit radiation under shock.
- To test the different working principles, and different probes, on the measurement of detonation velocity and detonation pressure of high explosives.

This work will be divided into five main chapters:

1. Shock and detonation theories, where it is introduced pyrodynamics, and it is described the shock wave phenomena, the hydrodynamic model, the Hugoniot curve on different planes, the shock wave transmission between two different media, the detonation wave phenomena, the Chapman-Jouget theory, the Zeldovich, Von Neumann, and Döring theory, and the analytical characterization of the detonation wave, to understand the detonation and shock parameters measured throughout this work.
2. Bibliographic review about metrologies for detonation characterization of energetic materials, which presents detonation velocity and detonation pressure techniques used over the years until nowadays. The detonation metrologies will be divided according to the measuring parameter. The detonation velocity techniques will be divided into five main groups, while the detonation pressure techniques will be divided into two main groups, both according to the applied

method. This chapter will include a description of each technique, examples of acquired results, how to analyze them, and also the techniques' limits, advantages, and disadvantages.

3. It is presented the developed worked about the passive and active optical methods. This chapter describes the materials and infrastructures used in this work, the characterization of the optoelectric converter system used, the progress of the passive and active optical methods (OPM and OAM, respectively) applied to the detonation of Seismoplast (PETN based explosive), as well as their abilities and restrictions.
4. Demonstration of the experimental methods applied to the measurement of detonation velocity and pressure of three high explosives: Seismoplast, HWC, and TKX-50. Here it will be presented the thermochemical calculations performed to predict the CJ pressure and detonation velocity of Seismoplast (only known composition from the three); the detonation properties of Seismoplast, where will be shown the two published papers about these matters; and the detonation properties of HWC and TKX-50.
5. Conclusions of the developed work.

1. SHOCK AND DETONATION THEORIES

This chapter will be present the shock and detonation theories, to understand the phenomena that define the parameters that will be measured throughout this work. This chapter starts to introduce pyrodynamics, where are presented the important thermodynamic aspects that lay behind the shock and detonation theories. In the shock theory will be presented the shock wave phenomena, the respective hydrodynamic model, the Hugoniot curve represented in different planes, and the shock wave transmission between two media with different shock impedances. In the detonation theory will be described the Champan-Jouguet (CJ) and the Zeldovich, Von Neumann, and Döring (ZND) models, as well as the presentation of the analytical characterization of the detonation wave.

1.1. Pyrodynamics - Thermodynamic and fluid dynamics fundamentals

The process of converting chemical into mechanical energy, performed by fluid dynamics and thermodynamics changes on the combustion phenomena, is called pyrodynamics (Kubota, 2015).

Pyrodynamics is applied to condensed energetic materials, such as explosives and pyrotechnics, since they produce molecules with high temperatures. Focusing on explosives, they are conceived to generate a shock wave (SW), followed by high-pressure combustion products (or detonation products), that produces destructive power (Kubota, 2015).

The following points will present the thermodynamics and fluid dynamics fundamentals necessary to understand the explosives' pyrodynamics, based on the SW and detonation wave (DW) phenomena.

1.1.1. The first law of Thermodynamics

The first law of thermodynamics is applied to an explosive system when there is a conversion from the energy generated on the chemical reaction, to work that acts on the explosive system.

The chemical reaction produces heat (q), which is converted into reaction products' internal energy (e) and work done on the system (w) (Kubota, 2015). This is expressed by equation (1.1):

$$dq = de + dw \tag{1.1}$$

The work is performed by the expansion of the reaction products, as shown in equation (1.2), where p is the pressure, V is the volume per mass unit – specific volume – of the reaction products, and ρ is the density ($\rho = 1/V$) of the reaction products (Kubota, 2015).

$$dw = p\, d\left(\frac{1}{\rho}\right) \tag{1.2}$$

Enthalpy, h, is defined by equation (1.3).

$$dh = de + d\,(pV) \tag{1.3}$$

Substituting equations (1) and (2) on equation (3), enthalpy can be rewritten in the form of equation (1.4).

$$dh = dq + Vdp \tag{1.4}$$

To solve equations (1.2) to (1.4) is needed an equation that represents the *P*-*V* behavior of the reaction products gases. Let's consider the easiest case, where these gases are considered to be perfect. One mole of a perfect gas can be described by equation (1.5), the known equation of state (EoS) for perfect gases. T is the absolute temperature and $\mathcal{R}$ is the perfect gases constant (Kubota, 2015).

$$p = \rho\, \mathcal{R}\, T \tag{1.5}$$

For n moles of a perfect gas, equation (1.5) takes the form presented in equation (1.6).

$$p = n\, \rho\, \mathcal{R}\, T \tag{1.6}$$

1.1.2. Specific heat

Specific heats are parameters that represent the conversion of energy in temperature. The specific heats are defined at constant volume (c_{V}) and constant pressure (c_{P}) by equations (1.7) and (1.8) (Kubota, 2015).

$$c_{\mathrm{V}} = \left(\frac{de}{dT}\right)_V \tag{1.7}$$

$$c_{\mathrm{P}} = \left(\frac{dh}{dT}\right)_P \tag{1.8}$$

Using equations (1.4) and (1.5) and correlating them with equations (1.7) and (1.8), it is possible to obtain equation (1.9), which relates specific heats with the perfect gases constant.

$$c_P - c_V = \mathcal{R} \tag{1.9}$$

The specific heat ratio, γ, is defined by the equation (1.10).

$$\gamma = \frac{c_P}{c_V} \tag{1.10}$$

Dividing equation (1.9) by c_V and substituting it on equation (1.10), we obtain equation (1.11) for c_V.

$$c_V = \frac{\mathcal{R}}{\gamma - 1} \tag{1.11}$$

Doing the same procedure as above, but now dividing equation (1.9) by c_P, we get equation (1.12) for c_P.

$$c_P = \frac{\gamma}{\gamma - 1}\mathcal{R} \tag{1.12}$$

Equations (1.4), (1.7), and (1.8) define specific heats, which are important parameters to define the energy conversion, through temperature, from heat to mechanical energy (Kubota, 2015).

The kinetics theory, which will not be presented here, says that the energy of a molecule is given by the sum of the following energies: translational, rotational, vibrational, electronic, and energy resulting from the interaction between molecules. When there is an increase in the molecule temperature, it also increases its internal energy, due to the excitation of its rotational and vibrational modes. While the translational and rotational modes of a molecule are completely excited at low temperatures, the vibrational modes just start getting excited at temperatures above room temperature. The electrons excitation, as well as the interaction modes, normally happen at temperatures that are much higher than the combustion temperature. Also, molecules dissociation and ionization are possible at very high combustion temperatures (Kubota, 2015).

Experimentally, as shown in Figure 1-1, the specific heats of monoatomic gases are kept constant while the temperature is increasing. However, the diatomic and polyatomic gases specific heats increase with the rising temperature, due to the excitation of their rotational and vibrational modes (Kubota, 2015).

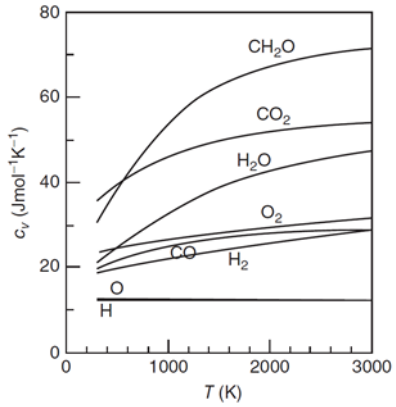

Figure 1-1: Specific heats, at constant volume, of some gases as a temperature function. Image from (Kubota, 2015).

1.1.3. Entropy change

Entropy, *s*, is mathematically defined by equation (1.13).

$$ds \equiv \frac{dq}{T} \tag{1.13}$$

Equation (1.14), which represents entropy variations, is obtained by substituting equations (1.4), (1.5), and (1.8) on equation (1.13).

$$ds = \frac{c_P}{T} dT - \frac{\mathcal{R}}{p}\, dp \tag{1.14}$$

For isentropic changes, which means that there are no entropy variations ($ds = 0$) during the change, equation (1.14) has the form of its integration (equation (1.15)), where the subscript 0 indicates the initial state 0 (Kubota, 2015).

$$\frac{p}{p_0} = \left(\frac{T}{T_0}\right)^{\frac{c_P}{\mathcal{R}}} \tag{1.15}$$

Another form of equation (1.15) is equation (1.16), which is obtained by substituting equation (1.12) on equation (1.15).

$$\frac{p}{p_0} = \left(\frac{T}{T_0}\right)^{\frac{\gamma}{\gamma-1}} \tag{1.16}$$

And equation (1.17) is obtained with the help of equation (1.5).

$$p\left(\frac{1}{\rho}\right)^{\gamma} = p_0\left(\frac{1}{\rho_0}\right)^{\gamma} \tag{1.17}$$

It is considered that a system goes under an isentropic change when there is a small heat loss from the system or small heat gain of the system, and the dissipative effects, such as

friction due to molecules collision or turbulence from the non-uniform molecular distribution, are very small (Kubota, 2015).

1.1.4. Conservation equations in a one-dimensional steady-state flow field

A one-dimensional steady-state flow without viscous stress, or a gravitational force, is considered a simplified flow.

The continuity, or mass conservation, equation is given by the mass rate that goes in less the mass rate that goes out, and it is represented by equation (1.18), where u is the local flow velocity in a flow field (Kubota, 2015).

$$d(\rho u) = 0 \tag{1.18}$$

The momentum conservation equation is given by equation (1.19), where $\rho\ u\ du$ is the momentum rate gain by convection, and dp is the pressure difference action on the flow.

$$\rho\ u\ du\ +\ dp = 0 \tag{1.19}$$

The conservation equation for the energy is given through the rate of energy input by conduction, plus the rate of energy input by convection, being equal to zero, as represented in equation (1.20).

$$d\left(h + \frac{u^2}{2}\right) = 0 \tag{1.20}$$

Combining equations (1.19) and (1.4), it is possible to get the relationship for the enthalpy change due to a flow velocity change, which is expressed by equation (1.21).

$$dh = dq - u\ du \tag{1.21}$$

1.2. Shock wave phenomena

A shock wave (SW) can be understood as a discontinuity surface, with kinetic and thermodynamic quantities, that propagates supersonically in the inner part of a material. Having has base the conservation laws of mass, momentum, and energy, and assuming that the thickness of the SW is infinitely small, it is possible to explain the propagation of a SW in a material media (Mendes, 1994).

It is necessary to do a brief introduction to the stress-strain characteristics of the materials, to understand the shock phenomena. In the elastic domain of a material, the strain is directly proportional to the stress applied to it. This linear behavior is kept until the point where

the material cannot come back to the same initial state (shape and dimensions). This point is called the elastic limit. If the applied stress is higher than the elastic limit, then the material will suffer a plastic deformation (Gois, 1989) (Mendes, 2000).

In detonation, a phenomenon characterized by a specific kind of shock wave (detonation wave), it is possible to consider that the solid materials are described by a hydrodynamic behavior since the acquired pressures can reach tens of GPa. The hydrodynamic behavior, where the tensorial notion of force is undervalued, admits that the solid behaves like a perfect fluid, presenting resistance only to dilatation. Due to this, the characterization of a material state can be done with scalar quantities as hydrostatic pressure (p), specific volume (V), and temperature (T), and wave propagation on the material can be treated uni-axially, according to the normal direction related to the wavefront (Mendes, 2000).

In the referred range of pressures, the perturbation propagation velocity on a material increases with the increase of pressure. This velocity is called the sound velocity of a material (C_b) and it is given by equation (1.22), where V is the specific volume, p is the pressure, ρ is the density of the material and the subscript s represents constant entropy (Mendes, 2000).

$$C_b^2 = -V^2 \frac{dp}{dV}\Big)_s = \frac{dp}{d\rho}\Big)_s \qquad (1.22)$$

This is a determining property for a shock wave formation. Thus, a compression wave accelerates gradually with the pressure, until it propagates as an abrupt transition in the material properties. Shock is the designation for the material properties discontinuity. A shock wave formation is represented on the scheme of Figure 1-2 (Mendes, 2000).

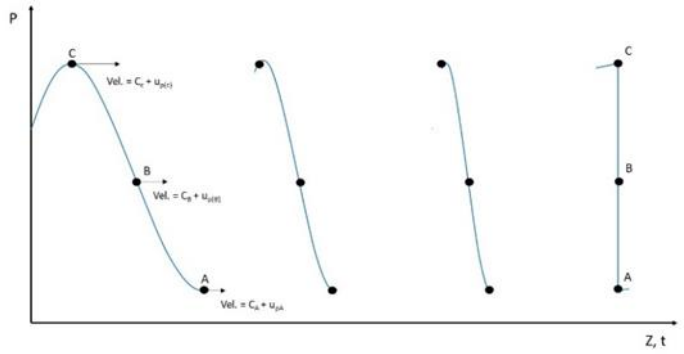

Figure 1-2: Shock wave formation scheme. Adapted from (Mendes, 2000).

The velocity at which the perturbation is moving is determined by $C_b + u_P$, which is the sound velocity on the media plus the velocity acquired by the particle, u_P. Now it is

important to distinguish the difference between shock wave velocity (U_S) and material point velocity, or particle velocity (u_P).

The concept of shock wave assumes in it a perturbation, or a change in the physical state, of a body material point and, thus, the U_S means the velocity at which the perturbation is transmitted to the next material point. The particle velocity, u_P, means the real velocity acquired by the material point, which represents the material point displacement rate related to a referential. The phenomenon, called shock, generates an abrupt discontinuity on the material properties such as density, pressure, material media velocity, energy, and temperature. In reality, an effective discontinuity is never formed, because the increase of the deformation rate corresponds to the increase of the dissipative mechanisms, like viscosity, and they promote the wave dissipation. The competition of these effects has an important role when the deformation rates are extremely high but, for the majority of the materials, the shock thickness is so small that allows us to characterize the shock as an abrupt discontinuity (Mendes, 2000).

1.3. Hydrodynamic model: discontinuity conditions and conservation equations

The most usual way to calculate the variables associated with shock propagation is based on the conservation equations of mass, momentum, and energy. They are applied at the shock wave discontinuity and they are known as Rankine-Hugoniot equations. As said before, it is assumed that the material has a hydrodynamic behavior when it is under shock. During this text, the displacement rates of a media perturbation (wave) and of a particle are called velocity.

According to the hydrodynamic theory, the shock wave is considered plane, it has an infinitesimal thickness and it crosses the material with a constant velocity. Assuming a control surface with a cylindrical shape and with a unitary transversal section area, it is possible to define the conservation equations applied to the material initial (represented by the subscript 0) and final states (no subscripts), considering that the material is crossed by the shock wave (Figure 1-3) (Gois, 1989).

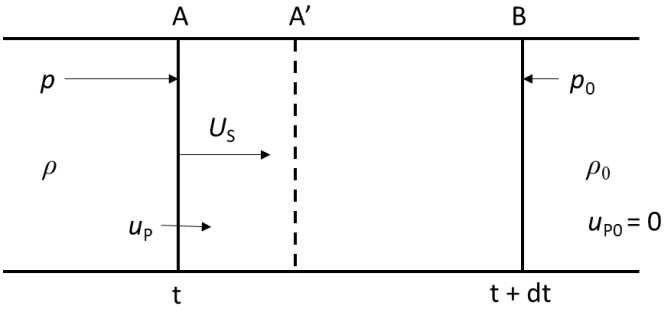

Figure 1-3: Displacement scheme of the shock wave. Adapted from (Gois, 1989)

Figure 1-3 shows the shock wave crossing the material volume control. It is considered that the media, or the material, is initially in rest (p_0, ρ_0, e_0 and $u_{P0} = 0$), the shock wave velocity (U_S) is constant and, in the instant t the shock wave is at A while, at the instant $t+dt$, it is at B. After the shock wave passage, the material has new properties (p, ρ, e, and u_P) (Gois, 1989). With this, it is possible to obtain the relation (1.23).

$$U_S = \frac{\overline{AB}}{dt} \tag{1.23}$$

In this way, at the instant t, the material A section received the shock and got a velocity u_P, which made the A section move from A to A':

$$u_P = \frac{\overline{AA'}}{dt} \tag{1.24}$$

All the material that was between A and B, with a density of ρ_0,

$$m_{\overline{AB}} = \rho_0 \overline{AB} = \rho_0 U_S \, dt \tag{1.25}$$

After dt, all material is now between A' and B, but with a new density ρ,

$$m_{\overline{A'B}} = \rho \overline{A'B} = \rho \, (U_S - u_P) \, dt \tag{1.26}$$

Since there is mass conservation:

$$m_{\overline{AB}} = m_{\overline{A'B}} \Leftrightarrow \rho_0 U_S = \rho \, (U_S - u_P) \tag{1.27}$$

According to the dynamic's fundamental law, $F = m \times a$, and remembering that we are considering a unitary area, it is possible to write:

$$(p - p_0) \, dt = m_{\overline{AB}} \, du_P \tag{1.28}$$

Since the material was initially at rest ($u_P(0) = 0$):

$$du_P = u_P \tag{1.29}$$

Substituting equations (1.26) and (1.29) in equation (1.28), we have:

$$p - p_0 = \rho_0 U_S u_P \tag{1.30}$$

The application of the conservation energy principle assumes that the energy received by the mass element $m_{\overline{AB}}$, during the interval *dt*, is equal to the work done by the external forces, where there are no heat losses. This received energy has in it an increase of internal energy (e-e_0) per mass unit, and also an increase of kinetic energy, $\frac{1}{2}u_P^2$, per mass unit (Gois, 1989).

Since surface A was the only one that moved, the work (*dw*) done by the external forces (*F*) is the pressure (*p*) that is acting on the surface A ($P = \frac{F}{a}$), which has a unitary section area (a =1) and is only variable throughout the x-axis:

$$dw = F\,dx \Leftrightarrow w - w_0 = p\,(x - x_0) \tag{1.31}$$

Since the material is initially in rest, there is no work done by the external forces ($w_0 = 0$) and, according to Figure 1-3 and rearranging equation (1.24), equation (1.31) assumes the form of equation (1.32):

$$w = p\,\overline{AA'} = p\,u_P\,dt \tag{1.32}$$

According to what was said before about energy conservation, it can be assumed that the system has the initial (e_0) and final (e) energies expressed by equations (1.33) and (1.34):

$$e_0 = m_{\overline{AB}}\left(e - e_0 + \frac{1}{2}u_P^2\right) \tag{1.33}$$

$$e = w \tag{1.34}$$

By the energy conservation, where $e = e_0$ (eq. (1.33) = eq. (1.34)), and considering equation (1.25), we can represent the energy variation of the system through equation (1.35):

$$e - e_0 = \frac{p\,u_P}{\rho_0 U_S} - \frac{1}{2}u_P^2 \tag{1.35}$$

Rearranging equation (1.30) and applying it to equation (1.35), we get equation (1.36).

$$e - e_0 = \frac{p_0\,u_P}{\rho_0 U_S} + \frac{1}{2}u_P^2 \tag{1.36}$$

If we sum equations (1.35) and (1.36), equation (1.37) is obtained.

$$2(e - e_0) = \frac{u_P}{\rho_0 U_S}(p + p_0) \tag{1.37}$$

Equation (1.27) can be rewritten and substituted at equation (1.37), to have an energy equation:

$$e - e_0 = \frac{1}{2}(p + p_0)\left(\frac{1}{\rho_0} - \frac{1}{\rho}\right) \quad (1.38)$$

Equation (1.38) is the so-called **Hugoniot relation**.

1.4. Hugoniot curve on different planes

The mass and momentum conservation relations present variables that belong to the shock, like particle velocity (u_P) and shock velocity (U_S). The energy equation, or Hugoniot relation, connects three thermodynamic quantities: *e*, *p*, and ρ. But there is another equation, the so-called equation of state (EoS), that correlates the same three quantities, *e = e (p, V)*, and which represents all the possible equilibrium states that the material can reach.

If it is admitted that, after the shock wave passage, the material reaches an equilibrium state, then both equations will need to be satisfied simultaneously. This allows that the energy variable is eliminated to obtain a single relation (p - $1/\rho$), the already presented equation (1.38): the Hugoniot relation or, the Hugoniot curve. The Hugoniot curve represents all the equilibrium states that are possible for the material to reach, after the shock wave passage. But this Hugoniot curve does not represent the way taken by the material, from its initial to its final state (Mendes, 2000).

Since in the conservation equations there are three equations with five variables, it is necessary to establish relations between some of those variables. The relations $U_S - u_P$, P - $1/\rho$, and $P - u_P$ are particularly important for this case because they are easy to determine and frequently used. The determination of one of these relations, mostly known by the Hugoniot Curve, allows the complete characterization of the final state that a material can reach under shock (Mendes, 2000).

1.4.1. $U_S - u_P$ plane

The relation $U_S = f(u_P)$ can be considered an equation of state that, together with the conservation equations, allows the determination of all variables of the shocked media according to an independent variable. The experimental results allow verifying that, for the majority of the materials, the shock wave velocity U_S, according to the particle velocity of the media u_P, can be approximated to a linear law (eq. (1.39)) (Mendes, 2000).

$$U_S = C_0 + S\,u_P \quad (1.39)$$

The constant C_0 has the physical meaning of being the intersection of the straight line, with slope S, with the vertical axis, being S a dimensionless constant, and they were found by the method of least squares (Marsh, 1980).

When a material shows a phase change, or physical-chemical change, due to a shock action, the relation U_S - u_P is well approximated by two straight lines. Sometimes, it is presented a second-order polynomial to represent the relation U_S - u_P, but the only reason for this is that a polynomial adjustment fits better together with the obtained points than a linear law (Marsh, 1980).

To show the U_S – u_P relations for inert materials, Figure 1-4 contains these experimental data obtained for PMMA, copper, and aluminum. These are the inert materials used in this work to obtain the CJ Pressure for the used explosive – Seismoplast.

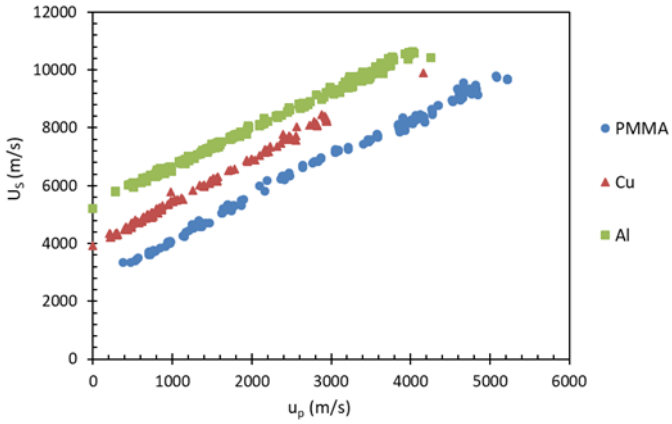

Figure 1-4: Shock wave velocity (U_S) according to the particle velocity (u_P) of the media for PMMA, copper, and aluminum. Data were taken from (Marsh, 1980).

1.4.2. $P - 1/\rho$ plane

Considering the typical case, where $u_P(0)=0$ and $p_0=0$, and combining the relation $U_S - u_P$ with the momentum and mass conservation equations, the relation $P = f(1/\rho)$ transforms in equation (1.40). The Hugoniot curve, in the plane P-$1/\rho$, is presented in Figure 1-5 (Mendes, 2000).

$$P_1 = C_0^2 \left(\frac{1}{\rho_0} - \frac{1}{\rho_1}\right)\left[\frac{1}{\rho_0} - S\left(\frac{1}{\rho_0} - \frac{1}{\rho_1}\right)\right]^{-2} \qquad (1.40)$$

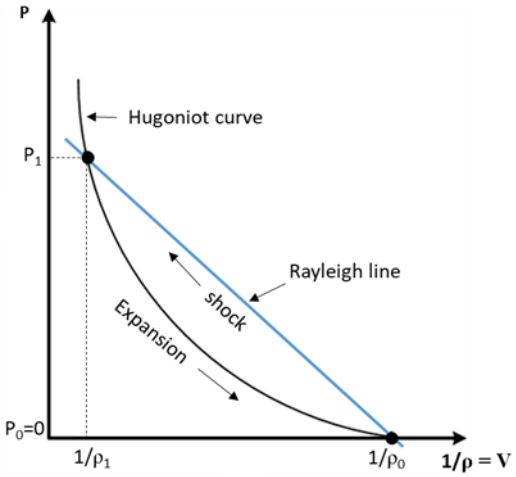

Figure 1-5: Hugoniot curve and Rayleigh line in the P-1/ρ diagram. Adapted from (Mendes, 2000).

As said before, the Hugoniot curve represents the group of all possible states that the material can reach from its initial state 0. The straight line between the initial (P_0, V_0) and the final (P_1, V_1) states, the so-called Rayleigh (R) line, represents the discontinuity condition, due to the shock wave. This straight line is characterized by equation (1.41), through the elimination of the media particle velocity u_P, in the moment and mass conservation equations (Mendes, 2000).

$$P_1 - P_0 = \frac{U_S^2}{V_0} - \frac{U_S^2}{V_0^2} V_1 \tag{1.41}$$

From equation (1.41) it is easy to see that the slope of the Rayleigh line is $\frac{U_S^2}{V_0^2}$, or $U_S^2 \rho_0^2$. So, knowing the initial and final states, the shock wave velocity is given by $U_S = (slope)^{1/2} V_0$ (Mendes, 2000).

Still on the plane *P - 1/ρ*, or *P-V*, shown in Figure 1-5, it is possible to analyze the changes in internal and kinetic energies of a shocked material. It is considered that the material, in the initial state 0 (P_0, V_0) suffered a shock that takes the material to state 1 (P_1, V_1), and that the specific kinetic energy is given by $\frac{1}{2} u_P^2$ (Mendes, 2000).

So, considering always that the initial state is characterized by $P_0=0$, equation (1.27) takes the form of equation (1.42) for the final state 1, solved in order to U_S:

$$U_S = \frac{\rho_1}{\rho_1 - \rho_0} u_{P1} \tag{1.42}$$

From (1.30), for the final state 1 it is possible to write equation (1.43):

$$P_1 = \rho_0 U_S u_{P1} \tag{1.43}$$

Substituting (1.42) in (1.43):

$$u_{P1}^2 = P_1\left(\frac{1}{\rho_0} - \frac{1}{\rho_1}\right) \tag{1.44}$$

From this equation (1.44) it is possible to obtain equation (1.45), which represents the referred specific kinetic energy:

$$\frac{1}{2}u_{P1}^2 = \frac{1}{2}P_1\left(\frac{1}{\rho_0} - \frac{1}{\rho_1}\right) \tag{1.45}$$

In the equation (1.45) the second member represents, in the *P*-*V* plane, the area of the triangle defined by the Rayleigh line between $\frac{1}{\rho_0}$ and $\frac{1}{\rho_1}$, and by $P=P_1$. This means that the increase of the material's specific kinetic energy is equal to the triangle area, in Figure 1-5 (Mendes, 2000).

As said before, the specific kinetic energy is given directly by equation (1.44), which represents, in Figure 1-5, all the area below the Rayleigh line, between the initial state $\frac{1}{\rho_0}$ and the final state $\frac{1}{\rho_1}$. As consequence, when the initial pressure can be neglected when compared to the final pressure, the total energy acquired by the material, by mass unit, and by time unit, resulting from the shock compression, is divided into equal parts, between the kinetic and the internal energies (Mendes, 2000).

A material, under a pressure state, discharges to the environmental pressure through an expansion wave, by an isentropic process. The expansion wave is a continuous and a different curve from the Hugoniot curve. Although for expansion wave studies in engineering, the isentropic curve can be approximated to the Hugoniot curve, and that is why in Figure 1-5 just the Hugoniot curve is represented (Mendes, 2000).

So, if a material is shocked until the state 1 (P_1, V_1), and it discharges until the initial state 0 (P_0, V_0) along the Hugoniot curve, the energy value dissipated by the material during the expansion is equal to the area bellow to the Hugoniot curve, between its initial and final states. This means that the increase of specific internal energy induced on the material is equal to the area between the Rayleigh line and the Hugoniot curve, from the initial to the final states. The consequence of the specific internal energy increase is the increase of the material temperature. If the shock pressure is too high, the material under shock can melt, or even vaporize (Mendes, 2000).

1.4.3. $P - u_P$ plane

The characterization of the Hugoniot curve in the $P - u_P$ plane is important to solve problems related to shock waves' interactions (Mendes, 2000).

To obtain the $P - u_P$ relation is necessary to consider that the material is initially in rest ($u_P(0) = 0$), and that the value of P_0 (normally in the order of Pa) is negligible when compared to P_1 (in the order of GPa). So, starting from the momentum conservation equation (eq. (1.43)) and putting it together with the Hugoniot $U_S - u_P$ relation (eq. (1.39)), it is possible to eliminate U_S and then to obtain the $P - u_P$ relation (equation (1.46)) (Mendes, 2000).

$$P_1 = \rho_0 \, C_0 \, u_{P1} + \rho_0 \, S \, u_{P1}^2 \qquad (1.46)$$

Until now, it was always considered that the material was initially at rest ($u_{P0} = 0$). But if we consider that the material is moving before the shock ($u_{P0} \neq 0$), then equation (1.46) is transformed into equation (1.47) (Mendes, 2000). These two equations are represented graphically in Figure 1-6.

$$P_1 = \rho_0 \, C_0 \, (u_{P1} - u_{P0}) + \rho_0 \, S (u_{P1} - u_{P0})^2 \qquad (1.47)$$

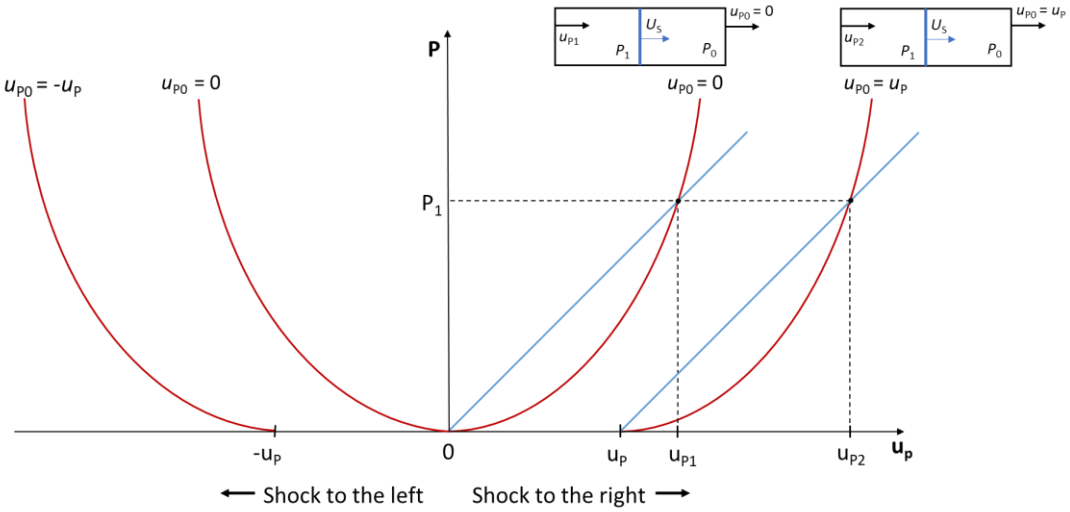

Figure 1-6: Characteristic Hugoniot curves of a shock wave moving to the left and the right. Adapted from (Mendes, 2000).

Until now it was always considered that the shock wave always moves from the left to the right side. But knowing that velocity is a vector, when the shock wave moves to the left side, the particle velocity should be $-(u_{P1} - u_{P0})$. So, to differentiate for which side is the shock wave moving, we will consider that P_L represents the pressure which the material is under when the shock wave moves to the left side, and P_R when the shock wave is moving to the right side. When the shock wave is moving to the right side, its Hugoniot curve is represented by

equation (1.48). When the shock wave is moving to the left side, its Hugoniot curve is represented by equation (1.49) (Mendes, 2000). These equations are schematically represented in Figure 1-6.

$$P_R = \rho_0 C_0 (u_{P1} - u_{P0}) + \rho_0 S(u_{P1} - u_{P0})^2 \quad (1.48)$$

$$P_L = \rho_0 C_0 (u_{P0} - u_{P1}) + \rho_0 S(u_{P0} - u_{P1})^2 \quad (1.49)$$

In Figure 1-7 are represented the Hugoniot curves for the inert materials used in this work since it will be needed to evaluate the induced pressure on these materials by the studied explosive – Seismoplast.

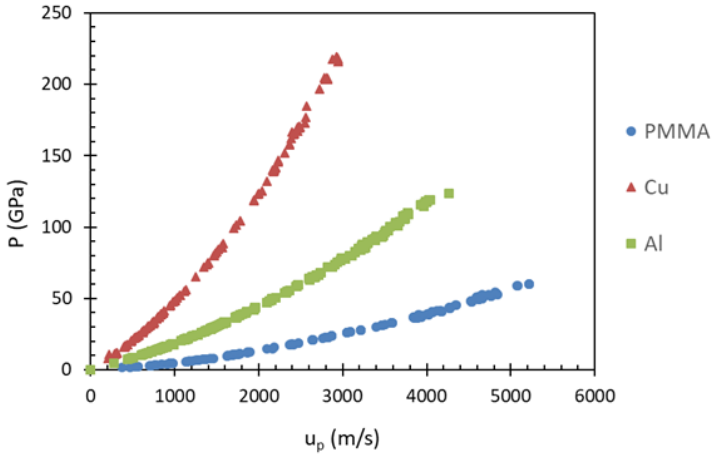

Figure 1-7: Hugoniot curves of PMMA, aluminum, and copper. Data were taken from (Marsh, 1980).

The Hugoniot curve $P(u_p)$ of each material can be obtained by substituting the $U_S - u_P$ relation and the density of each material in equation (1.46).

1.5. Shock wave transmission between two different media

Let's consider that two different materials (A and B) are in contact through a common section. At the instant $t=0$, both materials are in rest ($u_{PA} = u_{PB} = 0$). When a planar shock wave propagates from media A to media B, the separation interface between the two media should be kept in mechanical equilibrium. It means that the two contact surfaces will have the same particle velocity, u_P ($u_{PA} = u_{PB} = u_P$), and the same pressure value (P_A=P_B) (Mendes, 1994). At the interface, this SW that started to propagate in A will generate another SW in B and a reflected wave in A (Gois, 1989).

After the shock, the new equilibrium state can present two situations, which are characterized by the impedance relation (Z) of the two media. This impedance relation is

defined by equation (1.50), where ρ_0 is the initial density of the media and U_S the shock velocity on the media (Gois, 1989).

$$Z = \rho_0 U_S \quad (1.50)$$

The shock impedance also allows the correlation between the pressure P generated on the media, and the particle velocity u_P induced on it (Gois, 1989), by equation (1.51), which is equivalent to equation (1.30), considering $P_0 = 0$.

$$P = Z u_P \quad (1.51)$$

Having in mind the moment when the SW reaches the separation interface of the two media, this SW will originate two waves: one transmitted on the media B and another reflected on the media A (Mendes, 1994).

Since the shock impedance of a media varies mostly with its density, two situations can occur when the analysis of shock transmission between two media is done: the impedance of A is lower than the impedance of B ($Z_A < Z_B$); or the impedance of A is higher than B ($Z_A > Z_B$) (Gois, 1989).

1.5.1. Shock transmission when $Z_A < Z_B$

Let's consider that a shock wave with P_1 and u_{P1} is moving in material A (point 1 in Figure 1-8). When the SW passes from material A to B, it induces on the material B a shock wave moving to the right and a reflection wave in A moving to the left. . The transmitted shock wave in B is responsible for the pressure and particle velocity increase from 0 to P_2 and from 0 to u_{P2}, respectively (see Figure 1-8). On the other side, the reflected wave in A is responsible for the pressure increase from P_1 to P_2, and the particle velocity decrease from u_{P1} to u_{P2} (Mendes, 1994). This means that point 2, which characterizes the equilibrium state at the interface, will be located on the intersection between the shock Hugoniot curve of material B, with its origin in a zero state, and the curve that represents the compression isentropic generated on the material A (curve A'), that had its origin in the state 1 (Gois, 1989).

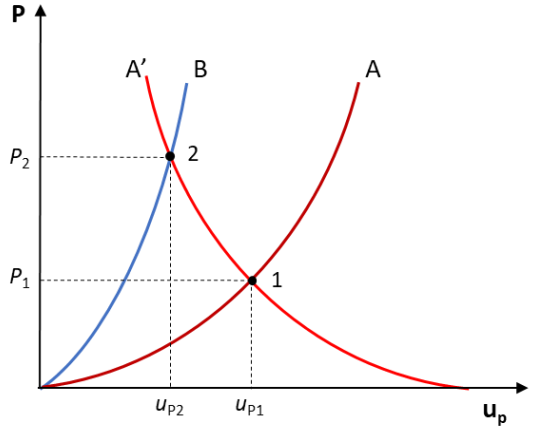

Figure 1-8: Shock transmission between two media when $Z_A < Z_B$. Adapted from (Mendes, 2000).

1.5.2. Shock transmission when $Z_A > Z_B$

Let's consider that material A is under the influence of a SW and, before the shock with material B, it has a pressure P_1 and particle velocity u_{P1} (state represented by point 1 in Figure 1-9). When the SW passes from A to B, it induces on the interface a pressure P_2 and a particle velocity u_{P2}(point 2 in Figure 1-9). The transmitted SW to B is responsible for a pressure and particle velocity increase from 0 to P_2 and from 0 to u_{P2}, respectively. On the other hand, the reflected wave in A is responsible for the decrease of pressure from P_1 to P_2 and an increase of particle velocity from u_{P1} to u_{P2} (Mendes, 1994). The interface equilibrium point, which is represented by number 2 in Figure 1-9, is located at the intersection between the shock Hugoniot curve of the material B, with its origin in state zero, and the expansion isentropic generated in the material A, with its origin in the state 1 (Figure 1-9) (Gois, 1989).

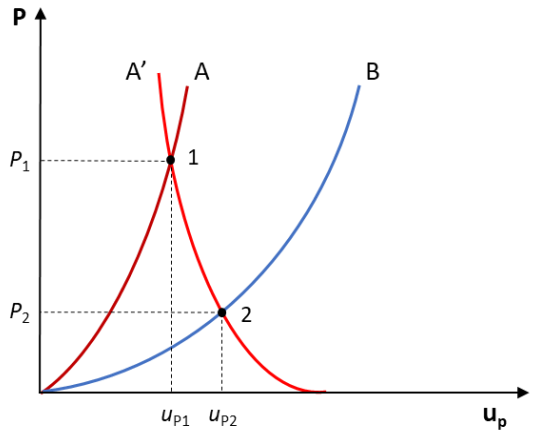

Figure 1-9: Shock transmission between two media when $Z_A > Z_B$ Adapted from (Mendes, 2000)

1.6. Detonation wave phenomena

A material that can provide, in a very short time, a large amount of gases at very high temperature and pressure, is known as an explosive. This energy is chemically generated and, part of it is used to make the reactions develop (Davis & Fauquignon, 1995).

The term "explosion" is embracing all the phenomena that are characterized by a violent chemical reaction. The phenomena that are englobed inside "explosions" vary a lot between them: in their reaction front velocities, their temporal variation of pressure, temperature, and energy released by mass unit. For a deeper knowledge of these phenomena, it is also needed to know about the kind of chemical bonds that the studied material has, as well as the order of the chemical reactions, and the thickness of the reaction zones. But, if we just focus on the reaction zone propagation rate, we will be able to distinguish deflagration from detonation (Davis & Fauquignon, 1995) (Gois, 1989).

Deflagration is a chemical reaction of a material, in which its reaction front propagates with a lower velocity than the sound velocity, in the same material. This characteristic makes that deflagration is propagating in a subsonic regime. Detonation is a supersonic regime since the wave that is crossing the material has a higher velocity than the characteristic sound velocity of the fresh material (Gois, 1989) (Lee, 2008).

A deflagration to a detonation transition (DDT) is possible when it is allowed to increase the pressure and the turbulence at the reaction front of the fresh material (observed typically in gases and dusts explosions), until a point where it is possible to induce an acceleration on the reaction front when compared to the sonic front. As a consequence of this reaction front acceleration, it is formed a compression waves train that forms a strong SW. This strong SW will be the trigger for the heat release and for the species diffusion on the fresh material (Gois, 1989) (Lee, 2008). The chemical reaction that is developed behind the shock front, which can vary from hundred angstroms to millimeter units (depending on the sensitivity of the explosive), ensures now compression enough to keep a stable detonation regime. When a stable detonation regime is achieved, it means that it is observed a detonation wave (DW) going through the media (Gois, 1989) (Urtiew & Hayes, 1991).

A detonation wave has the properties of being supersonic and compression SW. The fact of being supersonic makes that the reactants in front of it are not disturbed before its arrival, which means that they remain in their initial state; its compression characteristics make that the density of the explosive increases during the detonation and, as result, the particle

velocity of the explosive is in the same direction as the wave motion (Lee, 2008). Although, some experimental results allowed to conclude that the fresh explosive was exposed to the radiative phenomena of the DW before its arrival (Plaksin, et al., 2009) (Plaksin, et al., 2010).

The biggest difference between a shock wave (SW) and a detonation wave (DW) is that there are no chemical reactions that support the wave propagation on a SW. This means that the particles prevail the same (no chemical changes) during and after the shock process. In the DW, the shock front is followed by a chemical reaction, where the particles react with each other, passing from solid to gases (for example), which give origin to the detonation products.

Michelson, Chapman, and Jouguet made the first thermodynamic analysis of the detonation phenomena that gave origin to the first detonation theory, which is based on shock waves theory. They considered the detonation as a plane discontinuity, associated with an abrupt pressure variation and characterized by an instantaneous chemical reaction. They also represented the DW as a SW with energy release inside of the wavefront (Gois, 1989) (Dremin, 1999).

Further on, Zeldovich - von Neumann – Döring (ZND) improved this theory, which is accepted until today, with the idea that the energy released during the chemical reaction was not instantaneous (Gois, 1989). They postulated that a DW is characterized by a SW that is followed by a reaction zone, which is also followed by a zone where the reaction products are relaxing to normal conditions. The SW passage makes a sharp increase in the thermodynamic states (temperature and pressure) of the material where it is acting, which results in a chemical reaction, which can occur immediately or after a certain induction period. This chemical reaction happens in the reaction zone, which is associated either with a pressure falling down or with a falling preceded by a slight rise. Immediately after the reaction zone is the area where the detonation products (normally gases) will expand, cool down, and, after some time, going back to environmental temperatures. This area is considered the expansion region and it is called “release wave”, due to its propagation as a wave. This expansion region is mostly known as the “Taylor wave” (Urtiew & Hayes, 1991) (Lee, 2008).

The end of the reaction zone for ideal explosives is known as the Chapman-Jouguet (CJ) state. For non-ideal explosives, the chemical reactions can continue after this plane, but they do not support the detonation front anymore. For each explosive, this CJ state is defined by characteristic values of particle velocity ($u_{P,\,CJ}$), pressure (P_{CJ}), temperature (T_{CJ}), specific volume (V_{CJ}), and energy (E_{CJ}). The detonation velocity (D) is also characteristic of each

explosive and it is the velocity at which the whole detonation complex propagates into the undisturbed medium (Urtiew & Hayes, 1991).

The Chapman-Jouguet (CJ) theory, the Zeldovich - von Neumann – Döring (ZND) theory, and the conservation equations applied to the DW, fundamental to understand the detonation phenomena and the mathematical models during this thesis, will be presented in detail in the next points, as well a detonation products thermal equation of state (EoS), to complete the detonation theory.

1.7. CJ Theory

Detonation theory based on SW theory was formulated in the early beginning of the 20th century by Donald Leonard Chapman (1869-1958) and Ehrile Jouguet (1871-1943), giving their contributions in 1899 and 1904-1905, respectively. At the same time, in 1893, Michelson also developed a similar detonation theory. But, unfortunately, his Ph.D. thesis with his reported analysis was not known outside Russia and, due to this, only Chapman's and Jouguet's names are associated with this detonation model – The Chapman-Jouguet (CJ) theory. This theory allows the prediction and characterization of the variables that characterize the stable detonation of an explosive (Dremin, 1999) (Mendes, 2000) (Lee, 2008).

The CJ theory was based on the works of Rankine (1870) and Hugoniot (1887, 1889), where was analyzed the conservations equations across a SW (see point 1.3) (Lee, 2008). The CJ model assumes a reactive supersonic flow, which is self-sustained by the SW and it is steady until the reactions' end: the equilibrium of all the exothermic reactions is reached at the same time and it is a function of the temperature and pressure (Davis & Fauquignon, 1995) (Lee, 2008). Further than this point, it is a nonstationary rarefaction that takes place. This nonstationary rarefaction is controlled by the explosive charge boundary conditions. But this model fails on neglecting the conductive and radiative effects, and on assuming a laminar non-viscous flow (Davis & Fauquignon, 1995). In this detonation model, the DW shock front δ (zero reaction zone, Figure 1-10) is responsible for the explosive compression and its change into detonation products (Dremin, 1999) (Mendes, 2000).

Chapman verified that, from all the straight lines that can be drawn from the 0 point, only the tangent (Rayleigh line) to the Hugoniot curve of the detonation products (HP) has a single common point (point 1 in Figure 1-10) with it. Therefore, Chapman proposed that a stable

detonation wave should have the parameters corresponding to the ones in point 1 (P_1, V_1) (Figure 1-10). This point is the so-called CJ point, as a tribute to the authors of the classical detonation theory (Davis & Fauquignon, 1995) (Dremin, 1999) (Mendes, 2000). Essentially, Chapman's criterion was to choose the minimum velocity solution, since experiments for a given explosive mixture showed only one observed detonation velocity (Lee, 2008).

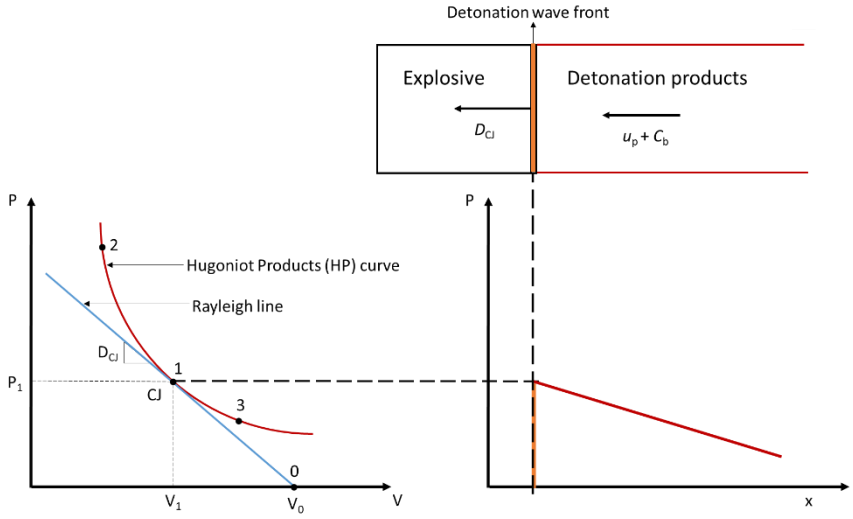

Figure 1-10: Scheme of the Chapman-Jouguet detonation model, its representation in the *P-V* and P-x planes, and the correspondence between them. Adapted from (Dremin, 1999) and (Mendes, 2000).

To verify this rule Jouguet showed that, from all supersonic combustion waves, just the DW characterized by the tangent to the HP curve (Rayleigh Line) admits a stable propagation. To keep a stable DW propagation is necessary that the SW, responsible for the detonation ignition in successive layers, is not attenuated by rarefaction waves, which are generated by the detonation products. For this is necessary that the detonation products' velocity (u_P) is larger than the sound velocity (C_b) in the detonation products since rarefaction waves move in the detonation products with the local sound velocity (Davis & Fauquignon, 1995) (Dremin, 1999) (Mendes, 2000).

If the Rayleigh line intersected the products' Hugoniot at a slope greater than that at the tangent, then two states (2) and (3) would be possible for the products, one at each of the two points. At state 2 in Figure 1-10, the rarefaction wave velocity $(dp/dv)^{1/2}$ is higher than the slope of the Rayleigh line and the reaction zone, and the rarefaction wave would be overtaking the shock front, decreasing its intensity and violating the statement above that these are all at the same velocity. So this state is not possible (Gois, 1995) (Dremin, 1999) (Mendes, 2000) (Lee, 2008).

At state 3 in Figure 1-10, the rarefaction wave velocity $(dp/dv)^{1/2}$ is lower than the slope of the Rayleigh line; therefore, the rarefaction wave would be slower than the shock front, making the reaction zone continuously spread out in time that leads to detonation extinction. The only place on the product's Hugoniot where the slope of the Hugoniot equals the slope of the Rayleigh line, and the reaction zone, rarefaction wave, and shock front, are all at the same velocity is at the tangent point 1, the CJ state (Mendes, 2000) (Gois, 1995) (Dremin, 1999) (Mendes, 2000) (Lee, 2008). So, the condition to have a stable DW is that the DW has to be sonic concerning the detonation products This condition is only verified at the CJ point (point 1), where $u_P = u_{P,CJ}$ and $C_b = C_{b,CJ}$, and it is represented by the equation (1.52) (Davis & Fauquignon, 1995).

$$D_{CJ} = u_{P,CJ} + C_{b,CJ} \tag{1.52}$$

Basically, Jouguet determined the entropy variation along the HP curve and found a minimum, leading him to postulate the minimum entropy solution, or the sonic solution, which corresponds to the sonic condition of a stable detonation (equation 1.52) (Lee, 2008).

In synthesis, the CJ theory only considers the energetic characteristics of the explosive, it does not count with its chemical reactions' kinetics. This leads to the thinking that, in this theory, the explosive compression and its chemical transformation in detonation products happen simultaneously inside the DW front. This is why this model is called as "zero reaction zone". This model does not consider a finite reaction zone, neither any perturbation that is originated behind this zone, which can reach the stable DW front. Since this model does not consider a chemical reaction zone, its application fails in the explanation of the detonation critical diameter - the explosive charge's smallest diameter in which a stable detonation wave can propagate without external influences (Davis & Fauquignon, 1995) (Dremin, 1999) (Mendes, 2000).

1.8. ZND theory

At the beginning of the '40s of the last century, Zeldovich, Von Neumann, and Döring developed, independently and quasi-simultaneously, the ZND detonation physical model that adds the notion of reaction thickness, or reaction zone, behind the detonation front (Davis & Fauquignon, 1995) (Mendes, 2000) (Lee, 2008).

As referred to before, the CJ classical theory is based on the idea of a zero-reaction zone. On the other hand, the ZND theory considers that the DW has a well-defined reaction thickness (Dremin, 1999) (Mendes, 2000).

The ZND model assumes that initially, due to the passage of a DW, the unreacted explosive is compressed, without chemical change, inside the detonation wave front δ (Figure 1-11). With this compression occurs chemical decompositions and reactions, that are located in the chemical reaction zone - behind the DW front - under the influence of high temperatures, due to the shock compression. The reaction is considered to be complete at the CJ point. After the CJ point, there is an expansion of the detonation products which, graphically, occurs starting at the CJ point and keeps below it along the products' Hugoniot (HP) curve (see Figure 1-11) (Gois, 1989) (Dremin, 1999) (Mendes, 2000).

Considering that the detonation process has a finite reaction zone, *a*, the ZND model assumes that the detonation process has two different zones between the fresh explosive and its detonation products: a detonation wavefront, where occurs the compression of the fresh material, and the chemical reaction zone, where occurs the chemical decompositions and the consequent reactions, which includes the CJ point. It also assumes that these two zones propagate together with the same velocity, relatively to the fresh explosive in its initial state 0. So, the problem with the ZND model is to determine one point in the HP curve where all the detonation zones have the same velocity (Mendes, 2000).

The HE curve, presented in Figure 1-11, represents the compression of the fresh explosive without changing its chemical species, and the HP curve represents the relaxation of the detonation products formed by the same explosive. Let's assume that the fresh explosive is compressed by a SW until point 2 and that the CJ point (point 1) belongs to the HP curve (Figure 1-10 and Figure 1-11). So that all the DW zones have the same velocity, these points (1 and 2) have to be collinear, starting at point 0 (P_0, V_0). The determination of the CJ point, or the state 1 (P_1, V_1), characteristic of a stable detonation, is done by the elimination of all the lines that are not tangent to the HP curve and which start at point 0. All these lines are eliminated through the same parameters that were used in the CJ model. In this DW structure, state 2 is the so-called Von Neumann (VN) peak or spike (Dremin, 1999) (Mendes, 2000).

The scheme of Figure 1-11 (top) shows the DW passage (from the right to left direction) on the fresh explosive and its different complementary zones, where D_{CJ} is the CJ velocity, u_P is the particle velocity of the detonation products and C_b is the sound velocity of

the detonation products, as well as the *P-V* diagram (bottom left) with the Hugoniot curve for shock wave without chemical reaction on the fresh explosive (HE-black curve), the Hugoniot curve for the detonation wave that originates the detonation products (HP-red curve), the Rayleigh line (blue), and the Champan-Jouguet and the von Neumann points. C_0 is the sound velocity in the fresh explosive. It also shows the correspondence of the *P-V* diagram and the ZND detonation model scheme on the *P-x* diagram (bottom right), where δ is the thickness of the detonation wavefront (negligible when compared to the chemical reaction zone), and *a* is the thickness of the reaction zone (Dremin, 1999) (Mendes, 2000).

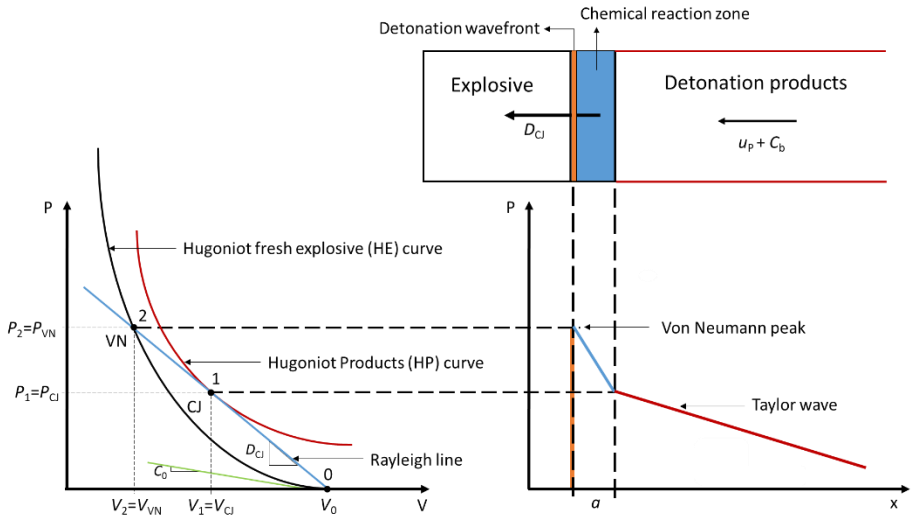

Figure 1-11: Scheme of the ZND detonation model its representation in the *P-V* and P-x planes, and the correspondences between them. Adapted from (Dremin, 1999) and (Mendes, 2000).

The structural model proposed by ZND for a DW (*P-V* diagram of Figure 1-11) assumes that fresh material shocked by a shock front reaches point 2 (intersection between the HE curve and the Rayleigh line), the known von Neumann peak, or spike, without any chemical reaction. After this, there is a pressure decrease along the Rayleigh line until the CJ point (point 1). At this moment, the detonation velocity reaches the value D_{CJ} (Kubota, 2015).

Resuming, the ZND model is based on the following assumptions:

1. It is a unidimensional flow.
2. The detonation front represents a discontinuity on the kinetic properties of the explosive and, due to that, it can be treated in the same way as a SW on non-reactive media.
3. The reaction products, released from the chemical reaction zone, are in chemical equilibrium, and the chemical reaction is complete.
4. The thickness of the chemical reaction zone is different from zero.
5. The detonation velocity variation rate is zero.

Having into account these restraints, the DW structure can be understood as a SW that is moving along the explosive, where the DW front compresses and heats it. Due to this high compression and temperatures, represented by the von Neumann peak in Figure 1-11, the fresh explosive is broken into chemical species, with the release of energy, which will start a chemical reaction in the so-called chemical reaction zone. At the end of this chemical reaction, at the CJ point (Figure 1-11), the detonation products are formed. After the formation of the detonation products, which are in equilibrium, they suffer an expansion - the so-called Taylor wave (Figure 1-11). In this model, the velocity of the DW front propagation is controlled by the energy released in the chemical reaction zone (Mendes, 2000).

As shown, the ZND model describes the mechanism responsible for the DW propagation: ignition by adiabatic compression of the leading shock, which is kept by the push generated by the gases formed in the reaction zone and their expansion in the products zone (Lee, 2008).

1.9. Analytical characterization of the detonation wave: conservation equations and thermal equation of state for the detonation products

The CJ and ZND models, which describe a stable DW, can be analytically characterized through a unidimensional analytical study applied to the plane detonation wavefront of an explosive (Mendes, 2000). To characterize the characteristic variables of a stable DW it is necessary to consider the mass, momentum, and energy conservation principles described in 1.3. Applying the conservation principles to the initial and final states of a stable detonation (CJ point (1) in Figure 1-11), the conservation equations are the same as the ones defined for a one-dimensional plane SW (point 1.3), but with some alterations: the SW velocity, U_S, is substituted by the DW velocity, D; it is considered that the explosive is initially in rest, which means that $u_{P0} = 0$, and that the initial pressure value, P_0, can be neglected when compared to the final pressure value, P_{CJ} (Mendes, 2000). With these changes, the mass and momentum conservation equations ((1.27) and (1.30) in 1.3, respectively) are now given by equations (1.53) and (1.54), respectively.

$$\rho_0 D = \rho\,(D - u_{\mathrm{P,CJ}}) \tag{1.53}$$

$$P_{\mathrm{CJ}} = \rho_0\, D\, u_{P,CJ} \tag{1.54}$$

The combination of the equations (1.53) and (1.54) gives the equation (1.55), which describes the slope between the points 0 and CJ, or the slope of the Rayleigh line, which gives the detonation velocity value *D* (Mendes, 2000).

$$D^2\rho_0^2 = \left(\frac{P_{\mathrm{CJ}}}{V_0 - V_{\mathrm{CJ}}}\right) \tag{1.55}$$

The energy conservation equation applied to the detonation front is defined by equation (1.56), where *e* represents the explosive specific internal energy.

$$e_{\mathrm{CJ}} + P_{\mathrm{CJ}}V_{\mathrm{CJ}} + \frac{1}{2}\left(D - u_{P,CJ}\right)^2 = e_0 + P_0V_0 + \frac{1}{2}D^2 \tag{1.56}$$

Combining equation (1.56) with equations (1.53) and (1.54), we obtain equation (1.57), the known Hugoniot curve, represented as Hugoniot products (HP) curve in Figure 1-11.

$$e_{\mathrm{CJ}} - e_0 = \frac{1}{2}\left(\frac{P_{\mathrm{CJ}}}{V_0 - V_{\mathrm{CJ}}}\right) \tag{1.57}$$

Since equations (1.53), (1.54), and (1.56) are not enough to solve all the existent variables, will be determined the thermal equation of state (EoS) that describe the behavior of detonation products, so that all variables have a solution (Mendes, 2000).

The easiest way to deal with the detonation products is to consider that they behave as perfect gases obeying the EoS given by equation (1.5). Since these gases are under high pressures, the ratio between the specific heats (γ – equation (1.10)) is now substituted by Γ. For an ideal monoatomic gas γ = 1.667, while for most of the explosives Γ≈3 (Mendes, 2000).

In the ZND theory, where it is considered that the chemical reaction is finished at the CJ point, the detonation products' thermal EoS is given by the equation (1.58), where *q* is the energy per mass unit released during the detonation.

$$e = \frac{PV}{\Gamma - 1} - q \tag{1.58}$$

Substituting equation (1.58) in the energy conservation equation (1.57), and neglecting the e_0 value (much smaller than *q*), it is possible to rewrite the HP curve equation (1.59).

$$e\frac{PV}{\Gamma - 1} = \frac{1}{2}P(V_0 - V) + q \tag{1.59}$$

To obtain the HP curve in the P-u_P plane is necessary to eliminate the volume V in equation (1.59) using equation (1.44), and solve the equation to P. The result is the equation (1.60).

$$P = \rho_0 \, (\Gamma - 1) + \frac{1}{2}\rho_0(\Gamma + 1)u_P^2 \tag{1.60}$$

To determine the pressure and the velocity of the detonation gases in the CJ point, it should be used the CJ relation, where the Rayleigh line has to be tangent to the HP curve in the P-u_P plane, which means that $dP/du_P = P/u_P$ (Mendes, 2000). So, to obtain the pressure on the CJ point (P_{CJ}), it is needed to make the derivative of equation (1.60) to u_P and equalize it to P/u_P. The obtained result is equation (1.61).

$$P_{CJ} = \rho_0 \, (\Gamma + 1) \, u_{P,CJ}^2 \tag{1.61}$$

Determining u_P through equation (1.54) and substituting that in equation (1.61), it will be possible to reach equation (1.62), which is largely used in explosives engineering (Mendes, 2000). Since for most of the explosives $\Gamma \approx 3$, it is possible to simplify equation (1.62), as shown below.

$$P_{CJ} = \rho_0 \, \frac{D_{CJ}^2}{\Gamma + 1} \approx \, \rho_0 \, \frac{D_{CJ}^2}{4} \tag{1.62}$$

To obtain the detonation products' velocity in the CJ point (equation (1.63)) it is necessary to substitute P_{CJ}, shown in equation (1.62), on P_1 (CJ point and point 1 are the same – see Figure 1-10) of equation (1.54).

$$u_{P,CJ} = \frac{D_{CJ}}{\Gamma + 1} \tag{1.63}$$

This is the easiest way to take care of the detonation products, to find an EoS that better describes the real behavior of these gases (Mendes, 2000).

Adding the conservation equations, based on the hydrodynamic model applied to the detonation, to the presented thermal EoS it is possible to solve all the characteristic detonation variables for a stable detonation: P_{CJ}, D_{CJ}, $u_{P,CJ}$, and e (Mendes, 2000).

A more precise method to estimate the detonation pressure (P_{CJ}) from the initial density of the fresh explosive (ρ_0) and its detonation velocity (D), as well as the Hugoniot curve of the detonation products (HP) in the P-u_P plane was developed by Cooper (1996). Cooper (1996) collected experimentally derived data from a large number of explosives and explosive mixtures for which the initial density, CJ density, detonation velocity, and detonation pressure

were measured independently in the same experiment for each data set. With all the collected data, Cooper plotted the initial density (ρ_0) of the fresh explosives according to their respective density at the CJ state (ρ_{CJ}) and observed that the data could be fitted with a straight line when displayed on a log plot (Figure 1-12), which was described by equation (1.64) (Cooper, 1996).

$$\rho_{CJ} = 1.386\ \rho_0^{0.96} \tag{1.64}$$

From (1.62), the same relation is given by equation (1.65).

$$\rho_{CJ} = \frac{4}{3}\rho_0 \tag{1.65}$$

Both equations gave close agreement to the experimental points, however eq. (1.65) underestimated ρ_{CJ} at the lower densities, as shown in Figure 1-12 (Cooper, 1996).

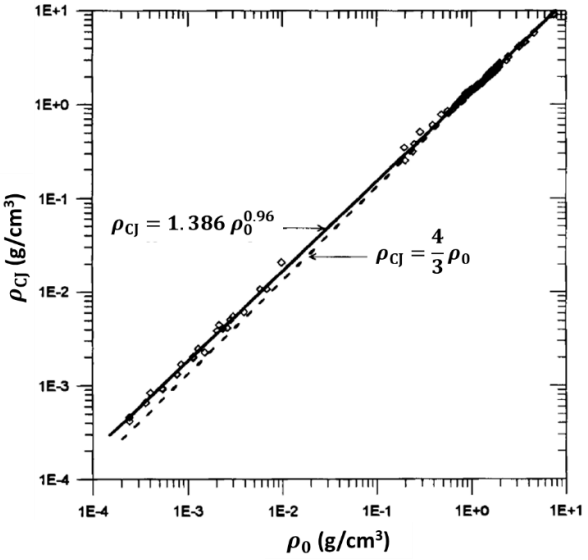

Figure 1-12: Correlations between CJ density and initial density of different explosives determined by Cooper (left) and by equation (1.65) (right). Adapted from (Cooper, 1996).

Rearranging equation (1.55) in terms of densities, it was possible to obtain the P_{CJ} according to the initial density and detonation velocity of the used explosive, as shown in equation (1.66).

$$P_{CJ} = \rho_0 D^2 \left(1 - \frac{\rho_0}{\rho_{CJ}}\right) \tag{1.66}$$

Combining (1.66) with (1.64), it was possible to obtain the equation (1.67) that allows the estimation of the P_{CJ} according to the parameters ρ_0 and D (Cooper, 1996).

$$P_{CJ} = \rho_0 D^2 (1 - 0.7125\ \rho_0^{0.04}) \tag{1.67}$$

According to Cooper (1996), equation (1.67) estimates the detonation pressure of an explosive within 5% of the values experimentally measured.

The Hugoniot curve of the detonation products (HP) is the combination and continuum of the two regimes that join at the CJ state, the shock adiabatic (states above CJ point), and the expansion isentrope of the detonation products (states below the CJ point).

To define a general HP equation that could be used to estimate the HP of any explosive, Cooper proposed the equation (1.68), fitted to the collected experimental data. This equation (1.68) is presented in the reduced form P/P_{CJ} and $u_P/u_{P,CJ}$, and is valid for the states above a reduced pressure of 0.08 (Figure 1-13) (Cooper, 1996).

$$P = \left(2.412\ P_{CJ}\right) - \left(\frac{1.7315\ P_{CJ}}{u_{P,CJ}}\right) u_P + \left(\frac{0.3195\ P_{CJ}}{u_{P,CJ}^2}\right) u_P^2 \tag{1.68}$$

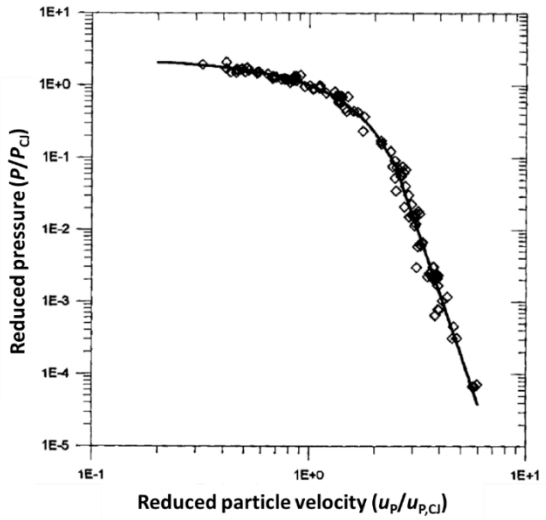

Figure 1-13: Reduced pressure versus reduced particle velocity and the fittings performed by Cooper. Image from (Cooper, 1996).

2. METROLOGIES FOR DETONATION CHARACTERIZATION OF ENERGETIC MATERIALS

This chapter intends to present some detonation metrologies that are available to measure the detonation parameters that were successfully measured throughout this thesis: the detonation velocity (D) and the detonation pressure (P_{CJ}) of an explosive.

The following detonation metrologies will be divided according to the measuring parameter. The detonation velocity techniques will be divided into five main groups, while the detonation pressure techniques will be divided into two main groups, both according to the applied method. This chapter includes a description of each technique, examples of acquired results, how to analyze them, and also the techniques' limits, advantages, and disadvantages.

2.1. Detonation velocity techniques

Detonation wave velocity D is one of the most important detonation parameters on the explosive's performance and also one of the easiest to measure (Sućeska, 1995) (Sućeska, 1997) (Agrawal, 2010) (Quaresma, et al., 2019).

The most common and simple way to determine detonation velocity is to measure the time interval that the DW needs to travel a very well-defined distance, determined between two points in an explosive charge (Sućeska, 1995) (Sućeska, 1997). Two measuring points are enough for explosive charges whose D does not change along the path (Sućeska, 1997) (Agrawal, 2010). However, there are many real situations where this does not happen, such as charge initiation, shock-to-detonation transition, and detonation failure, or very small scale measurements (Plaksin, et al., 2002). In these cases, it is needed to obtain the detonation velocity throughout all the charge, which requires a complete perception of the DW propagation path throughout the explosive (Sućeska, 1997).

The experimental methods used to determine D can be divided into five groups: 1. Dautriche method, 2. optical methods, 3. electrical methods, 4. optical fiber methods, and 5. microwave interferometry (Sućeska, 1995) (Sućeska, 1997) (Wei, et al., 2017). Instead of "optical method", in this work was decided to use the nomenclature used by D. Tete, et al.,

(2013) - photographic methods - to not make confusion with the optical fiber methods and with the ones developed during this thesis, since they are called optical passive and active methods. The following points will follow this division.

2.1.1. Dautriche method

The Dautrice method is based on the concept that two processes, which propagate with different linear velocities, will run distinct distances in the same time interval (D. Tete, et al., 2013). The difference between these distances will be a simple function based on the velocities of the two processes. Knowing the traveled distances and the velocity of one of the processes it is possible to determine the unknown velocity of the second process (Sućeska, 1997) (D. Tete, et al., 2013).

A scheme representing the experimental set-up for this method is presented in Figure 2-1. Inside the charge is an explosive which velocity is unknown (D_X) and has to be determined. For that, two holes (A and B), with a very well-determined distance between them ($\overline{AB}$), are used to fix the two ends of a detonating cord, which has a very well-known D (D_{DC}) and whose length was precisely determined (L_{DC}). Bellow the detonating cord should be put a witness plate, normally out of aluminum or lead, in a way that the detonating cord middle point (M) is well marked and near to one of the extremities of the plate. When the detonation of the unknown explosive starts, it will reach point A, which will initiate the detonating cord. After a while, the DW will reach point B and initiate the other extremity of the detonation cord. After some time, the two DWs generated in the two extremities of the detonation cord will meet at the collision point (C), which will be very well marked at the witness plate (Sućeska, 1995) (Sućeska, 1997) (Meyer, et al., 2007) (Agrawal, 2010) (Tete, et al., 2014). Measuring the distance between M and C ($\overline{MC}$), it is possible to determine D_X (Sućeska, 1995) (Sućeska, 1997):

$$D = \frac{\Delta x}{\Delta t} \Leftrightarrow \Delta t = \frac{\Delta x}{D}$$

$$t_{\overline{AMC}} = t_{\overline{ABC}}$$

$$\frac{\overline{AMC}}{D_{DC}} = \frac{\overline{AB}}{D_X} + \frac{\overline{BC}}{D_{DC}} \Leftrightarrow D_X = D_{DC}\frac{\overline{AB}}{2\,\overline{MC}} \quad (2.1)$$

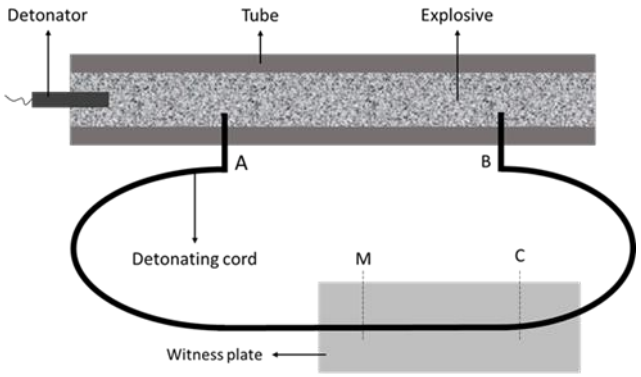

Figure 2-1: Scheme of Dautriche method. Adapted from (Tete, et al., 2014).

This very simple and inexpensive method, where no special and/or expensive apparatus are needed, is useful for rough estimations of *D* (Sućeska, 1995) (Sućeska, 1997) (Meyer, et al., 2007) (Agrawal, 2010), and suitable for testing cartridge explosives in unconfined spaces (D. Tete, et al., 2013).

However, it presents some disadvantages: it is dependent on the accuracy of $\overline{AB}$, $\overline{MC}$ and L_{DC} measurements and also on the detonation cord's D_{DC}, which means that this method lacks precision and accuracy (Sućeska, 1995) (Sućeska, 1997), being reported a data accuracy of around 4 to 5% (Agrawal, 2010). Such measurements have low reliability (Cybulski, et al., 1949). Nevertheless, all measurements, even performed with other methods, are conditioned by parameters as the type of confinement, charge diameter, and density.

2.1.2. Photographic methods

Since detonation is an auto luminous process, it is possible to continuously visualize and record its propagation throughout the explosive charge. With proper high-speed cameras, it is possible to calculate the detonation velocity by making a distance vs time plot from the DW propagation or calculate it from the motion images/ video (Sućeska, 1997) (D. Tete, et al., 2013).

The high-speed cameras can be divided into five groups, according to their working principles: 1. rotating prism cameras; 2. rotating-mirror streak (or scanning) cameras; 3. rotating mirror framing (or integral image) cameras; 4. electronic cameras; and 5. digital CCD (charged-coupled device) cameras (Sućeska, 1995) (Sućeska, 1997) (Honour, 2009). The digital CCD cameras are divided into four subgroups: single CCD sensor,

intensified CCD sensor (ICCDs), solid-state framing, and ultrafast electronic streak digital cameras (Honour, 2009). The following points will follow these groups' division.

2.1.2.1. Rotating prism cameras

Invented by Tuttle in the ’30s of the last century (Fuller, 2009), rotating prism cameras use the refraction properties of a prism to move an image while the prism is rotating (Taylor, n.d.). The rotating optical prism just transmits imaging rays when its parallel sides are perpendicular to the camera’s optical axis, in any other orientation the image is completely blocked to be registered on the sensitive recording media - photographic film. As result, it is formed two images for each prism rotation. The prism rotation is mechanically synchronized with the film speed, to provide optical compensation and to allow the formation of images coherently separated in time. This mechanical synchronization is made by the film movement (pull and pushed by spools and sprocket drives) that accelerates the prism until the wished rotational recording speed. These cameras operate in framing and/or streaking modes (Honour, 2009).

It is reported that these cameras have recording rates between 100 to 40000 frames per second (fps) (Honour, 2009) (Fuller, 2009), a typical spectral response on the visible range of the electromagnetic spectrum, a spatial resolution up to 65 line pairs per millimeter (lp/mm) and typical time resolution of 1 μs, that can be lowered to 50 ns by using Cu pulsed lasers (Honour, 2009).

For data processing, two consecutive images are always needed and the detonation velocity is calculated as the ratio between the distance traveled by the DW shown in such frames, and the time interval that passed between the same two frames of the film track (Sućeska, 1997). Figure 2-2 is an example of such two frames.

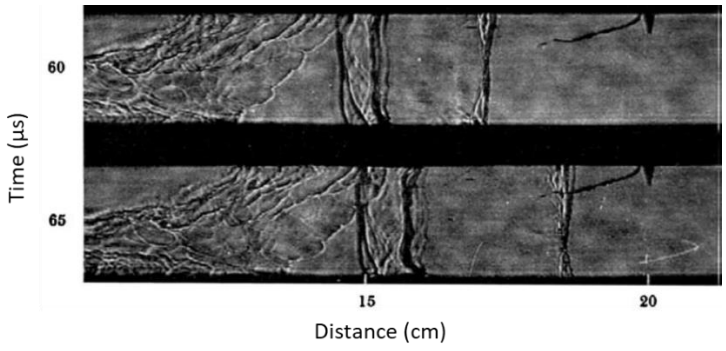

Figure 2-2: Two frames from a rotating prism camera’s cinematographic schlieren record that shows a self-sustained detonation propagating at CJ velocity, in an equimolar hydrogen-oxygen mixture. Adapted from (Oppenheim, 2008).

Rotating prism cameras have some attractive characteristics, like the recorded images are coherently separated in time; high framing rates; besides black and white, there is the possibility of colored images; and portability (Honour, 2009). Although with the development of high-speed cameras, these became unattractive, because they needed a large quantity of expensive photographic film (around 120 m), being the biggest part used only to mechanically rotate the prism at the wished recording speed; the part of the film used to register data needed very toxic chemicals for imaging processing, and it is hard to make the alignment between the camera and the explosive (Honour, 2009).

2.1.2.2. Rotating-mirror streak (or scanning) and framing (or integral image) cameras

The rotating-mirror cameras, as the prism ones, record the appearance and displacement of luminous zones coming from the propagation of the detonation process through an explosive charge (Sućeska, 1997).

For the streak cameras, these zones are scanned across the perpendicular direction of an observation slit, with constant velocity, through the fast movement of a mirror that reflects the image on a stationary film track (Sućeska, 1997) (Honour, 2009). As a result, the acquired image is a line with distance-time coordinates: the spatial information (displacement of the DW through the explosive charge) is given by the observation slit's direction, while the temporal information is supplied by the scanning direction (perpendicular to the slit) (Sućeska, 1997).

In the case of the framing cameras, the image that is formed on the rotating mirror will be reflected into different relay lenses, which are aligned according to the different mirror's angular positions. These reflections will be then recorded into the film, where it is possible to acquire one image for each lens. The mirror's rotation ensures the separation between images on the film track and in time. The framing speed is fixed by the angular separation between lenses and by the mirror's rotation speed; the exposure time is defined as the time needed for the light beam to go through each lens. The framing cameras also have a mechanical shutter that opens when it is reached the pretended writing speed. For both types, the rotating mirror speed (measured by a frequency meter) and trigger system are controlled electronically, being the mirror inserted into a high-pressure system to avoid mechanical stress, and the synchronization between the studied phenomenon and the

shooting can be made through a predetermined delay (Sućeska, 1995) (Sućeska, 1997) (Fuller, 2009).

The images obtained by the rotating-mirror framing cameras are similar to the ones presented in Figure 2-2 and their treatment is the same as described for the rotating-prism cameras. A typical record of a rotating-mirror streak camera is shown in Figure 2-3. The left bright border, shown as a relatively straight line, represents the path of the DW in distance-time coordinates; the right less bright border, much more perturbated than the left one, shows secondary processes of the detonation phenomenon (Sućeska, 1995) (Sućeska, 1997).

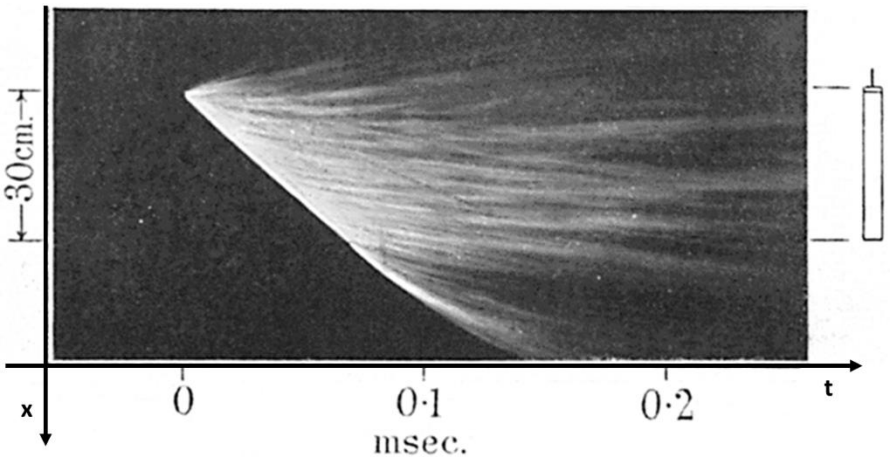

Figure 2-3: Buxton rotating-mirror streak camera photographic record of the detonation of a cylindrical charge of crystalline TNT. Adapted from (Cybulski, et al., 1949).

The detonation velocity along the explosive charge is obtained through the differentiation of the distance-time line:

$$D(t) = \frac{d\left(\frac{x}{f}\right)}{d\left(\frac{t}{v}\right)} = \frac{v}{m}\frac{dx}{dt} \tag{2.2}$$

Where v is the linear velocity of film track, m is the image magnification and the $\frac{dx}{dt}$ is the slope from the distance-time line (Sućeska, 1995).

The *D* of the Seismoplast was measured with a rotating-mirror streak camera (Held, 2002). The streak record is shown in Figure 2-4 and it was acquired with the help of three mirrors, where mirror A was parallel to the camera and the other two (B and C) were making 45 degrees with the axial position, above and below it. The detonation velocity in such streak records is given by the inclined streak line (c) shown in Figure 2-4 and, the average *D* obtained in this study was 7500 m/s (Held, 2002).

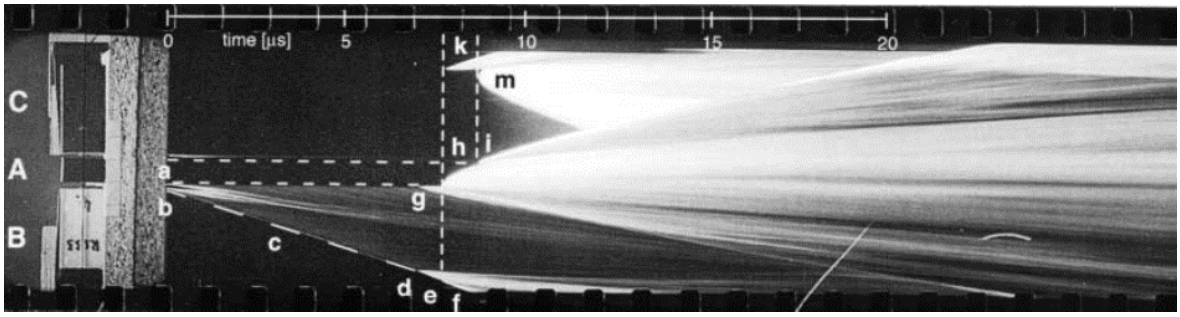

Figure 2-4: Rotating mirror streak camera record obtained from the detonation of Seismoplast. Image from (Held, 2002)

With recording rates up to 25 million frames per second (fps), these cameras have the same typical spectral response as the rotating-prism ones, a spatial resolution higher than 50 lp/mm and time resolutions of nanoseconds (Sućeska, 1995) (Sućeska, 1997) (Honour, 2009) (Fuller, 2009).

In the advantages of the rotating-mirror cameras are included: high precision; fast time resolution; short exposure times that reduce the blur characteristic of a fast movement phenomenon coming from a motionless position; high framing rates; one image contains all the space-time information; good spatial resolution; few additional electronics; and the possibility to use colored film (Sućeska, 1995) (Sućeska, 1997) (Honour, 2009).

As for disadvantages, these cameras present: as the previous ones, a hard alignment between the camera and the explosive charge, dependence on the detonation's auto luminescence (without it there is no way to acquire data), and requirement of film processing. Characteristic of these cameras are: the hard interpretation of the detonation's secondary processes; hard calibration of the working parameters that need to be coordinated between them, such as the rotation speed of the mirror, the angular separation between the lens (for framing cameras), the time synchronization between the explosive's initiation and the camera's trigger system; low sensitivity for faint events; complex optical system – requires many kinds of different lens; and low portability due to weight and size. Specifically, the framing ones have the disadvantage of needing more than one frame to determine the detonation velocity (Sućeska, 1995) (Sućeska, 1997) (Honour, 2009).

2.1.2.3. Electronic cameras

In the electronic cameras, the image of the phenomenon in study is formed, through the object lens, at the photocathode. The obtained optical image is converted into an electron beam, by means of electrode and anode focusing, which will form a sharp image of

the phenomenon on a phosphorus screen. This formed image is then photographed on a Polaroid or high-speed negative film (Sućeska, 1995) (Honour, 2009).

The electronic cameras can work in the two modes - streak and framing. When in framing mode, after completing all the framing sequences, the electron beam is horizontally deflected by the shift plates, and a new image is formed on the screen. Through compensating plates, the electron beam is vertically deflected, originating two vertical images in all the framing sequence. The synchronization between the camera and the phenomenon in study is directly made by the electronic delay generators incorporated on the camera, which are responsible for a shutter activation coincident with the firing impulse. When these cameras are operating in streak mode, the electron beam is continuously deflected vertically through the screen, allowing a continuous registration of the phenomenon (Sućeska, 1997). Images from detonation phenomena registered by electronic streak and framing cameras are shown in Figure 2-5.

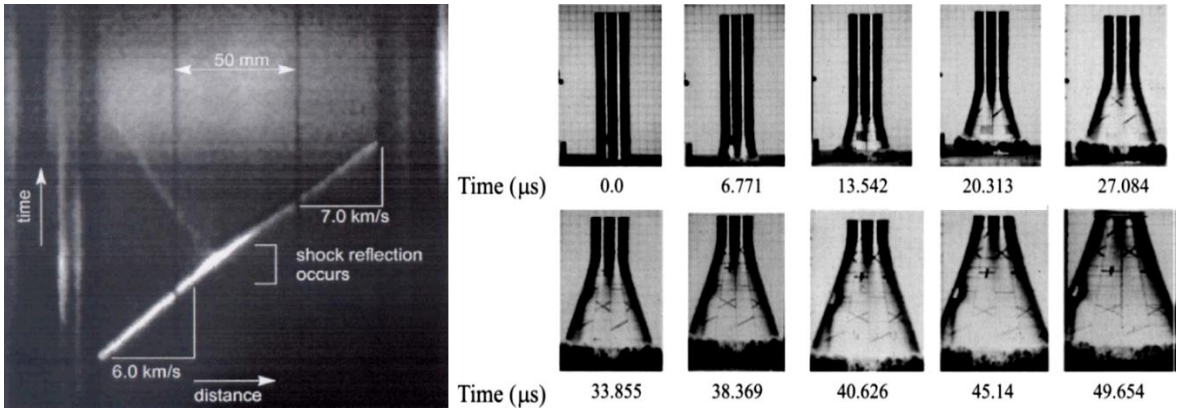

Figure 2-5: Electronic camera records. At the left, a streak camera image of detonation propagation in shock-compressed nitromethane (from (Petel, et al., 2004)). At the right, a framing camera images sequence of the expansion of a thin cylinder filled with a not specified high explosive (from (Martineau, et al., 2000)).

The analysis of the images presented in Figure 2-5 is done in the same way as already described for other streak and framing cameras presented before. For the left image, as indicated, the *D* of each phenomenon is given by the slope of each respective line. For the right framing sequence, the *D* is calculated by the different visible positions of the detonation phenomena in two (or more) consecutive frames, which time separation is well-known, as shown in Figure 2-5, right.

According to the literature, electronic cameras can reach scanning speeds of 100 mm/ms and in their characteristics are included: time resolutions that vary from nanoseconds (10^{-9} s) to tens of picoseconds (10^{-11} s); framing rates until 50 million fps; possible spectral

response from IR to UV (cover the electromagnetic spectrum from 200 to 900 nm); spatial resolutions of 5 to 10 lp/mm, depending on the framing rate; and the novelty that these systems, differently from the others described until here, have a gain, typically of 50 times. Other benefits of such cameras are: fast imaging processing - Polaroid films are readable in less than 1 minute; versatile working modes; and easier synchronization between the detonation process and the data acquisition, promoted by the incorporated electronic delay generators (Sućeska, 1995) (Sućeska, 1997) (Honour, 2009).

Nevertheless, electronic cameras present some drawbacks, mostly from the user's point of view: they have fragile image tubes; it is hard to make the focusing between the electrode and the anode, as well as to program the delay generators, due to the difficulty to determine precisely the delay between the explosive's initiation and the camera's shutter; they need expensive photographic films, being hazardous the high-speed negative ones, due to the need of chemical processing; the acquired images are few, small and can be distorted by the electronic optics; and they have lower spatial resolutions when compared to rotating cameras. To the streak ones, it is added the fact that they are not proper to measure *D* in big and/or heterogeneous explosive charges, due to their short acquisition times (Sućeska, 1995) (Sućeska, 1997) (Honour, 2009).

2.1.2.4. Digital CCD (charged-coupled device) sensor cameras

The CCD technology was developed at the end of the 1960s and, on such sensor, the images are registered on pixels (Honour, 2009) (Xing, et al., 2017). Pixels are microscopic picture elements produced in very high-resolution photolithographic film emulsions during a photomechanical process (Honour, 2009). This process is based on the generation of electronic charge when the incident rays hit the individual pixels, using the doped silicone-based material that forms the CCD sensor. These charges are then moved from the pixels to the buffer device, and from there to the amplifier. Then, through an analog-to-digital converter (ADC), it is generated an output in sequence. To increase the intensity of the available light on the optical system, image intensifiers are used in the digital CCD sensor cameras (Honour, 2009) (Xing, et al., 2017).

These cameras are divided into three groups: the single CCD sensor cameras that use only one sensor and a rotating mirror system for diverging the incident rays to the pixels; the intensified CCD (ICCD) sensor cameras, which possess a micro-channel plate (MCP) image intensifier connected to a CCD sensor, and a beam splitter to divide the incoming light

that is directed to the pixels; the solid-state framing cameras that use multiple ICCD sensors interfaced to an optical beam splitter; and the ultrafast electronic streak cameras, which possess high gain solid-state readout systems (Honour, 2009) (Xing, et al., 2017). For all of them, the acquired images are downloaded through an Ethernet connection between the camera and the control computer. They have local controls and an incorporated integral screen that allow focusing and image composition in real-time (Honour, 2009). For detonation studies, most of the presented cameras need additional light sources.

At the beginning of the 1950s, the rotating -mirror system was successfully adapted to digital cameras thanks to the Miller principle, where the incoming light, separated sequentially by the rotating-mirror, has to pass through multiple fixed focusing objects to reach the photosensitive medium (Xing, et al., 2017). High radiative sources, like xenon flashes, are needed to register non or little radiative processes, such as the detonation process of a cylindrical charge on an aquarium test presented in Figure 2-6 (Honour, 2009). This figure has an example of a streak record (on top) and two framing photographs (bottom) from a Hadland Imacon 468 CCD camera (Brousseau, et al., 2002). The detonation velocity can be acquired from such images as it was already described before.

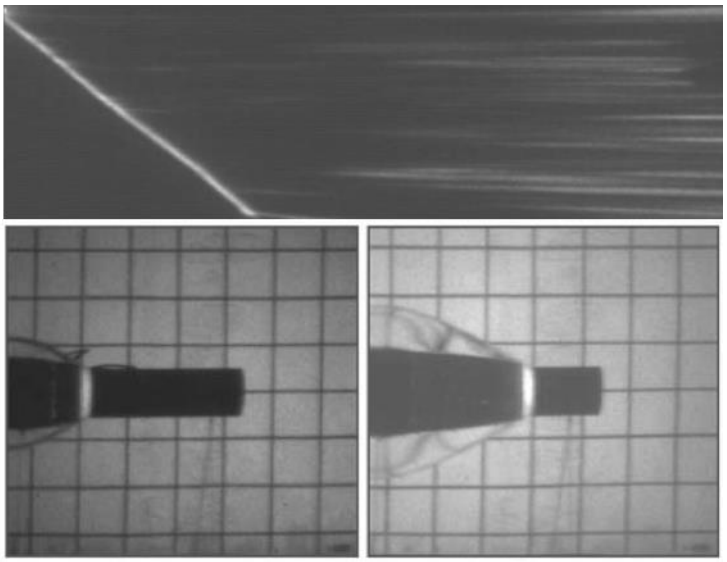

Figure 2-6: Streak record (top) and frame photographs (bottom) from an aquarium test performed to an TNT/Al cylindrical charge. Image from (Brousseau, et al., 2002).

The typical framing rates of these digital rotating-mirror cameras are in the range of mega frames per second (Mfps) and their resolutions between 2 and 8 megapixels per image (Xing, et al., 2017). Higher framing rates can be achieved by using binning methods

(the combination of a pixels' cluster into a single larger pixel), but they reduce effectively the number of active pixels in the sensor (Honour, 2009).

Among the advantages of these cameras are that the maximum speed and resolution can be achieved simultaneously, the image quality is comparable to the images produced by some film cameras and, for higher framing rates, multiple cameras can be complexed and controlled together. As for disadvantages, the movable mechanical device makes these cameras complex and fragile, one camera produces a limited number of frames, different manufactured CCD sensors used together can introduce measurement errors, spatially shifted frames can happen due to alignment issues, they have restricted portability because of their weight and size (Honour, 2009) (Xing, et al., 2017).

Later on, at the beginning of the 1990s, it was developed the ICCD sensor cameras base on MCP image intensifiers. The principal task of such an image intensifier is to amplificated the incident radiation signal through the multiplication of the incoming photons (Xing, et al., 2017). Such MCP intensifiers connected to the sensor by optic fiber allowed higher photonic gains, which resulted in very short exposition times and modest light requirements characteristic from these cameras. Another novelty in these cameras was the possibility of retriggering the sensor, allowing the acquisition of a higher number of images, but it demanded inherent optical technology that affected the overall image quality, like the electron depletion of the MCP and the phosphor screen where copies of the real event are displayed. Very short decay phosphors are used in such screens. They allowed the capture of two images in a single ICCD, and they are responsible for the photoconversion characteristics of these cameras (Honour, 2009). Typical records of such cameras are shown in Figure 2-7 and they were used to characterize the shape and the speed of the detonation products of triaminotrinitrobenzene (TATB) (Sollier, et al., 2012).

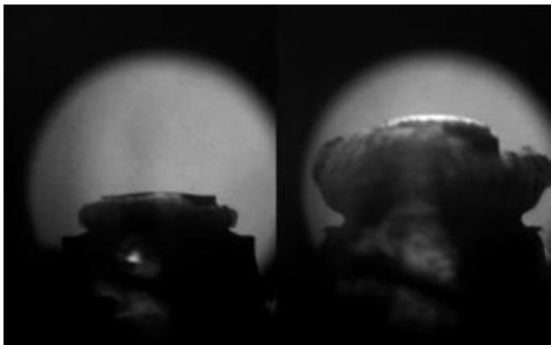

Figure 2-7: Expansion of the detonation products of TATB acquired by digital high-speed shadowgraphy with three gated ICCD cameras. 1.2 μs delay between images; 20 ns exposure time. Images from (Sollier, et al., 2012).

Commonly, the ICCD sensor cameras have photonic gains of few orders of magnitude and, at least, 8 channels of MCP-CCD sensors that allow the acquisition of 8 sequential frames at speeds until 200 Mfps. Other characteristics of these cameras are: a common spectral range from 400 to 900 nm, being also possible from 180 to 800 nm; typical gains of 10 to 7000 times; and a maximum spatial resolution of 70 lp/mm (Honour, 2009) (Xing, et al., 2017).

Other advantages, besides the ones presented until here, when compared to the single CCD sensor cameras are higher gain in the video signals, higher capturing rate and sensitivity, and improved image quality (Honour, 2009). The inconveniences associated with them are the increase of the noise level on the acquired images from the presence of image intensifiers; the number of recorded frames is quite low; hard to perform an accurate trigger; the optics associated with the retriggering system can hide details and degrade the global quality of the acquired image; phenomena as the MCP's electron depletion and the endurance of the phosphor screen can cause (alone or in simultaneous) ghosting and image retention; the used extremely short decay phosphors have weak photonic conversion characteristics; the increase on the video signal gain can have a prejudicial visual effect in the image quality (Honour, 2009) (Xing, et al., 2017).

Solid-state framing cameras are more advanced ICCD sensor cameras, which means that they capture image sequences at even higher framing rates since they possess multiple ICCD sensors interfaced with the beam splitter. This advancement was possible thanks to the developments on the beam splitters, like the application of the kaleidoscope principle, where a sequence of images is produced on a segmented intensifier connected to a high-resolution CCD. Such systems were improved with relay optics that, besides being responsible for controlling the image forming rays and giving depth to the image without damaging it, solved the problem of the amount of light that reached the recording media. The overall image quality was enhanced by the increase in the number of pixels in the CCD sensors and by improved ADCs that allowed 12-bit digitalization, also responsible for a reduction in the video noise. The higher spatial image quality and reduced distortion were reached by the use of more advanced (proximity-focused) image intensifiers, also responsible for the extremely short exposition times, the reduced use of big and powerful light sources, and for the control of the sensibility of each channel. In opposition to the ICCDs cameras, the solid-state framing cameras cannot be retriggered, which means that the

problems associated with the electron depletion of the MCP and with the phosphor decay characteristics no longer exist. The solid-state framing cameras accommodate a more advanced integrated display, which makes possible the in-situ image confirmation and the dismiss of a control computer for set-up proposes. These cameras also have complex, but more user-friendly, trigger systems that can be used to synchronize the camera with the experiment and/or with other equipment (Honour, 2009).

Figure 2-8 shows 6 inverted frames from a solid-state framing camera, the SI SIM 16 Channel Framing Camera (Specialised Imaging, n.d.). The shown test was done to determine the characteristic energy of the explosive in a cylinder test, but other detonation parameters can be taken from those framing images, such as a rough estimation of the detonation velocity.

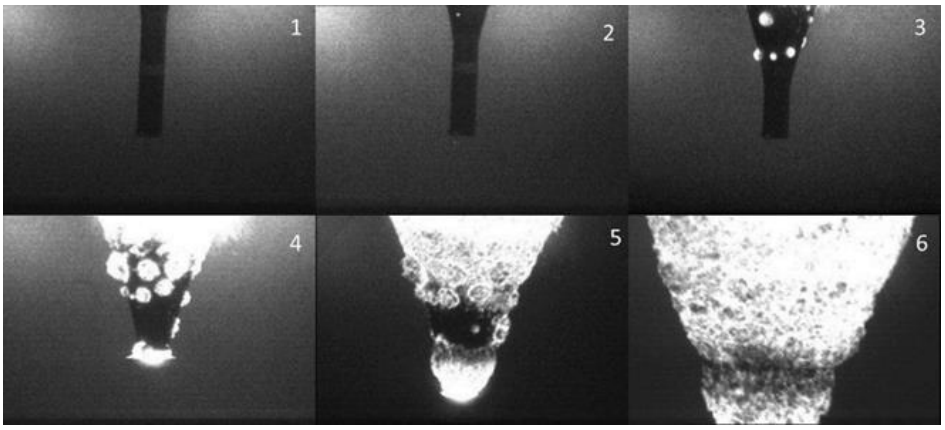

Figure 2-8: Inverted framing images from a cylinder expansion test from (Specialised Imaging, n.d.) acquired with a solid-state SI SIM 16 Channel framing camera.

The SI SIM 16 Channel Framing Camera has as features: 16 individual channels, a dynamic resolution between 36 and 50 lp/mm, exposure times between 3 ns and 10 ms, a single input optical beam splitter, time between frames from 1ns to 1 ms, framing rate up to 1 billion fps, an active CCD pixel 1360(H) x 1024(V), a delay to first exposure from 50 ns to 10 ms and a dynamic range of 12 bit (Specialised Imaging, n.d.). Other features included in the solid-state framing cameras are an overall system's resolution higher than 50 lp/mm, recordings up to 24 sequential frames with rates over 1 billion fps, and associated exposures times of 1 ns, being possible to reach exposure times until 200 ps (Honour, 2009) (Xing, et al., 2017).

Other "pros" from these cameras are: the higher flexibility provided by the higher framing rates; the small parallax discrepancy that their images may present can be

corrected with programmable software; the acquired images present higher contrast and no ghosting thanks to the fact that the image intensifiers cannot be retriggered; higher accuracy and reproducibility ensured by a quartz clock; when distances longer than 100 m are needed between the camera and the control computer and the Ethernet cables cannot be longer used, fiber optic media converters can be used instead, which are especially useful when these cameras have to work in an electrically noisy environment. The appointed "contras", in the beginning, were a low sensitivity and the long standard exposure periods of 100 ns; but the one that still prevails is that the image quality of these cameras is not good as the ones that use film as recording media. The quality of such images is still questionable because the light amount that reaches the recording sensor is still restricted to the extremely short exposition times that are needed to capture images from ultrafast movements (Honour, 2009).

Ultrafast electronic streak cameras were developed to register phenomena that change their luminous intensity profiles within picosecond or sub-picosecond time scales. They are included in the digital cameras, due to their high gain solid-state readout systems, formed by an MCP intensifier connected to silicone-based sensors by optical fiber, that overcome the need for additional intensification of the registered images, and their complex image acquisition system is based on microprocessor technology. They could be also included together with the electronic cameras (as the name suggests) since they use image tubes to direct the light to the recording media. These cameras are even more versatile than the ones presented until here since their mainframe has the option to insert different modular drive circuit configurations. Such drive configurations include single-shot operation, where a single exposition has to supply enough photoelectrons to produce a registrable image; synchroscan operation that registers low-intensity repetitive events, and it is dependent on a very fast frequency power oscillator to scan the electron beam across the phosphor screen, constructing an image with time; and retrace blanking operation can be used similarly as the synchroscan, however, so that this operation is advantageous, the return sweep of the electron beam is biased off the phosphor screen.

An image from a streak record is shown in Figure 2-9. This streak record was obtained to observe the space-time breakout curvature of the DW generated on a CL-20 pellet by a detonator, with sub-nanosecond resolution. This record was captured at a

maximum sweep speed of 25 ns/mm, which corresponds to an achieved temporal resolution of 0.225 ns/pixel for all experiments (Murphy, et al., 2019).

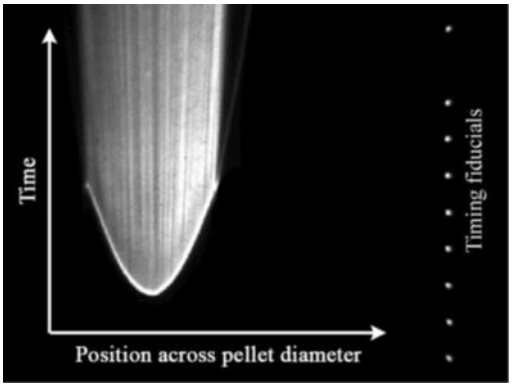

Figure 2-9: Streak record of the DW breakout through the surface of a CL-20 pellet, acquired with an Optronis SC-20 streak camera. The image develops from bottom to top. Image from (Murphy, et al., 2019).

According to the producer (Optronis GMBH, 2020), these series of cameras have temporal resolutions inferior to 600 ps, a time base between 120 ns and 3 μs, a spectral response between 350 nm and 950 nm, and a readout time of around 6 seconds. But, in general, such systems have a typical spectral response between 200 and 800 nm, but it is possible to have it between 200 and 1600 nm; a minimum temporal resolution of 200 fs; a system gains from 50 times that can exceed 500 times and a spatial resolution of 20 lp/mm (Honour, 2009).

Other characteristics of the ultrafast electronic streak cameras that are valuable are the versatility and commodity that come from the different trigger systems that depend on the experiment; the broad spectral response, from IV to UV; more sensitive than the film cameras, because they do not need such great intensification to compensate the losses that come from the film cameras' complex optical systems; very high framing rates (up to 10^6 fps) are reachable using multiple framing image converter cameras with fast decay phosphor image intensifier screens; and accurate and reproducible recording sequences. The less pleasant features of these cameras include: rigid constraints on the tube and circuit designs, due to the high degree of sweep linearity that is needed to perform synchroscan and retrace blanking operations; high technological thoroughness, since the input optics has to be carefully matched with to the image tube spectral response; the need of additional sensitivity to produce a properly exposed image; complex control software that has to be written by computer programmers (Honour, 2009).

Common to all digital CCD sensor cameras is the possibility of local and remote control; the convenience and time-saving characteristics of these sensors that can display the acquired image sequence within seconds, which also allows the quantitative measurements of the recorded image sequence to be made in-situ and immediate changes on the experimental parameters; the existence of proper software to improve, modify and enhance the definition of the digitalized images; more convenient storage, fast sharing a fast reproducibility of the acquired images, since they can be kept in small and easy access electronic retrieval systems, it can be made copies from the copies and the quality of the copied images will be the same as the original one. Nevertheless, often the images produced by CCD sensors do not have the same quality, resolution, and detail as the ones registered in photographic films, because pixels have bigger areas and they are not randomly dispersed, like the silver halide crystals in the fine-grain emulsions of the photographic films (Honour, 2009).

2.1.3. Electrical methods

According to (Sućeska, 1997), the electrical methods use one of the two detonation phenomena to acquire data: the detonation products of a DW are strongly ionized, which means that they can conduct electric current that can be used to make a short circuit between two or more probes; and the destructive power (coming from the pressure) of the DW makes it able to mechanically destroy one or more probes.

The existing *D* systems can be divided into two major groups (Venkatesh, et al., 2001), the discrete and the continuous systems. The discrete systems, where *D* is measured between two or more discrete points, are systems that include two kinds of probes, ionization and electrocontact types, and two kinds of time acquisition systems, the electronic chronometers and the fast oscilloscopes (Sućeska, 1997). The continuous ones, that measure continuously *D* along its path, include the resistance wire, and the SLIFER (short Location Indication by Frequency of Electrical Resonance), and they are based on the reduction of the sensor's length by the action of the DW (Venkatesh, et al., 2001) (D. Tete, et al., 2013) (Tete, et al., 2014).

2.1.3.1. Discrete systems

In these systems, two or more probes are inserted into an explosive sample with a very well-determined distance between them. The time that the DW wave takes to travel

from one probe to the next one is recorded by electronic chronometers or fast oscilloscopes (Sućeska, 1997). The *D* is then commonly calculated by the ratio between the known distance between probes and the acquired time.

The most basic of these systems consists of two probes that are connected to an electronic chronometer. When the DW arrives at the first probe, the timing clock is started and it will be stopped when the DW arrives at the second probe (Sućeska, 1997) (D. Tete, et al., 2013) (Tete, et al., 2014). The velocity probes work like an electrical switch, where a short circuit between two conductors is generated by the passage of the DW. The electrical impulses, which control the electronic chronometer, are generated by a capacitor that discharges when the electric contact of the associated velocity probe is closed. Electronic chronometers can have time resolutions inferior to nanosecond scale and measuring time intervals up to 100 ms (Sućeska, 1997). A scheme of such a system is shown in Figure 2-10.

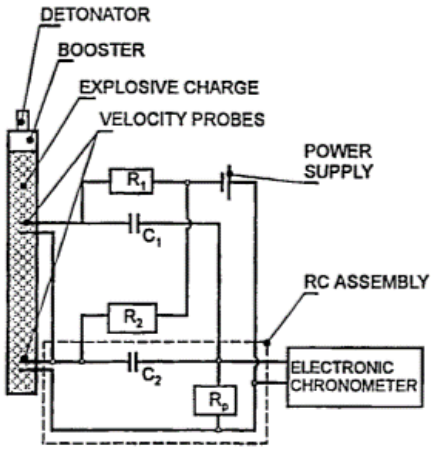

Figure 2-10: Scheme of a discrete *D* system based on two velocity probes and an electronic chronometer. Image from (Sućeska, 1997).

These point-to-point systems work with two different types of probes, the ionization, and the electro contact types. The ionization probes' performance is dependent on the ability that the strongly ionized detonation products of the DW have on conducting an electric current. This electric current, when the DW meets the probe, will short circuit the two conductors of the probe, originating then the discharge of the associated capacitor. There are four different types of such probes: the twisted wires, the pins, the printed circuits, and the stripped ionization probes (Gois, 1995) (Sućeska, 1997). The electrocontact, or mechanical probes are more complex and, probably due to that, are barely present in the actual literature, where just two works were found (Mendes, et al., 1993) (Gois, 1995) that are not on open access. The close or the breakage of the electrical circuity is made

mechanically, due to the pressure that the DW applies on the probes (Gois, 1995) (Sućeska, 1997). Two types of probes are described in (Sućeska, 1997), one that consists of a copper tube with a partially non-insulated copper wire inside, and another that consists of two conductive metal foils separated between them by a thin insulation foil. On both of them, the short circuit is caused by the compression that the DW applies on them in a way that, in the first, the non-insulated part of the copper wire is squeezed against the copper tube, while in the second type is the destruction of the insulation foil and consequent touch between the metal foils that originates the closure of the electric circuit (Sućeska, 1997).

The discrete systems can also be used with fast oscilloscopes. In these cases, the arrival of the DW to the sensor will cause the closure of the electric circuit, the capacitor's discharge, and a voltage jump on the resistor, which is recorded by the fast oscilloscope. The oscilloscope is triggered by an additional probe that is placed near the first measuring probe. The fast oscilloscopes can be analog or digital, both give oscillograms that show the voltage peaks described above and both can use the two probe types already defined (Sućeska, 1997). Although, the analog ones are obsolete, being the ultra-fast signal recording digital oscilloscopes with ionization pin probes used nowadays. A typical record from the pin ionization probes connected to a digital oscilloscope applied to HWC (RDX/Wax/Graphite) pressed charges is shown in Figure 2-11, as well as the equivalent graph with the important times and distances registered on it.

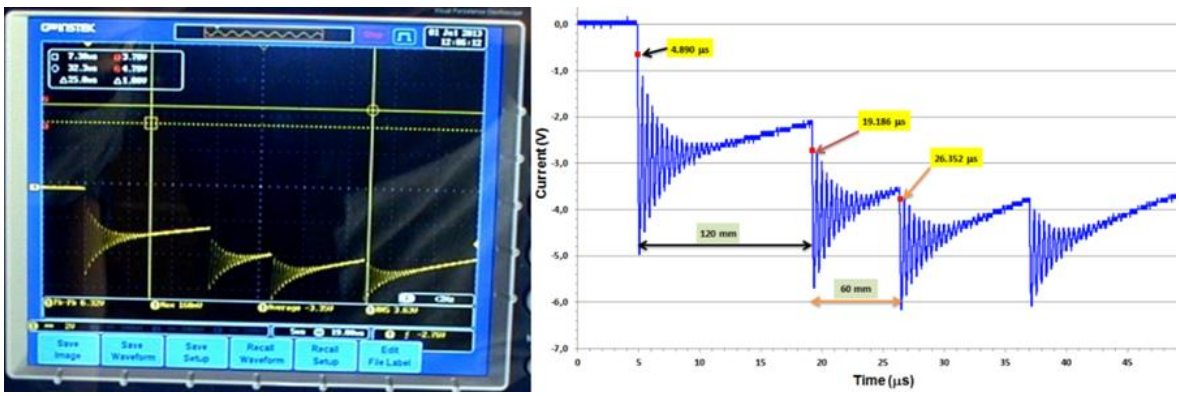

Figure 2-11: Raw image was taken directly from the oscilloscope screen (left) and its treated version by Excel (right), where it is shown the arrival time of the detonation front and the distance between the ionization pins. Both images were taken from (Nevstad, 2015).

2.1.3.2. Continuous systems

As said before, the continuous systems to measure *D* can be divided into two groups: the continuous resistance wire method, and the SLIFER, which will be presented.

The United States Bureau of Mines (USBM) developed the resistance wire continuous *D* system at the beginning of the 1960s. This system is based on Ohm's law. In practice, a resistance wire probe, with known resistance per length unit, is inserted into the explosive probe along its longitudinal axis, with a constant current passing through it. The electric circuit is then closed by the arrival of the DW, due to its strong ionization. While the DW is traveling through the explosive charge, the probe is being consumed with it, which makes a voltage change that is proportional to the length of the destroyed probe. In this way, the position of the DW can be continuously monitored (Sućeska, 1997) (Venkatesh, et al., 2001) (D. Tete, et al., 2013) (Tete, et al., 2014).

Analytically, the probe resistance according to time ($r(t)$) is given by equation (2.3), where $L(t)$ is the probe's length and r_p the probe's electric resistance per length unit.

$$r(t) = L(t) r_\mathrm{p} \tag{2.3}$$

A constant current (I_s) is flowing through the probe, which means that the voltage probe output (*V(t)*) in the moment *t* can be known through equation (2.4).

$$V(t) = L(t) r_\mathrm{p} I_\mathrm{s} \tag{2.4}$$

Rearranging (2.4) according to *L(t)* and substituting it in (2.3), it is possible to obtain the detonation velocity at any time instant by equation (2.5).

$$D(t) = \frac{dL(t)}{dt} = \frac{1}{r_\mathrm{p} I_\mathrm{s}} \frac{d\,V(t)}{dt} \tag{2.5}$$

At least, there are six different types of continuous resistance probes described in the literature (Sućeska, 1997), but the common are the ones formed by two insulated twisted wires together, and the ones that consist of one coated wire place inside of a small tube that performs as the second wire (Venkatesh, et al., 2001).

Mendes, et al. (1993) measured the detonation velocity of industrial explosives using a resistance wire continuous *D* system, with a parallel double thin resistive wire as a probe. The obtained oscillogram (*V(t)*) for dynamite is presented in Figure 2-12 (left). From this result, the authors could also trace the evolution of the detonation front displacement (*L(t)*). The obtained *D* for dynamite in this work was 5900 m/s.

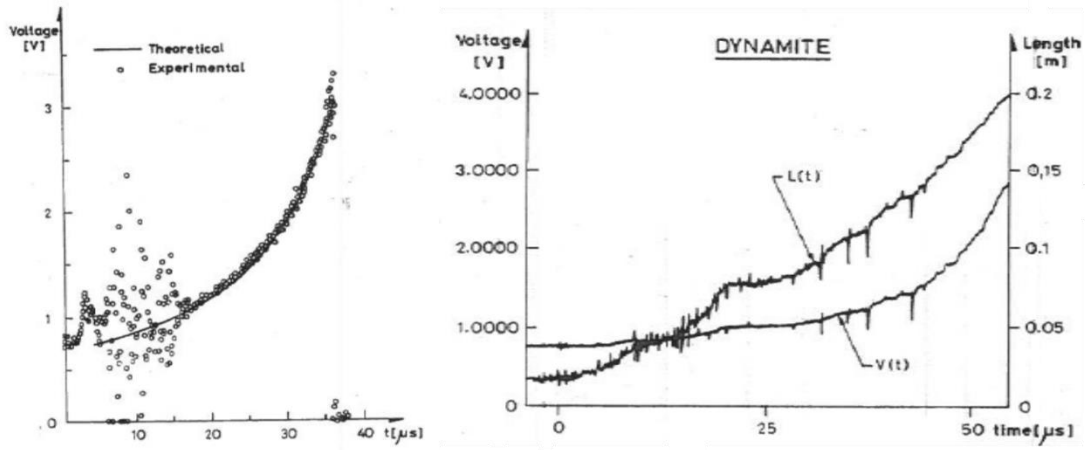

Figure 2-12: Obtained oscillogram from the detonation of dynamite (left) and variations of the voltage (V(t)) and the sensor length (L(t)) along the time from a resistance wire continuous measurement (right). Images from (Mendes, et al., 1993).

The continuous resistive wire method is an uncomplicated method, reliable, easy to assemble, with low-cost consumables, that truly provide continuous *D* measurement throughout an explosive charge when the wires are properly shorted during the detonation process. It also allows studying other phenomena, like the detonation initiation (signal transition on the oscillogram shown on the left side of Figure 2-12) and the detonation front displacement according to the time (*L(t)* on the right part of Figure 1-12) (Mendes, et al., 1993) (Venkatesh, et al., 2001) (D. Tete, et al., 2013). Nevertheless, these systems need a very stable direct current source, if the wire does not decrease its size continuously and reliably, they will give wrong results, excessive electronic noise, and severe dropouts (Sućeska, 1997) (Venkatesh, et al., 2001) (D. Tete, et al., 2013).

Sandia National Laboratories developed the SLIFER (Shorted Location Indication by Frequency of Electrical Resonance) continuous *D* system for measurement of the DW propagation in nuclear explosions. This system consists of a short coaxial cable, connected to an oscillator circuit, that is inserted into the explosive sample. While the detonation follows its path, this coaxial cable decreases its length, which makes an increase in the oscillation frequency (Figure 2-13, left). By monitoring this frequency along the time, it is possible to determine the rate of change in the cable length leading and, thus, determine the *D* of the studied explosive (Venkatesh, et al., 2001). The measured frequency can be converted in real-time to a voltage signal (Figure 2-13, center) using an onboard electronic package or by an external frequency to voltage converter (Heusinkveld & Holzer, 1964) (Venkatesh, et al., 2001). This data is then linearized and inserted into a consumed cable

length versus time plot, where the *D* can be acquired from the slope of the resulting trace (Figure 2-13, right) (Venkatesh, et al., 2001).

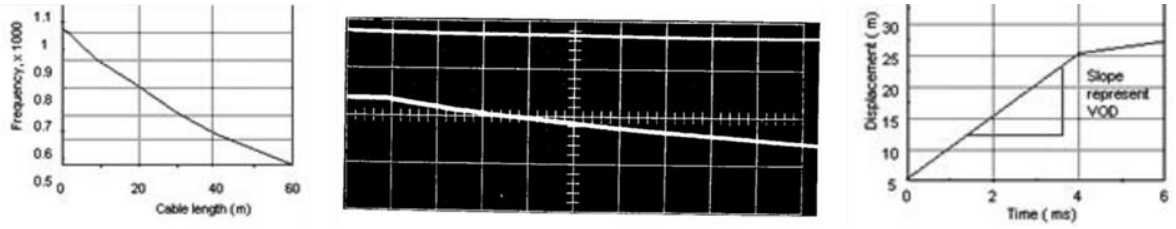

Figure 2-13: Representative images from the SLIFER data acquisition and treatment. The right and left images are from (Venkatesh, et al., 2001) and the middle one from (Heusinkveld & Holzer, 1964).

It is reported that the SLIFER is an excellent method to use in the laboratory environment, but it is not advised to use in field applications. This happens because each sensor must have an oscillator in line and such cable cannot be longer than 66 m, which means that the SLIFER system has to be put close to the experiment (Venkatesh, et al., 2001) (D. Tete, et al., 2013) (Tete, et al., 2014).

2.1.4. Optical fibers methods

The optical fibers (OFs) have the ability to detect and transmit light, which makes them viable as detonation velocity probes. Since the detonation phenomena emit radiation, using optical fibers it can be recorded by fast streak cameras, or converted into an electrical signal by a fast photodiode and recorded by a fast-digital oscilloscope, or another suitable ultrafast signal acquisition technique (Sućeska, 1997) (D. Tete, et al., 2013).

In this work, the OF methods are divided into discrete and continuous methods, according to their abilities to measure the D by determining, by point-to-point, the time that the DW needs to move between two or more probes inserted through the charge, or by tracking continuously the DW propagation by following a change of a known OF property like the refractive index, respectively (Pachmáň, et al., 2017). The OFs, as probes, also can be divided into two groups: the passive probes that are dependent on the detonation radiation, and the active probes, which are dependent on an external source of radiation.

2.1.4.1. Discrete passive optical fiber methods

The discrete passive optical fiber techniques consist of placing the OFs in very well determined positions, typically normal to the charge's axes, and throughout the explosive charge. Since these techniques are passive, it means that the optical probes detect

and transmit the radiation emitted by the DW. What varies most in these systems are the recording systems used to acquire signals from which the time intervals are obtained.

It was found in the literature that these systems can work with timing clocks (Xiaoyan, et al., 2011) (D. Tete, et al., 2013) (Tete, et al., 2014), ultrafast digital oscilloscopes (Quaresma, et al., 2016) (Prinse, et al., 1999), interface based on a microprocessor board (Pachmáň, et al., 2017), and a transient recorder (Quaresma, et al., 2018) (Quaresma, et al., 2019) (Quaresma, et al., 2020). In all these techniques, the detonation radiation is transformed into an electrical signal by photoelectric conversion.

Xiaoyan, et al. (2011) describes a timing clock system based on the field programable gate array (FPGA). This system is composed of two optical fibers to detect and conduct the detonation radiation to the photoelectric conversion circuit. There, the light signal is transformed and amplified into an electrical signal. The counting of the time is initiated when the first signal arrives at the FPGA processing circuit and is finished by the arrival of the second signal since this system is sensitive to the rising voltage of the converted luminous signals. In the end, the time between probes and the respective *D* is shown in the LCD module. The detonation velocity (D) is calculated by equation (2.6), where Δx is the distance between probes, *N* is the clock number and f_S is the crystal frequency of the system.

$$D = \frac{\Delta x}{N} f_S \tag{2.6}$$

The authors do not specify the time resolution of the system, but they claim that it is feasible, steady, has a high measuring precision, is simple to manipulate and it is not susceptible to electromagnetic interference (Xiaoyan, et al., 2011).

Prinse, et al. (1999) used one single optical fiber and a fast-digital oscilloscope to measure the *D* of an HNS II (Hexanitrostilbene type II) explosive. In this work, the OF is put in the detonation propagation axis. This probe, a PMMA OF with 1 mm diameter, has the particularity of being drilled with holes (0.2 mm diameter) lengthways, which distance between them is well known (increasing from 0.5 to 2 mm). So, when the DW reaches a hole, the air that is inside it will be ionized, due to the compression of the hole, and a light pulse is generated. This light pulse will then be converted by an optical-electrical converter and registered by the oscilloscope. Part 2 of Figure 2-14(right) shows the result obtained from this technique.

The reported characteristics of this system are: an optical-electrical converter with a bandwidth of 125 MHz; a rise time around 4 ns and a fall time of 14 ns for

measurements between 10 and 90% of the optical pulses, and the width of the signal at 10% of the amplitude is around 20 ns (Prinse, et al., 1999). This system looks to be of easy assemblage, but the drilling of the fibers seems to be a hard and time-consuming process that needs specialized handwork to be done precisely. A reported disadvantage about this system is the increase of the signals' intensity with the reduction of the length of the probe, which makes initial low-intensity signals; this happens due to the damage induced on the fiber by drilling the holes (Pachmáň, et al., 2017).

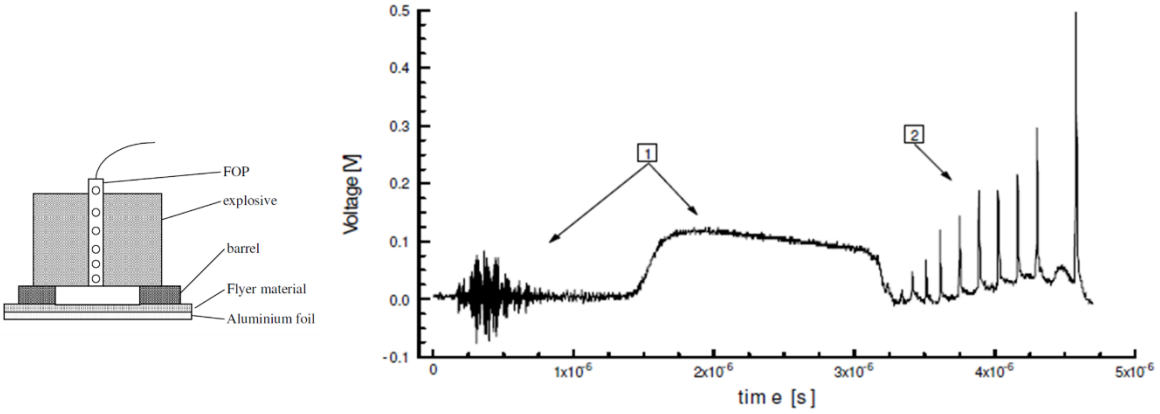

Figure 2-14: Experimental set-up (left) and acquired results (right) recorded with a single drilled OF inserted axially into the charge. Images from (Prinse, et al., 1999).

The OPTIMEX system, described in (Pachmáň, et al., 2017), is a *D* meter recently developed to study the detonation characteristics of explosives by passive optical probes. It consists of three subsystems connected between them by printed circuit boards: an analog front-end subsystem that is associated with each channel and makes the optical to electric conversion employing optical/electrical converters, amplifiers, and low-pass filters components; a digitizer subsystem that converts the analog electric signals in digital data, which is then stored in an internal memory of FPGA; and a microprocessor/microcontroller board used to communicate the data to the user and for the setup of the measurement parameters like triggering modes and insertion of distances between probes.

OPTIMEX works with glass (GOF) and plastic (PMMA) optical fiber (with 1 mm diameter) probes, it is available in handheld and table-top versions, where the first one has 8 channels and the other one can have up to 64 channels. Both systems are equipped with 12-bit ADCs with sampling rates of 250 MSa/s and 4 ns time resolution (Pachmáň, et al., 2017). An example of a measurement made with OPTIMEX to detonating cord, with 8 GOF probes is shown in Figure 2-15 (Pachmáň, et al., 2017). The authors also used the "S"

technique with a single PMMA OF and they reported the problems already referred to above: low data readability, partially overlapped signals, and peaks with unclear origin.

According to the authors (Pachmáň, et al., 2017), the passive PMMA OF probes are the most suitable for discrete *D* measurements, because of their high resistance to electrical noise and adverse environmental conditions; they are easy to assemble and do not require a special tool to handle with; and their commercial availability. As inconvenient, they point to the thickness of the fiber, where 2 mm diameter is excessive for some samples and their relatively high attenuation when compared to GOFs. By their side, GOF probes are cheap for being widely used in telecommunication systems; they are versatile due to their modes (single and multi), diameter ranges, and assemblage, being possible to have many in one single cable. The disadvantages of GOFs are their low mechanical robustness and, for some explosives, low light gain that leads to adjustments on the attenuation of the light detectors (Pachmáň, et al., 2017).

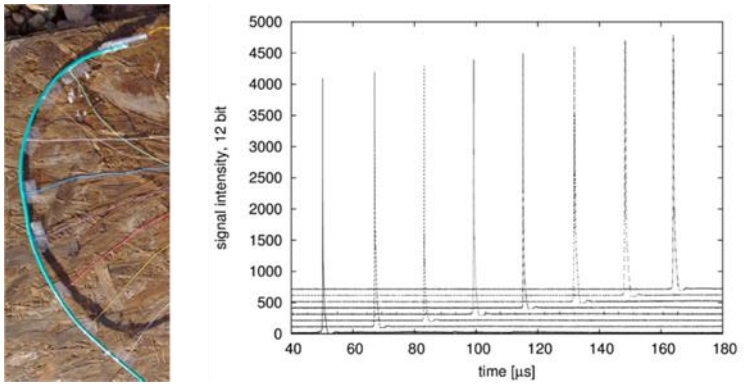

Figure 2-15: Experimental set-up (left) and the respective acquired results (right) from a *D* measurement of detonating cord using the OPTIMEX system. Images from (Pachmáň, et al., 2017).

2.1.4.2. Continuous passive optical fiber methods

The continuous passive optical fiber methods are the ones that use a strip of optical fibers to detect and transmit detonation light quasi-continuously to a signal recorder.

The works performed by Mendes et al. (2006, 2012) to characterize emulsion explosives (EEx) used a multi-fiber optical probe (MFOP), a strip with 64 independent PMMA optical fibers with 250 µm diameter each; one of its ends was inserted 12 mm inside the EEx charge, while the other was connected without any intermediate optics to an electronic streak camera Thomson TSN 506 N, which allows a quasi-continuous evaluation of the DW velocity. The last 4 mm of the MFOP was embedded in a PMMA plate and put at the end of the explosive charge, to acquire the SW velocity in PMMA induced by the DW

of EEx. The used experimental set-up and the respective acquired results are shown in Figure 2-16. A description of electronic streak cameras and how to determine the *D* from their records was made in point 2.1.2.3.

This high-resolution optical fiber method has a spatial resolution of 250 μm and a maximum temporal resolution of 0.6 ns. It is useful to determine the characteristics and performance of new energetic materials and their compositions, it allows the study of the ignition phase of the DW formation in explosive crystals and it works with small samples (around 1 g) (Plaksin, et al., 2002) (Plaksin, et al., 2002 (2)). This method allowed to observe detonation phenomena occurring at mesoscale, namely the kinetic oscillations occurring in the detonation reaction zone (DRZ) that induces local variations on detonation velocity (Plaksin, et al., 2006) (I. Plaksin, 2008) and showed the interrelation between the irradiation from the reaction front surface (nonuniform and time-varying) and the DRZ structure. Specifically, it was observed the effect of the absorption and localization of radiative energy, transferred from the reaction zone to the PBX bulk, on the formation of the DRZ 3D structure during the shock-to-detonation transition (SDT). Experimental evidence obtained at a wide variation of the HMX particle sizes (0.58 μm < d50 < 960 μm), point to the fact that the 10 - 30 ns-width precursors arise as a result of the photoexcitation and radiation heating while the reaction light is scattered within the bulk of the HMX composite and absorbed by the HMX particles (Plaksin, et al., 2010).

Besides the advantages e disadvantages already presented in 2.1.2.3. for the electronic cameras, like their high costs, it seems to be the hard the acquisition of such fiber strips, which implies a laboratory preparation that should be very time consuming and needs specialized worker skills.

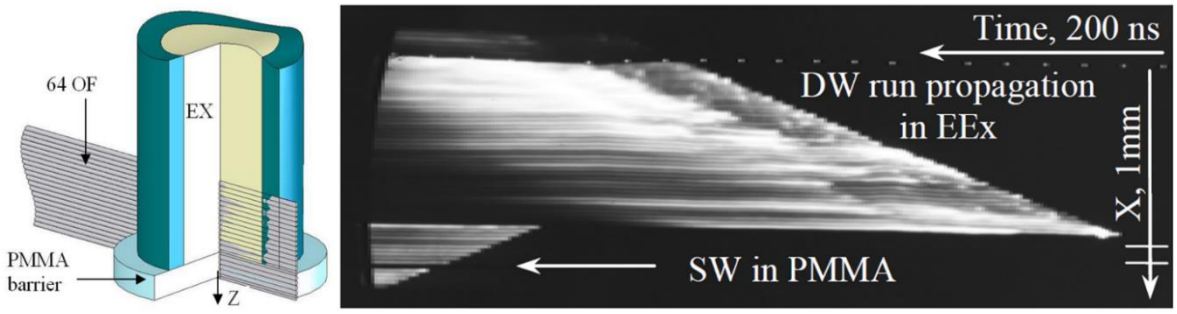

Figure 2-16: Experimental set-up (left) and photo chronogram (right) for the DW propagation in an EEx with 30% Al and its resultant SW propagation in PMMA. Images from (Mendes, et al., 2006) (Mendes, et al., 2012).

2.1.4.3. Continuous active optical fiber methods

The continuous active optical fiber methods measure continuously the *D* of explosives through the variation of an external or induced source of radiation, like an amplified spontaneous emission (ASE) source or a laser diode, that is caused due to the destruction of the optical fiber probes by the DW that are inserted into the explosive or in its surface. Examples of such probes are the chirped fiber Bragg grating (CFBG) that work with ASE source (Rodriguez, et al., 2014) (Barbarin, et al., 2015) (Rodriguez & Gilbertson, 2017) (Wei, et al., 2017), and the rare-earth-doped fibers that use a laser diode to induce spontaneous emission of the rare-earth sources (Pooley, et al., 2019). Both methods use fast oscilloscopes to register the obtained signals.

The CFGB was developed in 2004, at the McDonnell Douglas and Blue Road Research by Eric Udd to measure the shock velocity in water. A CFGB sensor consists of an optical fiber, typically with 150 μm diameter, which core was grated with a known chirp rate. Since the refraction index of the optical fiber varies with the grading, it is possible to establish a relation between the wavelength of light reflected from the CFBG and the grating position by the Bragg wavelength equation (Wei, et al., 2017). A scheme of the experimental set-up associated with the CFBG sensors is shown in Figure 2-17. Light from an ASE source, centered at the telecommunication C-band (1525 – 1565 nm), is sent to a 3-port power circulator via a single-mode fiber system. The power circulator directs the light to the CFBG sensor through port 2, which can be inserted into the explosive sample or on its surface. While the DW travels throughout the explosive charge, the shock-processed portion of the grating in the probe does not transmit or reflect any light, because of the high change on the local refraction index and damage to the grating structure. Since the chirp in the CFBG is linear, the spectral encoding of the CFBG wavelength reflection band is linear with the length. The reflected light that comes from the CFBG sensor is again directed to port 2 of the power circulator, where it is then detected at port 3 using a fast photodetector and recorded by the fast oscilloscope (Rodriguez, et al., 2014).

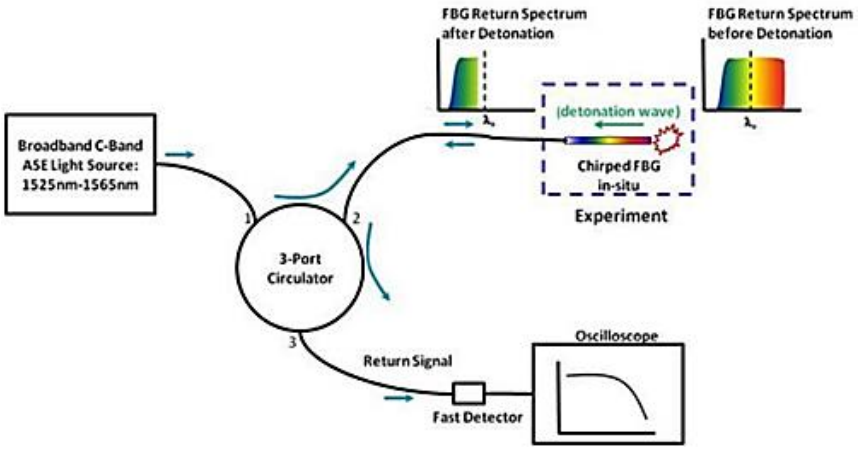

Figure 2-17: : CFBG detonation detection system. Image from (Rodriguez, et al., 2014).

The measurement of the reflected light intensity, by the CFBG during the detonation process, gives a ramp-down signal type (Figure 2-18, left) that can be linear if the detonation is established and ideal optical components are used. The signal's intensity can be transposed into a position (Figure 2-18 middle) through calibration and, consequently, can be obtained the DW position according to time which allows determining the *D* profile of the studied explosive, through the slope of the obtained graph (Figure 2-18 right) (Barbarin, et al., 2015). The CFBG sensors can be used to determine the *D* of individual explosives (Barbarin, et al., 2015) (Rodriguez & Gilbertson, 2017) (Wei, et al., 2017), they can be used to study the *D* of different consecutive explosives charges and they can also track shock position of a SW in inert materials (Rodriguez, et al., 2014) (Rodriguez & Gilbertson, 2017).

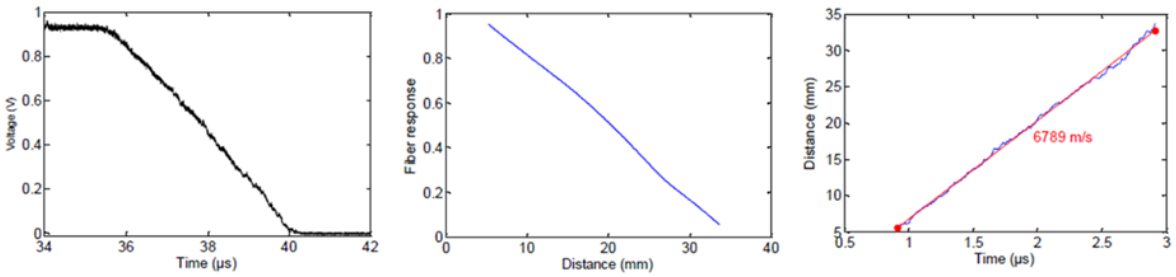

Figure 2-18: Experimental result of TNT *D* using the CFBG sensor and the system described above, where the graph of the left is the oscilloscope signal, the middle one the CFBG response in function of distance, the right one is the position vs time diagram with the fitted *D*. Image from (Barbarin, et al., 2015).

Rodriguez and his co-workers (Rodriguez, et al., 2014) (Rodriguez & Gilbertson, 2017) claim that the temporal resolution of the method is at the ten-nanosecond level and the spatial resolution along the CFBG is in the 50 µm to the sub-millimeter range, but it is dependent on other parameters' like length, chirp rate, and spectrum; the chirp rates

can vary between 0.35 and 3.45 mm/nm and the length of the sensors between 10 and 200 mm; They measured the *D* of PETN datasheet with CFBG sensors and they showed an accuracy level of 0.13% when compared with the results from the electrical wire pins that were performed in parallel. It is reported that the relative standard uncertainty of the *D* is below 1%, higher chirped rates give more accuracy to the measurements (Wei, et al., 2017).

Comparing with other methods, like streak cameras or electrical pins, the CFBG sensors provide very good detonation and shock tracking performance; they are adequate for experiments that need embedded sensors and/or for experiments where the *D* should be track continually, but it can change suddenly; good tracking on the *D* changes of the interfaces when applied to different explosives in simultaneous (Rodriguez, et al., 2014) (Rodriguez & Gilbertson, 2017). These sensors can be considered non-intrusive and flexible when fixed on the charge's surface; they allow a good signal-to-noise ratio due to the grating reflectivity; the system becomes insensitive to spectral distortions when it is properly calibrated (Barbarin, et al., 2015). They can be used in liquid explosives and metals; they are versatile in their application mode since they can be inserted into the sample or just in contact with it; it is a method with good stability, high accuracy, and good reproducibility; the small size is advantageous when the probe is needed to be into the explosive sample (Wei, et al., 2017).

As for disadvantages: this system is expensive; the short sensor's lengths sometimes are not enough for establishing a steady flow across reactive boundaries; they lose their abilities to track the SW position on an inert material when the pressure generated by the SW is not strong enough to properly damage the probe, but this can be surrounded by a complex time-streak spectrally-resolved approach (Rodriguez, et al., 2014) (Rodriguez & Gilbertson, 2017). The linear part of the grating response is normally distorted, due to the non-flat spectrum provided by the optical source and to the non-perfectly flat spectral response from the different fiber components; the reflected spectra of two CFBG sensors from the same batch can be different; this system is hard and complex to calibrate; the calibration has to be performed always before each experiment and without damaging the sensors; the real active grating length of the probe is shorter than the advised by the producer; to have a clear result, a steady detonation should be established (Barbarin, et al., 2015). The CFBG sensors are challenging to implement since they are sensitive to strain and temperature nonuniformities; the manufacture of these probes is difficult and expensive

when their lengths exceed few centimeters, because of their structural complexity; the acquired raw results always need to be processed to be analyzed (Pooley, et al., 2019).

The use of rare-earth-doped optical fibers as *D* continuous and active probes was initially applied in 1994, by J. D. Weiss, who used elongated-cladding optical-fiber probes, co-doped with neodymium and phosphorous, to measure shock propagation in detonating cord with lengths up to 19 m. This technique is based on the fact that the total power of fluorescence captured from a pumped active fiber is dependent on its length (Pooley, et al., 2019).

The description and application of this technique are made in a recent work performed by Pooley and his co-workers (Pooley, et al., 2019), where they used commercially available Erbium (Er) fibers to perform *D* tests to sensitized liquid nitromethane. The Er-doped fibers, due to their composition, can be induced into fluorescent spontaneous emission by being pumped by a laser diode. In this system, this emitted fluorescence, which is omnidirectional and dependent on the dopants number into the fiber, is filtered through a wavelength division multiplexing (WDM) coupler and acquired by a photodetector. When these fibers are embedded in the explosive sample, the DW will consume the fiber, which provokes a strong reduction in the fiber's fluorescent dopants and, consequently, a decrease in the power measured by the photodetector. A scheme representative of this concept is presented in Figure 2-19

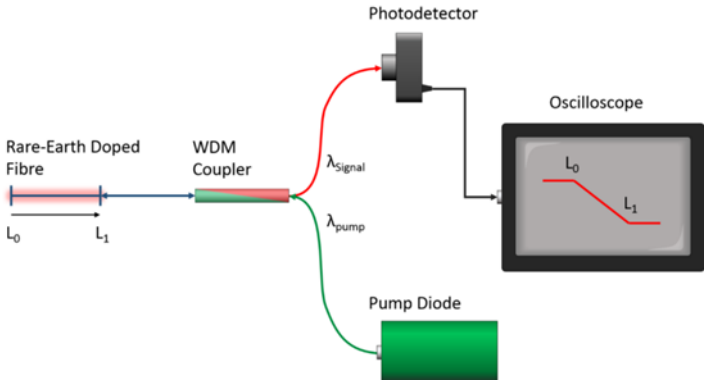

Figure 2-19: Basic set-up for the application of a rare-earth-doped fiber as an active and continuous *D* probe. Image from (Pooley, et al., 2019)

To measure the *D* of an explosive composition with such technique is needed to achieve a linear correspondence between the length of the fiber and its emitted power, which demands a complex calibration procedure that is dependent on five parameters: dopant type, dopant concentration, pump power, pump wavelength, and fiber length. When this is

achieved, the system is able to record the evolution of the DW position over time and, after some mathematical treatment, graphs like the green ones shown in Figure 2-20 (right) can be obtained (Pooley, et al., 2019). Figure 2-20 (left) shows the set-up that Pooley et al. (2019) used to measure the *D* of liquid nitromethane. It consisted of a 1 m long Er-doped fiber rolled helically around a copper tube (30 cm long), where the explosive was inserted. This test was performed two times in identical ways and the acquired *D*s, from the slope of the graphs, showed in Figure 2-20 (right), were 6.37 and 6.38 km/s.

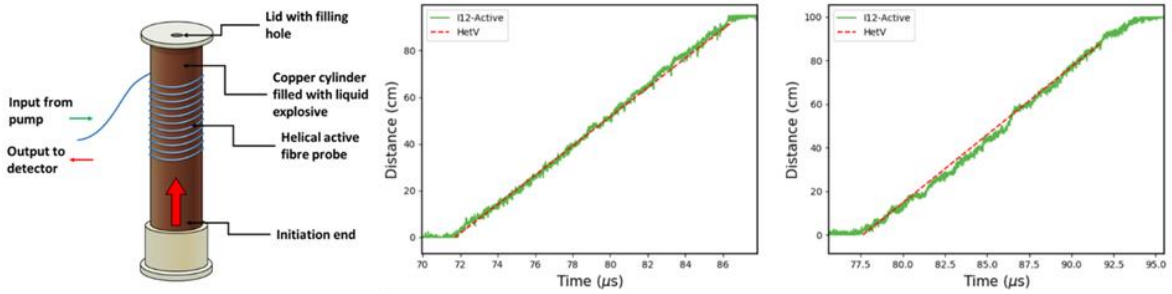

Figure 2-20: Scheme of the set-up using an Er-doped fiber as *D* probe (left) and the graphs resultant from the system's acquired data. Images from (Pooley, et al., 2019)

It is reported (Pooley, et al., 2019) that this technique was able to measure the *D* within 2% of the expected value, it has its highest spatial resolution (± 2 mm) when the fiber is helically inserted on the probe; the probe length had an associated uncertainty of ±2.5%; the used fibers (I-12) had total fluorescent power of 4.5 nW/mm; the fluorescent signal was monitored by a 125MHz detector and the output voltage was recorded by a 10-bit DAQ system with 1.25 GS/s.

According to the authors (Pooley, et al., 2019), the strong points of this method as a continuous measurement of *D* are: simplicity, scalability, low cost, ease to implementation, minimally invasive, commercially available probes; relatively insensitive to strain and temperature variations, which make them user friendly to non-specialized users; the probes can be scaled up to multimeter lengths; few post-processing data work.

The drawbacks of rare-earth-doped fibers as active continuous *D* sensors are, mostly, the very hard, complex, and time-consuming pre-calibration that they need to perform linearly. Besides that, the sensors never work totally linearly; the selection process of the pump laser diode and the rare-earth-doped fibers is hard and complex, since their characteristics should match as much as possible, and it can limit the length of the probe; low power fluorescent signals; big charges are needed; very long probes (1 m) are needed for small measurement lengths (10 cm) (Pooley, et al., 2019).

2.1.5. Microwave interferometry

Microwave interferometry (MI) is a continuous *D* measuring system that is based on the Doppler effect (Cook, et al., 1955) (McCall, et al., 1985). In MI it is produced a fringe pattern, resultant from an advancement in phase of the reflected microwaves in relation to the incident microwaves. This phenomenon can be used to measure the *D* of explosives because SWs and DWs can reflect microwaves. The detonation front performs as a dielectric discontinuity, which makes incident microwaves be reflected with a continuously advancing phase in relation to the incident signal. The phenomena that contribute to the good reflectivity of the shock and detonation waves are the density discontinuity of the shock front and the ions from the chemical reactions (Cook, et al., 1955) (Vuppuluri, et al., 2018).

MI has been used to study deflagration- and shock-to- detonation processes in explosives, but it is most commonly used to determine their *D*. Detonation velocity (*D*) can be determined by MI through equation (2.7), where λ_g is the interference wavelength and f the frequency (Vuppuluri, et al., 2018).

$$D = \frac{\lambda_g}{2} f \tag{2.7}$$

The interference wavelength is calculated from equation (2.8) that is dependent on the free-space wavelength (λ_0), the relative permittivity of the material (ε_r) and on the cutoff wavelength (λ_c), which is defined as the minimum wavelength under which electromagnetic waves will not propagate within the confiner and it is dependent on the confinement's geometry (Vuppuluri, et al., 2018).

$$\lambda_g = \frac{\lambda_0}{\sqrt{\varepsilon_r - \left(\frac{\lambda_0}{\lambda_c}\right)}} \tag{2.8}$$

The permittivity for a mixture is given by the Landau-Lifshitz/Looyenge relation that, simplified for an explosive material and air, is given by equation (2.9),

$$\varepsilon_r^{1/3} = \left(\varepsilon_{r,TMD}^{\frac{1}{3}} - 1\right)\frac{\rho_0}{\rho_{TMD}} + 1 \tag{2.9}$$

where ρ_0 is the explosive density and ρ_{TMD} is its theoretical maximum density (TMD) (Vuppuluri, et al., 2018).

D experiments were performed by Vuppuluri and coworkers (Vuppuluri, et al., 2018) using MI. They used this technique on HMX charges, MDNT/CL-20 cocrystals, and MDNT/CL-20 physical mixtures. The experimental set-up used by them and the raw data

from a typical detonation test are shown in Figure 2-21 and Figure 2-22, respectively. This set-up consisted of an Al foil between the booster and the explosive sample to ensure that the start of the detonation could be clearly felt by the MI signal, and a PTFE rod, inserted into the end of the sample, used as a waveguide. The end of the PTFE waveguide was inserted into a port on the custom-built 35 GHz microwave interferometer, that was connected to the oscilloscope by triple-shielded cables.

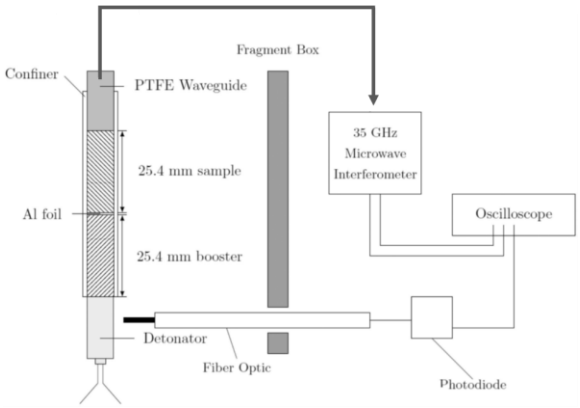

Figure 2-21: Microwave interferometry experimental set-up used by Vuppuluri et al. Image from (Vuppuluri, et al., 2018)

A portion of the MI typical unfiltered data from a detonation experiment is shown in Figure 2-22 (left) and it needs an elaborated mathematical analysis to reach the distance-time plots (Figure 2-22, right), where the *D* of the explosive can be determined. The original signal is the one presented as CH1 in Figure 2-22, while CH2 is a quadrature signal that has 90º phase offset from CH1 and was used to improve the spatial resolution of the method. The shape of the waveform is used to make an estimative of the duration of the detonation process and, having as a base that time interval, the correspondent part of each waveform is selected. Both signals have to be filtered, to reduce noise, and their amplitudes normalized. With the filtered and normalized waveforms, the instantaneous phase (φ(t)) is calculated resorting to a phase unwrapping algorithm. From the instantaneous phase, the detonation velocity can be defined by equation (2.10) (Vuppuluri, et al., 2018).

$$D(t) = \frac{\lambda_g}{4\pi} \frac{d\phi}{dt} \tag{2.10}$$

Making the integral of equation (2.10) according to time, the position of the waveform according to time is given by equation (2.11) (Vuppuluri, et al., 2018).

$$x(t) = \frac{\lambda_g}{4\pi} \phi(t) \tag{2.11}$$

The dynamic interference wavelength is obtained by solving equation (2.11) according to λ_g, by knowing the length of the explosive sample and the total phase of the detonation experiment. The position-time plots shown in Figure 2-22 (right) are built using equation (2.11) and the wavelength obtained by measuring the permittivity of HMX, but the interference wavelength obtained from the detonation test can also be used (Vuppuluri, et al., 2018). As always, the slope of the plots will be correspondent to the *D* of the explosive in study.

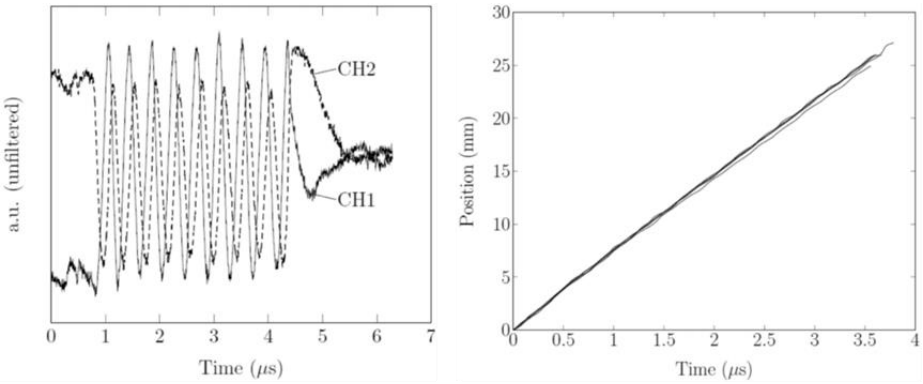

Figure 2-22: Microwave interferometer's raw data from a typical detonation experiment (left) and the resultant position vs time plots of HMX detonation tests. Images from (Vuppuluri, et al., 2018).

In this work (Vuppuluri, et al., 2018), the interference wavelength determined by detonation measurement (dynamic wavelength) was 2.66% lower than the one measured by permittivity (measured wavelength), due to the error in the determination of the detonation's duration needed to determine the total phase. After some corrections on the average density of the tests, the HMX detonation velocity was 7130 ± 27 m/s at an average density of 1.4 g/cm^3, being its standard deviation below the measurement uncertainty (Vuppuluri, et al., 2018). It is reported that MI has a position error of 0.2 mm, time errors of ± 10 ns, phase error of ± 2^o, the accuracy is around 4% of the wavelength of the microwaves conducting cable (McCall, et al., 1985).

MI is an advantageous technique because it is sensible to *D* differences small as 100 m/s or less; it suitable for *D* measurements when few quantities of the energetic material are available (less than 1.5 g); it is claimed to have a much higher resolution than the pins measurements; it is a non-intrusive technique (McCall, et al., 1985) (Vuppuluri, et al., 2018).

The less bright side of the method shows that it is very sensitive to density changes, so the sample-to-sample control was very tight; it needs very precise hardware; the microwaves have to be carefully chosen in a way that they pass through the fresh explosive,

but they have to be reflected by the DW; so that the measurement is trustable, the detonation needs to be steady in its entire path, so a perfect match between the densities of the booster and the charge is needed; sometimes, the waveguides are large structures that perturb the experiment; raw signal subject to noise; the raw signal can be of complex analysis and, thus, hard to peak pick and to define the detonation's duration; complex mathematical analysis to reach the distance vs time plot; suitable to error propagation since many parameters are determined experimentally (Cook, et al., 1955) (McCall, et al., 1985) (Vuppuluri, et al., 2018).

2.2. Detonation pressure techniques

In the first half of the previous century, dynamic methods based on different physical principles, to determine detonation wave parameters, were developed worldwide (Sućeska, 1995). Despite DW velocity being a relatively easy measurement, the detonation pressure (or CJ pressure) was, and still is, one of the most relevant parameters of biggest relevance (Chaos, et al., 2018). However, some authors consider that the experimental determination of this parameter is not widespread and computational calculations are preferred over the experimental tests (Pachman, et al., 2018).

The detonation pressure (P_{CJ}) of an explosive charge can be determined, through equation (1.54). To measure experimentally the CJ pressure of an explosive, considering that ρ_0 is easily measured, as well as D by one of the techniques presented in point 2.1 of this chapter, it is necessary to measure one of the other three parameters: $P_{CJ,}$ $u_{P,\ CJ}$, or U_S (*interface*).

According to some authors (Sućeska, 1995) (Al'tshuler, et al., 1989), the methods that are able to measure these parameters can be divided into two groups: the internal methods group, that record directly the detonating parameters, and the external group which methods are based on the registration of the final state of an inert material barrier after being shocked by the DW. In this work, these methods will be divided into direct and indirect methods.

The direct methods imply that the used technique is assembled directly into the explosive charge and can measure *in situ* one of the desired parameters, *P(t)* or $u_P(t)$. The indirect methods are the methods that register the state of an inert material barrier, which Hugoniot curve is known, after it was shocked by a SW or DW. The indirect methods can

be divided into three subgroups (Pachman, et al., 2018): i) methods that measure the particle velocity in inert materials adjacent to the charge; ii) methods that determine the shock wave velocity in inert materials; and iii) methods that determine the *P(t)* history through a gauge embedded in an inert material. The following points will present techniques that fit into the referred division of methods.

2.2.1. Direct methods

The direct methods, where the used techniques are directly assembled into the explosive charge, can measure directly one of these two parameters: $u_P(t)$ or *P(t)*. A method found that was quite used in the past to measure the particle velocity according to time was the electromagnetic method, which will be described in the following point. To determine the pressure according to time, it was found some works where manganin (Anderson, et al., 1981) (Urtiew, et al., 1986) and polyvinylidene fluoride (Bauer, 1999) gauges were inserted into the explosive sample, but since these gauges always have insulation/protection package, it is important to have in mind that the *P(t)* profile is referent to the inert material where the shock wave is propagating. Some authors just consider that the inert material has a density very close to the explosive and, thus, the *P(t)* profile in the inert material is the same as in the explosive and they extrapolate immediately the CJ pressure in the explosive (Bauer, 1999) (Vantine, et al., 1980).

In this work, it is considered that the protective inert material should be taken into account, even with low changes of densities between the inert material and the explosive. An impedance matching calculation is always needed to obtain the CJ pressure. For this reason, the manganin and the polyvinylidene fluoride will be described in the indirect methods.

2.2.1.1. Measurement of the particle velocity - Electromagnetic induction method

When a magnetic field passes throughout an electric circuit, it is generated an electromotive force (EMF) which is independent of the variation of the field (Gois, 1989). This phenomenon is called electromagnetic induction and it is used in the determination of the particle velocity histories of the detonation products of an explosive. For that purpose, electromagnetic particle velocity (EPV) gauges are embedded into the explosive sample (Cowperthwaite & Rosenberg, 1981) (Cowperthwaited & Rosenberg, 1983).

The EPV gauge is based on the principle that an EMF is generated when an electrical conductor is moving in a fixed magnetic field, and it is proportional to the velocity of the conductor. Since in these experiments it is required that the conductor, the motion, and the magnetic induction are mutually orthogonal and each uniaxial, the Faraday's law of induction for moving circuits (2.12) is applicable (Cowperthwaite & Rosenberg, 1981) (Cowperthwaited & Rosenberg, 1983):

$$E(t) = B\, l\, u(t) \tag{2.12}$$

where $E(t)$ is the EMF, t is time, B is the magnetic induction field, l is the length of the conductor, and $u(t)$ is its velocity.

Inserting an EPV gauge, into an explosive and submitting it into a uniform magnetic field, it will get animated with the velocity u perpendicular to B and, in its terminals, it is produced a voltage difference that is possible to read on an oscilloscope (Gois, 1989). EPV gauges can be made from different materials, like aluminum (Gois, 1989) (Cowperthwaite & Rosenberg, 1981) (Cowperthwaited & Rosenberg, 1983) and copper (Urtiew, et al., 1986). The first ones are never shielded, while the second ones can be (Lorentz gauge) or not (Faraday gauge). Normally, these aluminum gauges have a rectilinear "U" shape, where the crossbar of the "U" is the active element of the gauge, and its "legs" (or leads,) are responsible to conduct the signal out of the experiment, using shielded cables, a resistor and oscilloscopes to register the voltage across the resistor (Cowperthwaite & Rosenberg, 1981) (Cowperthwaited & Rosenberg, 1983). In the case of the copper EPV gauges, these can be formed by a thin copper foil (Lorentz gauge) or by a thin copper disk (Faraday gauge), with the same electric circuit in the terminations as the previous gauges. These Cu gauges are represented in Figure 2-23 and a multiple gauge test in detonation RX-26-AF explosive is reported (Urtiew, et al., 1986).

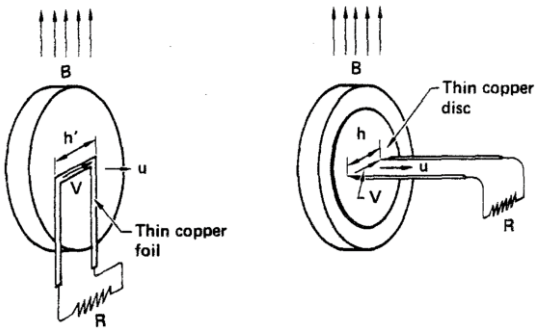

Figure 2-23: Schemes of the Lorentz (left) and Faraday (right) gauges. Image from (Urtiew, et al., 1986).

The most common (Al) EPV gauges were reported to be used single (Gois, 1989) or in series (Cowperthwaite & Rosenberg, 1981) (Cowperthwaited & Rosenberg, 1983), as represented in Figure 2-24. In the first one, the gauge is glued to a PMMA disk that closes the tube, it is an Al stripe with 0.2 mm thickness and 5 mm width that is molded in the way shown in Figure 2-24 (left), being 10 mm bright and 10 mm high (Gois, 1989). The gauge block that is shown in Figure 2-24 (right) is composed of Al stripes with 0.15 mm thickness and 3 mm width, their active elements are 25.4 mm long and the leads vary in high; the series of gauges is assembled on linen-phenolic blocks that support and ensure the position of the gauges while casting the used explosive (Composition B and Amatex 20) (Cowperthwaite & Rosenberg, 1981). To generate the magnetic field for the single EPV gauge, it was used two electromagnets composed of two Cu coils (strings with 0.6 mm diameter) (Gois, 1989). In the case of the gauge block, the magnetic field was generated by Helmholtz coils wound on plywood frames (Cowperthwaite & Rosenberg, 1981) (Cowperthwaited & Rosenberg, 1983). In both cases, the voltages were measured with oscilloscopes. An example of records from a gauge block inserted on coarse-grained Amatex 20 is shown in Figure 2-25, as well as the smoothed particle velocity histories obtained after the Lagrange analysis to such records (gauges 4, 6, 7, and 8).

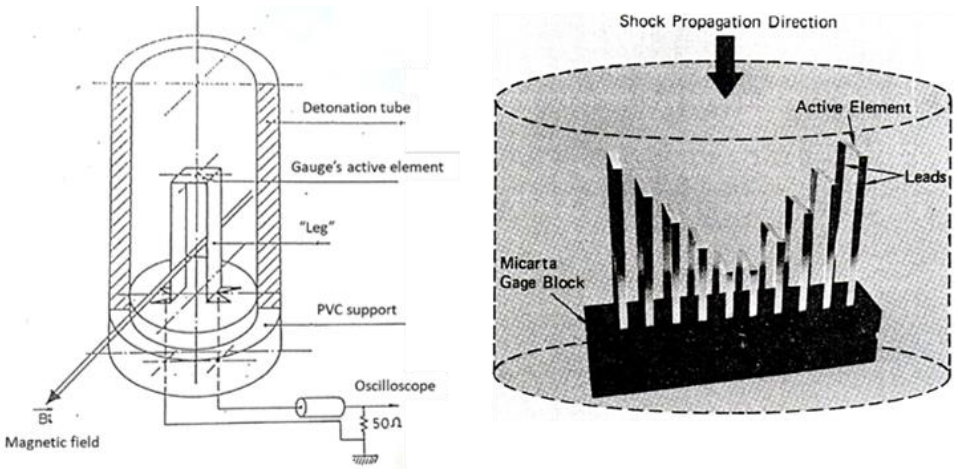

Figure 2-24: Schemes of a single EPV gauge (left) prepared on a detonation experiment (image adapted from (Gois, 1989), and a gauge block formed by EPV gauges in serie assembled on an explosive target with 0.2 m diameter (image from (Cowperthwaite & Rosenberg, 1981))

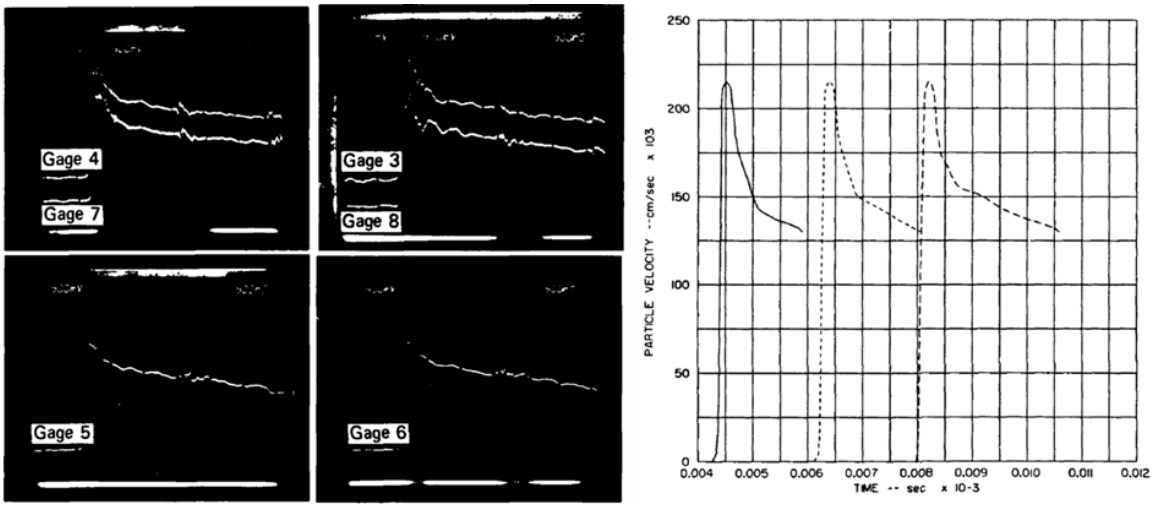

Figure 2-25: EPV gauge records from a gauge block (left) and the smoothed particle velocity histories obtained from them (right). Adapted from (Cowperthwaited & Rosenberg, 1983).

Gauges records, produced by thin foil gauges based on magnetic induction, are claimed to be highly resolved in time. Other advantages that the Cu gauges present are that they can achieve accuracies of 1% and they are more resistant to the detonation products than the Al gauges. The Faraday gauge works in conducting detonation products without protective insolation (Urtiew, et al., 1986), as well as the Al gauges (Cowperthwaite & Rosenberg, 1981). Advantages of both gauges are that they can be applied in single or multi configurations; from an *u(t)* diagram it is possible to determine the histories of the specific volume (V/V_0), pressure, and adiabatic gamma; they can be used in parallel with other techniques that do not use magnetic fields in their operations; they are suitable for casted explosives (Urtiew, et al., 1986) (Cowperthwaited & Rosenberg, 1983) (Cowperthwaite & Rosenberg, 1981). This technique is useful to determine CJ parameters and partial release isentropes from the CJ point (Cowperthwaite & Rosenberg, 1981).

As for disadvantages, the Cu gauges are not as good as the Al gauges in terms of shock impedance match; the Teflon armor that the Lorentz gauge needs to keep its integrity in the hostile detonation environment increases the gauge thickness, causing a decrease in the system response and, consequently, it limits the resolution of the method to fractions of microseconds instead of the desired few nanoseconds (Urtiew, et al., 1986). In general, this method just can be applied to non-magnetic, non-conducting materials which viscosity allow a uniform distribution around the gauges (Gois, 1989), limiting the energetic compositions that can be tested; the gauges are not easy to construct neither to assemble into the explosive samples (Urtiew, et al., 1986); records presented noise and disturbances on the

gauges when the downstream gauges entered the wavefront (Cowperthwaited & Rosenberg, 1983), the conductivity of the wavefront seems to affect the gauge circuits (Cowperthwaite & Rosenberg, 1981) (Cowperthwaited & Rosenberg, 1983); the gauge block needs a considerable amount of explosive to work properly (Cowperthwaite & Rosenberg, 1981); the magnetic fields are not easy to generate and calibrate and require expensive materials for such proposes.

2.2.2. Indirect methods

As said before, the indirect methods are the ones that register the final state of an inert material barrier, with a known Hugoniot curve, after it was shocked by a SW or DW. These methods are considered indirect because the CJ pressure is not acquired directly, it has to be always calculated by the impedance matching technique (IMT) since the SW parameters are always obtained at the interface point (i) between the inert material Hugoniot and the inverse of the Rayleigh (R^{-1}) line of the explosive. An example of the graphic to determine the CJ state by IMT is shown in Figure 2-26, where the experimental points (intersection points) are shown in black and white squares and triangles. In this example, four inert materials were used and it was determined the isentropic of the detonation products (and a part of the Hugoniot of the unreacted explosive, above the CJ state) by a quadratic fitting, instead of using the R^{-1} line of the explosive. But many works just use one inert material and the R^{-1} line of the explosive to determine the CJ state, as initially referred to.

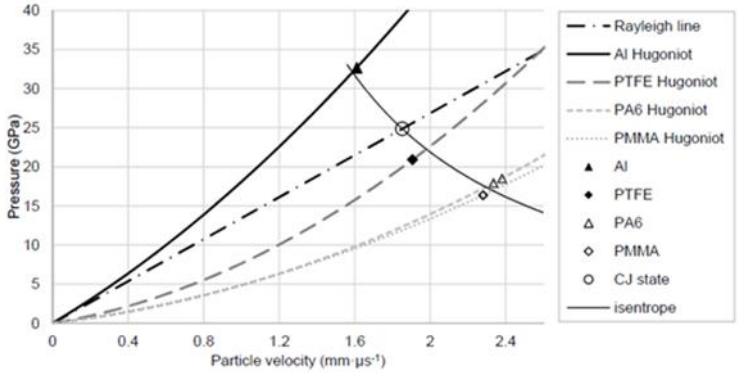

Figure 2-26: Graphical representation of the IMT technique applied to an RDX-based explosive by using four different inert materials. Image from (Künzel, et al., 2017).

These methods can be divided into three groups (Pachman, et al., 2018). In the first group is measured the particle velocity in inert materials adjacent to the explosive. One way to measure the particle velocity of an inert material (normally a metallic flyer with a

known Hugoniot curve) is to measure its free-surface velocity in air, which is known to be approximately double of the u_P at the interface explosive/inert material (Pachman, et al., 2018) (Cook, et al., 1962) (Lorenz, et al., 2015) (Duff & Houston, 1955). Some of the techniques that can measure the free-surface velocity of an inert material and that will be described further on are the streak camera and photonic Doppler velocimetry (PDV). Another way is to determine directly the particle velocity at the interface explosive/inert material. This can be achieved with laser interferometric techniques, but it implies using transparent inert materials, such as water, PMMA, and lithium fluoride (LiF). The laser interferometric techniques that will be described in this work will be Fabry-Perot, VISAR, and PDV.

The second group contains methods that register the shock wave velocity (U_S) in inert materials, also with known Hugoniot curves. These methods can measure the time that the SW needs to reach determined positions throughout the inert material. The techniques that are included in this group and will be further described are streak cameras registering images of the shock wave propagating in inert materials; and optical fiber techniques.

The third group determines directly the *P(t)* profile acquired by a gauge embedded in an inert material, which is then placed inside the explosive charge or at the end of it. The facts that the gauge is embedded in the inert material and that can be placed at the end of the charge are what differs them from the gauges presented at 2.2.1. In this group, it will be reported the manganin and the polyvinyl fluorine (PVDF) gauges.

2.2.2.1. Measurement of the free-surface velocity to determine the particle velocity at the interface explosive/inert material

The following points will present techniques that allow the determination of the free-surface velocity (u_{fs}) of an inert material, where $u_{fs} = 2\ u_P(i)$, as referred to before.

Generally, the velocity of a metal disk previously fixed at the end of the charge and accelerated by the DW is measured as u_{fs}. This experiment is repeated several times for discs with different thicknesses. As $u_{fs} = 2\ u_P(i)$, the particle velocity ($u_P(i)$) as a function of disk thickness presents a behavior depicted in Figure 2-27 where the point (b,v) is associated with the CJ point.

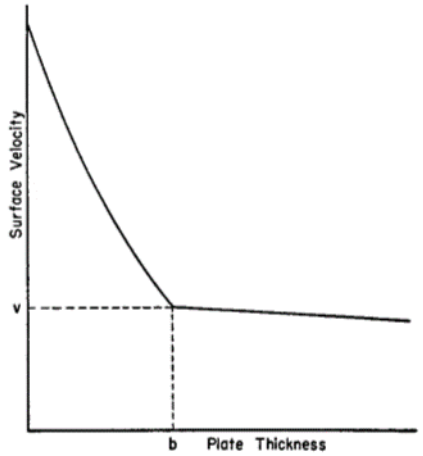

Figure 2-27: Representation of the free-surface velocity of a metal plate as a function of the plate thickness. Image from (Duff & Houston, 1955).

Streak camera

During the photographic methods (2.1.2.) it was intensively described four different types of streak cameras, according to their working principle and evolution of the internal components. This point will not focus on the characteristics of the cameras anymore, but on how they are used to measure the free-surface velocity of inert materials.

The free-surface velocity (u_{fs}), corresponding to the u_P(i), can be determined by the measurement of the free-surface velocity of an explosive-driven plate according to the plate thickness (Deal, 1957). There is a study (Deal, 1957) that achieved this by measuring the u_{fs} of 24 ST aluminum, which thicknesses varied between 1.85 and 50.88 mm, which was driven by four different explosive compositions (RDX, TNT, 34/36 Composition B, and 77/23 Cyclotol). It was used a rotating-mirror streak camera, with a writing speed of 3.2 mm/µm, that recorded the experiments through a slit and swept on the film in a direction perpendicular to the slit image.

The experimental set-up of this study (Deal, 1957) is shown in Figure 2-28 (left) and it consists of making the inert material, that is driven by the explosive, move through argon-filled gaps placed on Plexiglas blocks. When the inert plate starts to move, the argon gaps closer to its surface are compressed and, consequently, emit a shiny and fast flash of light. After the flying plate traveled the well-determined distance *d*, it meets again another argon gap, which will go under the same process. These flashes of light are recorded producing the record shown in Figure 2-28 (center). The time between these light flashes is the free-run time, which allows calculating the u_{fs}. By plotting the u_{sf} according to the IM plate thickness (Figure 2-28, right), it is possible to extrapolate the u_{fs} for zero thickness and,

thus, to have the u_P(i). Then, by IMT using the Hugoniot curve of 24 ST aluminum (Dural) and the R^{-1} line, it is possible to obtain the pressure and the particle velocity at the CJ point.

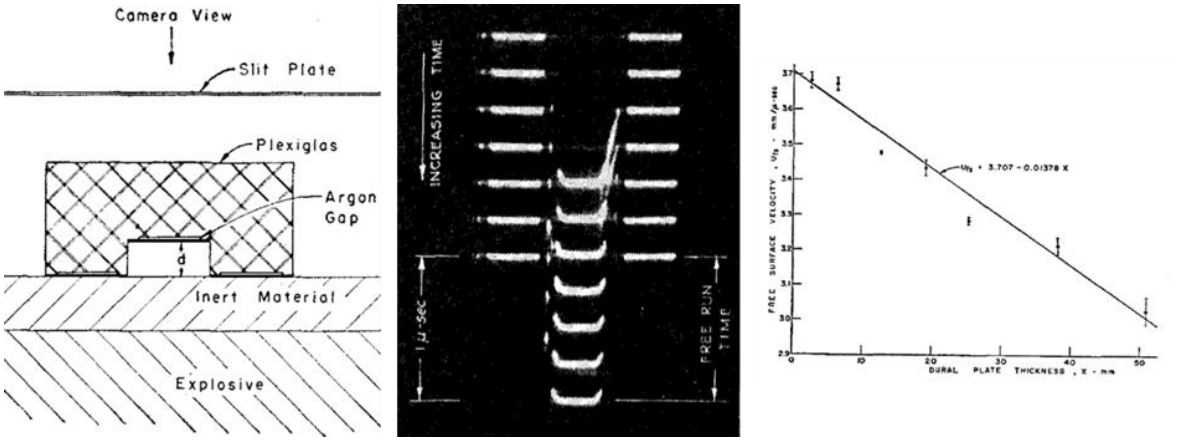

Figure 2-28: Experimental set-up for the measurement of u_{fs} using argon-filled gaps (left); an example of the record acquired by the streak camera (center); and an obtained u_{fs} vs Dural plate thickness graph, where u_{fs} is obtained. Images from (Deal, 1957).

The bigger advantage of this method is that in one single test several measurements of u_{fs} can be taken. On the other hand, the disadvantages of it are related to the extreme care that the experimental set-up needs to be made, as the high precision to keep the dimensions of the gaps always equal, as well as the depth of the offset, so that the measurements are taken before occurring shock reverberations. This last parameter limits the thickness of the inert material to be not smaller than 1mm (Deal, 1957).

Another method is to use water as a pressure gauge, by observing the free-surface velocity as the shock emerges from it (Cook, et al., 1962). It was used a rotating-mirror streak camera and an explosive flash bomb as backlighting. The aquarium set-up was used, which is represented in Figure 2-29 (left), with the slit view of the streak camera lying along the charge axis, being especially careful that the free surface was coincident with the system's optic axis. Varying the height (h) or varying the pressure generated by the shock-generator charge allowed to change the velocity of the SW in the air surface, and the set-up configuration ensured that the u_{fs} was constant over a relatively long distance. The record acquired by such configuration using Composition B is shown in Figure 2-29 (right), where it is possible to observe the attenuating shock wave, the release wave, and the free-surface "wave". By knowing the camera writing speed and by the application of the proper magnification factor, it was possible to determine the u_{fs} from the slope of the acquired trace (Cook, et al., 1962). With u_{fs} determined, the procedure described above was applied using the water's Hugoniot and the R^{-1} line of Composition B.

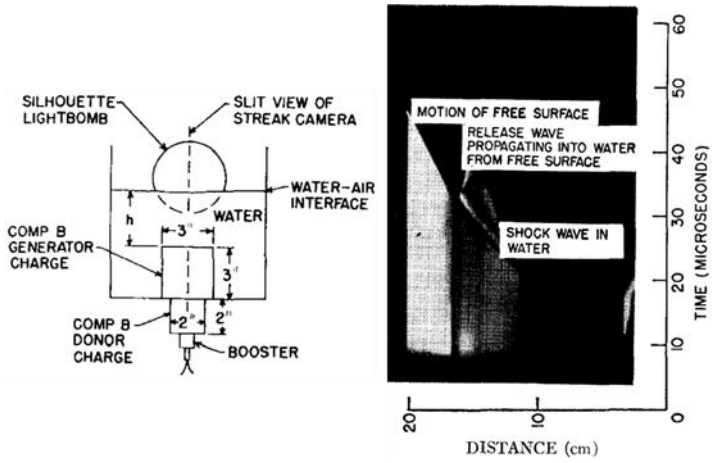

Figure 2-29: Aquarium test used to measure the free-surface velocity in water (left) and the correspondent obtained streak record. Images from (Cook, et al., 1962).

This technique had demonstrated to be reliable and in agreement with similar studies. The difficulties of this technique lay in the alignment of the streak camera with the experiment, the demand for aquariums with proper dimensions, so that the SW in water propagates faster than the shattering of the glass (Cook, et al., 1962).

Photonic Doppler velocimetry

The photonic Doppler velocimetry (PDV) is a technique that is quite recent, being its initial system reported by Strand, et al. (2006) as the heterodyne velocimeter.

According to Strand, et al. (2006), the heterodyne method can be schematically described in Figure 2-30. It consists of a probe that contains lens to focus light onto a moving surface. This light is supplied by a laser with a well-determined wavelength. This laser light (with frequency f_0) should be well focused on the target and, while the target is moving, a part of this light is reflected by it and it is collected by the same probe as Doppler-shifted light (with frequency f_d) that is, then, sent to the detector. At the same time, a similar amount of the incident light is sent directly from the laser to the detector. All the lights are transported from each component employing single-mode optical fibers. At this point, at the detector is generated a beat signal that consists of an interference of two individual signals of different frequencies, f_0 and f_d. This beat signal is recorded on a digitizer of large bandwidth.

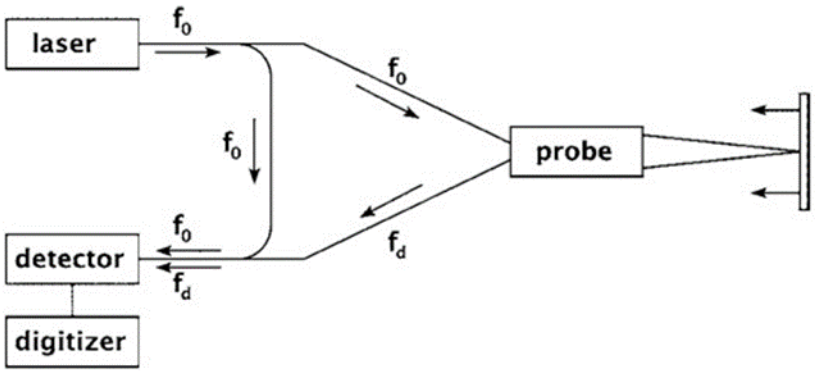

Figure 2-30: Scheme of the heterodyne velocimeter. Image from (Strand, et al., 2006)

The frequency of the beat signal ($f_b(t)$) is the absolute value of the difference between the (f_d)and the initial laser frequency (f_0) and it is related to the velocity $v(t)$ by equation (2.13), where *c* is the speed of light.

$$f_b(t) = 2\left(\frac{v(t)}{c}\right)f_0 \tag{2.13}$$

In reality, such apparatus is a displacement interferometer, because the beat signal reaches one full cycle when the moving surface moved along a distance correspondent to a half of the wavelength of the laser (λ_L), which means that each time that the target runs one of these lengths (normally some hundreds of nanometers), it is recorded a full beat cycle. The average of the velocity (v) over a cycle can be related to the period of a full beat cycle ($\mathcal{P}$) by the equation (2.14).

$$v = \frac{\frac{1}{2}\lambda_L}{\mathcal{P}} \tag{2.14}$$

The procedure to determine the period of a full beat cycle is not trivial, since there are signals that can have such high frequencies that the individual cycles cannot be resolved in a full-time base, like the one shown on the left side of Figure 2-31. Strand, et al. (2006) propose some different analysis to determine the beat signal period, but the elected method was a sliding Fourier transform method (1024-point Fourier transform windows), that is well described at (Strand, et al., 2006). Other authors also opted for methods related to Fourier transform techniques (Sollier, et al., 2012) (Pachman, et al., 2018) (Kucera, et al., 2018).

In this study (Strand, et al., 2006) it is described, between other applications, how to use this technique on an explosively driven metal. Figure 2-31 shows the obtained raw data (left), the spectrogram calculated through the 1024-point Fourier transform

windows applied to the raw data (center), and the velocity vs time graph that was extracted from the spectrogram (right). A detailed explanation of these acquired results is also given in (Strand, et al., 2006). Lorenz, et al. (2015) explains in a detailed way the correlation between the free-surface velocity vs time graph and the shock phenomenon on the moving plate.

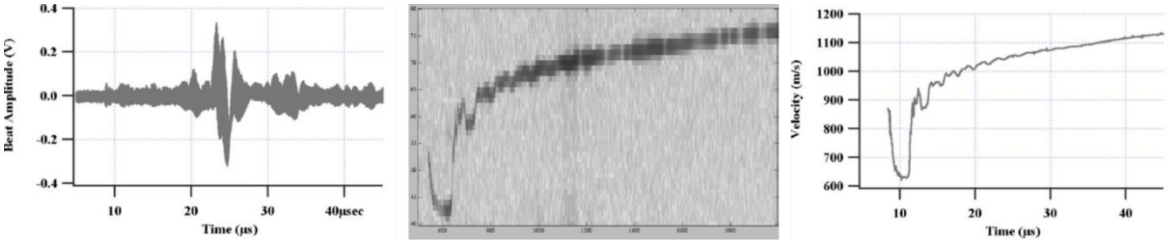

Figure 2-31: The raw data (left) obtained from an explosively driven metal experiment; spectrogram (center) obtained by treatment of the raw data with the 1024-point Fourier transform windows; and the graph velocity vs time (right) obtained from the spectrogram. Images from (Strand, et al., 2006)

In the last 10 years, it is possible to find works that used PDV on the measurement of the free-surface velocity. Examples of that are its application to the expanding products from the detonation of TATB (Sollier, et al., 2012); to determine the detonation pressure of A-IX-1 (RDX based explosive) with Al plates of different thicknesses (Pachman, et al., 2018); to calculate the CJ pressure and the expansion energy of LX-16 (PETN based explosive) by using Al or Cu plates in the disk acceleration experiment (DAX), where corrections to the calculation of the CJ pressure by IMT were suggested (Lorenz, et al., 2015); to study the LX-17 (TATB based explosive) detonation characteristic using Al plates (Tarver, 2010); to establish a methodology that is applied to the welding process with explosives that tracks the entire velocity history of an accelerate plate and its collision velocity in the welding process (Kucera, et al., 2018). The PDV technique can reproduce graphs of the two species described at the beginning of 2.2.2.1, as is shown in Figure 2-32, where the a) graph shows the determination of u_{fs} by the intersection between two velocity profiles dependent on the thickness of the material, and the c) shows linear adjustments to the decaying part of the first pullback region of the PDV record (b) for estimation the initial free surface velocity u_{FS}*of plate driven by DW.

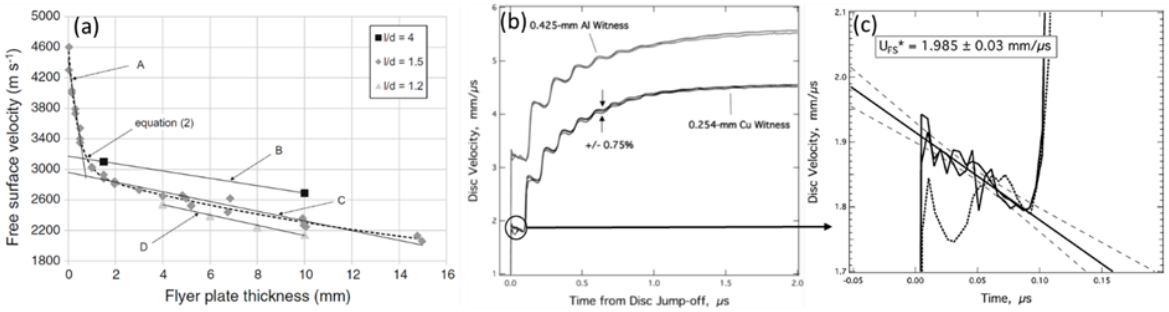

Figure 2-32: a) Free-surface velocity of aluminum flyers for different plate thicknesses (image from (Pachman, et al., 2018)); b) DAX spectrograms obtained from LX-16 for thin plates of Al and Cu; c) estimation of the initial free surface velocity u_{FS}*of Cu plate driven by DW (images from (Lorenz, et al., 2015)).

The advantages reported about the PDV are: good time resolution (2 ns), free-surface velocity records of long duration (Sollier, et al., 2012); simple, compact, commercial available parts can be used when is being custom built, no need of extra components to resolve effects like fringe jump ambiguities, robust against large variations of intensity fluctuations, Fourier transform techniques allow to see multiple discrete velocities and also dispersion (Strand, et al., 2006); high precision, few equipment needed, can be applied to small samples (75 mm length, less than 20 g) and to big samples, excellent repeatability, sensitive measurement of the CJ pressure, easy to assemble and field, allows a continuous record of the interaction of the DW with the moving plate (Lorenz, et al., 2015); permits the determination of the pressure and the particle velocity of the von Neumann spike, and of the time and the thickness of the reaction zone, with 10 shots it is possible to have a good quality of the particle velocity profile (Pachman, et al., 2018); gives very good insight of the explosive welding process (Kucera, et al., 2018).

The disadvantages presented by this technique are: the laser emitting wavelength should have quite narrow linewidths to originate a usable fringe contrast in the beat signal; medium-high cost; it cannot distinguish the direction of the movement (toward the probe or moving away from it) when it has the same velocity (Strand, et al., 2006); the velocity resolution of the PVD spectrograms are limited by the use of the Fourier transform for data evaluation, it is necessary to make many shots to have a full particle velocity profile, which is expensive and time-consuming, the extrapolation of the data to a zero flyer thickness causes uncertainty on the results (Pachman, et al., 2018).

Electro contact type of probe with oscilloscopes – pins

The working principle of the electro contact type of probes connected to oscilloscopes was already described in 2.1.3.1. This type of probes can also be applied to the measurement of the free-surface velocity of an explosively driven inert material (Duff & Houston, 1955) (Minshall, 1955), but it needs a more complex electronic system than the *D* measurements and it seems that is not a chosen technique nowadays, probably due to problems like the earlier discharge of the pins due to the preceding shock wave in the air, metal spray jetted out from the surface, the surface is not plane enough or the movement is not totally parallel to the probes, and the need of big amounts of explosive (Duff & Houston, 1955) (Minshall, 1955).

This technique consists of putting such probes on the periphery of the inert material, where each probe has a very well-known distance between it and the inert material that is going to be driven by the explosive in study (Duff & Houston, 1955) (Minshall, 1955). According to the studies found about this topic (Duff & Houston, 1955) (Minshall, 1955), it was used one or more sets of 6 pins, that were connected according to the scheme of Figure 2-33(left). Each time that the flyer plate reaches a pin, a signal appears in the oscilloscope (Figure 2-33, right), which polarity is dependent on the circuit. In one of the studies (Duff & Houston, 1955), the pins were steel screws, and a 30-megacycle calibrator was used to provide the time base. With the times given by the oscillogram and the known distances from the pins to the inert material is possible to make an *x(t)* graph where U_{fs} can be obtained, and then plot it according to the thickness of the inert material that gave such U_{fs}. This method was applied to Composition B that drove different types of steel and tungsten (Minshall, 1955), or to aluminum foils and dural (Duff & Houston, 1955).

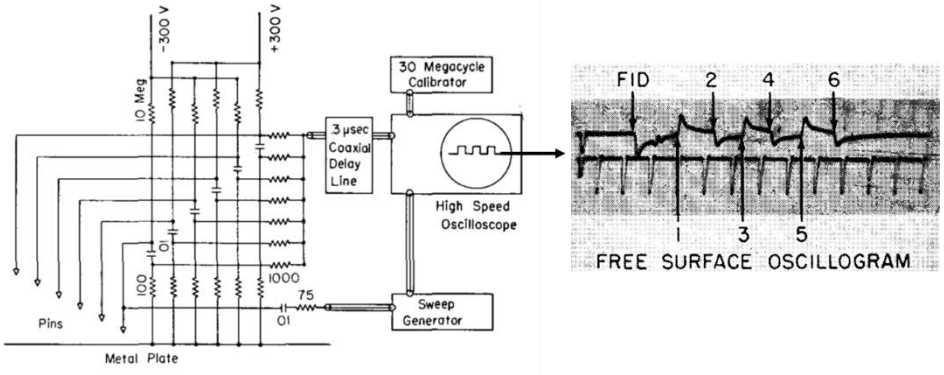

Figure 2-33: Electronic circuit used to measure the U_{fs} with electro contact pin probes (left) and an obtained oscillogram (right). Images from (Duff & Houston, 1955) and (Minshall, 1955), respectively.

2.2.2.2. Direct determination of the particle velocity at the interface explosive/inert material

The following interferometric technics allow the direct measurement of particle velocity profile ($u_P(t)$) of a moving reflective surface that is inserted between the explosive and the inert material and that is considered to move with the inert material due to the expansion of the detonation products. From this $u_P(t)$ is then possible to extract u_P(i) and proceed to the determination of the CJ state by IMT.

PDV

To use this technique to obtain the particle velocity profile of PMMA at the interface with an explosive it is necessary to place a thin metal layer, that can be Cu (Chaos, et al., 2018) or Al (Pachman, et al., 2018), between the explosive and the PMMA window. The PVD probe is placed on the end of the PMMA block, in a way that the laser is incident on the metal surface and reflected on it, as described before in 2.2.2.1.

In (Chaos, et al., 2018), a Cu disk was accelerated by the detonation wave of LX-16. The PDV technique was used to measure the free surface velocity of this disk. During the acceleration process was observed that the reverberations suffered by the disk were produced by the interactions of the shock wave with the detonation products, as is shown in Figure 2-34. It was assumed that each step change in velocity was correspondent to a reflection at the free surface of the disk. By the amplitude of each change ($u'_{P,x} - u_{P,x}$, x = even numbers on Figure 2-34 right), it was possible to determine $u_{P,y}$ ($u_{P,y} = ½ (u'_{P,x} - u_{P,x})$, y = even numbers on Figure 2-34 right). Applying the IMT with the Cu Hugoniot, it was possible to determine a polynomial equation representative of the detonation products.CJ point was found by intercepting such polynomial equation with the Rayleigh line of the explosive (Figure 2-34 left).

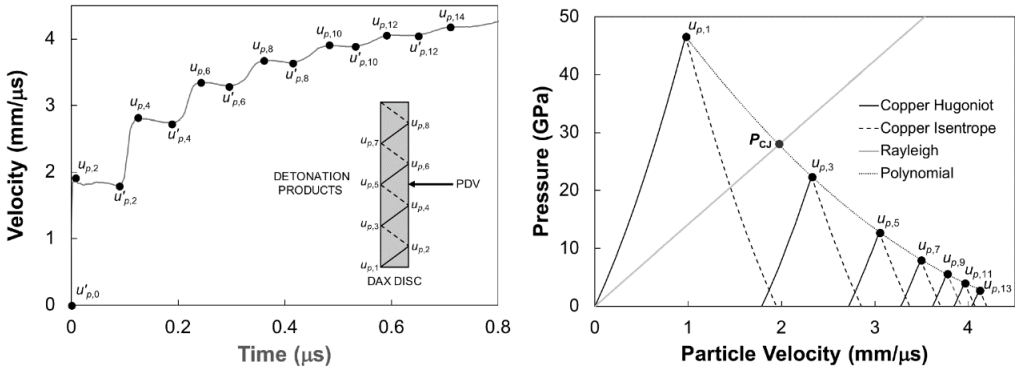

Figure 2-34: PDV spectrogram with the x-t diagram of the reverberation process (left); and determination of the CJ pressure with the Cu Hugoniot and isentropic curves passing by the obtained $u_P(i)$ points. Images from (Chaos, et al., 2018).

Another study (Pachman, et al., 2018) analyzed eight experiments performed always with the same set-up by plotting all the acquired points, and it was possible to visualize a graph that can be divided into two different areas (Figure 2-35). In the first area of points, they can be adjusted by a linear function with a high negative slope, while in the second area the adjustment made to the points will be characterized by a linear function with a lower negative slope. The first area is considered to be the representation of the shock front and the reaction zone that starts at the von Neumann spike and finishes at the CJ state, while the second area is considered to be the representation of the Taylor wave, that initiates at the CJ state. The interception between these two lines is considered to be the CJ state of the explosive transferred to the PMMA window. In this case, the authors considered the PMMA particle velocity at the CJ point as being the closest data point above this intersection.

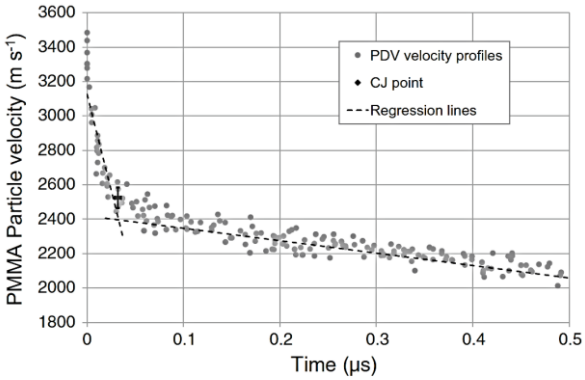

Figure 2-35: Particle velocity profiles at the explosive/PMMA interface from 8 identical tests and the respective linear regression lines. Image from (Pachman, et al., 2018)

Fabry -Perot interferometer

The Fabry-Perot interferometer (FPI), as the PDV, works based on the Doppler effect by measuring the wavelength of the returned light, but the apparatus needed is more

complex. In the FPI, a beam of light that enters it suffers multiple reflections in the two mirrors, and all the emitted rays are parallel to the incident one. Using lens and their focal points, all these beams are directed to the same point and interfere with each other, forming a ring (McMillan, et al., 1988). The rings are formed because the FPI just allows passing light through specific angles that are determined by the space between the Fabry-Perot mirrors and the light wavelength (Urtiew, et al., 1986). When the incident radiation changes, the angles at which the constructive interferences occur also change, resulting in rings with bigger or smaller diameters (McMillan, et al., 1988).

A simple scheme of this system is shown on Figure 2-36 at it is composed by (McMillan, et al., 1988): a laser that illuminates the target with a stable and monochromatic light; the shutter and the Pockels that control de beam pulse; the field lens to guide the beam to the target and collect the return light; the beam can be transported by air or by optical fibers; before the reflected radiation reached the FPI, it has to pass through the cylindrical lens, that give angular divergence in a single plane and its focal length will determine the number of rings that will appear in the record; the optical filter excludes useless radiation from the experiment; the spherical lens between the FPI and the streak camera define the size of the rings on the camera's slit and, consequently, the number of rings that will be recorded for a determined slit length; the mirrors conduct the path of the beam and they are very important, because the space between them defines the focal length of the lens to produce the desired number of fringes on the record (normally 3 or 4) and it determines the sensitivity of the FPI, and their reflectivity affects the finesse and the width of the rings; to record the movement of the rings generated by the FPI, a high-speed streak camera is needed (McMillan, et al., 1988). An extensive description of this system, its principles, and mathematical analysis is done at (McMillan, et al., 1988).

Doppler-shifted light reflected from a target moving at constant velocity gives a static dot pattern. When the target is accelerated, the reflected beam will be Doppler shifted to higher frequencies, resulting in an expanding pattern, like the one seen in Figure 2-36. The pattern's change is related to the change of the velocity in the target through equation (2.15):

$$u(t) = \frac{\lambda c}{4L}\left(\frac{D_1^2(t) - D_{10}^2}{D_{20}^2 - D_{10}^2} + m\right) \tag{2.15}$$

where λ is the initial beam wavelength, c is the velocity of light, L is the separation between mirrors, D_{10} and D_{20} are the diameters of the adjacent pairs of dots in the static patter, and $D_1(t)$ is the diameter of the expanded dot patter (Urtiew, et al., 1986).

Examples of some studies about the direct measurement of the particle velocity profile in the different interface explosive/inert material are (Urtiew, et al., 1986) (Kury, et al., 1999), (Tarver, et al., 1997); (Fedorov, et al., 2011). Some of these studies include also the measurement of the free-surface velocity of an explosively driven target.

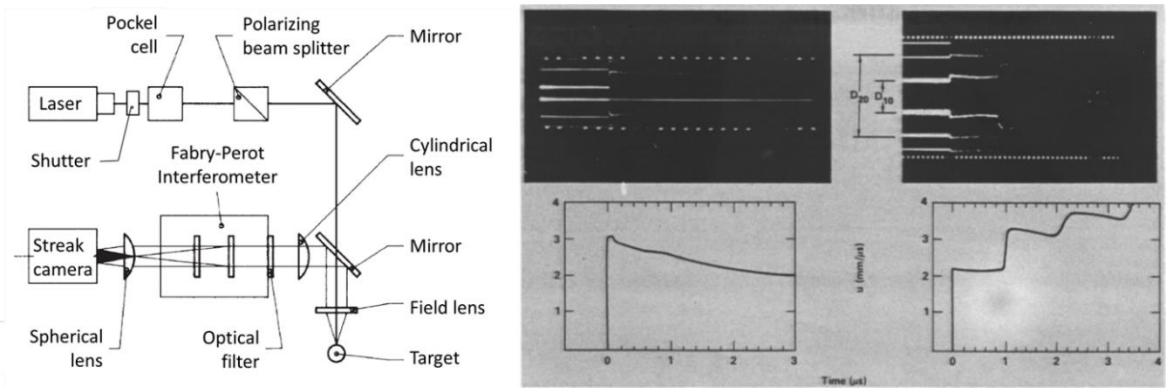

Figure 2-36: Scheme of the set-up used in the Fabry-Perot interferometry (left) adapted from (Suceska, 1995) and (McMillan, et al., 1988). Spectrograms and $u_P(t)$ from a flat plate accelerated into water (middle) and vacuum (right), images from (Urtiew, et al., 1986).

The following characteristics are recognized as being advantages of the FPI technique: nanosecond time resolution (McMillan, et al., 1988) (Kury, et al., 1999); reliable and easy to analyze with confidence (McMillan, et al., 1988); the inert material helps to protect the thin reflective surface to break up (Urtiew, et al., 1986); besides CJ pressure, it also allows the study of the von Neumann spike state, reactions rates, and the reaction products EoS in the ignition and growth detonation reactive flow model (Tarver, et al., 1997); it is vulnerable to abrupt changes in velocity; it can measure multiple discrete velocities simultaneously and also the velocity dispersion over a limited range (Strand, et al., 2006).

Disadvantages: the quality of the lens affects the shape of the fringes; the focal axis of the lens has to be parallel to the slit, in order that the focal plane lies on the slit, and perpendicular between them; the quality of the record is affected by the mirror reflectivity and by the resolution of the streak camera; not so efficient in the use of the laser light (McMillan, et al., 1988); the acquisition time of the FPI can be limited by the premature destruction of the reflective surface by the DW; LiF records are not so reproducible as the free-surface ones in the initial times of the record (Kury, et al., 1999); it is hard to find inert

materials with the same impedance as the explosive, so IMT is always required; it is reported that the exact CJ particle velocity and pressure cannot be directly determined, because the CJ state does not appear as a sharp break in the PVD spectrograms by using various lengths of explosive and/or different inert materials (Tarver, et al., 1997); expensive, generally custom build; the streak cameras can limit the length of the records; not so sensitive to the light changes common on shocked surfaces (Strand, et al., 2006); it requires big amounts of explosive, since more than one test is usually needed, and it seems very hard to assemble, due to its complex apparatus.

VISAR

Another interferometric technique that is still nowadays very used to measure DW parameters is the velocity interferometer system for any reflector, known usually as VISAR. Like PDV and FPI, its measurements are also based on the acquisition of Doppler-shifted radiation by a moving target, but its assembly is even more complex than the previous ones. A scheme of it is shown in Figure 2-37 (left), and it is made for laser radiation (represented by the left down vertical arrow) emitted by a diffusely reflecting specimen surface (RSS) (Barker & Hollenbach, 1972).

According to (Barker & Hollenbach, 1972) and following the laser beam path, it passes through the small hole localized at mirror M3 and then through the focusing lens L, which is directed to the diffusely RSS using the mirror M4 localized at the focal point of the lens L. The RSS can be diffusely or spectral. In the first case, the Doppler-shifted radiation will be diffusely reflected light that will be directed to the lens L through M4. In the second case, the Doppler-shifted radiation is a spectral reflected light beam that will be directed to an off-center position on lens L, also by M4. After being recollimated, M3 is responsible for separating the laser radiation from the reflected one and directing the reflected radiation to the telescope. If the reflected radiation is diffuse, the telescope condenses the reflected light into a beam of convenient diameter to be used by the interferometer; if the radiation is spectral, the telescope directs the beam into the desired diameter for transmission into the rest of the optical path. Here, the Doppler-shifted beam is polarized at 45^{o} from the horizontal to ensure that the intensities of the beams S e P are equal, as required by the interferometer. The polarized reflected light is then divided by a beam splitter, where about 1/3 of it is directed to the beam intensity monitor photomultiplier tube, which propose is to detect any change of the light intensity reflected from the RSS, that can be caused by shock-induced

alterations on the RSS. The beam intensity vs time data generated by the beam intensity monitor allows to correct the interferometer data for any beam intensity changes.

The 2/3 of the Doppler-shifted light enters into the VISAR interferometer and is directed to a part of the large beam splitter, with some degrees from the normal direction. Here, the reflected part of the Doppler-shifted light returns to M1, which will direct it back to a different location on the large beam splitter, where it is recombined with the transmitted Doppler-shifted light that had passed through the large beam splitter. In the while, the transmitted Doppler-shifted radiation was delayed, concerning the reflected part of the Doppler-shifted light, by one or more etalons. The delay (τ) is given by each etalon (where the large beam splitter should be included) is related to its effective length (h), its refraction index (n), and the velocity of light (c) through equation (2.16), and by the half of the thickness of the ¼ wave plane (the beam just passes there once).

$$\tau = \left(\frac{2h}{c}\right)\left(\frac{n-1}{n}\right) \tag{2.16}$$

The angle and the position of M2 are adjustable according to the interferometer alignment and to accommodate the needed etalons, respectively. The distance of M2 from the beam splitter has to be the same as the distance of the beam splitter to M1, plus the sum of x's given by equation (2.17).

$$x = h\left(1 - \frac{1}{n}\right) \tag{2.17}$$

The mirror M1 is mounted on a translator to vary the length of the left side leg of the VISAR, by few wavelengths of light, according to the translator's voltage.

After the recombination of reflected and the transmitted Doppler-shifted light at the large beam splitter, the resultant light is polarized at 45º to the vertical and divided into one half-S and one half-P polarized light. The ¼ wave plane is used to retard the P component of the light by 90º concerning the component S. So when the recombination occurs, the S and the P components form two 90º-out-of-phase fringe patterns. The two patterns are separated by the polarizing beam splitter and sent to their individual photodetectors.

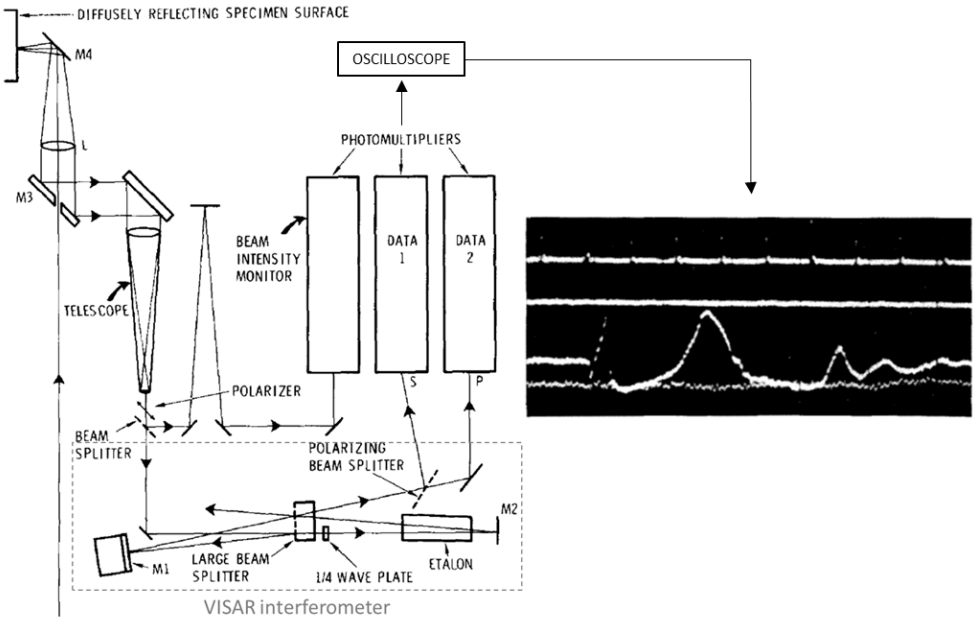

Figure 2-37: Scheme of the VISAR instrumentation system. Adapted from (Barker & Hollenbach, 1972)

An example of an oscilloscope record from the VISAR here described is shown in Figure 2-37 (right), but improved models were produced in the last 40 years. The first and top line is the timing trace, the second is the zero-line for both photomultipliers, the third is the signal from one of the photomultipliers, the fourth and bottom trace is the signal generated by the beam-intensify monitor (Barker & Hollenbach, 1972). With analysis software is then possible to transform the data into interface particle velocity versus time (Gustavsen, et al., 1998), where the velocity is approximately proportional to the fringe shift (Dolan & Specht, 2017), as shown in Figure 2-37 (right). At the right side of this figure is also presented a scheme of an experiment, (Bouyer, et al., 2009) where the beam towards the interferometer is the same as represented at the left side of Figure 2-37 as a vertical arrow.

Different studies that used VISAR to characterize directly the profile of the particle velocity in the interface explosive/inert material were found, where different explosives were studied with different inert materials and different spectral RSSs (Bouyer, et al., 2009) (Gustavsen, et al., 1998); emulsion explosives of different densities with a PMMA window with aluminum foil as RSS (Yunosheva, et al., 2012), (Utkin, et al., 2012). But it is also possible to find the application of VISAR on the measurement of the free-surface velocity of an explosively driven inert material (Barker & Hollenbach, 1972) (Duffy & Ahrens, 1994) (Bouyer, et al., 2010).

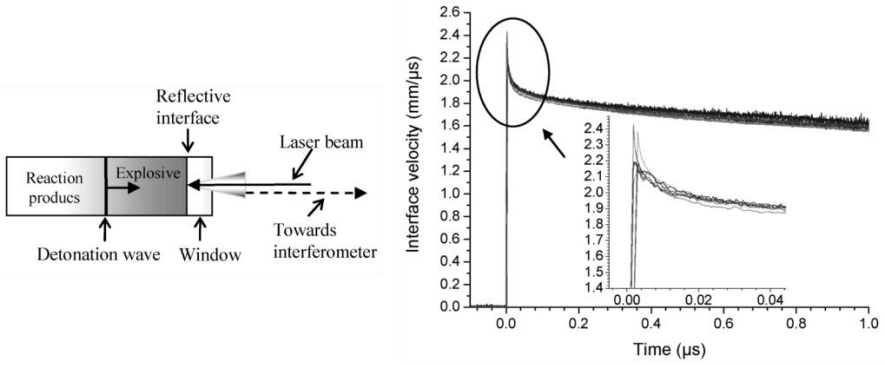

Figure 2-38: Scheme of an experiment using VISAR and the particle velocity profile at the interface NM/PMMA according to the time. Images from (Bouyer, et al., 2009).

VISAR's advantages: time resolution on the units of the nanosecond, faster than PDV or FPI (Bouyer, et al., 2009), the time resolution can be improved if the data is treated on the frequency domain (Dolan & Specht, 2017), allows to measure the width and the time of the reaction zone of low-energy detonation explosives (Yunosheva, et al., 2012), sensitive to the detonation structure, possible to resolve the VN spike, particle velocity and pressure at the CJ point with an error about 2% (Utkin, et al., 2012), more compact and less expensive than the FPI, commercially available, can register longer record lengths than the FPI for using oscilloscopes, vulnerable to abrupt changes of velocity, relies on absolute intensities to acquire velocity information, more sensitive than FPI (Strand, et al., 2006).

VISAR disadvantages: initially limited by the recording system, recovering true velocity from the VISAR approximation involves very large and infinite (sometimes) corrections, it suffers from noise amplification (Dolan & Specht, 2017), needs a second etalon to resolve fringe jump ambiguities, sensitive to the intensity changes on the light reflected by a shocked surface that occur during such detonation experiments, the analysis of the VISAR data demands the adjustment of some parameters to obtain good records and cannot measure multiple discrete velocities simultaneously either over a limited range (Strand, et al., 2006).

2.2.2.3. Measurement of the shock wave velocity in inert materials

In this point it will be described some techniques that allow the measurement of the SW velocity (U_S), generated by an explosive, that is trespassing an inert material. U_S(i) can be extracted from an *x(t)* graph (or spectrogram), or from a $U_S(x)$ plot, where *x* is the thickness of the studied inert material.

The following points will show how to use such techniques on the measurements of SW velocity propagation on an inert material, the experimental configurations, examples of the results that can be acquired, and how to read them.

Streak cameras

The measurement of the free-surface velocity of an explosively driven inert material with streak cameras was presented on 2.2.2.1. In that point was described the aquarium test to measure the free-surface velocity of water that was driven by Composition B (Cook, et al., 1962), but the authors, in the same test, could also determine the velocity of the shock wave (U_S) that was propagating in water. The experimental set-up and the acquired results are shown in Figure 2-29, where it is possible to see the record of this propagation. Knowing the camera writing speed and the magnification factor, it is possible to determine the shock wave velocity in water by the slope of the acquired trace. This study also reported the determination of the CJ pressure of an explosive by the measurement of the shock wave velocity in PMMA.

Similar experiments (with the charge totally or partially submersed), with water as the interface, were done using explosive formulations that contained Al (results shown on the top of Figure 2-6) (Brousseau, et al., 2002), and several pure and mixed explosives (Coleburn, 1964).

Like the study above, other studies were found using PMMA to determine the CJ pressure of an explosive. One of them (Held, 1987) determines the U_S by embedding distance gauges (Cu grating) into liquid PMMA (which became a solid parallelepipedal block of 70x70x100 mm), where the shock is produced by a mixture of TNT/HMX. A record from this experiment is shown in Figure 2-39, the U_S and correspondent P_{CJ} were calculated as said above. Besides water and PMMA, the air was also used as inert media to measure the shock wave generated by C-4 (McNesby, et al., 2013).

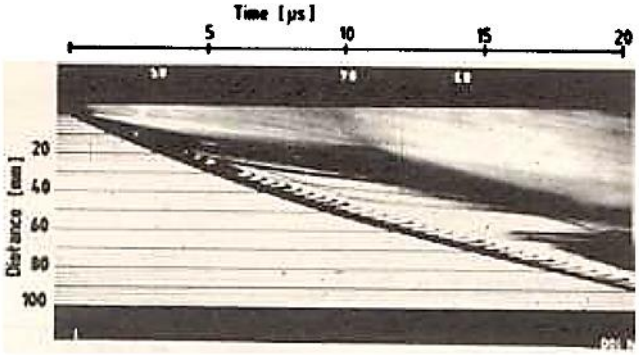

Figure 2-39: Shock wave propagation in PMMA where a fine Cu grid is inserted. Image from (Held, 1987)

Just transparent media can be used if it is intended to use the streak cameras to record the propagation of an SW in an inert material. However, with the use of optical fibers as light transmission media, photoelectric converters, and digitizers, opaque materials can also be evaluated. This will be described in the following topic.

Optical fiber methods

The optical fiber (OF) methods were already presented at 2.1.4. There, the methods were divided into discrete and continuous, where the detonation wave was tracked point-to-point or continuously; and into passive and active, which are related to the light source used to make the measurement, where the detonation light, or light originated by the compression of the SW on the inert material, is captured or where an external source of light is extinguished due to the detonation phenomena, respectively.

The OFs are used on continuous passive measurements of an SW propagating into an inert material when associated with streak cameras. The OFs can be used in stripes that contain some dozens of them (Mendes, 2000) (Plaksin, et al., 2001) (Plaksin, et al., 2002), or in a single configuration (Khurana, et al., 2011), where just one single OF is used on the measurement. The works found that used a strip of OFs connected to a fast streak camera, it was always used a strip composed of 64 PMMA OFs, with 0.25 mm diameter. Normally, the strips were divided into two minor strips, to place one of them into the explosive sample for *D* measurements, while the other was embedded into a PMMA block (Mendes, 2000) (Mendes, et al., 2006) (Mendes, et al., 2012), parallel to the detonation plane, or assembled in the surface of a Kapton stack (Mendes, 2000) (Plaksin, et al., 2001) (Plaksin, et al., 2002) perpendicular to the detonation's plane. In the first case, the light that is acquired by the OFs is the detonation light that is trespassing the PMMA (see Figure 2-16),

while in the second case, the OFs capture the ionized light generated by the SW's compression of micro gaps of air, or argon, that is between the Kapton sheets.

The experimental set-up and the streak record of measurement using Kapton are shown in Figure 2-40 (top left), as well as the streak record and pressure and U_S profiles acquired from such experiment. The calculation of U_S is based on the quotient between the distance between the flashes of light (correspondent to the thickness of a Kapton sheet), and the time between such flashes. $U_S(i)$ is then extracted from the point where the $U_S(z)$ profile changes from very fast to almost constant (around z = 200 µm in the blue graph of Figure 2-40). With a single fiber associated with the streak camera (Khurana, et al., 2011), it was made a cylinder of the inert material (nylon, PMMA, Teflon, and propylene) with a drilled hole in the center, 5 mm far away from the interface explosive/inert material. In this hole were inserted pallets of the same material (5-6 mm thickness) leaving an 0.25 mm gap of air. When the shock was transmitted between the pallets, a flash of ionized air was produced and recorded by the streak camera. U_S is then obtained in the same way as described for the Kapton stack.

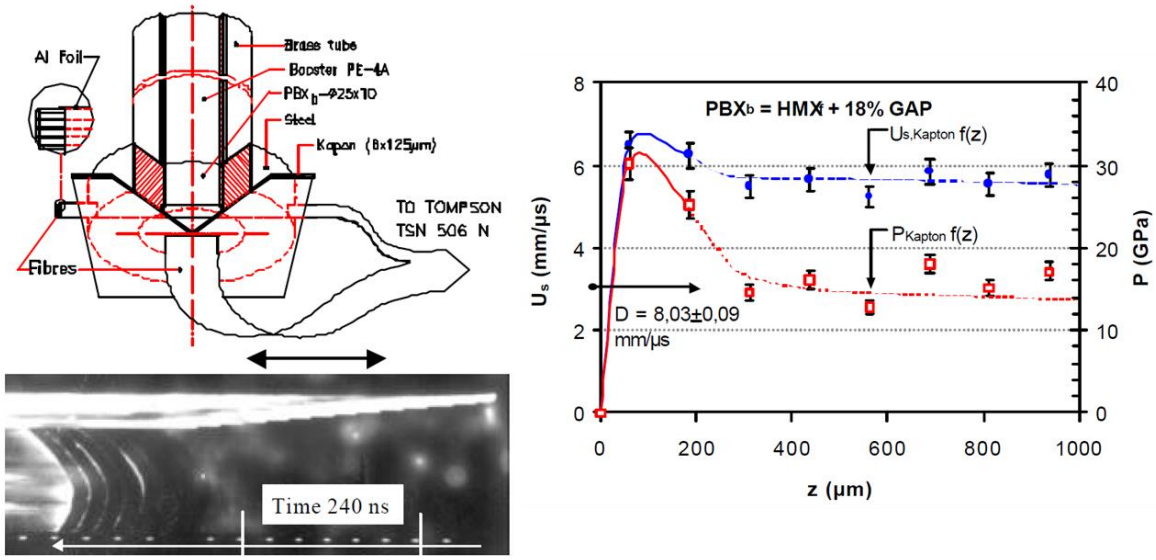

Figure 2-40: Experimental set-up used on the measurement of the SW velocity in a Kapton stack barrier (top left), the acquired streak record is shown in the bottom part of the it (left bottom), and the U_S (blue) and the pressure (red) profiles calculated from such record. Images from (Plaksin, et al., 2002).

In the continuous active optical fiber methods for D measurements (2.1.4.2), it was described the chirped fiber Bragg grating (CFBG) sensor and respective instrumentation. As referred there, the same technique is also able to measure the U_S in inert materials.

One way (Rodriguez, et al., 2014) that used exactly the same instrumentation as described in 2.1.4.2 consists of gluing CFBG sensors on desired positions of the detonating experiment (charge and inert material), as is shown in Figure 2-41 (a). This can be achieved with 100 mm and 10 mm long sensors. The CFGB spectra and the respective (*x*,*t*) diagrams are also shown in Figure 2-41. As it is shown, the U_S in the PMMA is correspondent to the slope of the linear adjustment.

With a more complex system on the output of port 3 (Figure 2-17) composed by an Erbium-doped fiber amplifier and spectrometer (or fiber filters), it is possible to determine the U_S in water induced by an explosively driven Cu plate (Sandberg., et al., 2014), in Phenolic plastic induced by a low fidelity detonator and an aluminum cylinder wall with PBX 9501 as shock generator (Rodriguez & Gilbertson, 2017). In this new configuration, since the CFBG sensors have predictable mechanical response properties, it is possible to determine pressures according to the wavelength shift given by the CFBG sensor. During the SW propagation in the inert material, the CFBG fiber is compressed, which makes the grating elements compress also, and the reflectance band shifts to shorter wavelengths (Sandberg., et al., 2014). By selecting these wavelengths using a spectrometer (or fiber filters) and knowing the calibration of pressurized CFBG, it is possible to determine the pressure according to the wavelength shift (Sandberg., et al., 2014) (Rodriguez & Gilbertson, 2017) or to make a *P(t)* profile (Rodriguez, et al., 2015). Actually, this technique allows the measurement of parameters like: shock to detonation transition, the detonation curvature profile (Barbarin, et al., 2020), and the direct measurement of the *P(t)* profile of the explosive sample (Hof, et al., 2007).

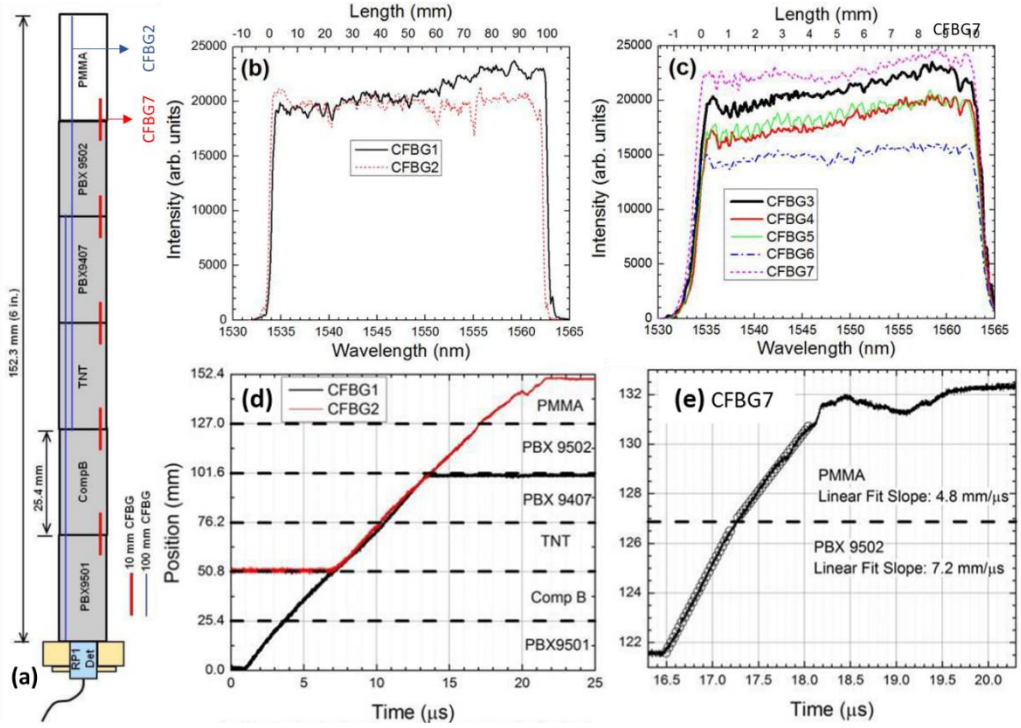

Figure 2-41: (a) experimental set-up used to measure the SW velocity generated by PBX 9502 in PMMA using 100 mm and 10 mm CFBG sensors; CFBG spectra for the 100 mm long (b) and 10 mm long (c) sensors and the respective (*x*,*t*) plots ((d) and (e)). Images from (Rodriguez, et al., 2014)

From the discrete passive optical fiber methods described in 2.1.4.2., just the technique used with the OPTIMEX system seems to be able to measure U_S in inert materials that were generated by explosive samples. The OPTIMEX system was already described in 2.1.4.2. and it has special relevance since it is the most similar method to the one developed along this thesis to perform measurements of the CJ pressure.

The application of the OPTIMEX system and optical fibers on the measurement of the U_S is detailed described at (Künzel, et al., 2017) by using A-IX-1 (RDX based explosive) as shock generator and PMMA, polyamide-6 (PA6), polytetrafluoroethylene (PTFE), and aluminum alloy AW-6061 (Al) as inert materials. In this work (Künzel, et al., 2017), it was used eight multimode glass optical fibers with 1 mm diameter (62.5 µm active core diameter) that were inserted into holes drilled (one central and seven 5 mm concentrically from the axis) in the inert material disks, like shown on Figure 2-42. These holes had different depths and the OFs were inserted in a way that space of air existed between the end of the hole and the beginning of the OF. When the shock wave reached these holes, by compression, the air was ionized and strong peaks of light were observed (Figure 2-42, top left). In transparent (PMMA) and translucid (PA6, PTFE) materials it was

also possible to see the peak generated by the interaction between the explosive and the inert materials. By taking the times where peaks appeared and plotting the thickness of the inert material according to the respective time, a plot like the one shown in Figure 2-42 (bottom right) was obtained. A quadratic fitting was done to the points and an *x(t)* equation was obtained (represented in the graph as *y(x)*). From the derivative of this equation and considering that the SW is transmitted to the inert material at $t = 0$ s, the U_S at the interface was determined. This interface point is then considered as the $U_S(i)$ and the CJ point can be calculated as described at the beginning of this part.

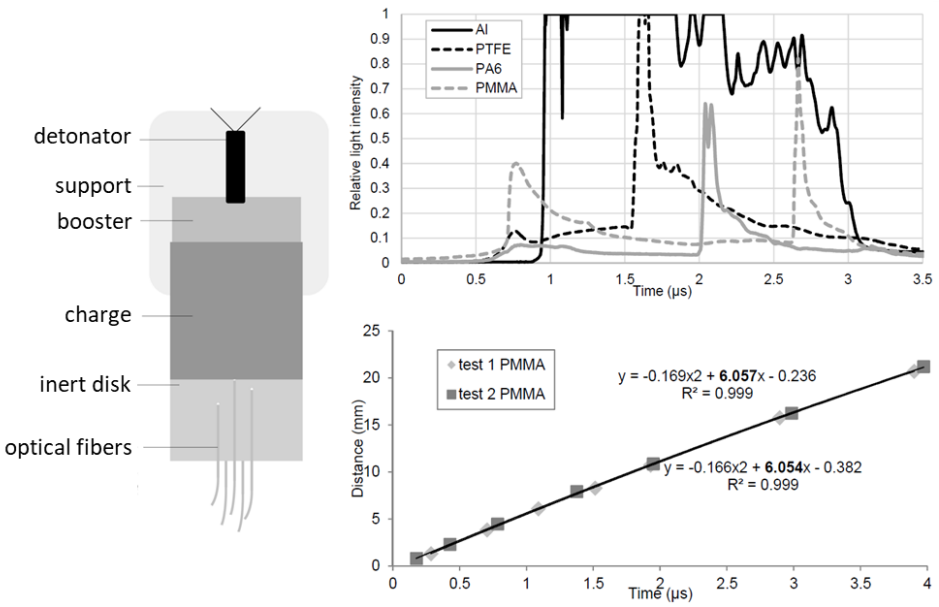

Figure 2-42: Scheme of the experimental set-up (left), example of acquired results for one OF inserted in each of the inert materials (top right), the *x(t)* plot acquired from two PMMA measurements (bottom right). Images from (Künzel, et al., 2017)

According to the authors (Künzel, et al., 2017), this technique is advantageous because it can be used with opaque inert materials, the record evaluation is simple, easy to assemble, enables a reasonable CJ pressure determination. As for disadvantages, they reported that it is still undesired (but predictable) light after the peak of the ionized air; porous materials (PTFE) can emit undesired light during longer distances, due to the shock interaction with the porous, which can give more intense signals than the shock ionized air; in transparent materials, there is always unnecessary radiation captured from the interaction at the interface; the intensity of the light is dependent on the shock pressure able to ionize the air, which decreases throughout the inert material, giving less intense signals; the light emission is also dependent of the impedance of the material, higher the impedance and shorter the distance traveled by the SW throughout the inert material, higher was the overall

light output; the t = 0 s point didn't match with the thickness x=0 because the first OF signal presented a different light trace than the other probes, which made less precise time determinations.

In the discrete-continuous active optical fiber methods, as said in 2.1.4.2., just the OAM developed along this work was found. Further details about this technique, how to use it to measure $U_S(i)$, the respective data treatment, and the advantages and disadvantages of it will be described throughout the next chapters.

Shock-induced polarization

The shock-induced polarization (SIP) is used to determine the induced pressure on an inert material originated by the detonation products of an explosive. For this, it is needed to use a dielectric material with a known Hugoniot curve (Gois, 1995) (Mendes, 1994). The SIP principle is based on the formation of electric dipoles when an SW trespasses a dielectric material. If the dielectric material has the shape of a plate and a conductive surface is assembled on the long faces of that plate, a plane capacitor is formed between the two electrodes. When the SW passes through the plate, it generates an electric displacement that can be expressed as electric potential, or voltage, between the electrodes of the capacitor. By connecting these electrodes to an oscilloscope, the voltage variations can be recorded. Considering the time where the voltage did not change its increasing behavior and knowing the thickness of the dielectric material, it is possible to calculate U_S. So that this measurement is valid, the dielectric material has to be isotropic and its thickness has to be small enough to not attenuate the SW (Gois, 1995) (Mendes, 1994). In this way, the measured U_S is considered to be the $U_S(i)$ used to extrapolate $u_P(i)$ that will be applied to the IMT.

In the works found (Gois, 1995) (Mendes, et al., 1993) (Mendes, 1994) that used this technique, this U_S gauge was composed of a PMMA plate with 1 mm thickness as a dielectric material and Al foil with some units of micrometers as conductive surface. On the face that is opposite to the explosive sample, a circumference with 5 mm diameter is cut out of the Al foil, and two metallic pins are inserted, one inside the circumference, the other outside. These two pins are connected between them by a 50 Ω resistor and connected to the oscilloscope using a coaxial cable. In two works (Gois, 1995) (Mendes, 1994), the U_S gauge was inserted at the end of the explosive charge, while in the other work (Mendes, et al., 1993) it was inserted at the end of a PMMA gap. In one of the works (Mendes, 1994), it was also varied the thickness of the PMMA in the U_S gauge.

2.2.2.4. Determination of the *P(t)* history by a gauge embedded in an inert material

At this point, it will be presented two techniques that allow the determination of the *P(t)* history by a gauge embedded in inert materials. It is considered that the following gauges cannot measure directly the *P(t)* profile of an explosive sample, because these gauges always need a protective and/or isolator layer between them and the explosive sample, which is called to be embedded in an inert material.

The following gauges use the piezoresistive (change of electrical resistance when mechanical strain is applied) and piezoelectric (change of electrical charge according to the applied mechanical strain) characteristics of alloys and polymers, respectively, as sensing elements to determine directly the pressure histories of the interaction between the explosive and the inert materials of the gauge. The manifestation of the CJ pressure of the explosive is extrapolated by its manifestation on the gauge and the IMT should be used to have accurate CJ pressure values. However, when the density of the explosive is close to the density of the gauge, some authors also consider that the gauge is measuring directly the pressure profile of the explosive sample.

Piezoresistive technique - Manganin gauges

The manganin gauges are formed by a manganin alloy that is normally composed of cooper (≈ 84%), manganese (≈ 12%), and nickel (≈ 4%). This alloy is suitable for determining the pressure profile of an energetic material because of its large positive piezoresistive coefficient and low-temperature resistivity coefficient (Urtiew, et al., 1986) (Yiannakopoulos, 1990). To have a large piezoresistive coefficient and a low-temperature resistive one means that, when the manganin alloy is dynamically compressed, the induced stress will generate a bigger change in its resistivity than in its temperature (Vantine, et al., 1980) (Yiannakopoulos, 1990). The manganin high piezoresistivity makes that just a small piece of it is enough to measure a resistance change, which is advantageous for detonation measurements because it can be so thin that it can be considered that it does not disturb the propagation of the SW and material flow (Yiannakopoulos, 1990).

When the stress applied to the manganin alloy is uniaxial and very high (GPa order), as a DW and SW can be, the dimension changes on it are so small that can be considered that the manganin's resistance change is just due to the variation in resistivity (Yiannakopoulos, 1990). In this work, it is considered that the manganin gauge is not able

to determine directly the *P(t)* profile of an explosive sample, because these gauges always need an insulator material, which makes that there is always an inert interface between the explosive and the sensing element.

The manganin gauge is constituted basically by four components: the sensing element that is the manganin alloy, which can be a foil (Vantine, et al., 1980) (Anderson, et al., 1981) (Urtiew, et al., 1986) (Song & Lee, 1989) (Mendes, et al., 2014), a wire, a strip or a thin film (Zhang, et al., 2018), with resistances that can vary from dozens of milliohms (low resistance gauges (Vantine, et al., 1980) (Anderson, et al., 1981) (Urtiew, et al., 1986) (Zhang, et al., 2018)with less than 0.1 ohm) to some hundreds of ohms (high-resistance gauges (Song & Lee, 1989) (Mendes, et al., 2014)) (Yiannakopoulos, 1990); the bounding agent that is used to glue the different layers of the manganin gauge and also acts as electrical insulator, normally it is used an epoxy system with a known Hugoniot curve (Vantine, et al., 1980) (Yiannakopoulos, 1990); the insulation, which is an non-conducting electrical material with a known Hugoniot curve that protects the gauge from the conducting environment, different kinds of polymers can be used, they can be applied to one or both sides of the gauge and they cannot become conductive under very high pressures (Yiannakopoulos, 1990); and the two (single ended) or four (double ended) terminal leads (Yiannakopoulos, 1990) (Urtiew, et al., 1986), normally made out of Cu, where the 4 lead configuration has two output and two input leads, that can be place all parallel or in "H" shape, it is mostly used in the low impedance gauges and reduces changes in the resistance of the lead provoked by stretching (Yiannakopoulos, 1990). The manganin gauge is connected to a bridge circuit, where a high current is used to generate a high output signal. To not change the initial resistance of the gauge, a pulsed power (constant current or constant voltage) supply is used. The signals can be then acquired by oscilloscopes, where is visible a voltage change due to the SW compression that made an increase in the gauge's resistance (Urtiew, et al., 1986) (Vantine, et al., 1980) (Yiannakopoulos, 1990) (Song & Lee, 1989). The voltage change is related by the resistance change ($\Delta R(t)$) in the gauge by equation (2.18) (Song & Lee, 1989)

$$\frac{\Delta R(t)}{R} = \frac{-A_1 V(t)}{E_0 + A_2 V(t)} \tag{2.18}$$

where R is the resistance of the manganin sensing element, $V(t)$ is the voltage output of the bridge circuit, E_0 is the constant voltage applied to the bridge circuit, A_1 and

A_2 are expressed in terms of the resistances of the bridge circuit. The resistance change is then defined by the relation between the pressure ($P(t)$) and the piezoresistive coefficient (R), which can be considered constant for a wide range of pressures through the empiric equation (2.19) (Song & Lee, 1989) (Zhang, et al., 2018):

$$\frac{\Delta R(t)}{R} = K\, P(t) \tag{2.19}$$

An example of a record with the thin film manganin gauge on the measurement of the detonation pressure of a microdetonator is shown on the top of Figure 2-43, where the first horizontal line is the signal of the gauge without power supply, the second one is the state of the gauge when a constant current is provided to the system, and the following voltage decay is considered to be the correspondent to the change in the resistance of the manganin sensing element. The phenomena that originate the other voltage states are not well determined (Zhang, et al., 2018). An example of a current trace for a low-impedance manganin foil gauge inserted on RX03-BB explosive and the respective digitized pressure record are shown on the bottom of Figure 2-43.

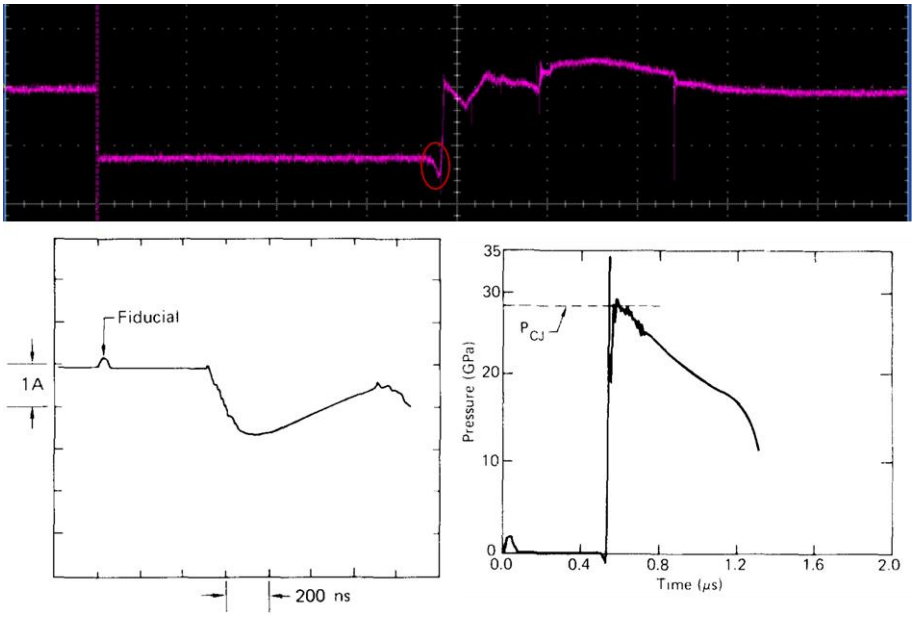

Figure 2-43: Voltage signal collected by an oscilloscope from thin-film manganin foil, where the area to analyze is surrounded by a red line (image from (Zhang, et al., 2018)), at the top. At the bottom is a current trace (left) and the correspondent digitized pressure record (right). Bottom images from (Vantine, et al., 1980).

In stress measurements, such as detonation experiments, the manganin gauges can be inserted directly into the material, or explosive (Vantine, et al., 1980) (Anderson, et al., 1981), that has to be evaluated, or they can be applied between the (energetic) material

to be studied and a known inert material (Urtiew, et al., 1986) (Song & Lee, 1989) (Petel, et al., 2004) (Mendes, et al., 2014) (Zhang, et al., 2018). The time resolution of the manganin gauges depends on several factors, like gauge's location, shock impedance of the manganin/bounding agent/insulator, and the response time of the used recording system (Yiannakopoulos, 1990). Different kinds of explosives were studied with manganine gauges (Vantine, et al., 1980) (Anderson, et al., 1981) (Urtiew, et al., 1986) (Song & Lee, 1989) (Petel, et al., 2004) (Mendes, et al., 2014) (Zhang, et al., 2018).

The reported advantages of the manganin gauges as high pressure sensors are: the strip sensing element allow the measurement of longer pressure profiles; if the gauge exists in the literature the calibration doesn't need to be done; the wheatstone bridge has greater linear range when is supplied by a constant current supply; the resolution of this technique can be increased by reducing the thickness of the gauge and by matching the impedances of the manganin/bounding agent/insulator group; (Yiannakopoulos, 1990) nanosecond resolution can be achieved (Yiannakopoulos, 1990) (Zhang, et al., 2018); calibration is possible with an accuracy of 2%; low impedance gauges record faithfully the pressure, the records can last several microsenconds; the pressure can be accurately recorded in a full detonating explosive; it disturbs the initiation process in a minimal way; (Vantine, et al., 1980) single-ended gauges are easier to assemble in detonation experiments; they can be used single or in stations (more than 1 gauge assembled between the some layers of insulation); (Urtiew, et al., 1986) high sensitivity; good linearity; (Zhang, et al., 2018)high-resistance gauges generate more accurate signals, they need less tests and smaller charges to obtain results and they can determine CJ pressures and reaction times of the explosives; (Song & Lee, 1989) and recently, microscale detonation pressure measurements can be done with thin film manganin gauges, which have shorter-responses than the foil ones, its thin sensitive element reduces the time response of the gauge and it is ideal for measurement of DWs, because its size is smaller than the radius of the detonation curvature and all waves can be considered plane, its accuracy is around 4% and the response time is 37 ns (Zhang, et al., 2018).

By the other hand, the reported disadvantages are: difficult and complex calibrations that can require shock experiments (dynamic) or an hydrostatic press (quasi-static), where both also have associated disadvantages; the gauge assemblage is complex and requires a lot of care; the gauge factor is not linear, which always require calibration; it

suffers from hysterises when unloaded; conductive environments can produce gauge errors; (Yiannakopoulos, 1990) expensive and complex calibration facilities are needed; the time response of the overall system is affected by the tilt of the shock front, so plane waves are desired (which are not so easy to achieve), and by the size of the sensing element (its reduction decreases this problem); (Vantine, et al., 1980) (Yiannakopoulos, 1990) electrical signal degradation can occur, so short electrical cables are advisable (which is inconvenient due to how close the experiment has to be from the recording system); the gauge response is what limits more the overall response time of this system; detonation experiments can be complicated to perform, because to have a gauge thick enough to last a long measurement, and that do not interfere with the SW it is hard to achieve; (Yiannakopoulos, 1990) the thinner gauges can have rapid failure; some gauges can measure the CJ pressure, but cannot give information about the reaction zone structure (Vantine, et al., 1980); low-resistance gauges generate a small voltage drop, which makes the results hard to evaluate; (Song & Lee, 1989) a large sensing element cannot accurately measure the pressure at the center of a tri or bi dimensional DW and a thick one extends the sensor's time; static piezoresistance coefficient does not have the same value as the dynamic one, which make dynamic calibration preferred that can be very expensive (Zhang, et al., 2018); and short recording times (very few microseconds) (Murata & Kato, 2010).

Piezoelectric techniques - Polyvinylidene fluoride gauges

In the late 1960s, it was found out that submitting polyvinylidene fluoride (PVDF), a semi-crystalline polymer composed of carbon, hydrogen, and fluorine, to mechanical stretching, and then to a strong electrical field, it would become strongly piezoelectric (Urtiew, et al., 1986). Then, Bauer started developing gauges based on this material that could be used under dynamic pressures and SW action (Bauer, 1983), which have been later on standardized (Lee, et al., 1988), since the Bauer procedure is important to achieve the desired level of reproducibility in the gauge's electrical properties (Bauer, 1999). Examples of PVDF gauges are given in Figure 2-44 (left), where the Bauer gauge is the top one, as well as the representation of the piezoelectric phenomenon that occurs on them, and an example of a circuit that can be used to perform pressure measurement with such gauges (right) (Murata & Kato, 2010). These gauges normally consist of a thin film of PVDF between two electrodes of copper (Murata & Kato, 2010), or sputtered gold (Urtiew, et al., 1986) (Lee, et al., 1988) or Al (Lee, et al., 1988) over platinum, which are inserted into

PVDF of small thickness (Urtiew, et al., 1986) (Lee, et al., 1988) or polyimide film (Murata & Kato, 2010). In the Bauer gauge (top left of Figure 2-44), the sensing part is referred to as "active area" and it is located where the electrodes overlap (Lee, et al., 1988). As for other gauges, Teflon or Kel-F are needed to provide electrical insulation to the gauge (Lee, et al., 1988) (Bauer, 1999) (Hodges & McCoy, 1999) and they are considered to have similar acoustic impedances to the PVDF, so the reflections within the gauge package are negligible (Hodges & McCoy, 1999) (Hodges, et al., 2000). Duralumin is also reported as being used as an insulator (Hodges, et al., 2000).

When the PVDF polymer is compressed, due to the detonation pressure, a polarization occurs and electric charge Q is generated (Murata & Kato, 2010) since it has its own stored energy (Urtiew, et al., 1986). Its piezoelectric characteristics make that the pressure applied on the PVDF material is directly proportional to the charge generated by it, as shown by the top equation in Figure 2-44 (right). Since charge cannot be directly measured by oscilloscopes, it has to be transformed in voltage employing a circuit like the one shown in Figure 2-45, where the relation $V=Q/\Sigma C$ is applied, being ΣC the total capacitance of the measuring system composed by the PVDF sensing element, the connecting cable, and the charge amplifier. When ΣC is constant, then the voltage is directly proportional to the charge and, consequently, to the pressure applied on the gauge (Murata & Kato, 2010). Another possibility is to record the current generated in resistive circuits, where the electrical charge is determined by numerical integration of the current, or in resistive-capacitive circuits that perform the integration in the line and record directly the value of the charge (Urtiew, et al., 1986) (Bauer, 1999).

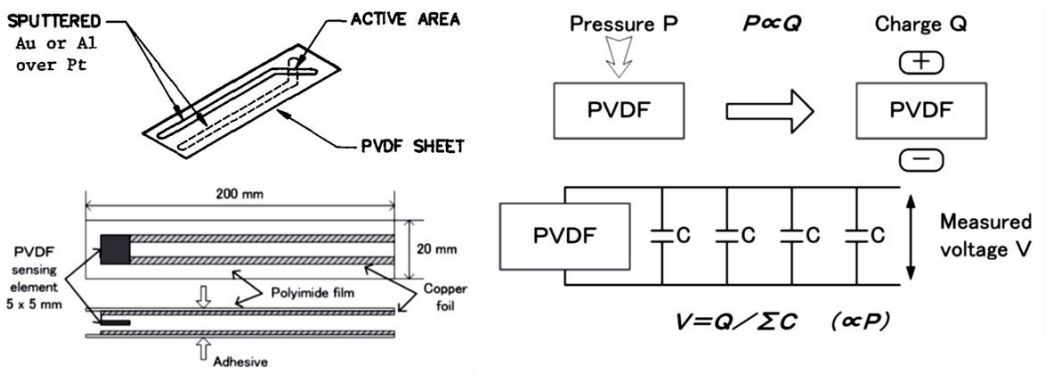

Figure 2-44: Scheme of two different PVDF gauges (top and side view for the bottom gauge), at the left. At the right is the representation of the piezoelectric phenomenon on the PVDF polymer and the equivalent circuit for pressure measurement. Images from (Lee, et al., 1988) (top left) and (Murata & Kato, 2010).

There is an interesting study (Hodges & McCoy, 1999) that correlates the pressure history acquired by a PVDF gauge and the shock phenomena that are occurring at the boundaries between the explosive, the flyer, and the gauge package used on it. Two different techniques were used to vary the gauge's pressure history, one based on the increase of the thickness of the gauge's backer (Kel-F) inserted into a dent block, and another varied the gap between the detonator and the gauge package. An example of a PVDF signal acquired from the first technique is given in Figure 2-45, where it is possible to see the recorded signal from a PDVF gauge with a backer of Kel-F with 2.3 mm thickness, and the respective pressure profile acquired by the integration of it. Computer simulations (WONDY) were also done to model the SW and its interactions through the target assembly.

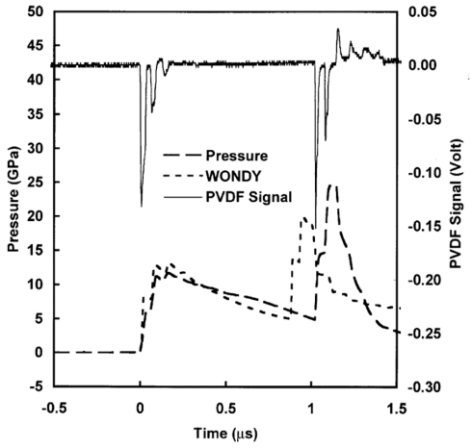

Figure 2-45: Signal acquired from a PVDF gauge with a 2.3 mm Kel-F backer, the correspondent pressure history, as well as the computer simulation for the same pressure profile. Image from (Hodges & McCoy, 1999).

Examples of studies that employed PVDF gauges as tools to measure pressure profiles of different explosives are (Murata & Kato, 2010), (Bauer, 1999), (Hodges & McCoy, 1999) (Hodges, et al., 2000) (Hodges, et al., 2000) and (Dolgoborodov, et al., 2005).

The advantages found in the literature about PVDF gauges were: longer recording times than manganin gauges; useful to measure detonation pressure profile of non-ideal explosives with long reaction zone; (Murata & Kato, 2010) they do not require an external energy source (Urtiew, et al., 1986); they can answer to shock loadings between 0.3 and 46 GPa (Lee, et al., 1988); the Bauer process for poling is important to produce high-quality gauges with high polarization; Bauer gauges are repeatable high fidelity, reproducible, time-resolved SW sensors, even the ones with smaller sensing areas; (Bauer, 1999) (Lee, et al., 1988) the PVDF gauges can be used in extremely harsh electrical

environment due to its inherent flexibility and its large signal to noise ratio (Lee, et al., 1988); they produce accurate, dynamic data for 1 to 1.5 μs after the impact (Hodges & McCoy, 1999); nanosecond time resolution; accuracy on the pressure calculation within 5%; (Hodges, et al., 2000)

The same literature indicates as disadvantages of the PVDF gauges the following characteristics: not all the PVDF polymers are good to be used as a gauge, they should be treated with the Bauer method; it is hard to get, with the Bauer gauges, a sharp edge definition for the total electrode area, and the accuracy of the *P(t)* measurement is dependent on the accuracy of the measurement of the sensor's area; masking techniques needed to produce a sharp edge definition; PDVF has the tendency to wrinkle during deposition; (Lee, et al., 1988) after 1.5 μs of record the PVDF gauges do not give reliable signals due to heat and structural damages, the measurement is affected by the increasing curvature and tilt of the flyer when using detonator flyers (Hodges & McCoy, 1999), by gauge flatness and bonding layer thickness (Hodges, et al., 2000).

3. PASSIVE AND ACTIVE OPTICAL METHODS

In this chapter, it will be presented the materials and infrastructures used in this work, the evaluation of the optoelectric converter system, the development of the optical passive and active methods (OPM and OAM, respectively) applied to the detonation of Seismoplast (PETN based explosive), as well as their capabilities and limitations.

3.1. Materials and infrastructures

This metrology was all developed on an industrial vertical detonation chamber KV2, like the one that is shown in Figure 3-1 (left). In the right part of this figure, it is shown how the fibers of the probes get out from the detonation chamber and the needed material to perform the optical active method (OAM), like the laser control boxes, the laser tower with the lasers on it, the filter cubes that are connected to the probes (black and red cables) and the optical fibers cables that are connected to the optoelectric converter system (orange cables).

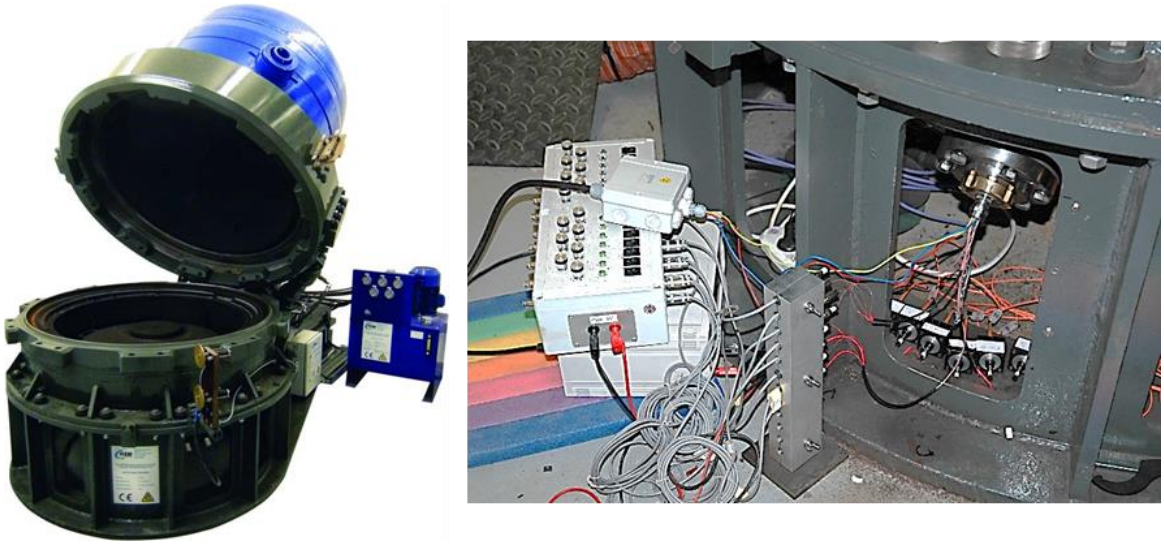

Figure 3-1: Detonation chamber KV2 (image from (OZM Research s.r.o, 2016)) at the left, and at the right is shown the experimental set-up to connect the optical probes, inside the charge, to the lasers, filters, and optoelectric converter system.

3.1.1. Energetic Materials

Besides the matter of availability in the Institute, Seismoplast was the chosen explosive to develop this work because it is a plastic bonded explosive (PBX) based on pentaerythritol tetranitrate (PETN). The PBXs are challenging explosives to study because their characteristics can have wide ranges due to their heterogeneities and hard assemblies in the charges. Seismoplast is barely present in the literature, but its PETN-based composition makes it easier to compare with other PETN-based explosives present in the bibliography, as it was done in Chapter 4. So, if the OAM could be proven to determine precisely and accurately Seismoplast's detonation characteristics, as D and P_{CJ}, it is also trustable to be applied on other explosives.]

Another two explosives were tested: HWC and TKX-50, whose compositions were not disclosed. HWC is an explosive based on RDX, wax, and carbon, while TKX-50 is dihydroxylammonium 5,5′-bistetrazole-1,1′-diolate, an energetic ionic salt.

Three types of explosive charges, the rectangular cross-section explosive charge (REC), circular cross-section explosive charge (CEC), and the pellets explosive charge (PEC) configurations, were used in this work. The first had a length of 150 mm and a rectangular cross-section of 8 x 8 mm, while the CECs had 150 mm length, and a circular cross-section of 15.8 mm inner diameter, and 2.5 mm wall thickness, and they are well described in Chapter 4, as well as Seismoplast, while the third configuration will be presented on point 4.3 and it was used with HWC and TKX-50. These three kinds of charges and the explosives used throughout this work are shown in Figure 3-2.

To assemble the Seismoplast in the charges, which was always done manually, specific tools were created. Such tools and images from the assembling process are shown in Figure 3-2.

Figure 3-2: Sample container, "U" plate, detonation port, and probes transport bucket ready to take to the detonation chamber (top left). Tools specially designed for the insertion of Seismoplast into the RECs and half REC assembled (top middle). Insertion of Seismoplast in the "U" plate (top right). Insertion of Seismoplast in a CEC with a tool specially designed for it and its scheme with the lateral and bottom view (bottom left). Assembled CEC charge for *D* and U_S measurements with OAM (bottom middle). A PEC assembled with HWC (dark gray) and TKX-50 (light gray) for measurement of the *D* of TKX-50 and U_S (middle right) and a package of Seismoplast (bottom right).

3.1.2. Optical fibers

The PMMA optical fibers with 250 µm diameter, (Raytela, PGR-FB250) were the most used during this work as probes. These PMMA optical fibers have the characteristics presented in Table 3-1, an image from the spool and their attenuation profile are shown in Figure 3-3. In the optical passive method (OPM), they always had 1.5 m length and one SMA connector in the end, while in the optical active method (OAM) they had 3 m length and SMA connectors in both ends. The connectors were assembled manually, with the help of a hot air blow machine and a razor blade to terminate them. When these probes were protected, it was mainly used stainless steel tubes with 0.51 mm external diameter and 0.26 mm internal diameter.

The silica (SiO_2) fibers used in this work were always used as interface fibers between the filters or the probes and the optoelectric converter system. These SiO_2 fibers were step-index multimode fiber optic patch cables, with SMA connectors, purchased from THOR Labs, with a core diameter of 200 µm and length of 25 m. An image from them and

their attenuation profile is shown in Figure 3-4. Some tests were performed with these fibers as probes, but they did not present any advantage in relation to the PMMA ones.

Table 3-1: Characteristics of the PMMA optical fibers used in this work according to the producer (Toray Industries, Inc., 2006) (Laser Components, 2016).

Parameter		Performance
Core	Material	Polymethyl Methacrylate (PMMA)
	Refractive Index	1.49
Cladding	Material	Fluorinate polymer
	Refractive Index	
Fiber type		Step index
Numerical aperture (N.A.)		0.5
Acceptance angle degree		60°
Temperature range for permanent use		-55 ~ 70 °C
Attenuation at 650 nm (dB/m)		~ 0.35
Main Usages		Data transmission; light guide; optical sensor; displays
Allowable bending radius (mm)		9

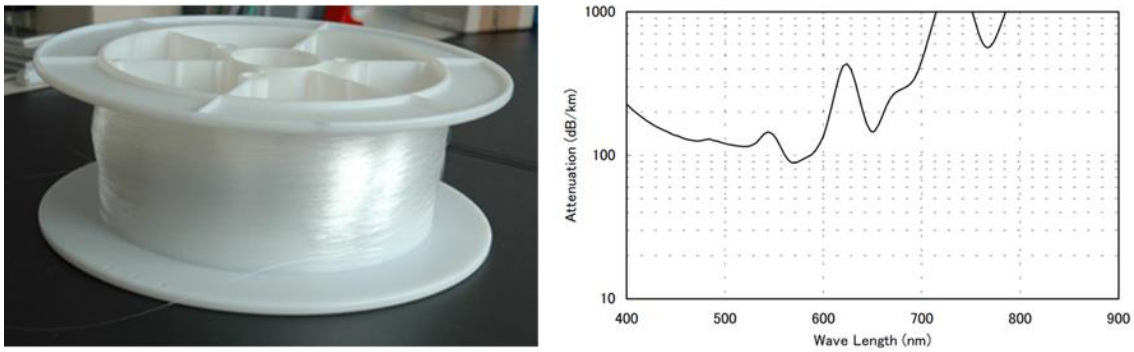

Figure 3-3: A spool of PMMA optical fiber and its spectral attenuation. Graph from (Laser Components, 2016)

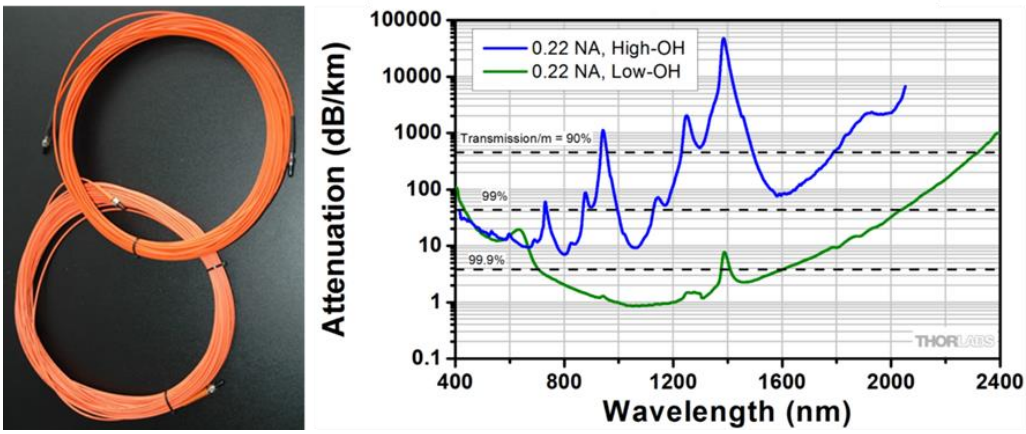

Figure 3-4: 25 m step-index multimode fiber optic patch cables and their spectral attenuation (in blue). Graph from (THORLABS, 2019)

3.2. Evaluation of the optoelectric converter system

The optoelectric converter system (OECS) shown in Figure 3-5 used in this work was developed at Laboratório de Enérgetica e Detónica (LEDAP).

Figure 3-5: Optoelectric converter systems used in this work.

The system is equipped with HFBR-2406Z optical to electrical analog receivers, with a frequency response of 125 MHz, from Avago Technologies. These receivers were conceived to pair up with transmitters HFBR-1404Z, to provide an optimized solution for Fast Ethernet Standard (100 Mbps) at 850 nm on multimode optical fibers (Avago Technologies, 2014). The dynamic characteristics and the spectral answer of such sensors can be observed in Figure 3-6.

-40 °C to +85 °C; 4.75 V ≤ Supply Voltage ≤ 5.25 V; R_{LOAD} = 511 Ω, C_{LOAD} = 5 pF unless otherwise specified

Parameter	Symbol	Min	Typ[2]	Max	Units	Conditions
Rise/Fall Time 10% to 90%	t_r, t_f		3.3	6.3	ns	P_R = 100 µW peak
Pulse Width Distortion	PWD		0.4	2.5	ns	P_R = 150 µW peak
Overshoot			2		%	PR = 5 µW peak, t_r = 1.5 ns
Bandwidth (Electrical)	BW		125		MHz	-3 dB Electrical
Bandwidth - Rise Time Product			0.41		Hz • s	Note 10

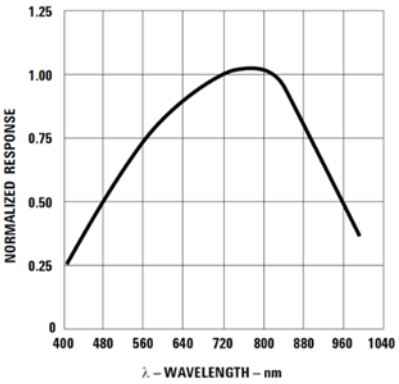

Figure 3-6: Dynamic characteristics, normalized at 820 nm, of the HFBR-2406Z receiver. Images from (Avago Technologies, 2014).

The OECS was used, during this work, in two ways: 1) converting the light coming from the detonation process into an electric positive signal (passive method); 2) interrupting a constant received laser light by the detonation or shock process, which results on a negative peak (active method). The signals were visualized using a transient recorder TransCom-CompactX-XL from MF instruments, with 12 acquisition channels, bandwidth 240 MHz, different sample rates (240 MS/s maximum).

The HFBR optoelectric converters were mounted in the OECS with slight changes concerning the circuit recommended by the producer, as shown in Figure 3-7. To work with an analog output signal, the digital output block (grey box) was not assembled. The sensor's output signal passed through an RC circuit, and at the R_{LOADS} resistance (510Ω) was recorded the analog output signal. The analogic output of the sensor was tested with a capacitor C with a capacity of 0.971 nF. The characteristic time of charge and discharge of this RC circuit is 495 ns, which corresponds to a cut-off frequency of 321 kHz.

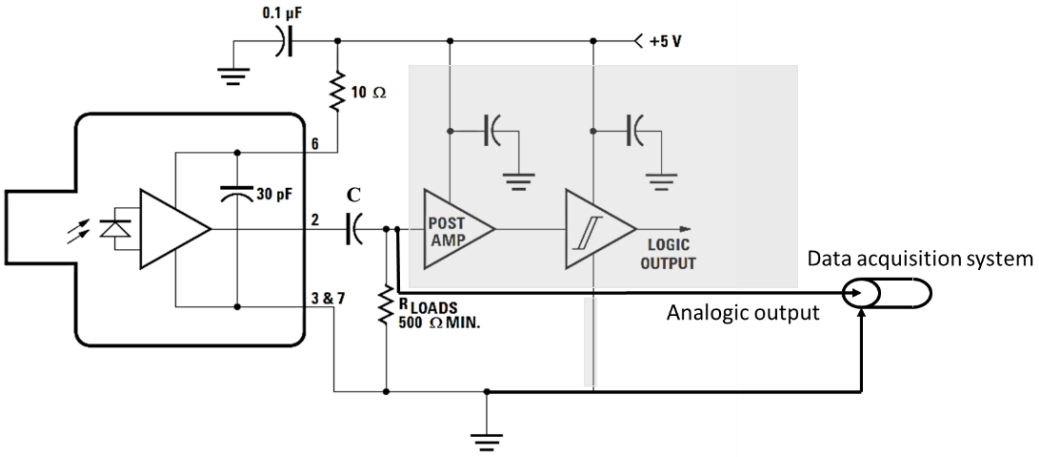

Figure 3-7: Scheme of the circuit recommended by the sensor's producer and the changes performed by the OECS producer.

This differentiating RC circuit at the sensor's output 2 is working as a highpass filter, where the output signal is correspondent to the input one, for frequencies higher than the cut-off frequency. The sensors in this work are not intended to reproduce the light phenomena associated with the detonation, neither their intensity, but to identify the transitions related to the spatial positions of the DW, or SW, inside the materials.

3.2.1. The answer of the sensors to the paired transmitter

The sensors installed in OECS were tested with the paired electro-optic transmitter HFBR-1404Z. This transmitter emits light with a center wavelength of 650 nm and a working frequency of 3.9 MHz.

All the 8 used channels of OECS were tested with this transmitting system according to the scheme shown in Figure 3-8. The transmission media was a 25 m SiO_2 step-index multimode fiber optic patch cable.

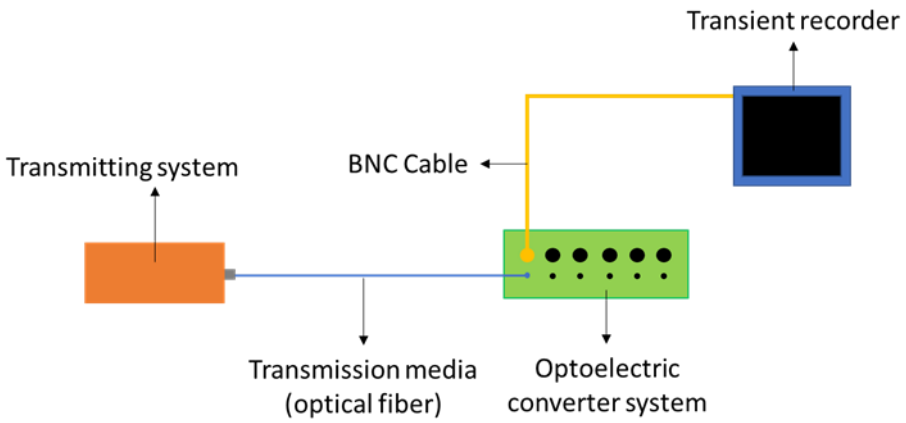

Figure 3-8: Scheme of the experimental set-up to evaluate the answer of each sensor to its correspondent transmitter.

Figure 3-9 shows the acquired results when the 8 used channels are receiving light from the transmitting system. This figure shows that the sensors' responses are proportional to the emitted light since it seems that the sensors are reproducing the pulsed light of the transmitting system. Channel 5 presents approximately half of the amplitude of the other channels. However, this is not important because the sensors will not be used to measure the radiation intensity. Whereas the rise time and fall time are very similar for all the channels, which indicates that all the channels respond with the same delay to the same stimulus.

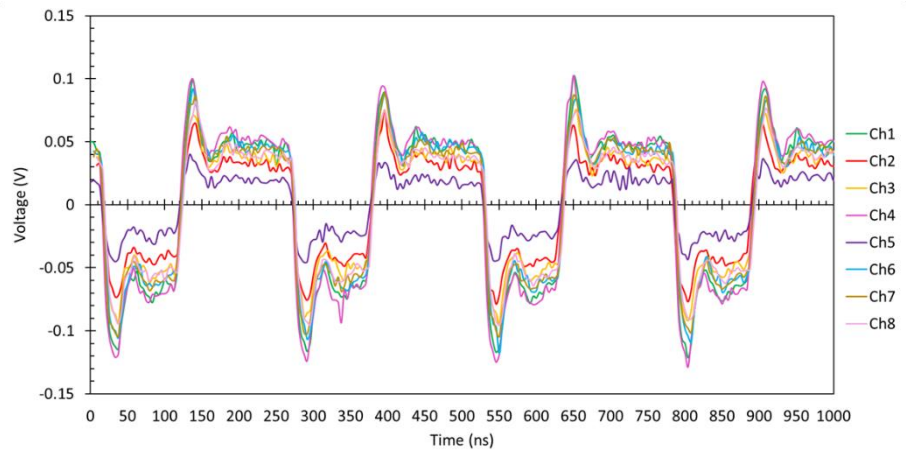

Figure 3-9: Acquired signals from all the channels when they are receiving light from the transmitting system through a SiO_2 patch cable.

The measurements of the rise times (RTs) and the fall times (FTs) in three periods of the signals are shown in Figure 3-10. These measurements were performed with the data acquisition application software, TranAX 3.4.1, of the transient recorder.

Considering three periods of oscillations, the mean rise time between the 8 channels changed from 4 to 8 ns, and the mean fall time varied from 4 to 8 ns.

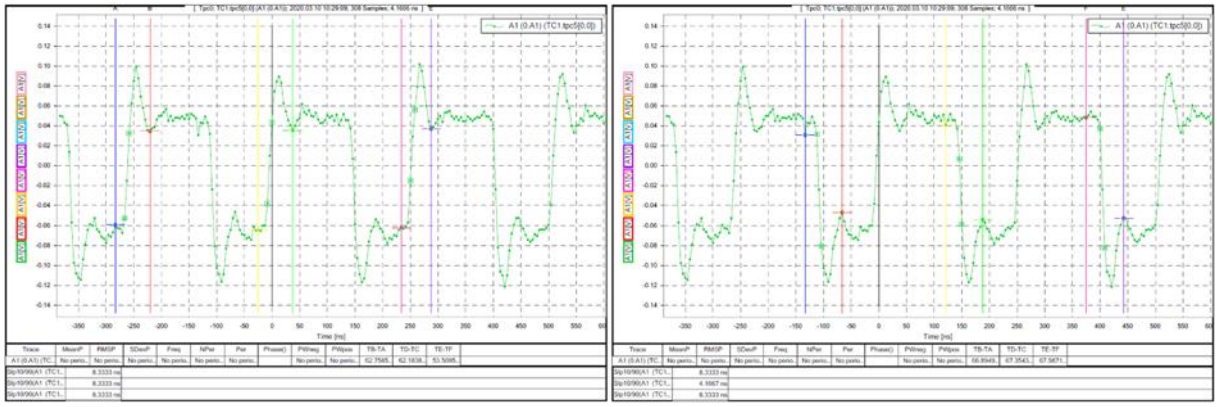

Figure 3-10: Examples of RTs and FTs measurements to the signal generated by channel 1 of Figure 3-9.

Changing the transmission media between the transmitter system from a 25 m step-index SiO_2 multimode fiber optic to a 3 m PMMA optic fiber is observed attenuation of half amplitude in all channels (Figure 3-11). This strong attenuation is justifiable due to the lack of coating on the PMMA optical fiber, which induces losses on the transmitted radiation. Besides that, the fall and rise times of all the channels are coincident, the same as before, proving that the transmission media does not affect the RT and FT parameters.

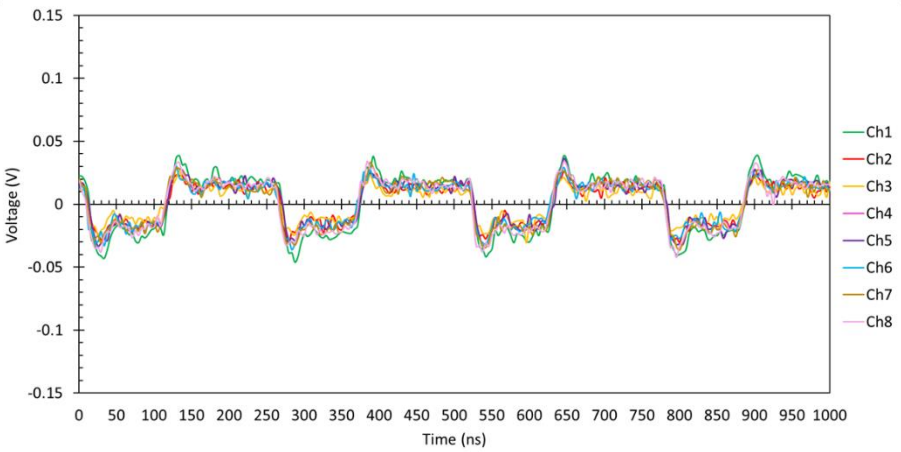

Figure 3-11: Acquired signals from all the channels when they are receiving light from the transmitting system through a 3 m PMMA optical fiber.

3.2.2. The answer of the sensors to modulated lasers

The sensors installed in the OECS were also tested with modulated laser radiation. Eight Flexpoint FP-SMA-650-30MD-1MHz laser diode module, with a wavelength of 650 nm, 30 mW, produced by Blau optoelektronik were used. The eight

channels laser control system (LCS) comprises a laser intensity regulator for the power source, which is controlled in frequency by a signal generator.

The answer of the sensors to pulsed light emitted from the same laser was tested according to the experimental set-up schematized in Figure 3-12. The lasers were modulated with the signal generator (Voltcraft 6 MHz sweep/function generator model FG-506). The laser light was modulated to be a square wave with a frequency of 3.6 MHz, and it always worked in the maximum amplitude allowed by the LCS, like in the detonation experiments. The 3.6 MHz was used to compare with the transmitter system. The filter cube was used as an SMA interface to connect the two male SMA, one coming from the PMMA fiber and the other from the SiO_2 cable, it was constituted by two collimators and a filter LC-HP660-HPB 20-24.4 Bandpass filter, from Laser Components. This was the same configuration that was used in the detonation chamber.

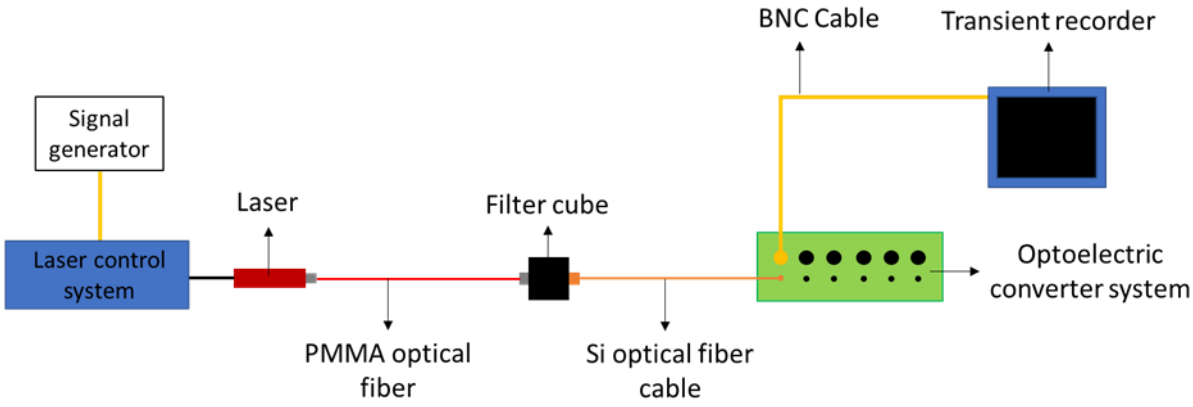

Figure 3-12: Experimental set-up used to evaluate the answers of the 8 used sensors to laser light modulated through a laser control system.

By modulating the laser light as a square wave with 3.6 MHz, with the maximum amplitude allowed by the LCS, it was possible to obtain the signals shown in Figure 3-13. This figure shows that all the sensors have the same answer to the same stimuli. The LCS seems to control properly the laser since the signals do not suffer abrupt changes in their shapes. The time deviations observed in the signals of Figure 3-13 can be attributed to the signal generator because the frequency generated was not so stable. To be precise, the frequency of the three pulses shown varied between 3.564 and 3.552 MHz.

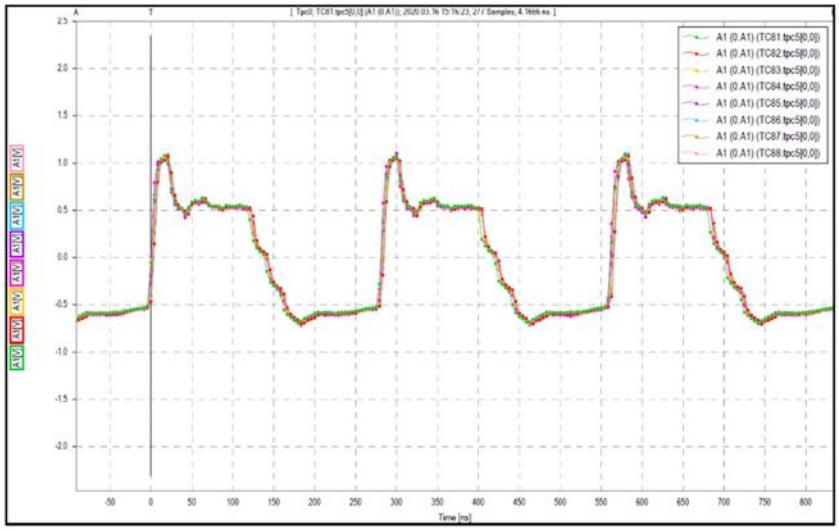

Figure 3-13: Signals obtained when the laser was modulated as a square wave, with 3.6 MHz and with the maximum amplitude allowed by the LCS. Channel 1 of the OECS is in green and channel 8 is in light pink. The vertical ax is in Volts and the horizontal one in ns.

The RTs and FTs of the three periods of each signal shown in Figure 3-13 were evaluated as demonstrated in Figure 3-10.

The average of the RTs of the 8 sensors varied between 4 and 7 ns, as before, all inside the time scale allowed by the acquisition properties of the transient recorder and by the sensors' characteristics. The FTs were substantially higher but very stable, varying between 41 and 43 ns. These high FTs seem to be due to the difficulty of modulating the laser in its "turn off" phase, and the laser was modulated with a frequency above the recommended one by the producer. The LCS seems not to influence the generated signal.

3.2.3. The answer of a sensor to different signal frequencies

To understand how the sensors answer to signals with the same amplitude, but with different frequencies, a sensor was subjected to 8 different frequencies. The set-up used was the same as presented in Figure 3-12, using channel 1. The laser was modulated with signal generator Rigol DG1062Z, 60MHz, 200MSa/s as a square wave with the maximum intensity allowed by the LCS. The frequencies varied between 20.3 Hz and 5 MHz (Figure 3-14).

According to Figure 3-14, for very low frequencies (top images) until 1 kHz, it is observed only vertical lines corresponding to the positive and negative transition of the square pulse. For these low frequencies, the input signals are not reproduced at the output. For frequencies of 100 kHz is observed the positive and negative transitions of the square

pulse, and the output capacitor's charge and discharge, respectively, but it still does not reproduce the square input signal. For frequencies above 500 kHz, the OECS works as a differentiating circuit, where the output signal is the derivative of the input signal. For square pulsed lasers modulated at 5 MHz is observed that the sensors can reproduce the square signals. As the sensor is mounted in an RC circuit, type high pass filter (Figure 3-7), it is verified that signals with frequencies higher than cut-off frequencies (321 kHz) are well reproduced.

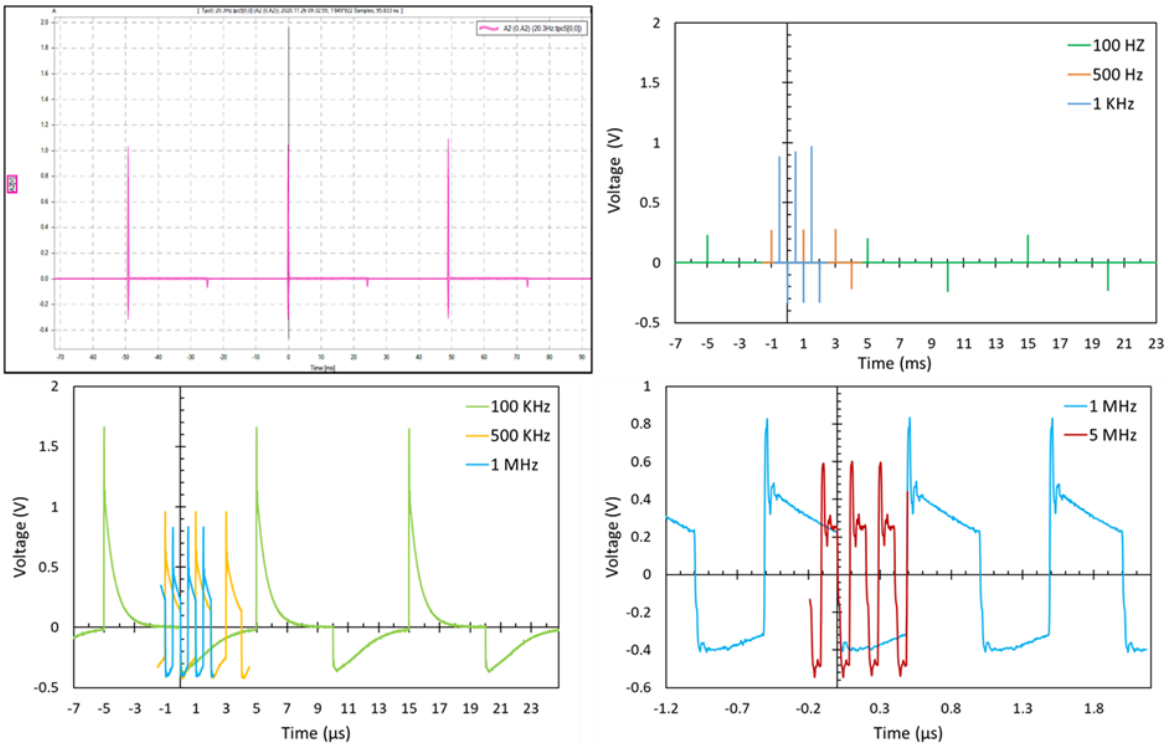

Figure 3-14: Modulated laser signals with different frequencies and maximum amplitude allowed by the LCS. The pink signal (top left) is correspondent to a frequency of 20.3 Hz, the vertical ax is in Volts and the horizontal in ms.

3.3. Optical Passive Method (OPM)

The main objective of this work was to developed a detonation metrology that could measure parameters like detonation velocity and detonation pressure at the Chapman-Jouguet point. Since the detonation radiation is one of the most used phenomena to characterize the DW, it was used optical fibers as probes and optoelectric converters to record the rising emitting light from the thermal radiation of the DW. Here, this process is called the optical passive method (OPM).

The used explosive where the OPM was extensively applied was Seismoplast, a plastic bonded explosive (PBX) based on pentaerythritol tetranitrate (PETN). The PBXs are normally the most challenging explosives to study because their characteristics can have wide ranges, due to their heterogeneities, and they are hard to assemble in the charges.

The following points will show the abilities of PMMA optical fibers on capturing and transmitting detonation radiation (passive bare optical probes, PBOP, or passive protected optical probes, PPOP) according to different positions. Some probes were inserted into the explosive charges in the axial position and other probes were fixed normal to the axis. They were inserted in rectangular cross-section explosive charges (RECs), employing a "U" plate (see the top of Figure 3-2) made of polypropylene (PP).

Silica (SiO_2) fibers were also tested, but the PMMA optical fibers were used since the beginning, because of their advantages: they are much easy to work with due to their malleability, it is easy to control their length, and to apply connectors on them, and they do not have a casing.

The following presented results were obtained with a capacitor C of 100 nF (see Figure 3-7).

3.3.1. Axial passive bare optical probes inside the explosive charge

To evaluate the working principle of the probes when they are inserted axially into the REC, four PBOPs were fixed normal to the axis, and two active bare optical probes (ABOPs) were inserted transversally to the axis in the explosive charge like is shown in Figure 3-15. The active optical probes and their working principle will be detailed in 3.4. The two active optical probes were used to register the passage of the DW and to measure the mean *D*. All the probes were inserted inside in the middle of the charge (4 mm depth).

Figure 3-15 shows the positive signals acquired by each passive BOP, the negative signal that was given by the second active probe, and four instants: the moment when the S8 sensor starts receiving light and its saturation moment (green dashed vertical lines), the moment when the DW reaches the passive BOPs (blue vertical line) and the end of the charge (dark red vertical line).

The moment when the sensor started acquiring light was determined by the intersection of the baseline with the line that fits the raising part of the signal as shown in

the zoomed part of Figure 3-15 right. The time interval between the APOPs was used to calculate the *D* of the experiment (7273 m/s).

Analyzing Figure 3-15, it is possible to see that all sensors take more or less the same time to saturate, being their average time of 1.31 µs. This means that the sensors started to detect radiation when the DW is around 9.5 mm far away from the top of the probe. All the passive probes started to capture radiation before the DW reaches the active BOP2. This proves that Seismoplast is transparent to the detonation radiation. The sensors were saturated around 419 ns before the DW reached the top of the passive probes (blue vertical line), which means that the DW was about 3 mm far away from the top of the probes when the sensors reached the saturation level.

These results show that passive BOPs oriented axially in the charge, with the used set-up (probes directly connected to the optoelectric converter system, without any attenuation), are not useful for detonation velocity calculations neither for the determination of the DW curvature, since it is not possible to determine the time when the DW shocks the top of the probes. However, they can be useful to study the detonation radiation inside the explosive charge.

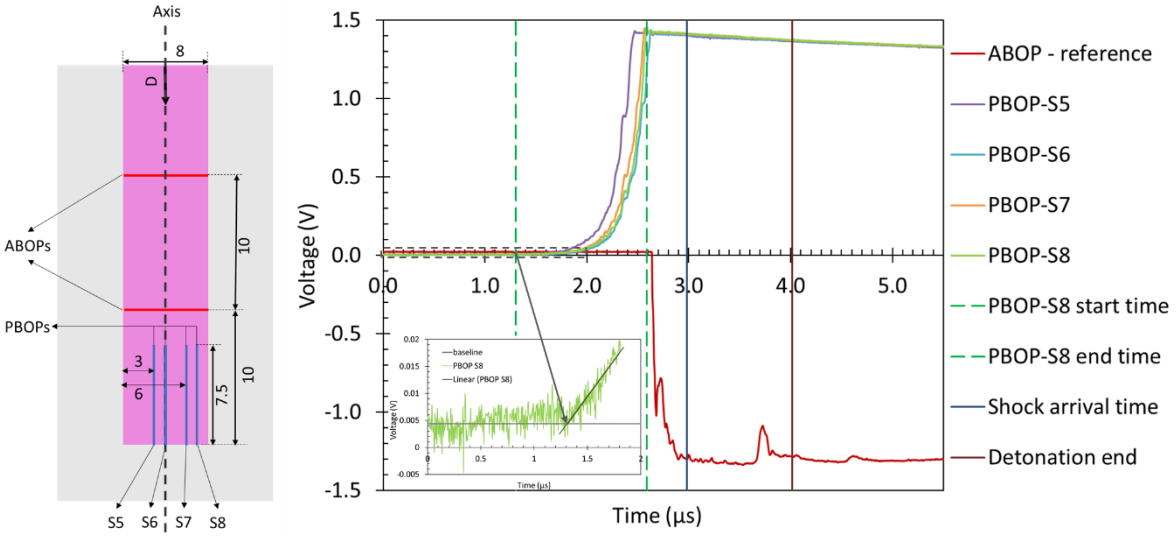

Figure 3-15: Scheme of the experimental set-up used when the passive BOPs are inserted normal to the axis, where the distances are in mm (left), a result of such set-up with the zoomed image of the methodology used to determine the moment when the sensors started acquiring light.

A similar test was performed with passive BOPs, inserted axially into the charge, which is depicted in Figure 3-16. This set-up is composed of eight PBOPs, separated between them by 250 µm, with 8 mm length inside the charge. The acquired results are also shown in Figure 3-16, as well as their 3D representation for better visualization.

The bottom of Figure 3-16 shows clearly, in both graphs, the pulsing behavior of the detonation radiation of a heterogeneous PBX. While the light intensity is increasing, it is possible to see that this increase is not done continuously, but it has a “wavy” behavior. This phenomenon is reported in the literature (Plaksin, et al., 2009) (Plaksin, et al., 2010) and it is associated with the localization of the reactive process in the particles, or in the cluster of particles, inside the PBX.

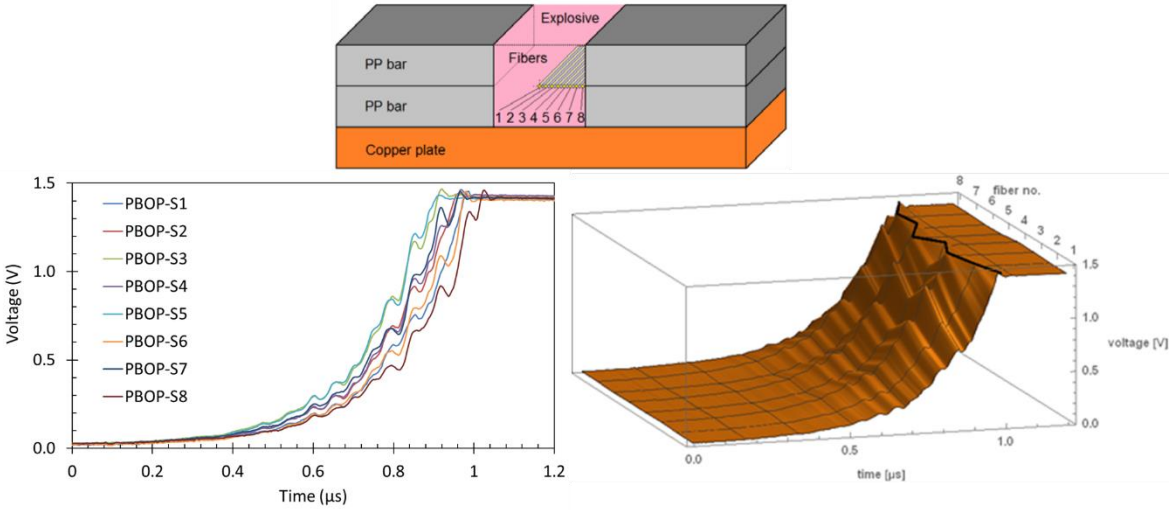

Figure 3-16: Scheme of the set-up with 8 axial PBOPs (top), the acquired result (bottom left), and the 3D representation of the acquired result (bottom right).

The same test was performed with the probes inside of stainless-steel tubes to protect the passive optical probes (PPOPs), to ensure the position inside the charge, and to avoid any lateral radiation entering into the probes. The acquired results were the same as for the passive bare optical probes, as shown in Figure 3-17.

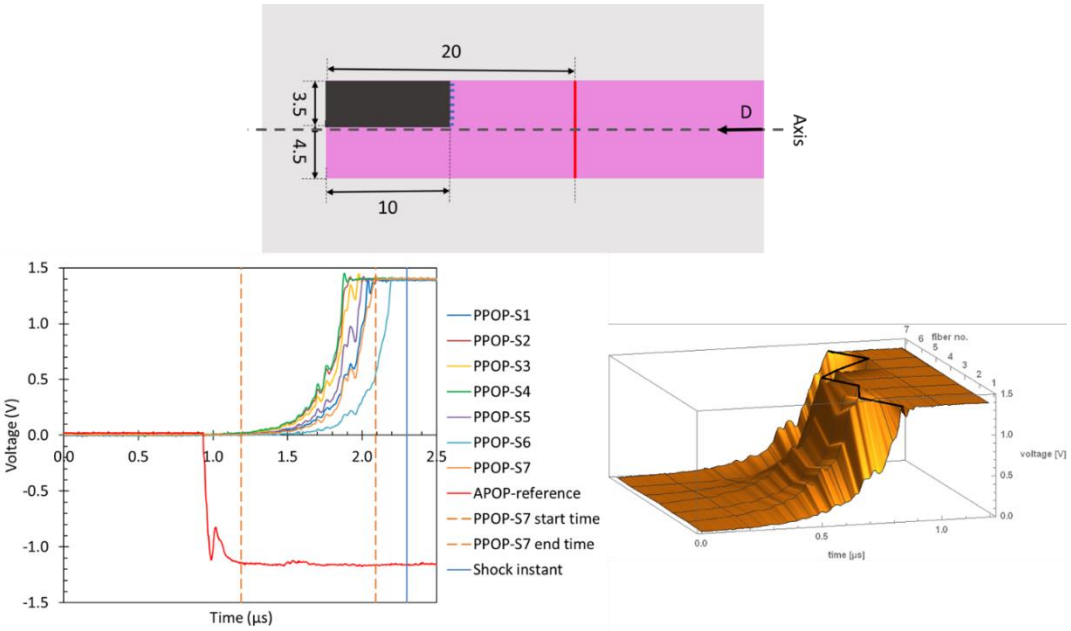

Figure 3-17: Scheme of the set-up with 7 axial PPOPs and one APOP for distance and time references, distances in mm (top), the acquired result (bottom left), and its 3D representation (bottom right).

Until here it was shown that, with the used experimental set-up, axial probes, concerning the detonation axis, are not able to determine precisely a time according to their position, because it would be needed to calibrate each probe immediately before the experiment after the insertion of Seismoplast in the container, which was not possible for security reasons (the explosive should be detonated shortly after the sample preparation, to avoid accidents, according to the ICT rules)..

3.3.2. Transversal passive bare optical probes inside the explosive charge

It was performed four different configurations using the passive optical probes transversally mounted concerning the axis of the charges. In the literature, for a point-to-point determination of the detonation velocity of explosives using optical fibers, is described frequently that the optical fibers are fixed in the interface wall/explosive. This configuration was tried as (1), and the other three consisted of inserting the probes (2) 4 mm into the explosive charge, (3) crossing completely the charge, and (4) crossing completely the charge at the interface charge/witness plate (base of the charge made out of Cu). The schemes of these four configurations are shown in Figure 3-18 accompanied by the respective results. Four probes were used in each configuration, except for configuration (4), where just two probes were used. In the schemes, the PBOPs are always represented by blue lines. In (4)

the blue lines are dotted to represent that they were inserted at the interface Seismoplast/Cu plate, while all the others were always inserted in the middle of the charge. All set-ups have the same dimensions as the ones presented at 3.3.1, with exception of the length and positions of the probes.

For configurations (1) and (2) just one result was present (from (1)) because the acquired results were very similar between them - probes inserted in the interface explosive/container's wall, or 4 mm inside and in the middle of the explosive charge, give wavy and slow rising signals followed by a plateau that shows the sensor's saturation; probes completely crossing the charge, and in its middle (configuration (3)), give signals with fast and sharpen rise times at the moment of the shock between the DW and without the "wavy" behavior, preceded from a very small rise due to the radiation that the bare probes can acquire transversally, and followed by an intense peak and the saturation's plateau; when the probes are inserted in the bottom of the charge, at the interface explosive/Cu plate (configuration (4)), there is a long low rise and more intense than in configuration (3), but when the DW shocks the probe, the signal has the same behavior as in (3), fast and sharpen rise time followed by a peak and the plateau of the sensor's saturation. Configurations (3) and (4) are the only ones where is possible to clearly see the moment when the DW shocks the probes, given by the fast and sharpen raising parts of the acquired signals.

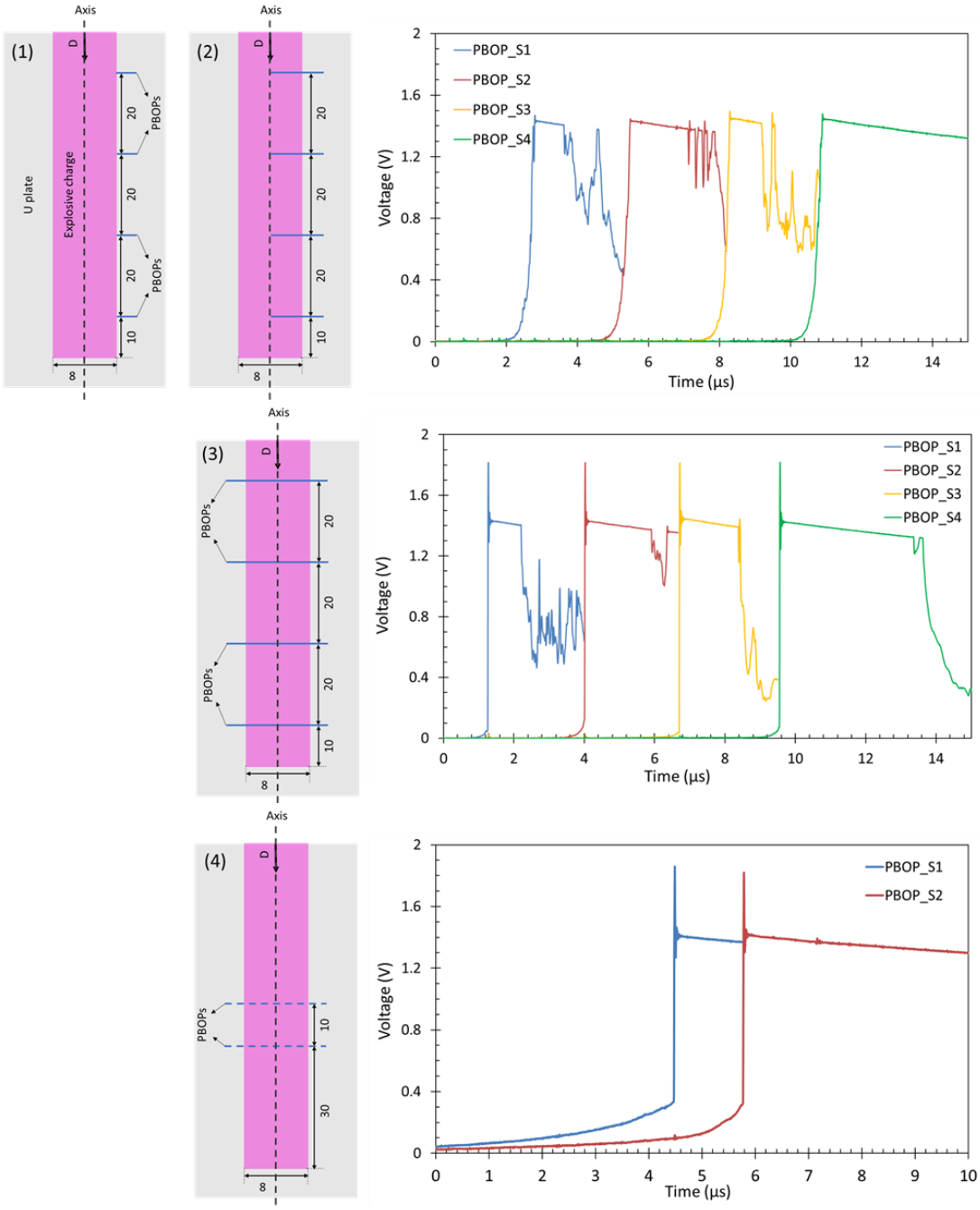

Figure 3-18: Set-ups schemes and respective acquired signals for four different transversally inserted passive bare optical probes into the middle of the explosive charge (4 mm deep). The exception was (4) where they were at the interface explosive/Cu plate. All distances in the schemes are in mm.

To show the different behaviors of the rising signals when the probes are inserted in the four different configurations referred above, Figure 3-19 was constructed. Taking into account the low saturation level of the sensors, the probes in configurations (1) and (2) show signals with relatively slow raising times followed by the sensors' saturations, and the wavy behavior observed by the axial probes is still visible by these transversal probes. When the

probes are completely crossing the charge (configurations (3) and (4)), the raise times are shorter, it is formed an intense peak that is followed by the saturation's plateau, and the wavy behavior of the radiation is not observed anymore. In configuration (4), there is a slow rising of the signal with significant intensity, before the abrupt rise of the signal, showing that in this position there is additional radiation that the probes can capture transversally.

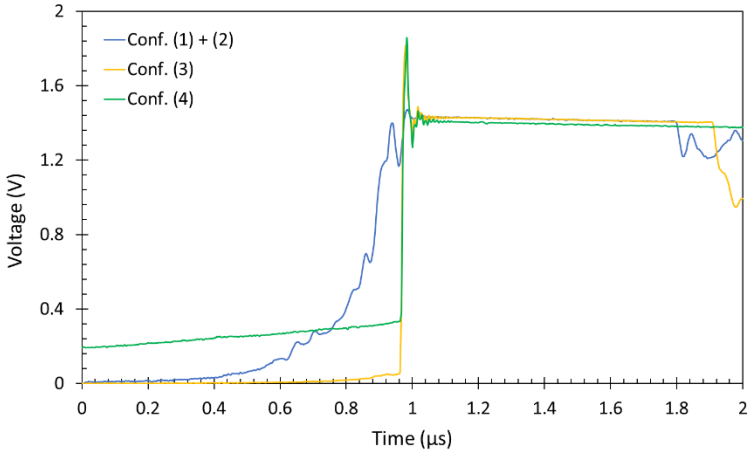

Figure 3-19: Rising signals from configurations (1) to (4). All the signals were acquired by sensor S1.

For the first three configurations it was determined the *D*, while it was not determined for configuration (4) due to the reduced number of probes. *D* was calculated by two different methods, the least square method, and the mean detonation velocity, like all the detonation velocities calculated throughout this work. They are properly described in Chapter 4. These results are presented in Table 3-2.

According to the measured *D*s, it is possible to affirm that configuration (2) is the most unprecise because is where the different calculation of *D* have the biggest difference between them, and the associated errors (*S* and $D_{\text{std dv}}$) are the highest from the three configurations. This is attributed to the saturation of the sensors before the DW reaches the probes, and the insertion of just 4 mm of the probe inside the charge makes additional errors in the probe's position. Configuration (1) is slightly more precise than (2), but the associated errors and the difference between calculated *D*s are still high. These errors are associated with the saturation of the sensors before the DW shocks the probes. The most precise configuration was (3), where the deviation between *D*s is small, as well as the errors associated with each calculation.

Table 3-2: Determination of detonation velocity of Seismoplast for experiments (1) to (3), according to the least square method and the mean detonation velocity determination.

Configuration	Least square method		Mean detonation velocity	
	D (m/s)	S (mm)	D_{mean} (m/s)	$D_{std\ dv}$ (m/s)
(1)	7349	0.628	7398	312
(2)	7039	1.024	7131	497
(3)	7262	0.369	7248	175

3.3.3. Filter application to passive optical probes

To avoid sensor saturation and surrounding radiation, it was added to the experimental set-ups filters (F_1) with a bandwidth between 640 and 680 nm (LC660HBP40, Laser Components), inserted between the end of the optical probes and before the optical cables that were conducting the radiation from the detonation camera to the optoelectric converter system, a filter cube assembled similar to the one shown on Figure 3-12. Configuration (3), which set-up is represented in Figure 3-18 (left), was composed of 4 passive BOPs, where the first and the last one had no filters and the middle ones had filters. The acquired results as well as the zoomed image in time of the filtered signals are shown in Figure 3-20.

As shown by the acquired results, the use of filters cut the surrounding radiation out of the filter's wavelength window (filtered signals do not have the little left rising "tail") and also avoids the saturation of the sensor (the plateaus after the maximum peaks do not exist in the filtered signals). The initial abrupt rising of the filtered signals indicates the moment of the shock between the DW and the passive BOP, but the number of peaks with different intensities makes it hard to choose one as a reference, mostly because the shape of such signals is not always the same, and the maximum peak is not always the first peak. The same experiment was performed with protected optical probes and the results were similar, showing that, in these cases, the protection of the probes does not change the shape of the acquired signals.

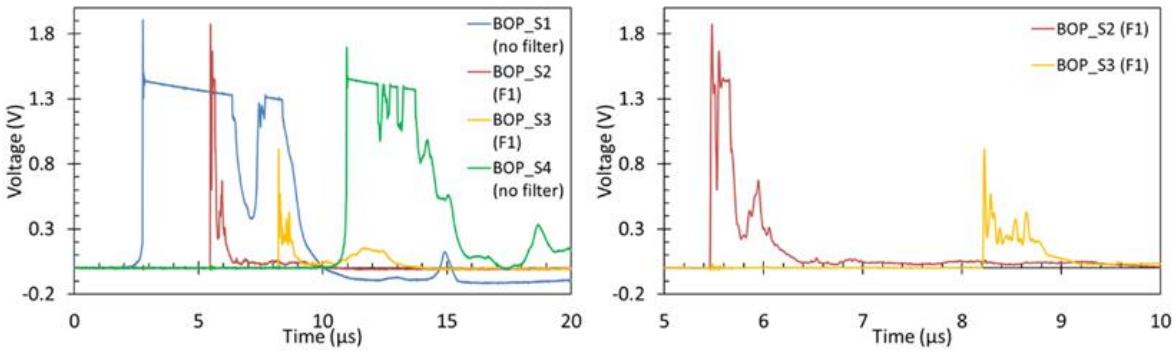

Figure 3-20: Acquired signals with passive BOPs (left) and zoom imaged (right) from the signals in which probes had filters in their ends.

Another advantage of the application of the filters on these set-ups is that is possible to make *D* tests using only one optical probe. Configuration (5) consisted of an optical fiber assembled in "S" shape, like it is shown in Figure 3-21 (left), inserted in the middle of the charge (layers of 4 mm Seismoplast above and below the optical probes). This probe was used bare and protected, connected to a filter F_1 and the acquired result is also shown in Figure 3-21 (right top for BOP, right bottom for POP).

When using one single passive BOP was possible to have a clear signal from the four well-determined positions where the BOP was passing, which was not possible before since the saturation of the previous signal would mask the beginning of the next signal, but the number of peaks close to each other with different intensities make the result impossible to read. When using POP, the signal was not so intense and clean (right bottom of Figure 3-21) like the one for BOP, maybe because the probes are not so well destroyed when protected and they still can capture light after the detonation front shock them, but it is possible to observe a pattern in the acquired peaks: after the first peak (signed with a black arrow), the following peaks lose intensity until one is more intense again (signed by the second black arrow), the following peaks lose again the intensity until appears one that is more intense again (third black arrow) after this peak appears another with high intensity, but its width makes it useless for the measurement until it appears again a peak with the same characteristics as the previous (intense and narrow, signed by the fourth black arrow). This last peak is followed by a more intense one, also narrow, but since the previous appeared first and meet the same characteristics as the previous ones, it was the one considered readable.

The times of the maximum peaks of the "S" BOP of Figure 3-21 (top right) were taken and the detonation velocity of Seismoplast was calculated by the same methods as

before (see Table 3-2 and respective description). By the least squared method, the obtained results were D = 7345 m/s and S = 0.262 mm, while the result for the mean detonation velocity was D = 7241 ± 179 m/s. Comparing these results with the ones from the experiment (3), it is possible to say that one single BOP is as efficient as 4 point-to-point BOPs to measure the D of Seismoplast, with the inconvenient of having signals with much more peaks. Considering the times indicated by the black arrows in Figure 3-21 (bottom right), when using an "S" POP, the D of Seismoplast calculated by the least square method was 7303 m/s and the S associated was 0.04 mm; the D calculated by the mean detonation velocity was 7306 ± 24 m/s. The similarity between the different D results (just 3 m/s difference) and their respective low errors associated show that, even if the signal is not so clear (but clear enough to be evaluated) and intense, the use of stainless steel tubes increase the precision in the position of the probes, which leads to more precise D results.

The use of 8 BOPs and 8 POPs connected to filters to measure detonation velocity of Seismoplast, assembled on RECs, will be detailed described in Chapter 4, but it will also be shown there that the use of protected probes increases the precision of the results.

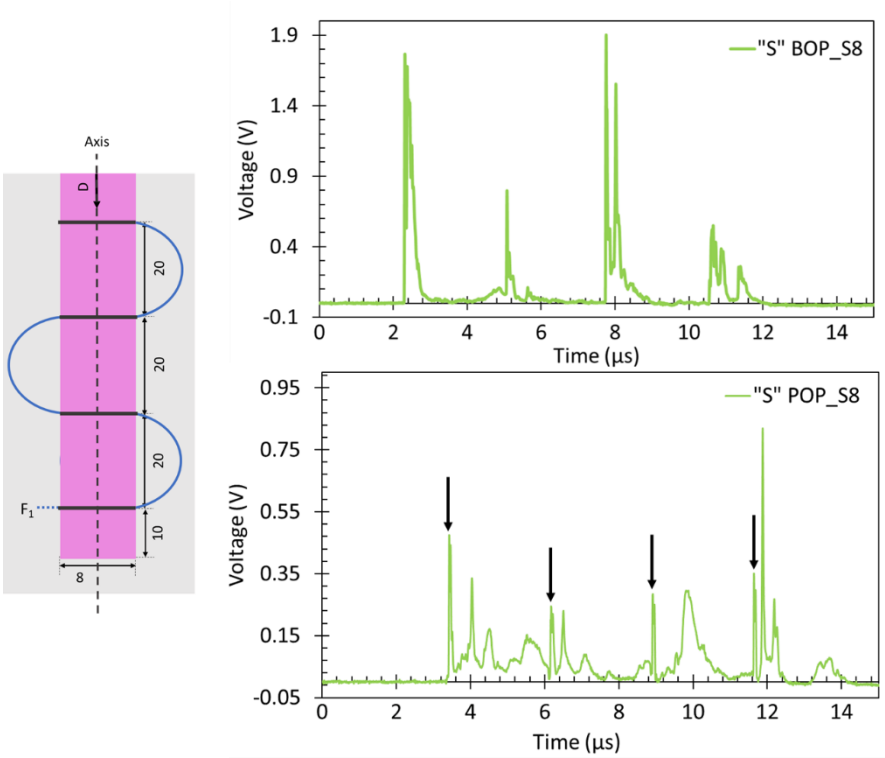

Figure 3-21: Scheme of the set-up of configuration (5) used to measure *D* with one single optical probe. Acquired results by an "S" bare (top right) and an "S" protected (bottom right) optical probe. The distances are in mm.

3.4. Optical Active Method (OAM)

The optical active method (OAM) was developed to eliminate the problems generated when acquiring detonation radiation, such as light acquisition before the instant of the shock on the probe, and uncertainties due to the most intense peak not being always correspondent to the shock's peak. Other problems, which lead to the OAM development, are that some inert materials (IMs) do not emit radiation under shock, while others are opaque, or the radiation that some IMs emit under shock is not detectable.

Since the metrology developed in this work is intended to be applied to determine different detonation parameters, where it is needed to use IMs to characterize these parameters (CJ pressure), the OAM had to be versatile enough to work under the conditions where the detonation radiation, or any other radiative phenomenon, is not useful for measurements. The OAM is so-called active because the optical fibers have active transmission of monochromatic radiation to the sensor, and it is the interruption of these transmissions that will determine the time when the DW, or the SW, is crossing the probes, which are always inserted in very well-determined positions.

The following points show the OAM development, the difficulties that it presented, and the solutions found to make the OAM a useful method.

3.4.1. Laser application to optical probes

To obtain signals that are not dependent on detonation's radiation and any other source of radiation generated by the shock of a DW, or an SW, it was needed a system where the acquired time had to be directed related to the moment when the probe is destroyed. For this, it was needed to play with the transmission abilities of the fibers and their losses when shocked. So, it was decided to transmit constant monochromatic radiation through the probes. This radiation, given by lasers with a wavelength of 660 nm, had as objective to saturate the respective sensor, to avoid the interference of external light on the signal. The signal should be acquired at the moment that the probes were shocked, so the received light had to be interrupted at that moment.

With this proposal, it was performed some experiments with configuration (6), which probes support ("U" plate) and respective experimental scheme are shown on the top of Figure 3-22. The passive (PBOPs, represented in blue) and the active (ABOPs, represented in red) bare optical probes are intercalated with each other, the length of

Seismoplast above PBOP_S1 was 60 mm and the last 20 mm were composed by the end of the detonator surrounded by Seismoplast. The active and the passive BOPs had to be intercalated to confirm if the time of the ABOPs was coherent with their positions since the OPM was giving already trustable results. At the bottom of Figure 3-22 is shown the acquired results from one of these experiments.

According to the characteristics of the sensors present in the OECSs, continuous monochromatic radiation is converted into a constant signal with 0 V, as shown by the beginning of the ABOPs signals in Figure 3-22 (bottom right). But, when the DW shocks the probes, this radiation is interrupted and the signal will have an abrupt fall down. After this fall down, the shape of the signal is dependent on the radiation that the probe is still receiving, and on the capacitor of the circuit where the sensor is integrated, but it has no relevant information for time measurements. Such signals can be observed in the bottom right of Figure 3-22.

By the set-up construction, it was expected to have the falling down of the laser signals (ABOPs) between the abrupt risings of the passive BOPs signals, but this did not happen. The acquired signals were much further in time than expected (Figure 3-22 bottom left) and they were heavily affected by the detonation radiation, since they do not fall abruptly to a minimum point, they have multiple peaks with different intensities and even new plateaus appear (most visible on ABOPs S6 and S7) until the sensor is not sensible to radiation anymore, given by the plateaus with around -1.3 V.

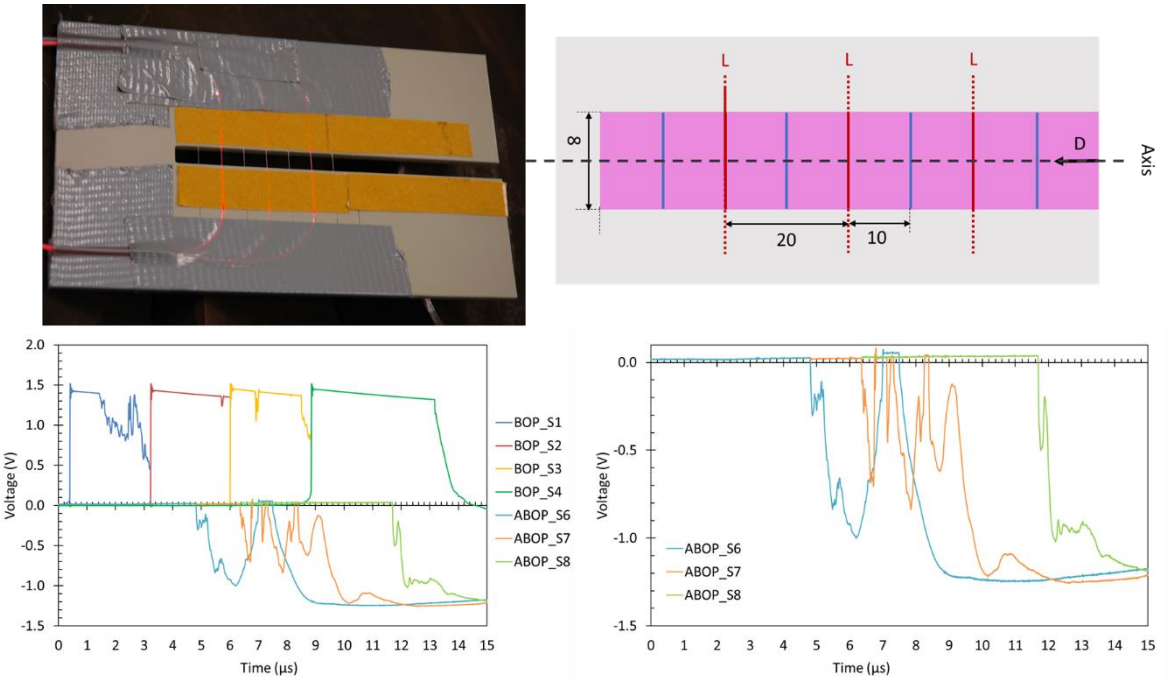

Figure 3-22: Configuration (6) - Image of an assembled "U" plate with passive and active BOPs, as well as its respective scheme (top). Acquired results and the zoomed image of the results acquired by the active BOPs (bottom). L- laser. Distances in mm.

3.4.2. Optical probes transmitting modulated laser light

The fact that the fall downs of the signals shown in Figure 3-22 did not appear in the expected times led to the idea that the sensors were saturated by the laser light and kept saturated while receiving the detonation radiation. It seems that they just started being sensible to the interruption of the light when the detonation radiation was not strong enough to saturate the sensors anymore.

To prove this theory, it was decided to modulate the laser light. In the first experiment, the configuration of the set-up was the same as the one shown in Figure 3-22 (top), but the lasers associated with the ABOPs were modulated to emit a square wave with 1 MHz frequency, with the help of a signal generator. The acquired signals by this configuration are shown in Figure 3-23.

These signals show that the detonation radiation keeps the sensors saturated, making them not sensible to the loss of the laser radiation. A clear example of this is the signal generated by ABOP_S7 (Figure 3-23 bottom left), where it was not possible to determine the instant when the DW shocks the probe. At this moment, the sensor was saturated by the laser light and kept saturated by the detonation radiation (shown by the plateau), just losing shortly its saturation at 9 µs, approximately. For the other two acquired

signals, ABOPs S6 and S8, it was possible to determine the moment when the DW shocked the probes since the acquired signals lost their shape at that moment (indicated by the dashed lines). The signal of ABOP_S6 (Figure 3-23 top right) also shows that the rise up and the saturation of signal given by the detonation radiation is very similar to the rise up and saturation of the same signal when it just shows the laser modulation, which means that both emit light with higher amplitudes than the ones of the working range of the sensors.

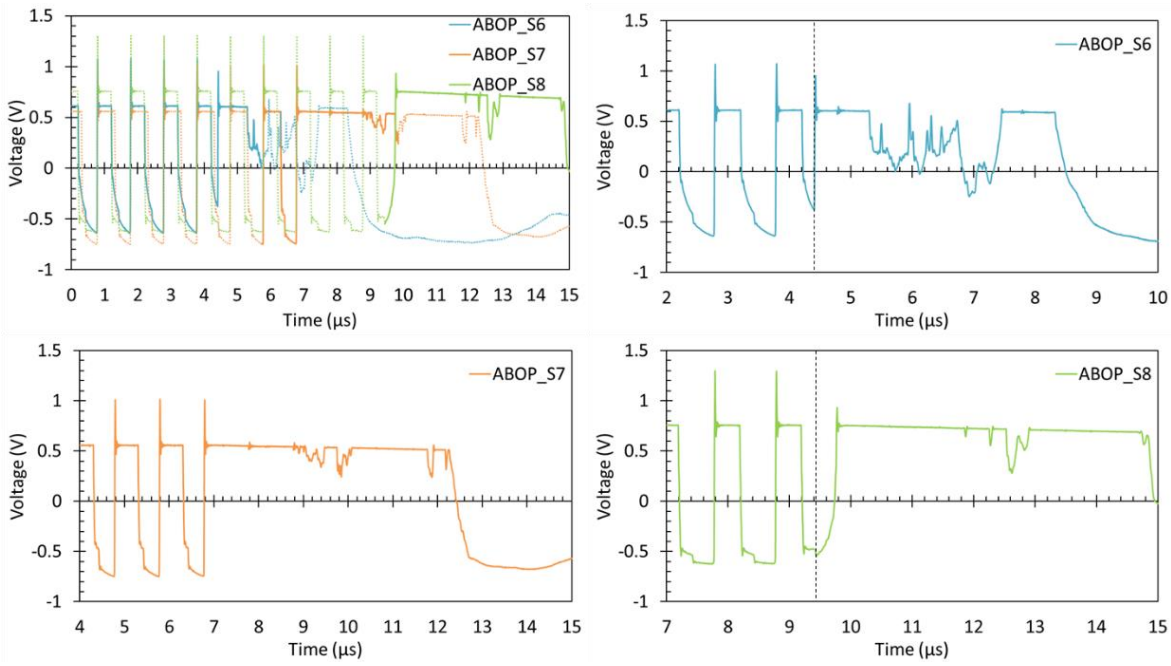

Figure 3-23: Acquired signals by the set-up shown in Figure 3-22, but with the lasers modulated as square waves with 1 MHz (top left), and images of the individual signals for better signals' visualization.

3.4.3. Filters application to optical probes transmitting modulated laser light

To use modulation on the lasers that are transmitting radiation into the probes showed to be useful to evaluate the sensors' saturation, but not good enough to determine the time when the probe is shocked. The solutions to this problem were to use a higher frequency on the lasers' modulation, to try to avoid that the moment of the destruction of the probe was coincident with the moment when the laser is emitting light, and apply filters F_1 (bandwidth between 640 and 680 nm) to reduce the detonation radiation without affecting the laser transmission. For this, configuration (6) was used, but with the lasers modulated as square waves with 2 MHz Figure 3-24 presents the acquired results only for the modulated probes, altogether (top left) and individually.

With this modulation frequency was already possible to determine the moment of the shock on the probes (given by the black dashed lines in Figure 3-24), since no shock happened at the moment that the laser radiation was saturating the sensors. The filters were very useful to separate the detonation radiation from the laser's light, which is shown by the intensity of the peaks and the shape of the signals after the DW reached the probes. At this moment, the signals lost their modulation and became an agglomeration of peaks, all of them with lower intensities than the modulated peaks.

The main objectives were reached, but the shape of the signals was still not satisfiable for time measurements, since the derivative method used to determine the times from the signals (described in chapter 4) is mostly sensible to their absolute maximums and minimums. It would be possible to use these signals to determine the *D* of Seismoplast, but it would demand much more work from the user. Another problem that this configuration presents is that the detonation radiation still has important influences under these signals.

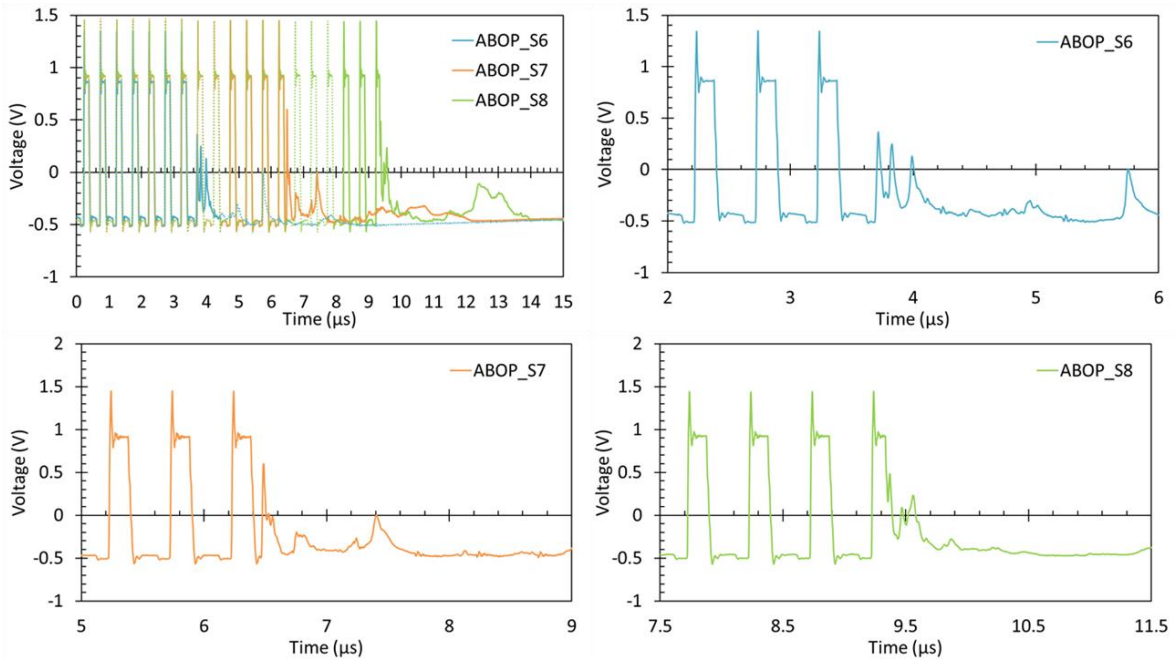

Figure 3-24: Signals from active BOPs modulated as square waves with 2MHz all together (top left) and separated. The instant where the DW shocks the probe is assigned with a black dashed vertical line.

3.4.4. Filters application to continuous laser light

Throughout this work, three different filters were used. The F_1 filters were filters LC660HBP40, centered at 660 nm and with a bandwidth of 40 nm (from Laser Components); the F_2 filters were Semrock FF01 filters centered at 650 nm and with 26 nm bandwidth (SEM-FF01-650/13-25, from Laser 2000); the filters F3 were LC660HBP20

filters, centered at 660 nm and with a bandwidth of 20 nm (LC-660HBP20-24.4 Bandpassflter, from Laser Components). The used lasers were always the same and they had their maximum intensity at 659 nm.

Figure 3-25 shows the spectroscopic measurements done to confirm the bandwidth of the filters and the emission wavelength of the lasers since the lasers' producer claimed to be 650 nm, which proved to be wrong. The wavelength of the tested laser is indicated by a black arrow.

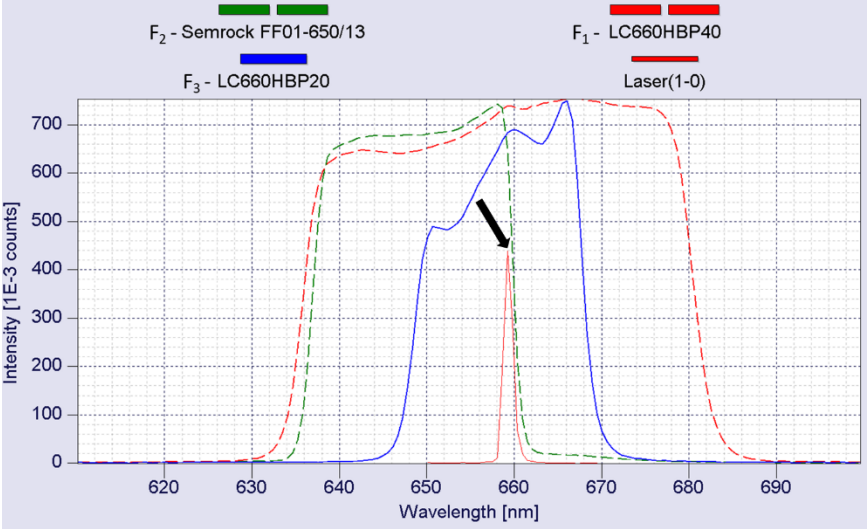

Figure 3-25: Spectroscopic measurements of one of the used lasers (red continuous line signed with a black arrow) and the three used filters.

When filters are applied on probes that are conducting continuous laser light but lose their transmission properties when shocked, the result is that the detonation light will no longer interfere in the measurements, and the obtained signal will fall from the baseline to a negative voltage, that represents the interruption of the light in the moment of the shock. Such signals can be observed in Figure 3-26. The signals represented at the bottom of Figure 3-26 are different from all the others because the capacitor C (Figure 3-7) changed from a capacity of 100 nF to 0.971 nF, to have more peak-shaped signals.

Figure 3-26 shows the results of three experiments using the three different filters. These experiments consisted of a circular cross-section explosive charge (CEC) with 15.8 mm inner diameter, length of 150 mm, with 8 active protected optical probes along its column, separated 10 mm between them.

Besides the clear differences between the shapes of the acquired signals, there are no big differences, because the filters are not so different between them. Three filters were used throughout this work because the first choice (F_1) was too wide in the passing

wavelength window, which made intense peaks very close to the fall downs. Reducing the bandwidth of the filters to F_2 already generated more clear fall downs without so intense peaks nearby. But F_2 filters presented a problem: their bandwidth limit was very close to the laser emission (see Figure 3-25) and, since the lasers' emission was not so stable, many times the laser wavelength would shift to blind part of the filter, which would make very noisy signals, or signals with false falling downs (related to the shift of the laser, not with the shock between the DW and the probe). The filters F_3 were finally chosen for having a narrow bandwidth and centered exactly at the emission wavelength of the lasers.

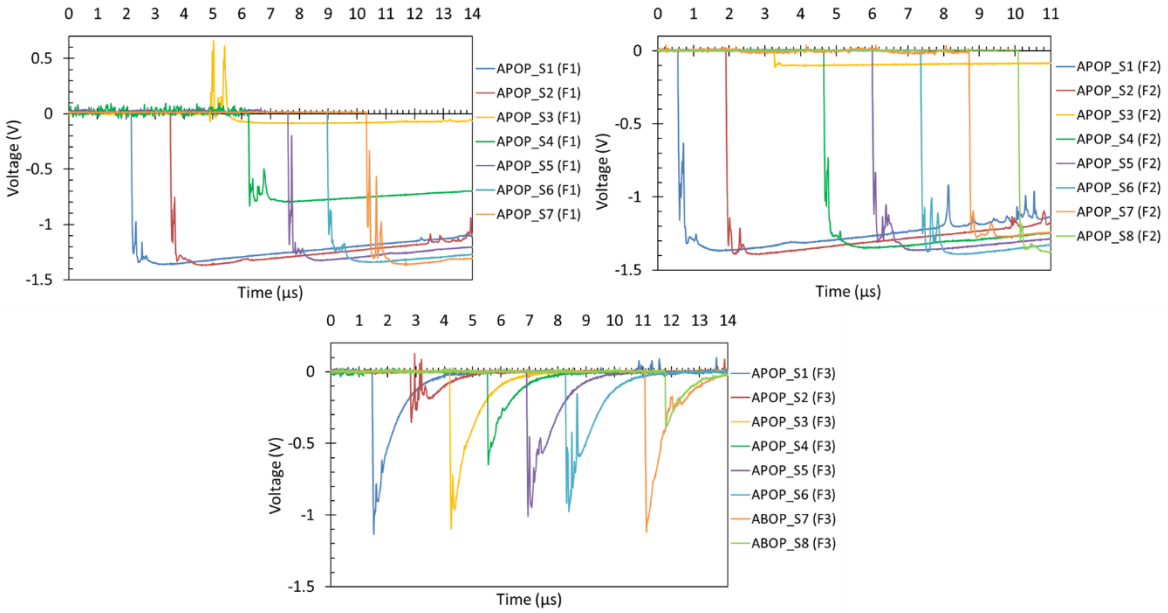

Figure 3-26: Detonation velocity signals acquired with different filters F_1, F_2, and F_3, and different capacitors C.

The *D* values of the 3 tests presented above that used POPs, which were conducting and saturating the sensors with continuous radiation, and three different filters are presented in Table 3-3. Considering that the *S* and the standard deviation associated with each measurement is relatively low, it can be considered that the effect of the filters does not affect the measurement.

Table 3-3: Determination of detonation velocity of Seismoplast for experiments that used different filters, according to two different calculation methods.

Experiment	Least Square Method		Mean Detonation Velocity	
	D (m/s)	S (mm)	D_{mean} (m/s)	$D_{std\ dv}$ (m/s)
F_1 filters	7352	0.04	7358	40
F_2 filters	7345	0.08	7350	75
F_3 filters	7343	0.09	7345	104

4. EXPERIMENTAL CHARACTERIZATION OF DETONATION VELOCITY AND PRESSURE

In the following points will be presented the thermochemical calculations performed to predict the detonation properties of Seismoplast, the measurements of detonation velocity and detonation pressure using the OAM, as well as the published papers about these measurements. The last point of this chapter will show the measurements of the *D* and the P_{CJ} of HWC and TKX-50, which are explosives that present different densities and physical forms from Seismoplast.

4.1. Seismoplast's thermochemical calculations

Computational thermochemical codes have been used to predict, between other detonation parameters, the *D* and P_{CJ} that known reactive compositions can achieve. Probably, the most known and commercially available detonation thermochemical codes are Cheetah and Explo 5 but, since the last decade of the 20th century, LEDAP has been developing its code, the so-called THOR, which is also available commercially.

In this work, Explo 5 and THOR were used to calculate detonation parameters of Seismoplast, with a special focus on the *D* and CJ pressure. P_{CJ} was the most important to predict, to have a clear idea of the expected pressures that could be obtained in experimental tests. These used thermochemical equilibrium codes will not be detailed described here, because it is not the focus of this work, and there is available literature about Explo 5 (Suceska, 1999) (Sućeska, 2001) (OZM Research, n.d.) and THOR (Durães, et al., 1996) (Duraes, et al., 1998) (Quaresma, 2013).

The chemical composition of Seismoplast used in both codes was 86% PETN and 14% Sylgard, with a density of 1.56 g/cm^3. In reality, the inert part of Seismoplast is composed of 13% silicone resin and 1% zinc stearate, but since this second compound does not exist in the database of Explo 5, neither on THOR's, and it is inert like the Sylgard, it was considered the 14% of Sylgard.

Explo 5 V6.04.02 allows the use of the BKW EoS, while THOR allows the choice of different EoS included in the program. Due to this, THOR used the BKW and the

HL EoS, the first to be comparable with Explo 5, and the second because it is adequated to work with condensed detonation products.

The results obtained by Explo 5 can be seen in Figure 4-1, where the calculated *D* of Seismoplast is 7219 m/s and its P_{CJ} is 22.1 GPa.

RESULTS OF CALCULATION:

Job title:	seismoplast	
Comment:		
Reactant density:	1.561	g/cm3
Reactant brutto formula:	C(3.771) H(7.181) N(2.361) O(7.493) Si(0.410)	
Oxygen balance:	-32.869	%
Energy of formation (at 298.15 K):	-2088.87	kJ/kg
Entalphy of formation (at 298.15 K):	-2186.17	kJ/kg
Relative molar mass:	217	

Composition of reactant is:

Ractant name:	Amount (%)
Pentrit (PETN)	86
Sylgard (silicone resin)	14

Parameters at C-J point:

Detonation parameters			Composition of detonation products							
Heat of detonation =	-5488.56	kJ/kg	(per mol of expl.)	(per kg o	(Mol %)	(per mol of expl.)	(per kg o	(Mol %)		
Detonation temperature =	3746.92	K	H2O	2.26524	10.439	29.2366	CH2O	9.6E-05	0.00044	0.0012
Detonation pressure =	22.064	GPa	CO	1.21241	5.58723	15.6481	CNO	3.2E-05	0.00015	0.0004
Detonation velocity =	7218.86	m/s	N2	1.11828	5.15344	14.4332	CHNO	2.4E-05	0.00011	0.0003
Particle velocity =	1958.02	m/s	CH2O2	0.92814	4.27721	11.9792	N	1.9E-06	8.8E-06	0
Sound velocity =	5260.84	m/s	C(d)	0.85107	3.92202	10.9844	NO2	2.9E-07	1.3E-06	0
Density of products =	2.142	g/cm3	CO2	0.66934	3.08455	8.6389	N2O	2.1E-07	9.6E-07	0
Specific volume of products	0.467	cm3/g	SiO2(s)	0.40969	1.88799	5.2877	SiO	3.9E-08	1.8E-07	0
Exponent 'Gamma' =	2.687		H2	0.10764	0.49604	1.3893	C(gr)	1.8E-09	8.3E-09	0
Moles of gaseous products	6.487	mol/mol EM	NH3	0.09518	0.43863	1.2285	SiO2(l)	9.8E-10	4.5E-09	0
Moles of condensed produc	1.261	mol/mol EM	CH4	0.04036	0.18598	0.5209	SiH4	4.6E-10	2.1E-09	0
Mean Mw of gas =	28.08	g/mol	HCN	0.02905	0.13389	0.375	SiO2	1.1E-10	4.9E-10	0
Mean Mw of condensed pro	27.633	g/mol	C2H4	0.01062	0.04895	0.1371	Si	2.7E-11	1.2E-10	0
Mean Mw of all prod. =	28.007	g/mol	C2H6	0.00894	0.04121	0.1154	SiN	1.3E-11	6E-11	0
Volume og gas at STP =	731.122	dm3/kg EM	CH3OH	0.00128	0.00592	0.0166	SiH	1.2E-13	5.3E-13	0
Internal energy of products	7405.5	kJ/kg	H	0.00028	0.0013	0.0036	Si(l)	1.6E-15	7.5E-15	0
Compression energy =	1916.94	kJ/kg	NH2	0.00018	0.00083	0.0023	Si(s)	1.4E-16	6.7E-16	0
Entropy of products) =	7.369	kJ/kg K	N2H4	0.0001	0.00048	0.0014				

Valus of other parameters:

- Compression energy of detnation products:	2.992	kJ/cm3	1916.94	kJ/kg
- Total internal energy of detonation products	11.56	kJ/cm3	7405.5	kJ/kg
- Total heat energy :	-8.568	kJ/cm3	-5488.56	kJ/kg

NOTES :

Equation of state: BKW EOS

Detonation parameters | Shock adiabat | Expansion isentrope | Expansion isentrope_JWL | Graphs

Figure 4-1: Results from Explo 5 considering the chemical composition and density of Seismoplast.

In THOR code, the detonation products were selected according to the ones that appeared at the Explo 5 calculation (composition of detonation products, Figure 4-1). The common detonation products that are presented in the calculations from both codes were: C(graf), CH_4, CO, CO_2, H, H_2, H_2O, N, N_2, and NH_3. THOR seems just to have the ability to work with a maximum of 20 detonation products, not using them all in the calculations. Explo 5 seems to generate the detonation products by itself and includes in its calculation much more and longer molecules than THOR.

The THOR calculations performed with BKW and HL EoS are shown in Figure 4-2. The *D*s obtained by BKW and HL EoS were 7668 m/s and 7666 m/s, respectively, while the CJ pressures were 20.8 GPa and 21.0 GPa, respectively.

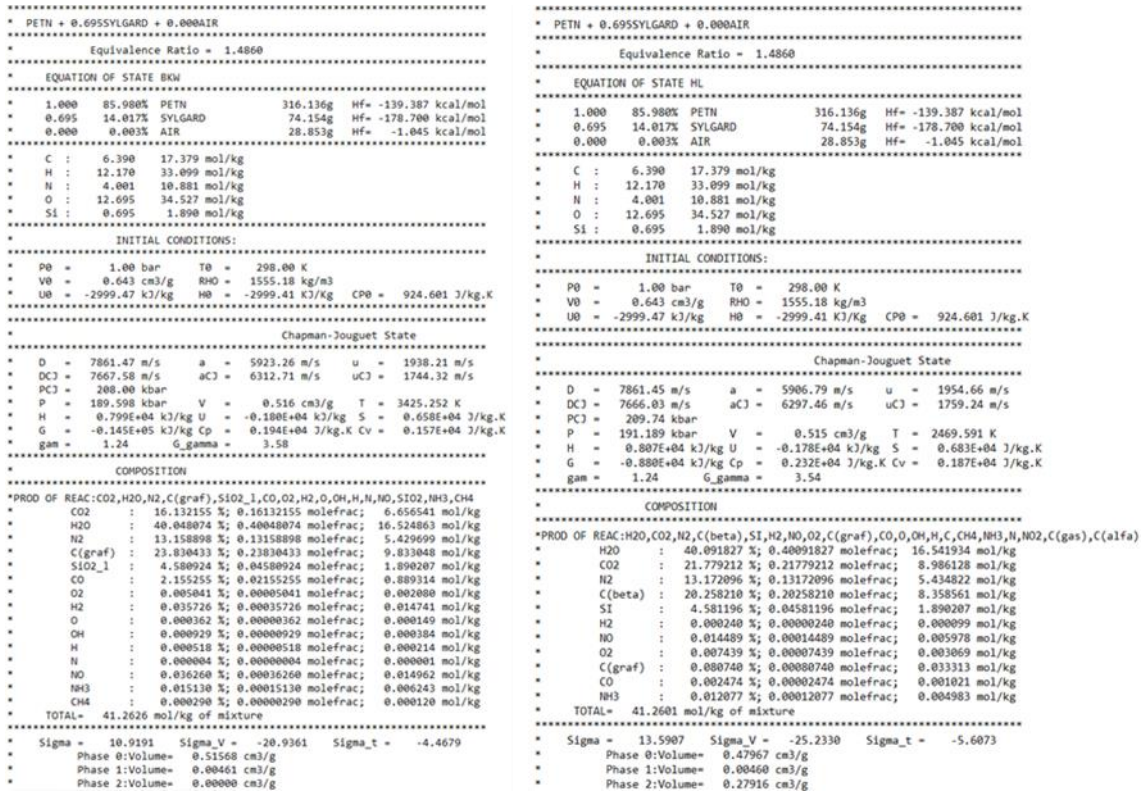

```
*  PETN + 0.695SYLGARD + 0.000AIR
*           Equivalence Ratio =  1.4860
*     EQUATION OF STATE BKW
*     1.000    85.980%  PETN              316.136g   Hf= -139.387 kcal/mol
*     0.695    14.017%  SYLGARD            74.154g   Hf= -178.700 kcal/mol
*     0.000     0.003%  AIR                28.853g   Hf=   -1.045 kcal/mol
*     C  :     6.390    17.379 mol/kg
*     H  :    12.170    33.099 mol/kg
*     N  :     4.001    10.881 mol/kg
*     O  :    12.695    34.527 mol/kg
*     Si :     0.695     1.890 mol/kg
*                INITIAL CONDITIONS:
*    P0  =      1.00 bar      T0  =    298.00 K
*    V0  =     0.643 cm3/g    RHO =   1555.18 kg/m3
*    U0  =  -2999.47 kJ/kg    H0  =  -2999.41 KJ/Kg   CP0 =   924.601 J/kg.K
*                                    Chapman-Jouguet State
*    D   =   7861.47 m/s      a   =   5923.26 m/s     u   =   1938.21 m/s
*    DCJ =   7667.58 m/s      aCJ =   6312.71 m/s     uCJ =   1744.32 m/s
*    PCJ =    208.00 kbar
*    P   =   189.598 kbar     V   =     0.516 cm3/g   T   =  3425.252 K
*    H   =    0.799E+04 kJ/kg U   =  -0.180E+04 kJ/kg  S  =   0.658E+04 J/kg.K
*    G   =  -0.145E+05 kJ/kg Cp   =   0.194E+04 J/kg.K Cv =   0.157E+04 J/kg.K
*    gam =     1.24       G_gamma =     3.58
*                COMPOSITION
*PROD OF REAC:CO2,H2O,N2,C(graf),SiO2_1,CO,O2,H2,O,OH,H,N,NO,SiO2,NH3,CH4
*         CO2       :   16.132155 %; 0.16132155 molefrac;   6.656541 mol/kg
*         H2O       :   40.048074 %; 0.40048074 molefrac;  16.524863 mol/kg
*         N2        :   13.158898 %; 0.13158898 molefrac;   5.429699 mol/kg
*         C(graf)   :   23.830433 %; 0.23830433 molefrac;   9.833048 mol/kg
*         SiO2_1    :    4.580924 %; 0.04580924 molefrac;   1.890207 mol/kg
*         CO        :    2.155255 %; 0.02155255 molefrac;   0.889314 mol/kg
*         O2        :    0.005041 %; 0.00005041 molefrac;   0.002080 mol/kg
*         H2        :    0.035726 %; 0.00035726 molefrac;   0.014741 mol/kg
*         O         :    0.000362 %; 0.00000362 molefrac;   0.000149 mol/kg
*         OH        :    0.000929 %; 0.00000929 molefrac;   0.000384 mol/kg
*         H         :    0.000518 %; 0.00000518 molefrac;   0.000214 mol/kg
*         N         :    0.000004 %; 0.00000004 molefrac;   0.000001 mol/kg
*         NO        :    0.036260 %; 0.00036260 molefrac;   0.014962 mol/kg
*         NH3       :    0.015130 %; 0.00015130 molefrac;   0.006243 mol/kg
*         CH4       :    0.000290 %; 0.00000290 molefrac;   0.000120 mol/kg
*     TOTAL=   41.2626 mol/kg of mixture
*    Sigma =    10.9191    Sigma_V =   -20.9361    Sigma_t =    -4.4679
*          Phase 0:Volume=   0.51568 cm3/g
*          Phase 1:Volume=   0.00461 cm3/g
*          Phase 2:Volume=   0.00000 cm3/g
```

```
*  PETN + 0.695SYLGARD + 0.000AIR
*           Equivalence Ratio =  1.4860
*     EQUATION OF STATE HL
*     1.000    85.980%  PETN              316.136g   Hf= -139.387 kcal/mol
*     0.695    14.017%  SYLGARD            74.154g   Hf= -178.700 kcal/mol
*     0.000     0.003%  AIR                28.853g   Hf=   -1.045 kcal/mol
*     C  :     6.390    17.379 mol/kg
*     H  :    12.170    33.099 mol/kg
*     N  :     4.001    10.881 mol/kg
*     O  :    12.695    34.527 mol/kg
*     Si :     0.695     1.890 mol/kg
*                INITIAL CONDITIONS:
*    P0  =      1.00 bar      T0  =    298.00 K
*    V0  =     0.643 cm3/g    RHO =   1555.18 kg/m3
*    U0  =  -2999.47 kJ/kg    H0  =  -2999.41 KJ/Kg   CP0 =   924.601 J/kg.K
*                                    Chapman-Jouguet State
*    D   =   7861.45 m/s      a   =   5906.79 m/s     u   =   1954.66 m/s
*    DCJ =   7666.03 m/s      aCJ =   6297.46 m/s     uCJ =   1759.24 m/s
*    PCJ =    209.74 kbar
*    P   =   191.189 kbar     V   =     0.515 cm3/g   T   =  2469.591 K
*    H   =    0.807E+04 kJ/kg U   =  -0.178E+04 kJ/kg  S  =   0.683E+04 J/kg.K
*    G   =  -0.880E+04 kJ/kg Cp   =   0.232E+04 J/kg.K Cv =   0.187E+04 J/kg.K
*    gam =     1.24       G_gamma =     3.54
*                COMPOSITION
*PROD OF REAC:H2O,CO2,N2,C(beta),SI,H2,NO,O2,C(graf),CO,O,OH,H,C,CH4,NH3,N,NO2,C(gas),C(alfa)
*         H2O       :   40.091827 %; 0.40091827 molefrac;  16.541934 mol/kg
*         CO2       :   21.779212 %; 0.21779212 molefrac;   8.986128 mol/kg
*         N2        :   13.172096 %; 0.13172096 molefrac;   5.434822 mol/kg
*         C(beta)   :   20.258210 %; 0.20258210 molefrac;   8.358561 mol/kg
*         SI        :    4.581196 %; 0.04581196 molefrac;   1.890207 mol/kg
*         H2        :    0.000240 %; 0.00000240 molefrac;   0.000099 mol/kg
*         NO        :    0.014489 %; 0.00014489 molefrac;   0.005978 mol/kg
*         O2        :    0.007439 %; 0.00007439 molefrac;   0.003069 mol/kg
*         C(graf)   :    0.080740 %; 0.00080740 molefrac;   0.033313 mol/kg
*         CO        :    0.002474 %; 0.00002474 molefrac;   0.001021 mol/kg
*         NH3       :    0.012077 %; 0.00012077 molefrac;   0.004983 mol/kg
*     TOTAL=   41.2601 mol/kg of mixture
*    Sigma =    13.5907    Sigma_V =   -25.2330    Sigma_t =    -5.6073
*          Phase 0:Volume=   0.47967 cm3/g
*          Phase 1:Volume=   0.00460 cm3/g
*          Phase 2:Volume=   0.27916 cm3/g
```

Figure 4-2: Results from THOR using the BKW EoS (left) and the HL EoS (right).

According to the thermochemical calculations performed for this work, it is expected that the *D* of Seismoplast varies between 7219 and 7668 m/s, and its CJ pressure varies between 20.8 and 22.1 GPa. The *D* and CJ pressures determined with the BKW EoS, in both thermochemical equilibrium codes, exhibit a difference of 439 m/s and 1.3 GPa, respectively. Among the possible reasons, one is related to the different values for the BKW constants (α, β, k, θ) used in both codes. EXPLO5 considers the BKWN EoS with (0.5, 0.38, 9.4, 4120), while THOR uses the BKW EoS with (0.5, β, 11.8, 400). The constant β is determined according to the richness of the mixture, varying between 0.16 (β for RDX, richness=1.5) and 0.096 (β for TNT, richness=2.75). Another reason may be related to the amount of solid carbon in the detonation products, which is almost double in THOR than is in EXPLO5, whereas the amount of SiO_2 (s) is similar in both codes.

4.2. Detonation properties of Seismoplast

The next points will present a summary of the work done to measure the detonation characteristics of Seismoplast (*D* and P_{CJ}), as well as the published papers about each parameter.

4.2.1. Detonation velocity

The following published paper (Quaresma, et al., 2020) presents some peculiarities that were observed during the testing of the passive/active optical methods to measure the detonation velocity of Seismoplast. Both methods were tested using bare optic fiber probes (BOPs) and optic fiber probes protected with a stainless steel tube (POPs). The active optical method uses a laser with a wavelength of 660 nm, and the recording system contains a window filter with a wavelength range of 650 to 670 nm. Using the passive optical method with the two different probes, the detonation velocities obtained ranged from 7233 to 7324 m/s, with standard deviations between 1.1 and 6.0 %. For the active optical method, the experimental results for detonation velocity varied between 7261 and 7351 and were obtained with a standard deviation of 0.6 to 1.7%. These results show clearly that the method that lowers the errors' amplitude of these measurements is the OAM with POPs. A detailed description of this work is presented in (Quaresma, et al., 2020).

Full Paper

Propellants, Explosives, Pyrotechnics

DOI: 10.1002/prep.201900197

Active and Passive Optical Fiber Metrology for Detonation Velocity Measurements

Joana Quaresma,*[a, b] Lukas Deimling,[a] Jose Campos,[b] and Ricardo Mendes[b]

Abstract: The reaction rate of an explosive – also called detonation velocity – is the easiest parameter to measure, and also one of the most important in characterizing the process of detonation front propagation in a 1D approach. This paper presents some peculiarities that were observed during the testing of our passive/active optical methods to measure detonation velocity. Both methods were tested using bare optic fiber probes and optic fiber probes protected with a stainless steel tube. The active optical method uses a laser with a wavelength of 660 nm, and the recording system contains a window filter that blocks any radiation outside the wavelength range of 650 to 665 nm. A plastic-bonded explosive based on PETN (seismoplast) was used to test both experimental methods. For rectangular cross-section charges using the passive optical method with the two different probes, the detonation velocities obtained ranged from 7233 to 7324 m/s, with standard deviations between 1.1 and 6.0%; for the active optical method, the experimental results for detonation velocity varied between 7261 and 7351 and were obtained with a standard deviation of 0.6 to 1.7%.

Keywords: Detonation velocity · Optical fibers · Laser light · Detonation radiation · Seismoplast

1 Introduction

Detonation velocity (D) is one of the most important properties of an explosive and has a significant influence on its performance. Various measurement methods for detonation velocity have therefore been developed to evaluate the performance of explosives [1, 2, 3]. These describe the velocity of the detonation wave (DW), which comprises a shock front followed by a chemical reaction zone where the detonation products are formed [4, 5]. Typically, this value is obtained by measuring the average velocity of the detonation wave propagation.

According to Suceska [5], the experimental methods to measure detonation velocity can be divided into four groups: 1) Dautriche method, based on the length of the detonation propagation in two different explosives in the same time interval; 2) Electrical methods, based on the short circuit between two conductors at the moment of the DW passage, which is recorded by an oscilloscope; 3) Optical methods, based on fast streak cameras that can record the radiation emitted by the detonation process; 4) Optical fiber methods, based on the ability of the optical fibers to detect and transmit light, which is the form of radiation most frequently emitted in the detonation process. This light can be recorded by high-speed cameras, or converted into an electrical signal by a fast photodiode and recorded by an oscilloscope.

As regards electrical methods, one of the first and most widely used methods to determine the average detonation velocity is based on ionization probes, in which two wires are short-circuited when the DW crosses them. This process allows the capacitor to discharge and, consequently, an electric pulse is generated on a load resistor [1, 2, 5, 6]. Another electrical method allows the detonation velocity to be measured in a continuous process, which involves a resistive electric wire [7]. According to this method, the DW propagation causes a continuous reduction in the sensor length, and thus in its electric resistance. Under constant current excitation, continuous voltage variation then occurs in one resistor (with constant electric resistance), which is in series with the probe resistor.

Regarding optical methods, the detonation velocity of seismoplast was measured through a rotating mirror streak and framing camera. [8] For this experiment, three mirrors were needed: one orientated directly to the charge, and two others at 45 degrees to the axial position (above and below it). The detonation velocity was determined through analysis of the luminescent trace acquired by the fast streak camera, where for each given time it is possible to de-

[a] *J. Quaresma, L. Deimling*
Fraunhofer-Institut für Chemische Technologie (ICT)
Joseph-von-Fraunhofer-Straße 7, 76327 Pfinztal, Germany
**e-mail: joana.quaresma@ict.fraunhofer.de*
[b] *J. Quaresma, J. Campos, R. Mendes*
LEDAP/ADAI – Department of Mechanical Engineering, University of Coimbra
Rua Luís Reis Santos, 3030–788 Coimbra, Portugal

termine the DW position. The measurement of detonation velocity using an electronic streak camera is complex and time-consuming due to the difficulty of aligning the camera and the sample. Furthermore, the acquired data always have a reduced resolution, due to reflections in many mirrors [8].

As regards optical fiber methods with high-speed electronic streak cameras, some authors have presented a non-intrusive method for continuous measurement of detonation velocity, based on 64 PMMA optical fibers, which are connected to an electronic streak camera. Each optical fiber has a diameter of 250 μm. This high-resolution optical method has a spatial resolution of 250 μm and a time resolution of 1 ns [9,10,11,12]. These measurements are very useful to determine the performance of new materials during the development of new compositions [1,9]. In this case, small samples, in the order of 1 g, can be tested [9,10]. However, this technique requires an electronic streak camera which is very expensive [3]. For the optical fiber methods which use photodiodes to convert the optical signal into an electrical signal, one of the most recent studies [13] describes an optoelectric converter system (OPTIMEX), which works with PMMA and/or silica fibers that collect the detonation radiation and transmit it to the OPTIMEX. Here the radiation is transformed into an electrical signal and then communicated to the user through an interface served by a microprocessor board, in which process useful information for the test, such as trigger modes and distances between probes, is also provided. This technique uses PMMA optical fibers with 1 mm diameter and measures the mean detonation velocity. To render the measurement method of the mean detonation velocity portable, low-cost and versatile for use in different environments – such as in the presence of magnetic fields - some authors have discussed detonation velocity measurement with single optical fibers. In all these cases, the light results from the thermal radiation of the DW [2,5,13,14,15], and/or from the shock-induced luminescence in PMMA, as described in [16].

This paper presents a newly developed and cost-effective technique based on optical fibers connected to an optoelectronic converter and to a digital recording system to measure detonation velocity. This technique was developed and characterized in two metrological configurations: (1) the optical passive method (OPM) that measures and records the rising emitting light from thermal radiation of the DW and from the shock-induced luminescence in PMMA (2) the optical active method (OAM) that measures and records the extinguishing of laser light.

To characterize the different methods and the different probes, individual and dual tests were performed. Both methods allow the operator to use two different types of probes (bare or protected). Dual tests were carried out in a single charge to compare the different probes using the same method, and to compare the different methods using the same probe.

2 Experimental Section

2.1 Explosive

The explosive used to perform these investigations was seismoplast – a plastic, water-resistant, cap-sensitive explosive based on PETN (85–86 %) and an inert binder – with a density of 1.55 g/cm^3. This value was measured for the same explosive at Fraunhofer ICT in an unpublished work (Table 1). The seismoplast was produced by Orica in Germany for seismic exploration (currently out of production) [8,17,18,19]. Few studies are reporting the detonation velocity values for this explosive, and they vary according to the authors (Table 1).

2.2 Optical System and Probe

The basic optical system was composed of 8 optical probes, which were multi-mode PMMA optical fibers with 250 μm diameter (Raytela, PGR-FB250, produced by Toray) and variable length, terminating in SMA905 connectors; or 8 optical probes based on the same optical fiber and protected with a stainless steel tube with 0.3 mm inner diameter and 0.5 mm external diameter, to fix the position and avoid undesirable bending of the fibers inside the explosive; 8 multimode silica fiber optic cable assemblies SMA to SMA, with 250 μm diameter and 20 m length; an acquisition system, developed at LEDAP, which use 8 optical to electrical converters HFBR-2406Z (sensibility between 640–820 nm, rise time of 6.3 ns, which corresponds to a maximum frequency of acquisition of 125 MHz) from Avago Technologies; and a digital transient recorder TransCom-CompactX-XL, with an

Table 1. Densities and detonation velocities of seismoplast according to bibliographic research and respective experimental method.

Reference	D (m/s)	ρ (g/cm^3)	Method
[8]	7500	NR	rotating mirror streak and framing camera
[17]	7100	1.52	X-ray absorption
[17]	7277	1.52	composite carbon resistors
[18]	7300	1.54	NR
unpublished	7380	1.55	ionization pins

NR – Not reported

Propellants, Explosives, Pyrotechnics

acquisition time of 4.2 ns, a sample rate of 240 MHz and a block size of 16 kS. According to the method used, the following were also added to the basic set up: laser lights with 660 nm wavelength, a power system and laser controls that were made at Fraunhofer ICT. Optical filters with a bandwidth between 650 and 665 nm were used to eliminate any radiation outside this window. These optical filters were inserted into cube boxes, which allowed them to have collimators in both faces.

The presented optical systems were operated according to two different methods: the optical passive (OPM) and the optical active (OAM) methods.

2.2.1 Optical Passive Method (OPM)

The OPM is based on 8 optical probes with 1.5 m length, which receive and transmit the light generated by the DW to the optical to electrical converters. In this method, two types of probes can be used: bare optical probes (BOPs – Figure 1 a), in which the optical fibers are in direct contact with the explosive, or protected optical probes (POPs), in which the optical fibers are protected with stainless steel tubes.

As will be described in section 2.3.1., the optical probes used for the OPM were placed across the charge and not on its surface (see Figure 1), as it is normally done. This was because of their ability to acquire light. As will be shown in 3.1.1, when the BOP is inside the explosive charge it acquires light before the BOP is shocked by the DW. When the top of the BOP is placed on the explosive surface, the light that crosses the fresh explosive [20, 21] saturates the sensor before the arrival of the DW, giving a high inaccuracy in the measuring times. Another reason to place the optical probes across the charge was to keep the configuration of OPM and OAM very similar, in order to easily compare the methods.

2.2.2 Optical Active Method (OAM)

The active method (OAM) measures the detonation velocity with optical probes (BOPs and POPs with 3 m length) that receive radiation from a laser. This laser radiation is saturating the sensors and, as the sensor output presents the derivative of the input, the output is presenting zero voltage. When the detonation front shocks the optical probe, it loses its transmission capabilities and, as a result, the output of the sensor drops rapidly. After that, without radiation in the sensor input, it presents again a zero voltage, since it returns to its initial "rest" position. The active method (OAM) requires the cube boxes in order to separate the laser from the detonation radiation. Figure 2 shows the OAM applied to the rectangular cross-section explosive charge configuration.

2.3 Experimental Set-Ups

Two different types of experimental set-ups were developed: the rectangular cross-section explosive charge and the circular cross-section explosive charge configurations. To shorten the names, in the following sections these configurations will be referred to as rectangular explosive charge (REC – Figure 1) and circular explosive charge (CEC – Figure 3).

2.3.1 Rectangular Cross-Section Explosive Charge Configuration (REC)

The REC set-up, presented in Figure 1, had a length of 150 mm and a rectangular cross-section of 8×8 mm, which can accommodate up to 8 optical probes.

The lateral confinement of the explosive charge was achieved with two PP plates, with a thickness of 4 mm each, and separated by 8 mm. The PP plates were glued to

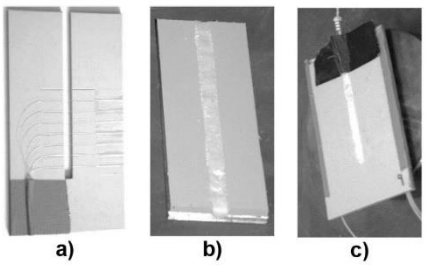

Figure 1. Experimental set-up: a) "U" plate for OPM-BOP; b) first layer of a REC; c) OAM final set-up applied to the REC.

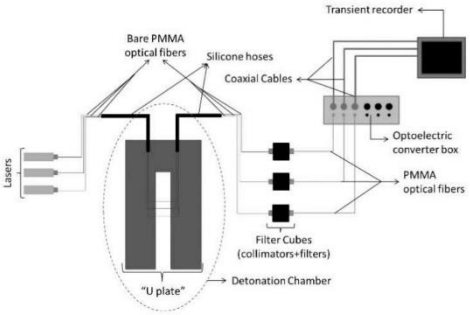

Figure 2. Schematic setup configuration for the OAM applied to the explosive charge.

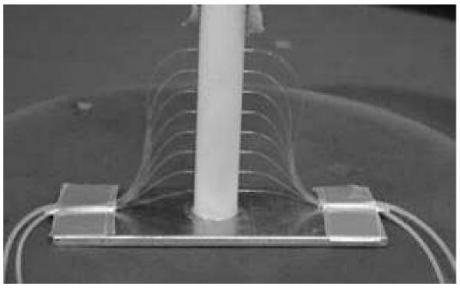

Figure 3. Experimental setup for circular cross-section explosive charge configuration with the OAM.

a metal plate and the channel between them filled with explosive (Figure 1b). The filling process was carried out manually using a tool developed for this propose. A "U" PP plate (Figure 1a), with the same thickness and an open face separation of 8 mm was glued to the PP plates (Figure 1b) and the open face separation was also filled manually with explosive (Figure 1c). Figure 1 a) shows seven PMMA BOPs with a diameter of 250 μm, inserted on slits of 0.5×0.5 mm (width and depth), passing through the open face of the "U" plate, separated by 10 mm. The optical probes fixed on the PP plate surface stay inside the explosive charge, in midplane, after the channels are filled with explosives. The final explosive charge has a cross-section of 8x8 mm and a length of 150 mm, as shown in Figure 1c). This set-up can work with both methods (OPM and OAM).

Dual tests were carried out to study one method using different probes (OPM with BOPs and POPs), and to study the different methods with the same type of probe (OPM and OAM with POPs), always simultaneously.

2.3.2 Circular Cross-Section Explosive Charge Configuration (CEC)

The CEC experimental setup, presented in Figure 3, comprises a PP tube (150 mm length, 15 mm inner diameter, 2.5 mm wall thickness) with 8 POPs separated by 10 mm. This set-up of the PP tube with the probes is prepared in the lab and then filled with explosive before the test, with tools specially developed for this propose.

The OAM was applied in a CEC set-up because this set-up is very useful to determine the detonation characteristics of explosives. This set-up will be used in the future for further measurements (such as CJ pressure and detonation front curvature).

3 Results and Discussion

This section presents the typical electrical signals obtained by the application of the OPM and OAM to measure the detonation velocity, in square or circular cross-section explosive charges.

For all electrical signals, the time when the detonation front shocks the optic probe is obtained by calculating the derivative of the electric signal and recording the time that corresponds to its maximum or minimum peak (according to the method used).

For each test, two different methods were used to calculate the mean detonation velocity (D):

1. The least-square method applied to the cumulative times and positions of the detonation front, as it propagates inside the explosive charge. In order to evaluate the precision of the different methods, the standard error of the regression line was calculated based on equation 1.

$$S = \sqrt{\frac{\sum (x - x')^2}{n - 2}} \tag{1}$$

x is the measured distance value, x' is the distance predicted value based on the linear adjustment made to the measured distances and n is the number of datasets.

2. The mean value of D_i between two consecutive probes, where D_i is calculated for each space and time interval, according to equation 2.

$$D_i = \frac{\Delta x_i}{\Delta t_i} \tag{2}$$

The mean detonation velocity (D_{mean}) presented in equation 3, as well as the standard deviation (equation 4), were calculated for all the tests.

$$D_{mean} = \frac{1}{n}\sum_{i=1}^{n} D_i \tag{3}$$

$$D_{std\ dv} = \sqrt{\frac{\sum (D_i - D_{mean})^2}{(n - 1)}} \tag{4}$$

3.1 Individual Tests

3.1.1 Acquired Signals

Using the OPM, it is possible to acquire two different types of signals, quite similar to each other, according to the type of probe used (BOPs or POPs).

Figure 4 shows the electrical signals obtained in the REC configuration using BOPs, without any transformation from

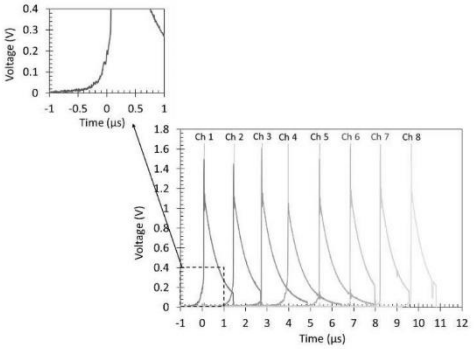

Figure 4. Electrical signals for the REC configuration, working with the OPM using BOPs and the zoom image of the initial rise of Ch1.

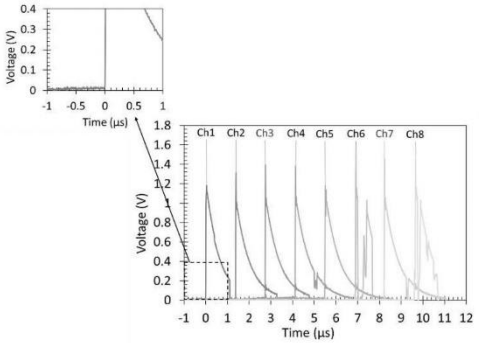

Figure 5. Electrical signals for the REC configuration, working with the OPM using POPs and the zoom image of the initial rise of Ch1.

filters and/or collimators: these signals presented a small increase in voltage (see zoom of Ch 1 in Figure 4) followed by a very fast increase, and ended with a slow decrease in voltage and then an abrupt drop. According to our understanding, the first voltage increase is due to the radiation collected by an optical probe just before it is shocked by the detonation front. The rapid increase in the voltage corresponds to the entrance of detonation radiation when the fiber is shocked, and/or to the luminescence generated in the PMMA at the moment when the fiber is shocked by the detonation front. The slow decrease in the voltage is a function of the saturation of the sensor and RC circuits constant in the output of the optoelectronic converter, and the abrupt drop corresponds to the moment when the bare optical fiber can no longer acquire radiation.

To ensure that the optic fiber probes were protected from any disturbance while placing the explosive inside the container, the optical probes were placed in stainless steel tubes (POPs). Since the inner diameter of the stainless steel tubes was 50 µm larger than the fibers' diameter, there was air between the tubes and the fibers. Figure 5 shows the electrical signals obtained by the REC configuration working with the OPM using protected optic probes (POPs).

Comparing the obtained signals in Figures 4 and 5, it can be observed that the signals in Figure 4 have a small "rising tail" (see zoom image in Figure 4), before the signals rise abruptly, while the signals in Figure 5 rise immediately (see zoom image in Figure 5) showing a very fast transition. This shows that the BOPs can collect some light slightly before the detonation front shocks the optical fiber. This phenomenon does not occur in the signals shown in Figure 5, because the fibers are protected by stainless steel tubes, so they cannot receive external radiation before being shocked. It should also be noted that the intensity of the peaks is slightly higher when the open fibers are not protected by stainless steel tubes. This shows that the fiber, when surrounded by explosives, receives DW radiation. When the fibers are protected by stainless steel tubes, the radiation acquired by the optoelectric converter is a combination of light emission by the ionization of air trapped between the optical fibers and the tubes, and the luminescense generated in the PMMA optic probe by the shock.

To be independent of radiation from the DW or from other radiation sources, and to have the possibility to use a single optical metrology method to characterize shock behavior in inert materials that are opaque, the optical active method (OAM) was developed.

Figure 6 shows the electrical signals obtained by the OAM with BOPs.

In the OAM, the optical fiber probes receive the light from a laser source. The output of these optical fiber probes is connected to the filter cubes (filters + collimators), which

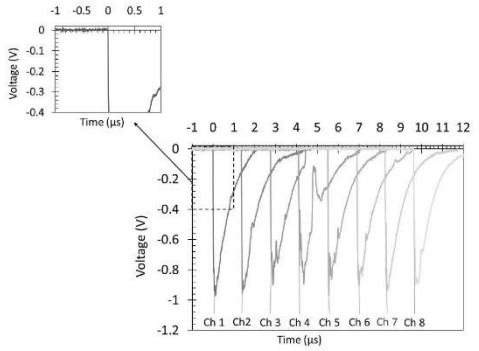

Figure 6. Electrical signals obtained by the OAM with BOPs and the zoom image of the initial drop in Ch1.

only allow laser light in a bandwidth of 650–665 nm to pass through. By this process, any interference of interfering radiation, which can come from broadband radiation source, is eliminated. After passing through the filter cubes, the optical signal is conducted to the optoelectronic converter system and transient recorder (Figure 2).

With this configuration, the electrical signals change their shape, as can be seen in Figure 6. This methodology does not work with light generated by the detonation wave but, instead, it works with the extinguishing of the laser light, due to the transmission losses of the optical fiber probe. While acquiring DW or air ionization radiation leads to increasing signals, the extinguishing of the laser light gives inverted signals, that drop abruptly immediately after the probe is shocked.

Taking a closer look at Figure 6, it is possible to see that this new type of signal starts with a zero voltage (see zoom image in Figure 6), followed by an abrupt drop, some peaks and then a slow increase, with some disturbances, until 0 V again. The zero voltage corresponds to the sensor saturation by the laser radiation, since the sensor output corresponds to the derivative of the input signal (see zoom image in Figure 6). When the fiber is shocked, it loses its transmission capabilities, which means that the sensor goes from a state of light saturation to a state of no light, leading to an abrupt drop in voltage; the peaks that are next to the abrupt drop, that disturb the relaxation of the sensor to its „rest" position, are due to detonation radiation that is between 650–665 nm, which can pass the filters and re-excite the sensors, although never back to the saturation point. The slow rise of the signal back to its initial position is characteristic of the sensors and their RC circuits.

The electrical signals obtained by the OAM using POPs are presented in Figure 7. The type of explosive charge configuration (REC or CEC) does not interfere with the shape of the acquired electrical signals. The signals shown in Figure 7 are therefore the same for CEC and REC configurations.

Comparing Figures 6 and 7 with Figures 4 and 5, it is possible to see that the signals in the OAM do not vary as much as the OPM signals, according to the different type of probe. This is because the OAM is not dependent on external radiation and the laser light is sufficient to saturate the sensors to a point that the light, which the fibers can acquire while they are not broken, is no longer detectable. The intensity of the signals depends only on the laser power (less power means less sensor saturation) and on the damage that the optical fibers can suffer while stored in their roll and while being mounted on the measuring setups.

3.1.2 Determination of the Detonation Velocity (D) by the Least Square Method

For all calculations, the measured time interval corresponds to the cumulative distances between the centers of each optical probe.

Figure 8 shows the (x, t) diagrams for the detonation front propagation for each studied configuration: REC working with the OPM with BOPs and POPs, REC working with the OAM with BOPs and POPs, and CEC working with the OAM with POPs.

Table 2 shows the slope of the linear trend lines, obtained by the least square method (Figure 8), that give us the mean detonation velocity of the detonation front propagation in a 1D approach, as well as the respective standard error of the regression lines.

As can be seen in Figure 8, all the configurations are accurate, because all the calculated detonation values are in the range of the bibliographic results presented in Table 1 (from 7100 to 7500 m/s), and precise, because the trend lines for each test are almost coincident and there are no points that fall outside the trend lines. This is confirmed by

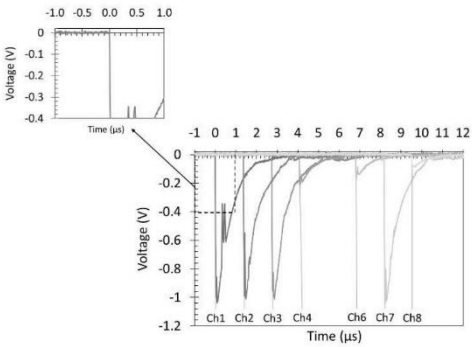

Figure 7. Electrical signals obtained by the OAM with POPs and the zoom image of the initial drop of Ch1.

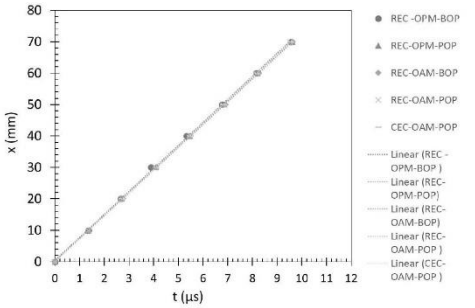

Figure 8. (x, t) diagrams for the detonation front propagation for each configuration.

Table 2. Mean detonation velocities (D), the slopes of the trend lines and the respective standard errors of the regression lines (S).

Test	X(t) slope (mm/μs)	S (mm)	D (m/s)
REC-OPM-BOP	7.324	0.613	7324
REC-OPM-POP	7.281	0.172	7281
REC-OAM-BOP	7.265	0.119	7265
REC-OAM-POP	7.351	0.075	7351
CEC-OAM-POP	7.339	0.009	7339

Table 2. The accuracy is shown by the close proximity of the calculated D values to the bibliographic ones, and the precision is shown by the S values, which represent the average distance between the measured distances and the predicted distance values based on the linear adjustment made to the measured distances. As the slits 0.5 x 0.5 ± 0.05 mm were made with a CNC machine with a dimensional tolerance of 0.05 mm, the systematic error in the distances is 0.50 mm for BOPs and 0.10 mm for POPs.

3.1.3 Measurement of the Mean Detonation Velocity (D_{mean})

Since this methodology is not cumulative, the calculation of the detonation velocity is based on time intervals and distances between two consecutive probes.

Table 3 shows the results obtained using the OPM-BOP: times ($\Delta t_{max\ peak}$), distances (Δx), results for the detonation velocity (D_i) determined according equation 2, and the mean value for the detonation velocity (D_{mean}) and standard deviation ($D_{std\ dv}$), calculated by equations 3 and 4, respectively. The results for OPM-POP, OAM-BOP, OAM-POP (all REC) and CEC-OAM-POP (D_{mean} and $D_{std\ dv}$), shown in Table 3, were calculated with the same procedure as was used for the OPM-BOP.

Comparing the values for detonation velocity obtained by the same optical method, but calculated in different ways (comparison between Tables 2 and 3) it can be seen that the mean detonation velocities do not vary more than 12 m/s between different calculations. This shows that the results are precise: we can obtain the same results from different calculations.

Table 3 also shows that the OPM is precise when using POPs because the standard deviation value is 2.4% of the mean detonation velocity value. In the case of the OPM with BOPs, the precision is lowest, because the standard deviation value is already above 5%. These are expected values because the POPs give more precision to the results than the BOPs.

The results obtained using the OAM working with BOPs and POPs, applied to both set-ups (REC and CEC) are also presented in Table 3. The parameters D_{mean} and $D_{std\ dv}$ were calculated as described for OPM-BOP and are shown in Table 3.

Once again, comparing the results in Table 2 with those in Table 3 for the same kind of test, it is possible to see that the detonation velocities vary as in the previous case (OPM). Here, the biggest variation is 13 m/s (for the REC-OAM-BOP), which is still very low since it is inside the range of the standard deviation. This proves that the OAM is also a precise method. The higher obtained standard deviation is 1.7% of the average value of the detonation velocity (REC-OAM-BOPs).

Comparing the presented measurement methods (OPM and OAM in Table 3), it can be concluded that the OAM is more precise since the standard deviations had lower values in the OAM than in the OPM.

A general overview shows that the best configuration to measure the detonation velocity is OAM-POPs because it has high precision (the D values, obtained by the two different calculations vary in a range of 11 m/s) and the lowest standard deviation errors which are between 1.1 and 1% of the mean values. It is also accurate since the obtained experimental values are inside the range of the bibliographic ones.

Table 3. Detonation velocity measured with the OPM using BOPs and POPs.

Test	Δx (mm)	$\Delta t_{max\ peak}$ (μs)	D_i (m/s)	D_{mean} (m/s)	$D_{std\ dv}$ (m/s)
REC-OPM-BOP	10.00 ± 0.500	1.371	7295	7336	441 (6.0%)
		1.296	7717		
		1.217	8220		
		1.450	6897		
		1.429	6997		
		1.383	7229		
		1.429	6997		
REC-OPM-POP				7287	178 (2.4%)
REC-OAM-BOP				7278	128 (1.7%)
REC-OAM-POP				7367	79 (1.1%)
CEC-OAM-POP				7350	75 (1.0%)

3.2 Dual Tests

To show how versatile these methodologies can be, and to make a comparison between the recorded electric signals of the two kinds of probes used (BOPs and POPs), one experiment was carried out with both kinds of probes, and another with both optical methods (dual tests). These dual tests were performed in rectangular explosive charge configuration.

In this section, each dual test will be analyzed individually and with both mathematical treatments.

3.2.1 Probes Comparison: OPM Using BOPs and POPs Simultaneously

Figure 9 shows the results obtained in a test where the detonation velocity was measured with the OPM, using BOPs and POPs simultaneously.

Analyzing Figure 9, it is possible to observe that the odd channels (with BOPs) present a higher peak voltage than the even channels (with POPs). This shows that the BOPs receive more radiation from several sources than the POPs. Besides this, all the signals are very similar.

3.2.1.1 Least Square Method Calculation (D)

Table 4 shows the results obtained from the (x, t) diagrams and respective trend lines for the detonation front propagation, in a REC working with OPM and using both type of probes simultaneously (BOPs and POPs).

This table contains the slope of the trend lines obtained for each set of points, the S values for each calculation and the mean detonation velocities calculated by the least square method, according to the probes used.

The OPM precision is shown by Table 4 through the obtained D values, which are very close to each other, only differing by 27 m/s; and also by the S values. However, it can be noted that BOPs are slightly less precise than POPs since the S value for the BOPs is higher than for the POPs. These acquired values are also accurate because they are in the range of the bibliographic values presented on Table 1 for seismoplast.

Through a comparison between individual (Table 2) and dual (Table 4) test results, it is possible to affirm that the BOPs are the least precise probes since they have the highest S values. For the dual test, the precision of BOPs is higher than for the individual test (lower S), which is explained by the larger distance between probes (10.00 mm for the individual test, double this distance for the dual test).

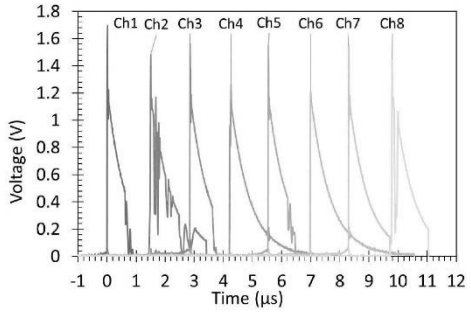

Figure 9. Signals obtained by a dual test OPM-BOP/POP. The BOPs were in channels 1, 3, 5 and 7 and the POPs were in channels 2, 4, 6 and 8.

Table 4. Mean detonation velocities (D), slopes from the equations of the trend lines and the respective standard errors of the regression lines (S). Tests performed in REC-OPM.

Test	X(t) solpe (mm/µs)	S (mm)	D (m/s)
BOPs	7.260	0.328	7260
POPs	7.233	0.196	7233

3.2.1.2 Mean Detonation Velocity Calculation (D_{mean})

Table 5 shows the results obtained for the calculation of the mean detonation velocity, with the experimental set-up using the OPM with BOPs and POPs simultaneously. In this table, the results are separated by probe type (BOPs or POPs), the space between the same kind of probe is $\Delta x = 20.00 \pm 0.050$ mm and the calculations were carried out as shown in Table 3 for OPM-BOP.

Through the analysis of the mean D in Table 5, which is acquired between two consecutive probes (now 20 mm due to the intercalation of probes), it can be demonstrated that the precision of the probes is similar since the acquired D_{mean} results varied only 7 m/s. However, POPs are more precise than BOPs, since they reduced the relative standard deviation error from 2.3 % to 1.1 %.

Comparing these results (Table 5) with the results obtained using the least square method (Table 4), the conclusions are the same: the accuracy of the probes is similar because all of them are able to produce results that match with the results already published for seismoplast (see Table 1); the precision of POPs is higher than BOPs as is proved by the S values in Table 4 and by the standard deviation errors in Table 5.

Comparing the individual (Table 3) and dual (Table 5) tests, it is clear that BOPs are less precise than POPs, since BOPs always had higher standard deviation errors than POPs, independently of the kind of test. Although, as expected, this error is lower if the probe separation is higher: it is possible to reduce the errors by half if we double the distance between the probes. With respect to accuracy, both probes can be considered accurate, since the obtained D values were always inside the range of the bibliographic values.

Table 5. Mean detonation velocity (D_{mean}) and the standard deviation ($D_{std\ dv}$) results for the OPM using BOPs and POPs simultaneously.

Test	D_{mean} (m/s)	$D_{std\ dv}$ (m/s)
REC-OPM-BOP	7244	166 (2.3 %)
REC-OPM-POP	7237	83 (1.1 %)

3.2.2. Comparison of the Methods: Simultaneous Application of the OPM and OAM Using POPs

Since it was proved before that POPs are the most precise probes, a measurement of the detonation velocity in REC, using the OPM and OAM simultaneously, was carried out with these probes. The signals obtained are shown in Figure 10.

As shown before, the signals obtained with the OPM are totally different from those obtained with the OAM: the OPM signals are rising, and the OAM signals falling. The OPM signals were already discussed above and so do not need further explanation. The OAM signals vary mostly in intensity, as shown also in Figure 7. These signal intensities are only dependent on the laser behavior (lasers lose intensity with time), and on the level of damage to the optical probe at the end of the set-up preparation. Since the optical probes are made of PMMA and are highly bendable, a little more forced bending or a little scratch are enough to cause a loss in the fiber transmission, then reducing the voltage on the falling signals.

3.2.2.1 Least Square Method Calculation (D)

Both optical methods (passive and active) using POPs were assembled to make a dual test. The obtained results were analyzed individually by method (OPM and OAM).

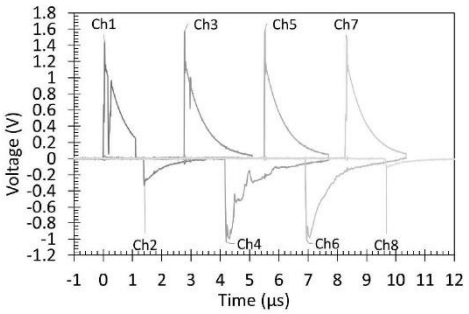

Figure 10. Signals obtained in a test with simultaneous application of OPM and OAM. The OPM-POPs are the positive signals and the OAM-POPs are the negative signals.

Table 6 presents the slope obtained from the trend lines of the acquired points, their respective S values and the obtained detonation velocity (D).

According to Table 6 the precision and the accuracy of the results do not decrease when two different optical methods, with protected optic probes, are used simultaneously in one test.

When using POPs, both methods become more precise, since the D values calculated by the least square method (Table 6) differ by only 9 m/s and the S values are similar, which shows that the precision depends more on the probe than the method.

Comparing this dual test (Table 6) with the equivalent individual tests (Table 2) with the same REC configuration, it is clear that both methods with POPs are more precise than with BOPs, because the S values vary in a small, low range (from 0.102 to 0.075 mm). All the D values obtained by the least square method are very similar (between 7252 and 7281 m/s), with the exception of the individual test REC-OAM-POPs (Table 2), where D had a slightly higher value (7351 m/s).

The accuracy of both methods in a dual test is also good because both results are inside the range of the already published results about seismoplast.

3.2.2.2 Mean Detonation Velocity Calculation (D_{mean})

As before, the mean detonation velocity calculation was also applied to the dual test using the OPM and OAM simultaneously. Table 7 shows the results (D_{mean} and $D_{std\ dv}$) of this calculation for each method, carried out as shown in Table 3. Considering the results of the mean D value presented in Table 7, it is possible to confirm the conclusions reached using the least square method calculations. Both methods are satisfactorily precise since the D_{mean} values differ by only 10 m/s.

Both methods are quite precise when using POPs since their relative errors vary between 1.1 and 0.6 %. From these results, it is possible to affirm that the OAM is more precise than the OPM, due to its very low standard deviation error (0.6 %), which is almost half of the OPM error.

Comparing this dual test (Table 7) with the equivalent individual tests (Table 3), it can be seen that the precision of the tests is mostly dependent on the distance between probes. In the dual test, the standard deviation errors are lower by approximately half when compared to the single tests, because the distance between the probes in the dual

Table 6. Mean detonation velocities (D), the slopes from the trend lines equations and their respective S values. Test performed with POPs for both OAM and OPM.

Test	X(t) slope (mm/μs)	S(mm)	D (m/s)
OPM	7.252	0.192	7252
OAM	7.261	0.102	7261

Table 7. D_{mean} and $D_{std\ dv}$ results obtained from the dual test working simultaneously with the OPM and OAM, and using the same type of probes (POPs).

Test	D_{mean} (m/s)	$D_{std\ dv}$ (m/s)
REC-OPM	7248	82 (1.1 %)
REC-OAM	7258	44 (0.6 %)

test (20.00 mm) is double the distance in the individual tests (10.00 mm). Concerning the accuracy, it is possible to affirm that all the obtained results are accurate since they all fall into the range of the literature results (Table 1).

4 Conclusions

The aim of this paper was to present precise optoelectronic metrology to measure the detonation velocity based on optical fiber probes with 250 μm diameter. This metrology can be very versatile, due to the different working methods and probes. The two different measurement methods and probes, tested in square charges of 8×8 mm, achieved good results in terms of precision and accuracy.

The OPM-BOP showed the worst S factor and standard deviation, due to the input of light before the DW shocks the probe and the possibility of bending of the probe. The OPM-POP showed positive and the OAM-BOP negative electrical signals, which indicated a very fast and precise transition due to the collision process of the DW with the probe. The electrical signals displayed comparable amplitude and both methods had a similar S factor and standard deviation.

Although the electric signals of the OAM-POP presented a precise transition, the electric signal amplitudes were not homogenous. However, the method that presented the lower standard deviation and/or S factor was the OAM-POP. The protection of the probes with stainless steel tubes also enabled an optical method capable of withstanding rough handling.

Dual tests showed that POPs had higher precision in position when compared to BOPs because their relative standard deviation errors and S values were low. The same pattern was observed in the individual tests. Dual tests also confirmed that the OAM is more precise than the OPM when used simultaneously and with the same kind of probes.

Symbols and Abbreviations

D	Detonation velocity
DW	Detonation wave
PBX	Plastic-bonded explosive
OPM	Optical passive method
OAM	Optical active method
PETN	Pentaerythritol tetranitrate or penthrite
NR	Not reported
PMMA	Poly(methyl methacrylate)
SMA	SubMiniature version A
ICT	Fraunhofer Institute for Chemical Technology
BOP	Bare optical probe
POP	Protected optical probe
REC	Rectangular cross-section explosive charge
CEC	Circular cross-section explosive charge
PP	Polypropylene
CJ	Chapman Jouguet
D_i	Local detonation velocity
D_{mean}	Mean detonation velocity
$D_{std\ dv}$	Detonation velocity standard deviation
RC	Resistance-capacity
S	Standard error of the regression line

References

[1] A. D. Tete, A. Deshmukh, R. Yerpude, Velocity of detonation (VOD) measurement techniques practical approach, *Int. J. Eng. Technol.*, **2013**, *2*, 267–265.

[2] M. Suceska, Chapter 4. Detonation, in *Test Methods for Explosives*, Springer-Veria New York **1995**, p. 91–119.

[3] P. Wei, H. L. T. Liu, D. Xia, Detonation Velocity Measurement with Chirped Fiber Bragg Grating, *Sensors* **2017**, *17*, 1–11.

[4] M. S. Shattuck, *Determination of detonation velocity of explosive compounds using optical techniques*, Master thesis, **2015**, New Mexico Institute of Mining and Technology, Socorro, New Mexico.

[5] M. Sućeska, Experimental determination of detonation velocity, *Fragblast*, **1997**, *1*, 261–284.

[6] G. O. Nevstad, *Introduction of ionization pin probes to measure detonation velocity*, FFI-rapport 2015/00178, Norwegian Defence Research Establishment, Kjeller, Norway, **2015**.

[7] R. Mendes, J. Campos, J. Gois, C. Moutinho, Shock initiation and detonation stability of industrial explosives, *24th Int. Annual Conference of ICT*, Karlsruhe, Germany, June 29–July 2, **1993**, p. 29/1–13.

[8] M. Held, Initiation Tests, *Propellants Explos. Pyrotech.* **2002**, *27*, 39–43.

[9] I. Plaksin, J. Campos, J. Ribeiro, R. Mendes, J. Gois, A. Portugal, P. Simoes, L. Pedroso, Detonation meso-scale tests for energetic materials, *Shock Compression Condens. Matter-2001*, Atlanta, Georgia, USA, June 24–29 **2001**, p. 922–925.

[10] I. Plaksin, J. Campos, P. Simoes, A. Portugal, J. Ribeiro, R. Mendes, J. Gois, Detonation study of energetic micro-samples, *Proceedings of the 12th International Detonation Symposium*, S. Diego, California, USA, August 11–16, **2002**, p. 42–50.

[11] R. Mendes, I. Plaksin, J. Campos, J. Ribeiro, Double slapper initiation of the PBX, *AIP Conf. Proc.* **1999**, *505*, 915–918.

[12] R. Mendes, J. Ribeiro, I. Plaksin, J. Campos, Non ideal detonation of emulsion explosives mixed with metal particles, *AIP Conf. Proc.* **2012**, *1426*, 267–270.

[13] J. Pachmáň, M. Künzel, K. Kubát, J. Šelešovský, R. Maršálek, M. Pospíšil, M. Kubíček, A. Prokeš, OPTIMEX: Measurement of Detonation Velocity with a Passive Optical Fibre System, *Cent. Eur. J. Energ. Mater.* **2017**, 14, 233–250.

[14] W. Xiaoyan, Z. Hui, W. Jian, W. Gao, Design of the Fiber Detonation Velocity Measuring System Based on the FPGA, *ICEOE 2011*, Dalian, Liaoning, China, July 29–31, **2011**, p. V4/29–32.

[15] J. Quaresma, J. Campos, J. Pimenta, A. Ribeiro, R. Mendes, J. Gois, L. Deimling, T. Keicher, Hot spots sensitization and optical detonation measurements of emulsion explosives, *47th Int. Annual Conference of ICT*, Karlsruhe, Germany, June 28- July 1, **2016**, p. 34/1–16.

[16] W. G. Proud, N. K. Bourne, J. E. Field, Shock-induced luminescence in polymethylmethacrylate, *AIP Conf. Proc.* **1998**, *429*, p. 801–804.

[17] K. Hollenberg, Time Resolved Pressure Measurement of the Initiation in Gap Test Experiments, *Propellants Explos. Pyrotech.* **1986**, *11*, 155–161.
[18] J. Köhler, R. Meyer, A. Homburg, Seismoplast, in: *Explosivstoffe*, 10 ed., Wiley-VCH, Weinheim **2008**, p. 263.
[19] S. Thiboutot, P. Brousseau, G. Ampleman, Deposition of PETN Following the Detonation of Seismoplast Plastic Explosive, *Propellants Explos. Pyrotech.* **2015**, *40*, 239–332.
[20] I. Plaksin, J. Direito, J. Campos, J. Ribeiro, R. Mendes, C. Cofey, J. Kennedy, Meso-scale probing of CRZ structure in PBX: DW oscillations from ignition to failure, *AIP Conf. Proc.* **2006**, 845, 1002–1005.
[21] I. Plaksin, C. S. Coffey, J. Campos, R. Mendes, J. Ribeiro, J. Gois, Shear induced reaction localization and mechanisms of energy dissipation in PBX subjected to strong shock, *AIP Conf. Proc.* **2007**, *955*, 1427–1432.

Manuscript received: June 17, 2019
Revised manuscript received: February 4, 2020
Version of record online: March 27, 2020

4.2.2. Detonation pressure

This point shows the calculations done to evaluate the P_{CJ} of Seismoplast having as base the theory presented in Chapter 1, as well as the experimental determination of this parameter.

Seismoplast is a PBX that is barely characterized in the literature, as is demonstrated by Table 1 of (Quaresma, et al., 2021). Since Seismoplast is a PETN-based explosive, bibliographic research was done about such compositions, to have an idea about its detonation pressure. This bibliographic review is presented in Table 2 of (Quaresma, et al., 2021) and, considering compositions with similar densities and/or detonation velocities to Seismoplast, it is predicted that its CJ pressure can be found between 19.8 and 24.0 GPa. Table 2 was also useful to estimate the parameter Γ of equation (1.62), which was 2.894.

The application of eq. (1.62) is a fast and rude way to predict the P_{CJ} of an explosive based on its detonation velocity and initial density, when Γ is rounded to 3. Nevertheless, considering the Γ calculated from Table 2, the density of Seismoplast (1.516 g/cm^3) and its range of D (7233 and 7351 m/s) presented in 4.2.1, eq. (1.62) predicts that the P_{CJ} of Seismoplast should be between 20.9 and 21.7 GPa.

An empiric way to estimate the P_{CJ} is to use eq. (1.67), which was proposed by Cooper relying on the experimental results of detonation parameters from many explosives. The equation (1.67) predicts that the CJ pressure of Seismoplast should be found between 22.4 and 23.2 GPa.

The computational calculations presented in 4.1, as well as in a more synthetic form in Table 4 of (Quaresma, et al., 2021), predict that the P_{CJ} of Seismoplast should be between 20.8 and 22.1 GPa. Both equations and the computational calculations give results for the P_{CJ} inside the range of the bibliographic research. The computational calculations present a very similar range to the one predicted by the equation (1.62), which is lower than the range given by equation (1.67).

The optical active method (OAM), based on PMMA optical fibers (250 μm diameter) and their radiation transmission loss when shocked, was used to characterize the detonation wave (DW) and shock wave (SW) in inert barriers and applied to measure the detonation pressure on condensed explosives. The induced shock velocities generated by Seismoplast on different thicknesses of PMMA, aluminum, and copper were measured. Based on the shock velocities at the interfaces between the explosive and the inert barriers,

the CJ pressure of Seismoplast was determined as 21.2 GPa. A detailed description of this work is presented in (Quaresma, et al., 2021)

With the obtained CJ point, where $u_{P,\,CJ}$ is 1847 m/s and P_{CJ} is 21.2 GPa, and with equation (1.68) proposed by Cooper, allowed the estimation of the Hugoniot of the detonation products (DP) of Seismoplast, as shown in Figure 4-3.

Comparing this Hugoniot DP predicted by Cooper with the poly. (interface points – Table 5) made to the interface points, it is possible to have an idea of the dispersion between the calculated interface points and the ones that would be supposed to find given the obtained CJ point. This comparison is shown in Figure 4-3. This figure shows that the calculated interface points lay very close to the ones predicted by Cooper when considering the CJ point determined in this work. To be more precise, the interface point for PMMA is slightly overestimated, while the other interface points (for Al and Cu) seem to be slightly underestimated. This can be due to the different set-up used to measure the shock velocity in inert materials, as detailed described in (Quaresma, et al., 2021).

Anyway, the calculated interface points are in agreement with the ones predicted by eq. (1.68) and the quadratic fitting is very close to the predicted Hugoniot DP of Seismoplast.

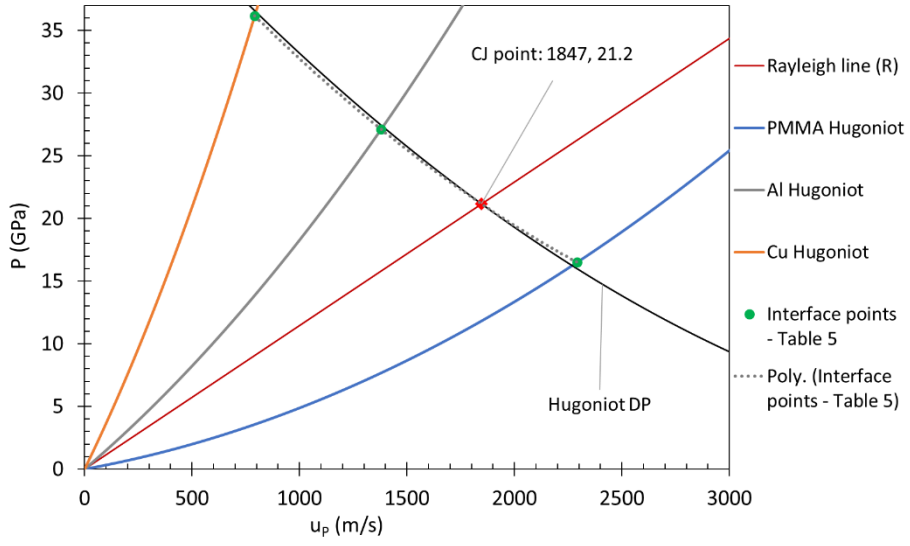

Figure 4-3: Hugoniot of the detonation products (DP) of Seismoplast predicted by eq. (1.69).

Full Paper

Propellants, Explosives, Pyrotechnics

DOI: 10.1002/prep.202000195

Characterization of the Detonation Pressure of a PETN Based PBX with the Optical Active Method

Joana Quaresma,*[a, b] Lukas Deimling,[a] Jose Campos,[b] and Ricardo Mendes[b]

Abstract: Detonation metrology is essential for the development of energetic materials, to characterize existing explosives, and to characterize materials behavior under high pressures. The optical active method (OAM), based on PMMA optical fibers (250 μm diameter) and their radiation transmission loss when shocked, was used to characterize the detonation wave (DW) and shock wave (SW) in inert barriers and applied to measure the detonation pressure in condensed explosives. The detonation velocity and detonation pressure of a PBX based on PETN (86% PETN, 14% Sylgard), known as Seismoplast were measured. The OAM with protected optical probes (POP) was used to determine the mean detonation velocity (7337 $m\,s^{-1}$), whereas the OAM with bare optical probes (BOP) was used to measure the induced shock velocities generated by Seismoplast on different thicknesses of PMMA (1–9 mm), aluminum and copper (1–7 mm). Based on the shock velocities at the interfaces between the explosive and the inert barriers, the CJ pressure of Seismoplast was determined as 21.2 GPa.

Keywords: optical active method (OAM) · detonation pressure · shock wave velocity · impedance matching technique (IMT) · PETN based explosive

1 Introduction

The detonation wave (DW) structure, according to the Zeldovich–von Neumann–Döring (ZND) model, is composed by the von Neumann or chemical spike, which corresponds to a shock front followed by a chemical reaction zone; the Chapman-Jouguet (CJ) plane; and the Taylor wave that defines the isentropic expansion of the detonation products [1,2].

In the first half of the previous century, dynamic methods based on different physical principles, to determine detonation wave parameters, were developed worldwide [3]. Despite DW velocity being a relatively easy measurement, the detonation pressure (or CJ pressure) was, and still is, one of the most relevant parameters of biggest relevance [4]. However, authors of [5] believe that the experimental determination of this parameter is not widespread and computational calculations are preferred over the experimental tests.

The experimental methods that make it possible to determine the DW parameters are divided into two major groups: the internal and external methods [3,4]. Internal methods permit the direct measurement of the DW parameters, such as the particle velocities (u_p) of the detonation products inside the explosive charge and the direct determination of CJ pressure (P_{CJ}). The former parameter and, consequently, the P_{CJ} can be measured by the electromagnetic induction method [2,5] and the X-ray method [6]. The CJ pressure can be measured directly through the insertion of manganin [2,3,5,7] and/or polyvinylidene fluoride (PVDF) [3,8] pressure gauges into the sample of the explosive.

The external methods can be divided into three groups, defined by their measuring parameter: 1) measurement of the free surface velocities of an inert material (normally, a metallic foil); 2) determination of the velocity of the shock wave (SW) in a condensed inert material in contact with the explosive; and 3) direct determination of the induced pressure profile in an inert material. For 1), techniques such as electrostatic measurements of the SW velocity in PMMA barriers [2]; an array of electric pins connected to an oscilloscope [9]; using a streak camera to record argon-filled gaps [10], or the smear camera technique [11]; laser interferometric techniques [2], like Fabry-Perot [12], VISAR [13] and photonic Doppler velocimetry (PDV) [5,14,15] are used. Group 2) comprises methods such as streak cameras that can register images of a SW in water (aquarium test) [16], a moving copper grid in PMMA [9], or they can be connected

[a] J. Quaresma, L. Deimling
Fraunhofer-Institut für Chemische Technologie (ICT)
Joseph-von-Fraunhofer-Straße 7,
76327 Pfinztal, Germany
*e-mail: joana.quaresma@ict.fraunhofer.de
[b] J. Quaresma, J. Campos, R. Mendes
University of Coimbra, LEDAP, ADAI
Department of Mechanical Engineering
Rua Luís Reis Santos, Polo II, Coimbra,
3030-788 Coimbra, Portugal

to optical fibers that are embedded in a PMMA barrier [17]; the short circuit of composite carbon-resistors embedded in a PMMA slab [18]; recording of the pulse voltages, originated by the detonation electric effect [19], with oscilloscopes; and the photoelectric method [20], where an inert liquid emits radiation proportionally to the pressure that it is being applied to it. In group 3), the induced pressure history is measured by manganin gauges embedded in thin Teflon barriers and the CJ pressure of the explosive calculated by the impedance matching technique. [7,17] The majority of these methods make it possible to determine the pressure at one point. However, determining the pressure field history $P(t)$ over a charge diameter is possible by recording the detonation wave breakout through a Kapton stack monitor with argon-filled gaps on a streak camera [21,22,23], or by a line imaging velocity interferometer [24].

The explosive used in this work was Seismoplast, a PETN (86%) based explosive normally used for civil purposes. In [18] was measured the CJ pressure of Seismoplast with composite carbon resistors. This method consists of putting two composite carbon resistors, which work as pressure transducers, into a polymethylmethacrylate (PMMA) slab. The pressures that these resistors can measure are a function of the nominal value of their resistance. These resistors are connected to a simple half-bridge circuit and their voltages are registered with an oscilloscope. The pressures are calculated, point by point, using calibration polynomials from SW experiments in water.

A device used to determine the detonation pressure based on the measurement of the SW propagation in inert materials with optical fibers, called OPTIMEX is described thoroughly in [25]. This technique is based on the measurement of the SW velocity, generated by the explosive A-IX-1 (95% RDX), on four inert materials (Al, PMMA, PA6, and PTFE). The detonation pressure was determined by the impedance matching technique. The procedure used consisted in inserting 8 glass optical fibers (1 mm diameter) in the holes drilled in the inert material, all of them at different and well-defined depths. To generate a light pulse from the ionization of the air under the influence of the SW, an air cavity between the end of the hole and the tip of the fiber was created. The arrival times of the shock wave were read from the light traces and plotted against the corresponding distances. A quadratic equation was fitted to the data sets and the initial shock velocities in inert materials at $t = 0$ s were found as the first derivatives of the fitted equation at $t = 0$ s.

Since Seismoplast was used in this study, comprehensive literature research about the detonation characteristics of Seismoplast and PETN-based explosives was carried out. Seismoplast has few studies reporting its experimental detonation characteristics, such as the detonation velocity and CJ pressure. Table 1 shows such values according to the explosive density and charge geometry. The study [18] that was found about the experimental determination of Seismoplast's CJ pressure presents values that seem to be under-evaluated for a PETN based composition. Since Seismoplast is a PETN based explosive, it was necessary to search the literature about the CJ pressures of PETN based explosives to evaluate which pressure range would be reasonable for the CJ pressure of Seismoplast. Table 2 shows these CJ pressures for PETN based explosives in different forms and compositions. It also includes the references used from the literature review, the sample's density, detonation velocity, and the technique used to determine the pressure. The "different techniques" in Table 2 include laser measurement of wave velocity, velocity electrostatic measurements of shock waves in PMMA barriers, and the indicator fluid method.

This work encompasses a methodological description of the use of the optical active method (OAM) [29] for the measurement of the shock velocities (U_S), generated by an explosive on three different inert materials-PMMA, aluminum (Al), and copper (Cu) – to determine the CJ pressure of the explosive. A mathematical approach based on the movement of the SW, according to time, through different thicknesses of an inert material ($x(t)$) was used to determine the shock velocity of the inert material/explosive interface ($U_S(l)$) that corresponds to the CJ state, which characterizes the steady-state of the detonation. Calculations with two thermochemical equilibrium detonation codes, THOR and Explo 5, were made to predict the CJ pressure of the Seismoplast.

Table 1. Densities, charge's dimensions, detonation velocities, and CJ pressures of Seismoplast according to the respective experimental techniques.

ρ_0 ($g\,cm^{-3}$)	*Ch. dim.* (mm)	D ($m\,s^{-1}$)	P_{CJ} (GPa)	*Technique*
1.52	NR	7100	14.5	X-ray absorption*
1.52	h = 30, d = 36	7277	16	Carbon resistors [18]
NR	1.5 × 1.5 3 × 3 l = 52.5	6830–7800	NR	Rotating mirror streak and framing camera [26]
1.54	NR	7300	NR	NR [27]
1.56	h = 400, d = 50	7380	NR	Ionization pins (unpub.)

* work not available. Value referred at [18] NR – Not reported; h – height; d – diameter; l – length; unpub. – Fraunhofer ICT unpublished work.

Table 2. Densities, detonation velocity and CJ pressure values of PETN and respective experimental technique.

PETN form	ρ_0 (g cm^{-3})	D (m s^{-1})	P_{CJ} (GPa)	*Technique*
Crystalline	1.66	7950	27.0	Different techniques*
	1.76	8260	30.8	
Desensitized	1.66	8120	24.0	
NR	1.703	8100	28.0	
LX-16 (96.5% w/w)	1.734	8162	27.91	Photonic Doppler Velocity [4]
LX-16 (96.5% w/w)	1.734	8162	30.7	
LX-16 (96.5% w/w)	1.734	8153	30.0	Photonic Doppler Velocity [15]
Pressed charge	1.538	7675	22.47	High-speed photography.
Pressed charge	1.568	7794	23.99	IM: Water [16]
Pressed charge	1.46	7220	19.8	Shock electric effect [28]
(99% w/w)	1.53	7490	22.5	
	1.59	7710	25.9	

IM – Inert material; * works not available. Values referred at [2].

2 Experimental Section

2.1 Explosive

This work was performed with Seismoplast, a plastic, water-resistant, cap-sensitive explosive, based on PETN (85–86%) and an inert binder, with a density of 1.562 g cm^{-3}, that was produced by Orica (Germany) for seismic exploration [18, 26, 27, 28, 30].

2.2 Inert Materials

The Hugoniot constants (C_0, s) and densities (ρ_0) of the inert materials used in this work are presented in Table 3, as well as the respective bibliographic reference.

2.3 Optical System and Probe

The optical measurement system and probes used are fully described in [29].

The optical active method (OAM) is based on PMMA multimode optical probes that transmit laser radiation with a wavelength of 660 nm and stop the transmission when the probes are subjected to a shock wave. After passing through the probe, and before the radiation is converted into a voltage signal, it passes through a window filter with a bandwidth of between 650 and 670 nm to cut all undesirable radiation. Two kinds of probes were used: bare (BOPs) and protected (POPs) optical probes. The BOPs were used to measure the shock velocities and they were in direct contact with the explosive and/or with the inert material. The POPs were protected by stainless steel tubes and were used to measure the detonation velocity.

Table 3. ρ_0, C_0, and s parameters for each inert material used.

Inert material	ρ_0 (g cm^{-3})	C_0 (m s^{-1})	s (-)	Ref.
PMMA	1.186	2598	1.516	[5]
Al (1100)	2.714	5392	1.341	[31]
Cu	8.930	3940	1.489	[31, 32]

2.4 Experimental Set-Ups

The experimental set-ups used throughout this work are shown in Figure 1. The explosive charges were encased in PVC tubes with 150 mm length, 15.8 mm inner diameter, and 2.5 mm wall thickness. Six 0.5 mm diameter holes, spaced at 10 mm were then drilled up their height, to insert POPs. The detonation velocity of Seismoplast was determined for all the tests, with 2 or 6 POPs (Figure 1). To measure the SW propagation in inert materials, two barrier configurations were used: 1) the stacks barrier (Figure 1 upper) and 2) the single barrier (Figure 1, lower). Configuration 1 had a PMMA block to support the PVC tube followed by the PMMA's stack of barriers, which were composed of three consecutive 1 mm thick plates, followed by two 2 mm thick plates, and support plate. All the PMMA plates were squares of 50 mm on all sides; each square had one slit (0.3 mm deep) on its upper face to accommodate BOPs; the BOPs slits were open at a distance of 4 mm from the center of the charge and the plates with the slits were arranged to space the slits equally between them, avoiding their superposition, as represented on the top right-hand side of Figure 1. All the experiments had an aluminum plate to support the whole set-up. Only one squared PMMA plate was used (100 × 100 mm), its thickness varied between 0.5 and 10 mm, and the two probes were crossed at the axis of the cylindrical charge, in configuration 2 (Figure 1, bottom).

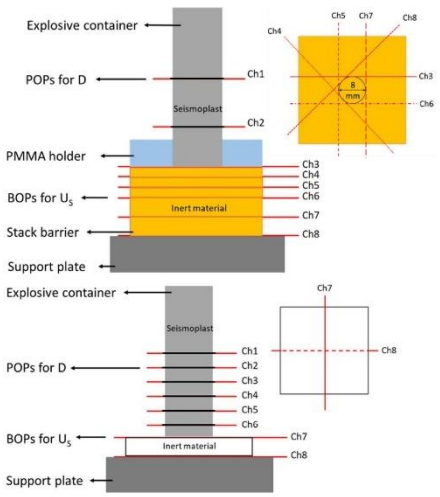

Figure 1. The configurations set-up to measure the shock velocity on inert stack barrier of PMMA, Al, and Cu (top) and a single plate (bottom).

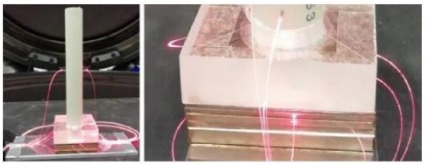

Figure 2. Complete sample assembly (left) and zoomed image (right) of a configuration 1 prepared to characterize the shock wave velocity in Cu. The PMMA block, above the Cu stack, worked as a charge holder. The active optical probes are conducting the red laser radiation.

Some experiments had slits to accommodate the probes, while others did not.

All the set-ups were prepared in the lab, only the Seismoplast was loaded manually into the container immediately before the experiment, with tools specially designed for this propose.

Configuration 1 was used for PMMA, Al, and Cu, while configuration 2 was only used for PMMA. Figure 2 shows a configuration 1 prepared to characterize the shock wave propagation in a Cu barrier.

3 Results and Discussion

The numerical calculations for the detonation velocity and CJ pressure of the Seismoplast, as well as a description of the experimental data recorded, the analysis of the shock velocity in inert barriers in terms of *x(t)* plot, and the mathematical procedures for the determination of CJ pressure, will be presented in this section.

3.1 Theoretical Predictions

Due to the lack of literature concerning Seismoplast (Table 1) and to complement the literature review for experimental data about PETN based explosives (Table 2), theoretical calculations about Seismoplast CJ pressure were made and used as reference values for comparison with the ones obtained experimentally in this work. These theoretical predictions were made resorting to two different thermochemical equilibrium detonation codes, THOR [33] and Explo 5 [34].

Table 4 presents the CJ pressures for Seismoplast determined with THOR and Explo 5 codes. Table 4 also shows the densities used in each calculation and the detonation and particle velocities predicted at the CJ point. These calculations were done for 86% PETN and 14% Sylgard (silicone resin) as the reactants. The actual composition of Seismoplast, according to [18] includes 13% of Sylgard and 1% of zinc stearate. Since the second compound is not present in THOR's database, it was substituted by Sylgard because both of them are components of the inert binder. Both codes used the BKW equation of state (EoS), except for the THOR* calculation. This was done using HL EoS [35], because this EoS is optimized on THOR [33], to work with condensed products of the reaction.

The computational data for P_{CJ} presented in Table 4 are higher than the ones for Seismoplast presented in Table 1. The experimental CJ pressure of Seismoplast in [18] seems under-evaluated for an explosive with 86% of PETN (Table 1) because, according to the literature about explosives with PETN compositions with a density and a detonation velocity similar to Seismoplast (Table 2), it is expected that the CJ pressure of such explosive composition varies between 19.8 and 23.99 GPa [28, 16].

Table 4. ρ_0, D, $u_{P,CJ}$ and P_{CJ} of Seismoplast according to the theoretical predictions.

Code	ρ_0 (g cm^{-3})	D_{CJ} (m s^{-1})	$u_{P,CJ}$ (m s^{-1})	P_{CJ} (GPa)
Explo 5	1.56	7219	1958	22.1
THOR	1.56	7670	1746	20.8
THOR*	1.56	7669	1761	21.0

* HL EoS

The computational results are shown in Table 4, which present a CJ pressure range from 20.8 to 22.1 GPa for a density of 1.56 g cm^{-3}, are more in agreement with the experimental data available for PETN based explosives (Table 2) with similar detonation velocity and density to Seismoplast.

3.2 Signal Interpretation

The signals obtained during this study for measuring the detonation and shock velocities were acquired using the OAM, whose principle is summarized at 2.3 and analyzed and described in more detail in [29].

Figure 3 displays the electrical signals generated by POPs and BOPs using the OAM, when this optical method is applied to measure the detonation pressure, according to the setup depicted in Figure 1. Channels Ch1 and Ch2 correspond to the passage of the DW through POPs 1 and 2. Channel Ch3 corresponds to the BOP inserted in the interface explosive/PMMA and channels Ch4 to Ch8 correspond to the BOPs that are between the PMMA plates. These signals obey the description made in 2.3. The electrical signals generated by the BOP's inside the Al or Cu barriers are similar to the ones obtained from the PMMA's stack of barriers and showed in Figure 3.

The abrupt break in the shape of the optoelectric signals obtained was used to identify the arrival time of the DW/SW to the probe and it was similar for all set-ups, independently of the inert material's nature (opaque, translucent, or porous) and independently of the radiation generated by the DW or by the compressed air gap, as opposed to what happed in [25], where it is stated that the shape of the optoelectric signal is dependent of the inert barrier used and the SW's ability to ionize the air in the cavity where the probe is inserted. In all the materials used (transparent and opaque), the optical active method using BOPs made it possible to identify the time instant when the probes were hit by the SW clearly without any constraints originating from the production of light

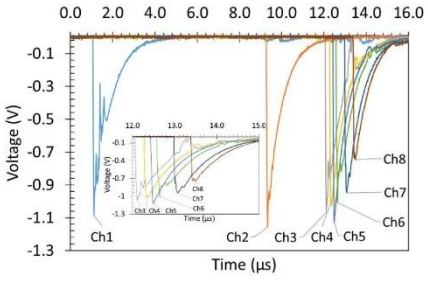

Figure 3. Electrical signals obtained for detonation velocity calculation (Ch1 and Ch2) and shock velocity calculation (from Ch3 to Ch8) in the PMMA stack monitor.

during the measurements. The time measurements were made according to [29].

3.3 Detonation Velocity

Depending on the set-up used, 2 or 6 velocity probes were used for an explosive column length of 50 mm to determine the detonation velocity (*D*). The *D* determined and used throughout this work was 7337 ± 52 m s^{-1} (associated relative error of 0.7%), and it was calculated according to equation (1), where D_i is the interval velocity value between two consecutive probes, calculated for each space (Δx_i) and time interval (Δt_i).

$$D_i = \frac{\Delta x_i}{\Delta t_i} \quad i = 0, \ldots, 5 \tag{1}$$

The displacement (Δx_i) corresponds to the distances between two consecutive probes and has a systematic error of ± 0.05 mm associated with the CNC machines used to open the slits. The time intervals (Δt_i) corresponds to the time difference between two consecutive probes, and have a systematic error of ± 4.2 ns, which is related to the temporal resolution of the transient recorder, and *i* corresponds to the interval analyzed. The recording of the times from the electric signals and the procedure to determine the detonation velocity (*D*) are described comprehensively in [29].

3.4 Detonation Pressure

The detonation pressure determination that will be presented is based on the impedance matching technique (IMT), performed to obtain the CJ pressure of Seismoplast by registering the movement of the SW along with the inert material according to time (*x(t)* plot), and the determination of the shock velocity of the Seismoplast/inert material interface ($U_S(l)$).

3.4.1 Determination of the Explosive-Inert Material Interface State

The Ch3 to Ch8 signals shown in Figure 3 make it possible to identify the time that the SW needs to reach each optical probe installed in the inert barriers and, consequently, to determine the (*x*, *t*) diagram for the SW movement. Figure 4 shows the movement of the SW generated by Seismoplast, through different thicknesses of PMMA, Al, and Cu, according to time.

The experimental points representing the propagation of SW in inert materials were fitted with a quadratic trend line to obtain the quadratic *x(t)* function that described the movement of the SW in the inert material. These fitting equations (*x(t)*) are shown in Table 5.

Table 5. Parameters calculated for PMMA, Al and Cu.

Parameter	*PMMA*	*Al*	*Cu*
$x(t)$ [mm]	$-0.638\ t^2+6.072\ t+0.076$	$-0.648\ t^2+7.242\ t+0.405$	$-0.849\ t^2+5.118t-0.03$
R^2	0.993	0.983	0.998
$U_S(I)$ [m s^{-1}]	6072	7242	5118
$u_P(I)$ [m s^{-1}]	2292	1380	791
$P(I)$ [GPa]	16.5	27.1	36.2

The shock velocity in the Seismoplast/inert material interface ($U_S(I)$) was obtained from the first derivative of $x(t)$ of each material, for t = 0 s, and they are displayed in Table 5.

After finding the interface shock velocity $U_{S,IM} = U_S(I)$, and using the C_0 and s values presented in Table 3, it was possible to calculate the particle velocity at the interface $u_{P,IM} = u_P(I)$ and the pressure $P_{IM} = P(I)$ at the Seismoplast/inert material interface according to eq. (2) and eq. (3) respectively, where the subscript *IM* means inert material.

$$U_{S,IM} = C_{0,IM} + s_{IM}u_{P,IM} \quad (2)$$

$$P_{IM} = \rho_{0,IM}U_{S,IM}u_{P,IM} \quad (3)$$

The calculated results ($u_P(I)$ and $P(I)$) for each inert material are presented in Table 5.

Considering that the loading off-axis is not 1D along the path of interest in configuration 1, some of the latter probes inserted in the inert material, suffer attenuation from the lateral release of the SW. The extension of this phenomenon depends on the ratio between the axial shock velocity and the velocity of the lateral release. This phenomenon will affect the shock velocity and the CJ pressure in a similar way as demonstrated by Bourne [36]. The errors caused by these phenomena will be evaluated in further investigations.

3.4.2 Impedance Matching Technique

Once the interface shock velocities for each inert material, as well as their respective interface pressures ($P(I)$) and particle velocities ($u_P(I)$), were obtained, it was possible to represent them graphically on the Hugoniot of each material (PMMA, Al and Cu), as it is shown on Figure 5.

Figure 5 shows the Hugoniot for each inert material, the R line, and the quadratic fitting made to the interface points. It also represents the interface state of each material after being shocked by Seismoplast, as well as the respective CJ point.

The CJ pressure was obtained as an intersection of a quadratic fit through the three interface states and the Rayleigh line. This fitting included the states above the CJ state, which are on the Hugoniot of the detonation products, as well as the states below CJ that are located at the isentropic of the detonation products. The intersection of this fitting with the Rayleigh line provided the P_{CJ}.

The CJ pressure obtained by this method was 21.2 GPa, which is very close to the results of the computational calculations.

3.5 Discussion of Results

The experimental value of the detonation pressure of Seismoplast calculated in this work was 21.2 GPa. This value is

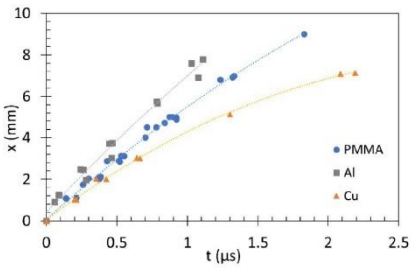

Figure 4. $x(t)$ diagrams of the shock waves generated through different thicknesses of the inert materials by Seismoplast.

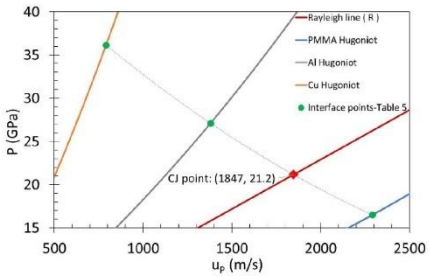

Figure 5. Determination of the CJ point of Seismoplast by fitting to the interface Seismoplast/inert material characteristic points ($P(I)$ and $u_P(I)$ values from Table 5).

significantly higher than the ones presented in Table 1. However, it is in line with the detonation pressures for the PETN based compositions presented in Table 2, for compositions that have similar densities or similar detonation velocities.

Further, the values obtained are in agreement with the computational calculations performed with different EoS and codes for Seismoplast with a density of 1.56 g/cm^3, which presents a detonation pressure range from 20.8 to 22.1 GPa. The CJ pressures determined with the BKW EoS, in both thermochemical equilibrium codes, exhibit a difference of 1.3 GPa. Among the possible reasons, one is related with the different values for the BKW constants (α, β, κ, θ) used in both codes. EXPLO5 considers the BKWN EoS with (0.5, 0.38, 9.4, 4120), while THOR uses the BKW EoS with (0.5, β, 11.8, 400). The constant β is determined according to the richness of the mixture, varying between 0.16 (β for RDX, richness = 1.5) and 0.096 (β for TNT, richness = 2.75). Another reason may be related to the amount of solid carbon in the detonation products, which is almost double in THOR than is in EXPLO5, whereas the amount of SiO_2 (s) is similar in both codes.

As previously mentioned, the SW arrival time to some of the latter probes was affected by the lateral release, in configuration 1. In future work, the errors revealed in these probes that slightly affect the $U_S(t)$, and consequently the value of the CJ pressure, will be clarified.

4 Conclusions

The optical active method (OAM) was applied to determine the detonation pressure of Seismoplast, a PETN based explosive. The experimental method was based on the analysis of the SW propagation in inert barriers, which were PMMA, Al, and Cu. Two different set-ups were used to measure the SW velocity: a single barrier and a stack of barriers.

According to the *x(t)* plot, the CJ pressure obtained by the quadratic fitting was 21.2 GPa for Seismoplast with a density of 1.56 g cm^{-3}.

All the measurement data shown in this work are in agreement with the calculations performed using the thermochemical equilibrium codes.

Symbols and Abbreviations

PETN	Pentaerythritol tetranitrate or penthrite
PBX	Plastic-bonded explosive
OAM	Optical active method
PMMA	Poly(methyl methacrylate)
DW	Detonation wave
SW	Shock wave
POP	Protected optical probe
BOP	Bare optical probe
IMT	Impedance matching technique
ZND	Zeldovich–Neumann–Döring
CJ	Chapman-Jouguet
u_P	Particle velocity
PVDF	Polyvinylidene fluoride
PDV	Photonic Doppler velocimetry
RDX	Cyclotrimethylenetrinitramine
Al	Aluminium
PA6	Polycaprolactam
PTFE	Polytetrafluoroethylene
U_S	Shock velocity
Cu	Copper
x(t)	Position of the SW according to time
D	Detonation velocity
P_{CJ}	Chapman-Jouguet pressure
ρ_0	Initial density
IM	Inert material
FPLI	Fabry-Perot Laser Interferometer
LiF	Lithium fluoride
EoS	Equation of state
C_0	Bulk sound velocity
s	Constant
D_i	Interval detonation velocity value
Δx_i	Distance
Δt_i	Time interval

Acknowledgement

Open access funding enabled and organized by Projekt DEAL.

Data Availability Statement

No Data available.

References

[1] R. E. Duff, E. Houston, Measurement of the Chapman-Jouguet Pressure and Reaction Zone Length in a Detonating High Explosive, *J. Chem. Phys.* **1955**, *23*, 1268. https://doi.org/10.1063/1.1742255.

[2] L. Al'tshuler, G. Doronin, V. Zhuchenko, Detonation regimes and Jouguet parameters of condensed explosives, *Combust. Explos. Shock Waves* **1989**, *25*, 209. Doi: 10.1007/BF00742019.

[3] M. Suceska, *Test Methods for Explosives*, Springer-Veria, New York **1995**.

[4] M. Chaos, E. L. Lee, K. T. Lorenz, Experimental Determination of Chapman-Jouguet Pressure Using Disc Acceleration eXperiment (DAX) Data, *16th International Detonation Symposium*, July 15–20, **2018**, Cambridge, MD, United States. https://www.osti.gov/servlets/purl/1465298.

[5] J. Pachman, M. Künzel, O. Ňemec, J. Majzlík, A comparison of methods for detonation pressure, *Shock Waves* **2018**, *28*, 217. https://doi.org/10.1007/s00193-017-0761–5.

[6] W. C. Rivard, D. Venable, W. Fickett, C. Davis, Flash x-ray observation of marked mass points in explosive products, *Fifth Symposium (international) on Detonation*, August 18–21, **1970**, Pasadena, California, USA.

[7] R. Mendes, J. Ribeiro, I. Plaksin, J. Campos, B. Tavares, Differences between the detonation behavior of emulsion explosives sensitized with glass or with polymeric micro-balloons, *J. Phys. Conf. Ser.* **2014**, *500*, 052030. doi:10.1088/1742-6596/500/5/052030.

[8] L. M. Lee, R. A. Graham, F. Bauer, R. P. Reed, Standartized Bauer PVDF Piezoelectric polymer shock gauge, *Le Journal de Physique Colloques* **1988**, *9*. doi: 10.1051/jphyscol:1988391.

[9] M. Held, Determination of the Chapman- Jouguet Pressure of a High Explosive from One Single Test, *Def. Sci. J.* **1987**, *37*, 1. doi: 10.1002/1521-4087(200203)27:13.0.CO;2-A.

[10] I. Plaksin, J. Campos, J. Ribeiro, R. Mendes, J. Gois, A. Portugal, P. Simoes, L. Pedroso, Detonation meso-scale tests for energetic materials, *AIP Conf. Proc.* **2002**, *620*, 922. https://doi.org/10.1063/1.1483688.

[11] W. C. Davis, B. G. Craig, Smear Camera Technique for Free-Surface Velocity Measurement, *Rev. Sci. Instrum.* **1961**, *32*, 579. https://doi.org/10.1063/1.1717443.

[12] A. V. Fedorov, A. L. Mikhailov, L. K. Antonyuk, D. V. Nazarov, S. A. Finyushin, Determination of Parameters of Detonation Waves in PETN and HMX Single Crystals, Combustion, *Explosion, and Shock Waves* **2011**, *47*, 601. doi:10.1134/S0010508211050145.

[13] V. Bouyer, M. Doucet, L. Decaris, Experimental measurements of the detonation wave profile in a TATB based explosive, *EPJ Web of Conferences* **2010**, *10*, 00030. doi:10.1051/epjconf/20101000030.

[14] J. Pachman, M. Künzel, O. Němec, S. Bland, Characterization of Al Plate Acceleration by Low Power Photonic Doppler Velocimetry (PDV), *40th International Pyrotechnics Society Seminar*, July 13–18, **2014**, Colorado Springs, Colorado USA.

[15] K. T. Lorenz, E. L. Lee, R. Chambers, A Simple and Rapid Evaluation of Explosive Performance–The Disc Acceleration Experiment, *Propellants Explos. Pyrotech.* **2015**, *40*, 95. doi:10.1002/prep.201400081.

[16] N. L. Coleburn, Chapman-Jouguet pressures of several pure and mixed explosives, United States Naval Ordnance Laboratory, White Oax, Maryland, USA, **1964**. https://apps.dtic.mil/dtic/tr/fulltext/u2/603540.pdf.

[17] R. Mendes, J. Ribeiro, I. Plaksin, J. Campos, Non ideal detonation of emulsion explosives mixed with metal particles, *AIP Conf. Proc.* **2012**, *1426*, 267. doi:10.1063/1.3686270.

[18] K. Hollenberg, Time Resolved Pressure Measurement of the Initiation in Gap Test Experiments, *Propellants Explos. Pyrotech.* **1986**, *11*, 155. doi:10.1002/prep.19860110506.

[19] B. Hayes, The Detonation Electric Effect, *J. Appl. Phys.* **1967**, *38*, 507. https://doi.org/10.1063/1.1709365.

[20] B. G. Loboiko, S. N. Lubyatinsky, Reaction Zones of Detonating Solid Explosives, *Combust. Explos. Shock Waves* **2000**, *36*, 716. https://doi.org/10.1023/A:1002898505288.

[21] I. Plaksin, J. Direito, J. Campos, J. Ribeiro, R. Mendes, C. Cofey, J. Kennedy, Meso-scale probing of CRZ structure in PBX: DW oscillations from ignition to failure, *AIP Conf. Proc.* **2006**, *845*, 1002. doi:10.1063/1.2263491.

[22] I. Plaksin, L. Rodrigues, S. Plaksin, J. Campos, R. Mendes, J. Ribeiro, J. Gois, Radiation-induced percursors in crystalline energetic composites, *AIP Conf. Proc.* **2009**, *1195*, 137. doi:10.1063/1.3295066.

[23] I. Plaksin, L. Rodrigues, S. Plaksin, J. Campos, R. Mendes, J. Ribeiro, Effect of the Reaction Light Absorption on the Formation of the Detonation Reaction Zone 3D-Structure, *14th International Detonation Symposium*, IDS **2010**, 241.

[24] P. M. Celliers, D. K. Bradley, G. W. Collins, D. G. Hicks, T. R. Boehly, W. J. Armstrong, Line-imaging velocimeter for shock diagnostics at the OMEGA laser facility, *Rev. Sci. Instrum.* **2004**, *75*, 4916. https://doi.org/10.1063/1.1807008.

[25] M. Künzel, A. C. Anastacio, J. Kucera, J. Pachman, OPTIMEX: Detonation pressure determination using passive optical system, *Proceedings of the 20th Seminar on New Trends in Research of Energetic Materials*, April 26–28, **2017**, Pardubice, Czech Republic, 726–730.

[26] M. Held, Initiation Tests, *Propellants Explos. Pyrotech.* **2002**, *27*, 39. https://doi.org/10.1002/1521-4087(200203)27:1<39::AID-PREP39>3.0.CO;2-A.

[27] J. Köhler, R. Meyer, Explosivstoffe, 10 ed., Wiley-VCH, Weinheim **2008**.

[28] H. C. Hornig, E. L. Lee, M. Finger, J. E. Kurrle, Equation of State of Detonation Products, *Fifth Symposium (international) on Detonation*, August 18–21, **1970**, Pasadena, California, USA.

[29] J. Quaresma, L. Deimling, J. Campos, R. Mendes, Active and Passive Optical Fiber Metrology for Detonation Velocity Measurements, *Propellants Explos. Pyrotech.* **2020**, *45*, 921. doi:10.1002/prep.201900197.

[30] S. Thiboutot, P. Brousseau, G. Ampleman, Deposition of PETN Following the Detonation of Seismoplast Plastic Explosive, *Propellants Explos. Pyrotech.* **2015**, *40*, 329. doi:10.1002/prep.201500019.

[31] S. P. Marsh, *LASL Shock Hugoniot Data*, University of California Press, Los Alamos **1980**.

[32] L. Davison, *Fundamentals of Shock Wave Propagation in Solids*, Springer, Berlin **2008**.

[33] J. Campos, R. Mendes, and J. Quaresma, Prediction of deflagration and detonation products properties, using THOR code procedures and parameters, *49th International Annual Conference of the Fraunhofer ICT*, June 26–29, **2018**, Karlsruhe, Germany, 7/1–7/12.

[34] M. Suceska, Evaluation of Detonation Energy from EXPLO5 Computer Code Results, *Propellants Explos. Pyrotech.* **1999**, *24*, 280. https://doi.org/10.1002/(SICI)1521-4087(199910)24:5<280::AID-PREP280>3.0.CO;2-W.

[35] L. Durães, J. Campos, J. C. Gois, New Equation of State for the Detonation Products of Explosives, *AIP Conf. Proc.* **1996**, *370*, 385. https://doi.org/10.1063/1.50802.

[36] N. K. Bourne, G. A. Cooper, S. J. Burley, V. Fung, R. Hollands, Re-Calibration of the UK Large Scale Gap Test, *Propellants Explos. Pyrotech.* **2005**, *30*, 196. doi: 10.1002/prep.200500005.

Manuscript received: August 4, 2020
Revised manuscript received: January 29, 2021
Version of record online: ■■, ■■

4.3. Detonation properties of HWC and TKX-50

The OAM was also used with two explosives in the pellets form: HWC and TKX-50. The pellets in a cylindrical form are shown in Figure 4-4. HWC is an explosive based on RDX, wax, and carbon, while TKX-50 is dihydroxylammonium 5,5′-bistetrazole-1,1′-diolate, an energetic ionic salt.

These kinds of charges were used to test the application of the metrology system to measure detonation properties, as detonation velocity, of non-malleable explosives. The containers were made out of PP (initial versions made out of Cu), had a length to insert pellets of 180 mm.

Figure 4-4: Pellets explosive charge where the darker pellets are HWC and the lighter are TKX-50.

4.3.1. HWC

4.3.1.1. Detonation velocity

Three tests with HWC pellets were performed to measure its *D*, the explosive charges were composed of 7 HWC pellets, and initiated with detonator no. 8. All the pellets (with 21 mm length and 21 mm diameter) had a slit on the top face to insert a probe, with 0.5 mm deepness. The density of all the pellets that were used on the charges was measured, and the mean value obtained was 1.683 ± 0.021 g/cm^3. The probes used in this set of experiments were active protected and bare probes (APOPS and ABOPs) connected to F_2 filters and they were all used to measure the *D* of HWC.

Figure 4-5 shows the used configurations as well as an example of each acquired result. All the signals acquired during these 3 tests were obtained with a capacitor of 100 nF at C (see Figure 3-7) installed in the optoelectric converter.

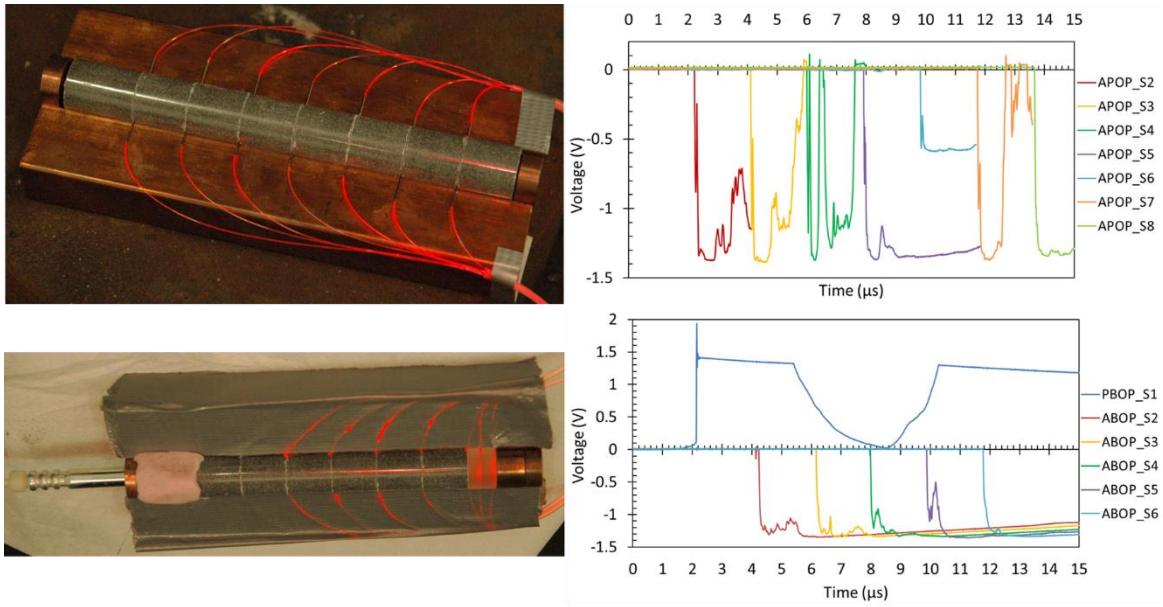

Figure 4-5: Experimental set-ups and an example of a respective acquired result.

The acquired signals during these 3 tests were all similar between them like as shown in Figure 4-5. The main difference appears to be that the protected probes presented more noise after the falling down of the signal than the bare ones. Most of the acquired signals by protected probes were more perturbed than the ones presented for Seismoplast. Nevertheless, all of the acquired signals presented the well-defined fall down, which allowed calculating the detonation velocities presented in Table 4-1. The detonation velocity of each test was determined by the two different calculations used during this work, the least square method and the mean detonation velocity, as well as their associated errors.

Table 4-1: Results of the tests performed with HWC in the three different used configurations.

Test	Least Square method		Mean Detonation Velocity	
	D (m/s)	S (mm)	D_{mean} (m/s)	$D_{std\ dv}$ (m/s)
1 - APOPs	8416	0.11	8415	46
2 - ABOPs	8575	0.24	8525	169
3 - ABOPs	8431	0.3	8457	151

In the three performed tests the values of mean D varied between 8416 and 8575 m/s. The results show that the measurement using protected probes presented the lowest standard deviation and S factor, proving that the use of protected probes ensures higher precision of the probes' positions.

The measurement of the detonation velocity of HWC charges with ionization pins was presented by (Nevstad, 2015). The HWC tested charges with 18.6 mm diameter and ρ_0 = 1.685 ± 0.008 g/cm^3 presented D = 8387 m/s , and charges with 31.8 mm diameter and ρ_0 = 1.671 ± 0.004 g/cm^3 presented a D = 8422 ± 37 m/s. Despite our values (D between 8416 and 8575 m/s for HWC charges with 21 mm diameter and a density of 1.683 ± 0.021 g/cm^3) are slightly higher than the Nevstad values. The measured values seem plausible taking into account that it can not be ensured that the composition of the charges was the same in both experiments.

The discrepancies between D values given by the different methods, presented in Table 4-1, can be associated with the damages done during the slits' preparation on the HWC pellets surface, and the different boosters used for the initiation of these experiments.

4.3.2. TKX-50

4.3.2.1. Detonation velocity

The detonation velocity of TKX-50 was measured in three tests, using the OAM. The TKX-50 pellets with 21 mm diameter, lengths of 20 and 12 mm, and an average density of 1.703 ± 0.007 g/cm^3, were assembled in PP containers, which example is shown in Figure 4-4. The density of all TKX-50 pellets was measured by the mass/volume ratio method.

The TKX-50 explosive charges were initiated with an HWC booster (90 mm long, 21 mm diameter) and a detonator no. 8. The charges were composed of 6 TKX-50 pellets, with 21 mm diameter. In the top faces of the pellets, it was opened one slit along the diameter, for probes' insertion, with 1 mm deep and 0.6 mm width. In all experiments, 6 active protected probes with F_3 filters, and the optoelectric converter with C=0.971 nF were used. Figure 4-6 shows a typical result of the voltage signals acquired from the protected probes working in the OAM.

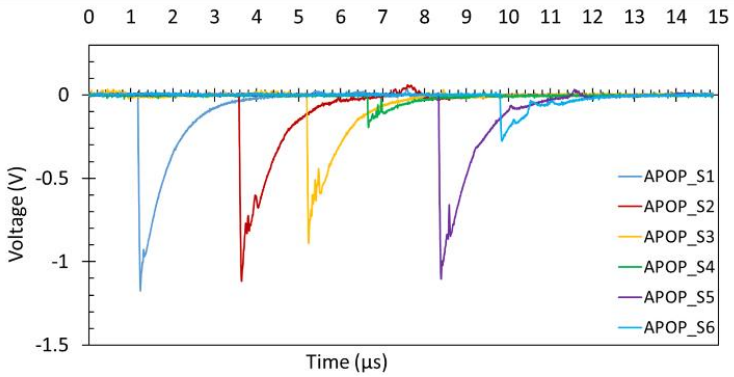

Figure 4-6: Example of the acquired signals to determine the *D* of TKX-50.

From the acquired results in these experiments was determined the average *D* of TKX-50 by two different methods, and the correspondent deviations, which are presented in Table 4-2.

Table 4-2: Densities and the detonation velocities for the tested TKX-50 charges.

Test	ρ_0 (g/cm^3)	Least Square Method		Mean Detonation Velocity	
		D (m/s)	S (mm)	D_{mean} (m/s)	$D_{std\ dv}$ (m/s)
1	1.704 ± 0.007	8076	0.2	8078	239
2	1.694 ± 0.016	7883	0.5	7915	481
3	1.710 ± 0.009	8000	0.3	7985	268

In this set of tests, the *D* of TKX-50 obtained by the LSM varied between 7883 and 8076 m/s. The detonation velocities obtained by both methods are very close between them and between each other. The associated errors to this set of measurements (*S* and $D_{std\ dv}$) are higher than the ones obtained for HWC. This set of measurements were susceptible to some unavoidable errors, like the slits were not perfectly done, having irregularities that can keep air between the probe and the explosive; the diameter of the probes was smaller than the deepness of the slits, which implied an increase on the error of the probe's position.

According to (Xing, et al., 2019), charges of 95.5 % TKX-50 and 4.5 % ETPE, with 20 mm length and 20 mm diameter, and a density of 1.79 g/cm^3 presented a *D* of 8699 m/s, while charges with 30 mm length and 30 mm diameter, and a density of 1.80 g/cm^3 presented a *D* of 8774 m/s. The presented data of detonation velocity as a function of the charge's diameter shows also, that for charges with diameters less than 40 mm, their detonation velocities were affected by the reduction of their diameters (Xing, et al., 2019).

Although (Xing, et al., 2019) indicated the method used to measure the *D*, he did not describe the experimental procedure (it is referred to neither the number of probes nor if the probes were located in a zone where the steady-state detonation was reached). This fact generates a lot of doubts about the presented results.

Since the composition and preparation of our charges and the measurement method were different from the ones used by (Xing, et al., 2019), and that the detonation process is affected by the charge's diameter used in this work (21 mm), the results presented in Table 4-2 are acceptable and relatively close to the results of (Xing, et al., 2019).

4.3.2.2. Detonation pressure

Three tests were performed with TKX-50 measured the U_S in a single plate of IM. Three plates of PMMA, with 50 x 50 mm and thicknesses of 1, 3, and 5 mm were tested. Each plate had a slit on its top face with 0.3 mm deepness. Active bare optical probes (0.250mm diameter) were used to measure the shock velocities. The used set-up can be seen in Figure 4-4, which consisted of holding a PMMA plate at the end of the charge. The measured thicknesses (Δx) and times (Δt), as well as the calculated shock velocities in PMMA, are shown in Table 4-3.

Table 4-3: Shock velocities (U_S) in PMMA originated by the detonation of TKX-50.

Test	Used probes	Δx (mm)	Δt (μs)	U_S (mm/μs)
1	ABOP8 – ABOP 7	4.95	0.754	6.565
2	ABOP8 – ABOP 7	0.95	0.117	8.112
3	ABOP8 – ABOP 7	2.95	0.442	6.674

Plotting the points shown in Table 4-3 in an (*x*, *t*) diagram, it was possible to obtain the graph presented on the left side of Figure 4-7, from which the $U_S(I)$ (U_S for t=0 s) was calculated as 6923 m/s. $u_P(I)$ and $P(I)$ were determined through the shock Hugoniot curve of PMMA, as being 2853 m/s and 23.4 GPa, respectively. Applying these values to the IMT, the obtained detonation pressure for TKX-50 pellets with 21 mm of diameter was 31.1 GPa, like is shown on the right side of Figure 4-7.

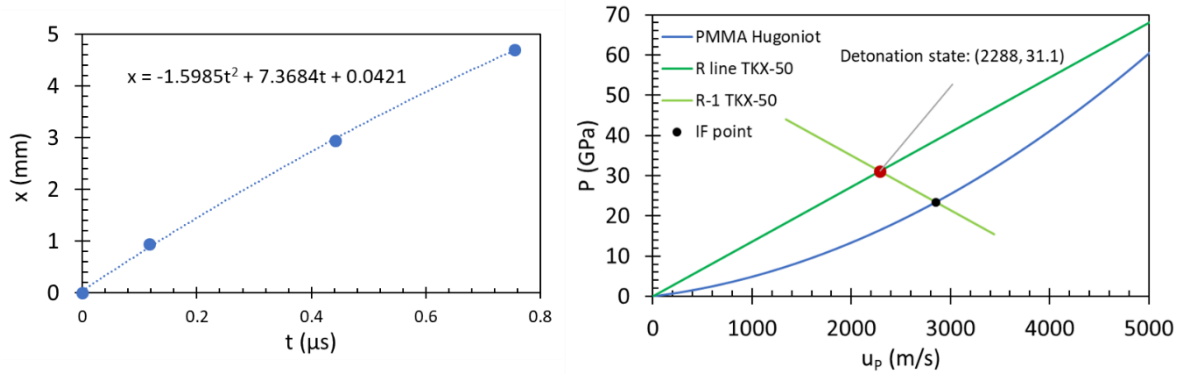

Figure 4-7: (x, t) diagram for the SW generated by TKX-50 in PMMA plates (left), and the detonation point determination by the IMT (right).

Using Cooper's equation (1.67), considering the experimental values of D (7986 m/s – mean value of the least square method of Table 4-2) and ρ_0 (1.703 g/cm^3) measured in this work, the predicted CJ pressure of TKX-50 is 29.6 GPa. Hence, the detonation pressure measured in this work for TKX-50 (31.1 GPa) is satisfactory, since it has an error of 5.3 % when compared with the value predicted by Cooper's equation.

Nevertheless, The detonation point of TKX-50 shown in Figure 4-7 is a rough estimation due to the short number of points to determine the *x(t)* plot. The PMMA plates used to perform this calculation had thin thicknesses (below 5 mm), which means that the von Neumann spike had a significant influence on these measurements. Larger thicknesses of PMMA should have been used, to attenuate the effect of the pressure peak given by the von Neumann spike and to give bigger relevance to the effect of the Taylor wave in these measurements.

In the future, HWC and TKX-50 can be properly studied with the OAM, by using the configuration presented in Figure 4-4 and the stack configuration.

5. Conclusions

The work developed in this thesis allowed the development of optical fiber metrology for the detonation characterization of energetic materials, according to the previously defined objectives. This precise optoelectronic metrology based on PMMA optical fiber probes with 250 μm diameter was applied on the measurement of detonation velocity and the detonation pressure of Seismoplast, a PETN-based explosive, and other two energetic compositions.

This metrology is versatile, due to the different used probes (bare (BOPs) and protected (POPs) optical probes) and working methods: the optical passive mode (OPM), where the detonation radiation is captured when the DW shocks the probe (transversal to the explosive charge), originating a voltage positive signal; and the optical active mode (OAM), where continuous monochromatic radiation is being conducted through the probes and a voltage negative signal is produced when the DW, or SW, shocks the probes.

The set of tests executed to measure the detonation velocity of Seismoplast with the OPM presented results that varied from 7237 and 7336 m/s, and the standard deviation errors ranged from 1.1 to 6%; while with the OAM these values varied between 7261 and 7351 m/s, and the standard deviation errors ranged from 0.6 to 1.7%. The OPM-BOP showed the worst *S* factor and standard deviation, due to the input of light before the DW shocks the probe and the possibility of bending of the probe; while the OAM method presented detonation velocities that varied between 7258 and 7367 m/s, and the lower standard deviations and/or *S* factors. The protection of the probes with stainless steel tubes also enabled an optical method capable of withstanding rough handling.

The optical active method (OAM) was also applied to determine the detonation pressure of the Seismoplast. The experimental method was based on the analysis of the SW propagation in inert barriers, which were PMMA, Al, and Cu. According to the impedance matching technique applied to the explosive/inert material interfaces for the three tested materials and the quadrating fitting to the referred points in the (P, u_P) plane, the CJ pressure obtained was 21.2 GPa, for Seismoplast with a density of 1.56 g/cm^3.

All the measurement data shown in this work for Seismoplast are in agreement with the calculations performed using the thermochemical equilibrium codes, as well as with the empirical equations.

The OAM was applied to another two energetic compositions. The detonation velocity of HWC, an RDX-based explosive with a density of 1.683 g/cm^3, was determined with protected and bare optical probes. The mean detonation velocity of this explosive varied between 8415 and 8525 m/s, where the protected optical probes had a special relevance in reducing the errors of the measurement.

TKX-50, an energetic ionic salt in the form of pellets with a density of 1.703 g/cm^3, was characterized with the OAM. Protected optical probes were used to determine its detonation velocity, which varied between 7883 and 8076 m/s, according to the least square method. Bare optical probes were used to determine the shock velocity generated by TKX-50 in PMMA plates (thicknesses of 1, 3, and 5 mm). With the shock velocity and the impedance matching technique, the CJ pressure of TKX-50 was estimated as 31.1 GPa.

6. BIBLIOGRAPHY

Agrawal, J. P., 2010. *High Energy Materials - Propellants, Explosives and Pyrotechnics.* Weinheim: WILEY-VCH Verlag GmbH & Co. KGaA.

Al'tshuler, L., Doronin, G. & Zhuchenko, V., 1989. Detonation regimes and Jouguet parameters of condensed explosives. *Combust Explos Shock Waves,* Volume 25, pp. 209-224.

Anderson, A. B., Ginsberg, M. J., Seitz, W. L. & Wackerle, J., 1981. *Shock initiation of porous TATB.* Annapolis, Maryland, USA, s.n., pp. 385-392.

Avago Technologies, 2014. *DatasheetsPDF.com.* [Online]
Available at: https://datasheetspdf.com/pdf-file/930954/Avago/HFBR-2406Z/1
[Acedido em 2017].

Barbarin, Y. et al., 2020. Development of a Shock and Detonation Velocity Measurement System Using Chirped Fiber Bragg Gratings. *Sensors,* Volume 20, pp. 1026-1056.

Barbarin, Y. et al., 2015. Optimization of detonation velocity measurements using a Chirped Fiber Bragg Grating. p. 94800S.

Barker, L. M. & Hollenbach, R. E., 1972. Laser interferometer for measuring high velocities of any reflecting surface. *Journal of Applied Physics,* 43(11), pp. 4669-4675.

Bauer, F., 1983. PVF2 polymers: Ferroelectric polarization and piezoelectric properties under dynamic pressure and shock wave action. *Ferroelectrics,* 49(1), pp. 231-240.

Bauer, F., 1999. *Advances in Piezoelectric PVDF Shock Compression Sensors.* Delphi, Greece, s.n., pp. 647-650.

Bourne, N. K. et al., 2005. Re-Calibration of the UK Large Scale Gap Test. *Propellants Explos. Pyrotech.,* 30(3), pp. 196-198.

Bouyer, V., Doucet, M. & Decaris, L., 2010. Experimental measurements of the detonation wave profile in a TATB based explosive. *EPJ Web of Conferences,* Volume 10, p. 00030.

Bouyer, V. et al., 2009. Experimental measurements of the chemical reaction zone of detonating liquid explosives. *AIP Conference Proceedings,* Volume 1195, pp. 177-180.

Brousseau, P., Dorsett, H. E., Cliff, M. D. & Anderson, C. J., 2002. *Deonation properties of explosives containing nanometric aluminum powder.* Wyndham San Diego, s.n., pp. 1-10.

Chaos, M., Lee, E. L. & Lorenz, K. T., 2018. *Experimental Determination of Chapman-Jouguet Pressure Using Disc Acceleration eXperiment (DAX) Data.* Cambridge, MD, United States, s.n., pp. 1-7.

Coleburn, N. L., 1964. *Chapman-Jouguet pressures of several pure and mixed explosives,* White Oax, Maryland, USA: United States Naval Ordnance Laboratory.

Cook, M. A., Doran, R. L. & Morris, G. J., 1955. Measurement of Detonation Velocity by Doppler Effect at Three-Centimeter Wavelength. 26(4), pp. 426-428.

Cook, M. A., Keyes, R. T. & Ursenbach, W. O., 1962. Measurements of Detonation Pressure. *Journal of Applied Physics,* 33(12), pp. 3413-3420.

Cooper, P. w., 1996. *Explosives Engineering.* New Yorck; Chichester; Weinheim; Brisbana; Toronto: Wiley-VCH.

Cowperthwaited, M. & Rosenberg, J. T., 1983. *Lagrange gage studies of nonideal explosives containing NH4NO3,* Research Triangle Park, North Carolina: U.S. Army Research Office.

Cowperthwaite, M. & Rosenberg, J. T., 1981. *Lagrange gage studies in ideal and non-ideal explosives.* Annapolis, Maryland, s.n., pp. 1072-1083.

Cybulski, W. B., Payman, W. & Woodhead, D. W., 1949. Explosion Waves and Shock Waves. VII. The Velocity of Detonation in Cast T.N.T.. *Proceedings of the Royal Society of London. Series A, Mathematical and Physical Sciences,* 197(1048), pp. 51-72.

D. Tete, A., Deshmukh, A. Y. & Yerpude, R. R., 2013. Velocity of detonation (VOD) measurement techniques practical approach. *International Journal of Engineering and Technology,* 2(3), pp. 259-265.

Davis, W. & Fauquignon, C., 1995. Classical Theory of Detonation. *Journal de Physique IV Colloque,* 05((C4)), pp. C4-3-C4-21.

Deal, W. E., 1957. Measurement of Chapman-Jouguet Pressure for Explosives. *J. Chem. Phys.,* 27(3), pp. 796-800.

Dolan, D. H. & Specht, P., 2017. VISAR Analysis in the Frequency Domain. *J. dynamic behavior mater.,* Volume 3, pp. 407-411.

Dolgoborodov, A. Y. et al., 2005. Detonation in an Aluminum–Teflon Mixture. *JETP Letters,* 81(7), pp. 311-314.

Dremin, A. N., 1999. *Toward Detonation Theory.* New York: Springer-Verlag.

Duff, R. E. & Houston, E., 1955. Measurement of the Chapman-Jouguet Pressure and Reaction Zone Length in a Detonating High Explosive. *J. Chem. Phys.,* 23(7), pp. 1268-1273.

Duffy, T. S. & Ahrens, T. J., 1994. Free surface velocity profiles in molybdenum shock compressed at 1400 °C. *AIP Conference Proceedings,* Volume 309, pp. 1079-1082.

Durães, L., Campos, J. & Gois, J. C., 1996. New Equation of State for the Detonation Products of Explosives. *AIP Conference Proceedings,* Volume 370, pp. 385-388.

Duraes, L., Campos, J. & Portugal, A., 1998. Reaction path of energetic materials using THOR code. *AIP Conference Proceedings,* Volume 429, pp. 341-344.

Fedorov, A. V. et al., 2011. Determination of Parameters of Detonation Waves in PETN and HMX Single Crystals. *Combustion, Explosion, and Shock Waves,* 52(5), pp. 601-605.

Fuller, P. W. W., 2009. An introduction to high speed photography and photonics. 57(6), pp. 293-302.

Gois, J. C. M., 1989. *Pressão de detonação (aula prática).* Coimbra: Universidade de Coimbra.

Gois, J. C. M., 1995. *Influência das Micro Esferas Ocas de Vidro na Detonação da mistura Nitrometano-Polimetilmetacrilato.* Coimbra: Universidade de Coimbra.

Good Will Instrument Co., Ltd., 2019. *Digital Storage Oscilloscope GDS-3000 Series USER MANUAL,* Taiwan: Good Will Instrument Co., Ltd..

Gustavsen, R., Sheffield, S. A. & Alcon, R., 1998. *Progress in measuring detonation wave profiles in PBX 9501.* Snowmass, CO, United States, s.n.

Held, M., 1987. Determination of the Chapman- Jouguet Pressure of a High Explosive from One Single Test. *Def Sci J.,* Volume 37, pp. 1-9.

Held, M., 2002. Initiation Tests. *Propellants, Explosives, Pyrotechnics,* 27(1), pp. 39-43.

Heusinkveld, M. & Holzer, F., 1964. Method of Continuous Shock Front POsition Measurement. 35(9), pp. 1105-1107.

Hodges, R. V. & McCoy, L. E., 1999. Comparison of Polyvinylidene Fluoride (PVDF) Gauge Shock Pressure Measurements with Numerical Shock Code Calculations. *Propellants, Explosives, Pyrotechnics,* 24(6), pp. 353-359.

Hodges, R. V., McCoy, L. E. & Toolson, J. R., 2000. Polyvinylidene Fluoride (PVDF) Gauges for Measurement of Output Pressure of Small Ordnance Devices. *Propellants, Explosives, Pyrotechnics,* 25(1), pp. 13-18.

Hof, P. G. v., Cheng, L. K., Scholtes, J. H. G. & Prinse, W. C., 2007. Dynamic pressure measurement of shock waves in explosives by means of a fiber Bragg grating sensor. *27th International Congress on High-Speed Photography and Photonics,* Volume Proc. SPIE 6279.

Honour, J., 2009. A brief history of principles used in high speed cameras. 57(6), pp. 303-316.

Khurana, R. et al., 2011. Studies on Shock Attenuation in Plastic Materials and Applications in Detonation Wave Shaping. *J. Phys.: Conf. Ser.,* Volume 377, p. 012051.

Kubota, N., 2015. *Propellants and Explosives - Thermochemical Aspects of Combustion.* Weinheim: Wiley-VCH Verlag GmbH & Co..

Kucera, J. et al., 2018. Experimental Determination of Acceleration of Explosively Driven Metal by Photonic Doppler Velocimetry in the Process of Explosive Welding. *Propellants Explos. Pyrotech.,* Volume 42, pp. 479-487.

Künzel, M., Anastacio, A. C., Kucera, J. & Pachman, J., 2017. *OPTIMEX: Detonation pressure determination using passive optical system.* Pardubice, Czech Republic, s.n., pp. 726-730.

Kury, J. W., Breithaupt, R. D. & Tarver, C. M., 1999. Detonation waves in trinitrotoluene. *Shock Waves,* Volume 9, pp. 227-237.

Laser Components, 2016. *Fiber Optics 'TORAY'.* [Online]
Available at:
https://www.lasercomponents.com/fileadmin/user_upload/home/Datasheets/toray/pof-katalog.pdf

Lee, J. H. S., 2008. *The detonation Phenomenon.* Cambridge: Cambridge University Press.

Lee, L. M., Graham, R. A., Bauer, F. & Reed', R. P., 1988. Standartized Bauer PVDF Piezoelectric polymer shock gauge. *Le Journal de Physique Colloques,* 9(49), pp. C3-651/657.

Lorenz, K. T., Lee, E. L. & Chambers, R., 2015. A Simple and Rapid Evaluation of Explosive Performance – The Disc Acceleration Experiment. *Propellants Explos. Pyrotech.,* Volume 40, pp. 95-108.

Marsh, S. P., 1980. *LASL Shock Hugoniot Data.* Los Alamos : University of California Press.

Martineau, R. L., Anderson, C. A. & Smith, F. W., 2000. Expansion of Cylindrical Shells Subjected to Internal Explosive Detonations. 40(2), pp. 219-225.

McCall, G. H., Bongianni, W. L. & Miranda, G. A., 1985. Microwave interferometer for shock wave, detonation, and material motion measurements. 56(8), pp. 1612-1618.

McMillan, C. F. et al., 1988. Velocimetry of fast surfaces using Fabry–Perot interferometry. *Review of Scientific Instruments,* 59(1), pp. 1-20.

McNesby, K. L., Biss, M. M., Benjamin, R. A. & Thompson, R. A., 2013. *Optical Pressure Measurements of Explosions,* Aberdeen Proving Ground, MD, USA: Army Research Laboratory.

Mendes, R. A. L., 1994. *Contribuição para o estudo da geração e caracterização de ondas de choque,* Coimbra: Universidade de Coimbra.

Mendes, R. A. L., 2000. *Iniciação de Detonação de Explosivo Plástico de RDX.* Coimbra: Universidade de Coimbra.

Mendes, R., Campos, J., Gois, J. & Moutinho, C., 1993. *Shock initiation and detonation stability of industrial explosives.* Karlsruhe, Fraunhofer Institute fur Chemische Technologie, pp. 29.1 - 29.13.

Mendes, R., Ribeiro, J. B., Plaksin, I. & Campos, J., 2012. Non ideal detonation of emulsion explosives mixed with metal particles. *AIP Conference Proceedings,* Volume 1426, pp. 267-270.

Mendes, R., Ribeiro, J., Plaksin, I. & Campos, J., 2006. *Detonation wave characterization of aluminized and non-aluminized emulsion explosives.* Karlsruhe, Fraunhofer Institute for Chemical Technology, pp. V15.1-11.

Mendes, R. et al., 2014. Differences between the detonation behavior of emulsion explosives sensitized with glass or with polymeric micro-balloons. *Journal of Physics: Conference Series,* Volume 500, pp. 1-7.

Meyer, R., Köhler, J. & Homburg, A., 2007. *Explosives.* Weinheim: Wiley-VCH Verlag GmbH.

Minshall, S., 1955. Properties of Elastic and Plastic Waves Determined by Pin Contactors and Crystals. *Journal of Applied Physics,* 26(4), pp. 463-469.

Morra, J., 2015. *6 Digital Oscilloscopes For Testing High-Speed Communications.* [Online]
Available at: https://www.electronicdesign.com/technologies/test-measurement/article/21800956/6-digital-oscilloscopes-for-testing-highspeed-communications
[Acedido em 2020].

Murata, K. & Kato, Y., 2010. Application of PVDF Pressure Gauge for Pressure Measurements of Non-ideal Explosives. *Int. J. Soc. Mater. Eng. Resour.,* 17(2), pp. 112-114.

Murphy, M. J., Tilger, C. F. & Hill, L. G., 2019. *Nanosecond Imaging Techniques to Characterize Detonator Breakout Performance.* Portland, Loas Alamos National Laboratory, pp. 1-7.

Nevstad, G. O., 2015. *Introduction of ionization pin probes to measure detonation velocity,* Kjeller: Norwegian Defence Research Establishment.

Oppenheim, A. K., 2008. *Dynamics of Combustion Systems.* Leipzig: Springer-Verlag Berlin Heidelberg New York.

Optronis GMBH, 2020. *OptoScope SC-20 Systems.* [Online]
Available at: https://optronis.com/en/products/optoscope-sc-20-systeme/
[Acedido em May 2020].

OZM Research s.r.o, 2016. *Explosive Testings.* [Online]
Available at: https://mueller-instruments.de/fileadmin/Downloads/deutsche_medien/OZM-Katalog_2016.pdf

OZM Research, s.d. *Explosive Testings, EXPLO-5 product datasheet.* [Online] Available at: https://mueller-instruments.de/fileadmin/Downloads/instruments-medien/Analysensoftware_-_Explo-5.pdf

Pachmáň, J. et al., 2017. OPTIMEX: Measurement of Detonation Velocity with a Passive Optical Fibre System. *Central European Journal of Energetic Materials,* Volume 14 (1), pp. 233-250.

Pachman, J., Künzel, M., N˘emec, O. & Majzlík, J., 2018. A comparison of methods for detonation pressure. *Shock Waves,* Volume 28, pp. 217-225.

Petel, O. E. et al., 2004. Detonation Propagation in Shock-Compressed Liquid Explosives. 706(883), pp. 883-886.

Plaksin, I. et al., 2001. *Detonation meso-scale tests for energetic materials.* Atlanta, Melville, N.Y.: American Institute of Physics, pp. 922-925.

Plaksin, I. et al., 2002. Detonation meso-scale tests for energetic materials. *AIP Conference Proceddings,* Volume 620, pp. 922-925.

Plaksin, I. et al., 2002 (2). *Detonation study of energetic micro-samples.* S. Diego, California, USA, s.n., pp. 42-50.

Plaksin, I. et al., 2006. Meso-scale probing of CRZ structure in PBX: DW oscillations from ignition to failure. *AIP Conference Proceedings,* Volume 845, pp. 1002-1005.

Plaksin, I. et al., 2008. Novelties in physics of explosives welding and powder compaction. *Materials Science Forum 566,* pp. 135-140.

Plaksin, I. et al., 2009. Radiation-induced percursors in crystalline energetic composites. *AIP Conference Proceedings,* Volume 1195, pp. 137-140.

Plaksin, I. et al., 2010. Effect of the Reaction Light Absorption on the Formation of the Detonation Reaction Zone 3DStructure. *14th International Detonation Symposium, IDS,* pp. 241-250.

Pooley, J., Price, E., Ferguson, J. & Ibsen, M., 2019. Detonation Velocity Measurements Using Rare-Earth Doped Fibers. 19(1697), pp. 1-8.

Prinse, W. et al., 1999. *Fibre-Optical techniques for measuring various properties of shock waves.* Moscow, Proceedings of SPIE, pp. 1-6.

Quaresma, J. et al., 2016. *Hot spots sensitization and optical detonation measurements of emulsion explosives.* Karlsruhe, Germany, Fraunhofer ICT.

Quaresma, J., Deimling, L., Campos, J. & Mendes, a. R., 2021. Characterization of the Detonation Pressure of a PETN Based PBX with the Optical Active Method. *Propellants Explos. Pyrotech.,* Volume 46, pp. 1-9.

Quaresma, J., Deimling, L., Campos, J. & Mendes, R., 2019. *Optical fiber metrology for detonation velocity measurements.* Pardubice, University of Pardubice.

Quaresma, J., Deimling, L., Campos, J. & Mendes, R., 2020. Active and Passive Optical Fiber Metrology for Detonation Velocity Measurements. *Propellants Explos. Pyrotech.,* Volume 45, pp. 921-931.

Quaresma, J. et al., 2018. *Optical fiber metrology for detonation and shock transmission measurements.* Karlsruhe, Fraunhofer ICT.

Quaresma, J. F. P. O., 2013. *Homemade Explosives based in Ammonium and Urea Nitrates.* Coimbra: Universidade de Coimbra.

Rodriguez, G. & Gilbertson, S. M., 2017. Ultrafast Fiber Bragg Grating Interrogation for Sensing in Detonation and Shock Wave Experiments. 17(248), pp. 1-20.

Rodriguez, G. et al., 2015. Coherent pulse interrogation system for fiber Bragg grating sensing of strain and pressure in dynamic extremes of materials. *Optics Express,* 23(11), pp. 14219-14233.

Rodriguez, G. et al., 2014. *Fiber Bragg sensing of high explosive detonation experiments at Los Alamos National Laboratory.* Seatle, Journal of Physics: Conference Series, pp. 1-9.

Sandberg., R. L. et al., 2014. Embedded optical probes for simultaneous pressure and temperature measurement of materials in extreme conditions. *Journal of Physics: Conference Series,* Volume 500, p. 142031.

Sollier, A. et al., 2012. Dynamics of the detonation products of a TATB based high explosive: Photon doppler velocimetry and high-speed digital shadowgraphy of expanding species. 1426(339), pp. 339-342.

Song, S.-y. & Lee, J. W., 1989. *A detonation pressure measurement system employing high resistance manganin foil gauge.* Portland, Oregon, USA, s.n., pp. 471-476.

Specialised Imaging, s.d. *Instrumenting Cylinder Expansion Test. EMTAP Test No 44.* [Online]
Available at: https://www.specialised-imaging.com/application/files/8915/4292/7609/SI_RA__Cylinder_Expansion_Test_Proposal_v1d.pdf
[Acedido em May 2020].

Strand, O. T. et al., 2006. Compact system for high-speed velocimetry using heterodyne techniques. *Rev. Sci. Instrum.,* Volume 77, pp. 083108-1/8.

Sućeska, M., 1995. *Test Methods for Explosives.* New York: Springer-Veria.

Sućeska, M., 1997. Experimental determination of detonation velocity. *Fragblast,* Volume 1:3, pp. 261-284.

Suceska, M., 1999. Evaluation of Detonation Energy from EXPLO5 Computer Code Results. *Propellants Explos. Pyrotech.,* 24(5), pp. 280-285.

Sućeska, M., 2001. *EXPLO5 - Computer program for calculation of detonation parameters.* Karlsruhe, Germany, Fraunhofer ICT.

Tarver, C. M., 2010. Corner Turning and Shock Desensitization Experiments plus Numerical Modeling of Detonation Waves in the Triaminotrinitrobenzene Based Explosive LX-17. *J. Phys. Chem. A,* Volume 114, pp. 2727-2736.

Tarver, C. M., Kury, J. W. & Breithaupt, R. D., 1997. Detonation waves in triaminotrinitrobenzene. *Journal of Applied Physics,* 82(8), pp. 3771-3782.

Taylor, K., s.d. *Dissecting time... A review of the development of the ultra high-speed imaging techniques.* [Online]
Available at: https://www.specialised-imaging.com/application/files/4615/4297/2831/dissecting-time.pdf
[Acedido em April 2020].

Tete, A. D., Y.Deshmukh, A. & Yerpude, R. R., 2014. Design and Implementation of Sensor for Velocity of Detonation Measurement. *IOSR Journal of Electrical and Electronics Engineering,* 9(3), pp. 77-83.

THORLABS, 2019. *Step-Index Multimode Fiber Optic Patch Cables: SMA to SMA.* [Online]
Available at: https://www.thorlabs.com/drawings/9655a308cc4c45a0-0DF223BC-AA6C-6A99-8C67F42BB188273A/FG200UEA-SpecSheet.pdf

Toray Industries, Inc., 2006. *Raytela polymer optical fiber.* [Online]
Available at: https://www.toray.co.jp/english/raytela/index.html

Urtiew, P. A., Erickson, L. M., Hayes, B. & Parker, N. L., 1986. Pressure and particle velocity measurements in solids subjected to dynamic loading. *Combust Explos Shock Waves,* Volume 22, pp. 597-614.

Urtiew, P. A. & Hayes, B., 1991. Empirical estimate of detonation parameters in condensed explosives. *Journal of Energetic Materials,* 9(4), pp. 297-317.

Utkin, A., Lavrov, V. & Mochalova, V., 2012. Experimental determination of detonation parameters of explosives based on amonium nitrate. *AIP Conference Proceedings,* Volume 1426, pp. 205-208.

Vantine, H. et al., 1980. Precision stress measurements in severe shock-wave environments with low impedance manganin gauges. *Review of Scientific Instruments,* Volume 51, pp. 116-122.

Venkatesh, H. S. et al., 2001. *Evaluation of explosives performance through in-the-hol detonation velocity measurement,* Kolar Gold Fields, Karnataka, India: National Institute of Rock Mechanics.

Vuppuluri, V. S. et al., 2018. Detonation Performance Characterization of a Novel CL-20 Cocrystal Using Microwave Interferometry. Volume 43, pp. 38-47.

Wei, P., Lang, H., Liu, T. & Xia, D., 2017. Detonation Velocity Measurement with Chirped Fiber Bragg Grating. 17(2552), pp. 1-11.

Xiaoyan, W., Hui, Z., Jian, W. & Gao, W., 2011. *Design of the Fiber Detonation Velocity Measuring System Based on the FPGA.* United Sates, 2011 International Conference on Electronics and Optoelectronics (ICEOE 2011).

Xing, H. Z. et al., 2017. High-Speed Photography and Digital Optical Measurement Techniques for Geomaterials: Fundamentals and Applications. Volume 50, pp. 1611-1659.

Xing, X. et al., 2019. The Detonation Properties Research on TKX-50 in High Explosives. *Propellants, Explos. Pyrotech.,* Volume 44, pp. 408-412.

Yiannakopoulos, G., 1990. *A review of manganin gauge technology for measurements in the gigapascal range,* Maribyrnong, Australia: DSTO Materials Research Laboratory.

Yunosheva, A. S., Plastinin, A. V. & Sil'vestrov, V. V., 2012. Effect of the Density of an Emulsion Explosive on the Reaction Zone Width. *Combust Explos Shock Waves,* 48(3), pp. 319-327.

Zhang, G. et al., 2018. A Manganin Thin Film Ultra-High Pressure Sensor for Microscale Detonation Pressure Measurement. *Sensors,* 18(3), pp. 736-747.